Title

Rational Design of High-Performance Electrocatalysts for Electrochemical Energy Technologies: From Structural Engineering of Nanocomposite Catalysts to Mechanistic Understanding of Electrocatalytic Activity

Author

Lu, Bingzhang

Publication Date

2020

Peer reviewed|Thesis/dissertation

UNIVERSITY OF CALIFORNIA
SANTA CRUZ

RATIONAL DESIGN OF HIGH-PERFORMANCE ELECTROCATALYSTS FOR ELECTROCHEMICAL ENERGY TECHNOLOGIES: FROM STRUCTURAL ENGINEERING OF NANOCOMPOSITE CATALYSTS TO MECHANISTIC UNDERSTANDING OF ELECTROCATALYTIC ACTIVITY

A dissertation submitted in partial satisfaction
of the requirements for the degree of

DOCTOR OF PHILOSOPHY

in

CHEMISTRY

by

Bingzhang Lu

December 2020

This Dissertation of Bingzhang Lu
Is approved:

Professor Shaowei Chen, Chair

Professor Yuan Ping

Professor Ilan Benjamin

Quentin Williams

Interim Vice Provost and Dean of Graduate Studies

TABLE OF CONTENT

LIST OF FIGURES

Chapter 1

Figure 5. High-resolution XPS scans of (a) C1s, (b) N 1s and (c) Fe 2p electrons in the series of nanofiber precursors and doped carbon nanotubules. Grey curves are experimental data and colored curves are deconvolution fits. (d) Content distributions of various types of nitrogen dopants in the samples.

Figure 6. Raman spectra of the Fe,N-codoped carbon (MF-Fe-T) nanotubules.

Figure 7. ORR performance of N and Fe N doped carbon nanofibers.

Figure 8. The configuration of OOH species on neighbor carbon of pyridinic N (a) before and (b) after relax calculation.

Figure 9. Atomistic models of N and FeN_4-doped graphene. The numbers indicate tested candidate active sites for ORR activity.

Figure 10. Correlation between the adsorption energies of the OOH and OH intermediate species.

Figure 11. Reaction free energy diagram of reaction steps (1) – (4) in ORR at the various atomistic sites that are defined in Figure 9.

Figure 12. Density of state (DOS), projected density of states and spin density distribution in N doped and Fe-N4 doped graphene systems. DOS plots of (a) Graphene 2Nm, (b) Zoom-in around the Fermi level of panel (a) showing the DOS contribution of various carbon sites (Figure 9), and (c) Normal FeN_4. The yellow broken lines show the location of the Fermi level. Spin density distribution plots of

(d) Graphene 2Nm and (e) Normal FeN_4. The green isosurface is the unpaired electron distribution (spin up-spin down).

Figure 13. (a, c) Side view and simulated STM image of normal FeN_4 doped graphene sheets. (b, d) Side view and simulated STM image of Stone-Wales FeN_4 (FeN_4 SW) doped graphene sheets. (e) Density of state (DOS) of normal FeN_4 and FeN_4 SW doped graphene sheets. (f) DOS of FeN_4 SW and Fe 3d. (g) Free energy diagrams of ORR processes on normal FeN_4, normal FeN_3, FeN_4SW and FeN_3SW at the applied of 0.9 V.

Figure 14. Top view of normal FeN_4 and FeN_4 SW moieties in graphene.

Figure 15. Top view and side view of normal and SW FeN_3 and FeN_4 moieties in graphene.

Figure 16. Identification of nanowrinkle in the sample of the $NCA_{C\text{-}Zn}$/Fe carbon aerogel. AFM images of $NCA_{C\text{-}Zn}$/Fe aerogels: (a) adhesion force image and (b) current flow image.

Figure 17 ORR performance in alkaline media. (a) ORR polarization curves of CA_C, CA_C/Fe, NCA_C/Fe and $NCA_{C\text{-}Zn}$/Fe, as well as the Pt/C at 1600 rpm in 0.1 M KOH at the potential sweep rate of 5 mV s^{-1}. (b) H_2O_2 yield of CA_C, CA_C/Fe, NCA_C/Fe, $NCA_{C\text{-}Zn}$/Fe and Pt/C.

Chapter 3

Figure 2. Interfacial structures of alkyne-modified TiO_2: (a) when the ligands are placed on Ti atoms initially, and (b) the corresponding structure after relax calculation where the ligands moved to the O atoms spontaneously.

Figure 3. (A) FTIR spectra of octyne, EPy, TiO_2-HC8, and TiO_2-EPy. (B) ^1H NMR spectra of TiO_2-HC_8 and TiO_2-EPy nanoparticles in CD_2Cl_2. (C) Configuration of the TiO_2-alkyne interface, with the atoms in blue, red, brown and white for Ti, O, C, and H, respectively.

Figure 4. Total density of states (TDOS) calculated by HSE and PBE of (a) TiO_2-alkyne (b) TiO_2-carboxy structures.

Figure 5. (A) UV-vis spectra of TiO_2-HC8. Inset is the corresponding Tauc plot, where α is the absorbance and $h\nu$ is the photon energy. (B) SSPL spectra of TiO_2-HC8 at various excitation wavelengths. The shadowed ones represent maximal emissions at select excitation wavelengths. (C) Schematic illustration of the band structure of TiO_2-HC8 based on the SSPL results. (D) Total density of states (TDOS) plot of TiO_2-C≡C-CH_3 (black curve) and projected density of states (PDOS) plot of the 2p orbitals of C2 (red), C1 (green), and O (blue) atom, and the 3d orbital of the Ti (pink) atom. The corresponding energy-resolved charge density distributions are included in panel (E) for zone I, panel (F) for zone II, panel (G) for zone III, and panel (H) for zone IV. The isovalue is 0.1 e/au^3 for panels (E) and (H), and 0.005 e/au^3 for panels (F) and (G).

Figure 6. Optimized geometrical structures by CDFT calculation of (A) Ti(OH)3-O-C≡C-CH=CH2, and (B) Ti(OH)3-OOC-CH=CH2. The extra electron is placed and localized on -CH=CH2 and -Ti(OH)3, respectively, for the calculations of electronic coupling (Hab) between the two sites.

Figure 7. (a) Three-layer fixed bottom model with two ligands on the surface, and (b) 3, (c) 5, (d) 9-layer relaxed surface model with alkyne ligands on the surface. (e) The corresponding total density of states (TDOS) profiles of the various models.

Figure 8. Total density of states (TDOS) and interfacial configurations of a pristine TiO_2 slab, and a slab functionalized with carboxy (-COOH), alkyne (-C≡C-), and alkane (-CH_2-CH_2-) ligands.

Figure 9. Charge transfer between ligands and metal oxide slabs: (A) ZnO-alkyne, (B) RuO2-alkyne, (C) ZnO-carboxy, and (D) RuO2-carboxy. The cyan area indicates electron loss, and yellow area indicates electron gain.

Figure 10. Charge transfer between ligand and TiO_2 slab: (A) TiO_2-alkyne (B) TiO_2-carboxy. The cyan area indicates electron loss and yellow area indicates electron gain. The isosurface value is 0.003 e/au^3.

Figure 11. (A) UV-vis spectra of monomeric EPy, TiO_2-HC8, and TiO_2-EPy. Inset shows the corresponding Tauc plots. (B) Normalized steady-state excitation and emission spectra of monomeric EPy, TiO_2-HC8, and TiO_2-EPy. (C) Schematic illustration of the charge transfer process at the Ti-O-C≡C-Py interface. (D) TRPL decay profiles of monomeric EPy, TiO_2-HC8 and TiO_2-EPy. The grey curve is the

LIST OF TABLES

Chapter 2

Chapter 3

Chapter 4

RATIONAL DESIGN OF HIGH-PERFORMANCE ELECTROCATALYSTS FOR ELECTROCHEMICAL ENERGY TECHNOLOGIES: FROM STRUCTURAL ENGINEERING OF NANOCOMPOSITE CATALYSTS TO MECHANISTIC UNDERSTANDING OF ELECTROCATALYTIC ACTIVITY

Bingzhang Lu

ABSTRACT

Developing sustainable, high efficiency and clean energy technologies is one of the urgent missions for modern chemistry. Fuel cells with their high energy conversion efficiency, high reliability, low CO_2 emission and extensive applications, show promising outlook among all new energy devices. However, the expensive electrocatalyst and their sluggish electrode reaction kinetics greatly hamper the commercialization of fuel cells. Thus, the advanced electrocatalyst should be designed and synthesized, meanwhile, the reaction mechanism should be better understood for material structural modification and activity enhancement. My thesis focused on design, synthesis of nano materials for advanced electrocatalysts and understanding and exploring the catalytic mechanism. Based on series of research projects, a systemic strategy framework for electrocatalyst preparation and understanding is established by combination of experimental and theory method. This framework contains a wide range of aspect of electrocatalyst studies.

Specifically, **Chapter 1** introduces the background of fuel cell, water electrolyzer and their related critical electrochemistry reactions. A systematic overview of electrocatalyst design, modification and reaction mechanism understanding is

illustrated. Based on the current and previous results, the strategy loop and the central dogma of electrocatalyst design is proposed. Each of the work introduced in other chapters was carried out based on one or several aspects of the strategy loop, which including material synthesis, activity measurement, active site revealing, electronic structure understanding, modification of electronic structure. **Chapter 2, chapter 3, chapter 4** introduces series work of carbon nanowires for electrocatalyst. These works include the aspects of material synthesis, activity understanding, active site identifying or understanding the source of activity. Specifically, **chapter 2** introduces the design and synthesis of a novel nitrogen and iron-doped carbon nanowires material for great activity for alkaline oxygen reduction reaction, with the performance even surpass the commercial platinum carbon. Moreover, the active site was identified, and their activity was compared as the order of Stone-Wales FeN4 sites> Normal FeN4 sites> neighboring carbon atom of nitrogen atom in the carbon matrix. In addition, the source of activity of each important activity site were also revealed. The great activity of FeN_4 comes from the d-orbital of Fe atom provide great chance for oxygenous intermediate species to absorb and detach. While, the neighboring carbon to nitrogen atom have much better ability for adsorption than normal carbon, due to the charge transfer from themselves to the nearby nitrogen atoms. **Chapter 3** introduces the design and synthesis of novel ruthenium and nitrogen doped carbon nanowires for excellent activity for hydrogen evolution reaction in alkaline electrolyte, with the performance better than commercial platinum carbon and other noble metal-based material as reported previously. Moreover, it was

identified that the activity is coming from a novel single atom ruthenium site, RuC_2N_2 structure embedded in the carbon, other than ruthenium nanoparticle or normal RuN_4 sites as assumed previously. The ruthenium and its neighboring carbon atoms of RuC_2N_2 can provide efficient water dissociation process which is critical for overall reaction. **Chapter 4** introduces a typical work for adopting theoretical calculation to reveal active sties and for guiding experimental electrocatalyst synthesis. In this work, a high throughput first principle calculation was first carried out and find that the platinum needs a minimum domain size (about 0.9 nm of diameter) to maintain activity for catalyzing oxygen reduction reaction. Any platinum species smaller than that limit will suffer great difficulty of adsorbing oxygen molecules due to the lack of states and electron near Fermi level. Moreover, it was further revealed cobalt atom doping can greatly assist in oxygen adsorption when the domain size of platinum is too small. The following experimental work confirmed the theoretical finding and successfully synthesized PtCo few atom clusters as high efficiency electrocatalyst for oxygen reduction reaction, which can have an ultrahigh mass activity as much as 48 times better than commercial platinum carbon.

Chapter 5 and **chapter 6** mainly focus on several individual works about interfacial charge transfer of nanomaterial and its induced electrocatalytic activity enhancement. For instance, **Chapter 5** introduce several works about charge transfer induced electrochemical activity enhancement. In one work, it was observed oxygen vacancy doped TiO2 can transfer electrons to the palladium nanoparticles loaded on them. This charge transfer can significantly enhance the activity of ethanol oxidation

reaction catalyzed by palladium nanoparticles. In another work, it was found that black phosphorus can donate significant number of electrons to the platinum, gold and silver nanoparticle load on it. This charge transfer can induce the activity decrease for platinum nanoparticles and increase for gold and silver nanoparticles towards oxygen reduction reaction. **Chapter 6** introduces developing new methods for charge transfer. Specifically, TiO_2 nanoparticles functionalizing with alkyne ligand can induce significant one-way charge transfer from ligand to surface of metal oxide through M-O-C≡C- core-ligand linkages. This linkage can also induce novel states inside of band gap. Moreover, this unique charge transfer can be universally observed on other metal oxide, exhibiting a powerful ability for increasing the charge density of metal oxide catalyst.

Finally, all of finding are systemically summarized in **chapter 7**. In addition, a perspective of future works was put forward based on the previous works.

ACKNOWLEDGEMENT

Time flies very fast! I can still clearly remember the day of Sept 6, 2015, when I arrived at San Jose International Airport as my first-time setting foot in this great land. I had a very difficult time about everything for the first several weeks here. At very beginning, I didn't know if I could survive in this country and have no ideas about what I can do here. It is amazing that I could have a very productive five years and get my PhD degree! I am very grateful to thank the people who help me during these years.

Firstly, I gratefully thank my advisor, Professor Shaowei Chen for his great supporting in past five years. In these years, I learned a lot knowledge not only about experiment, electrochemistry, data analysis and paper writing, but also a integrate thinking of design a project. I benefited greatly from his patient guidance, abundant knowledge, innovative academic thought, cohesive and collaborative research team, as well as great opportunities he provided then I can finish these projects and have this long list of publications and awards. He also gives me valuable helps and critical advices about my live, postdoctoral searching and my future career planning. I much appreciate all his enthusiastic help to me in this five year! The experience I gain here will be a valuable treasure for my entire career and life.

I would like to thank Professor Yuan Ping, who directs my theoretical calculation works. I am very grateful that she kindly provides me a wonderful opportunity for this long-time collaboration, so I can finish series of high-quality research projects

combined experiment with theory. She generously provides me the computing resources, patiently instructs me theoretical work since very beginning and provides me many critical advices on research projects with her abundant knowledge and experience. She also gives me great help for my postdoctoral searching. I learned a lot during working with her and her groups these years and I expanded my research field significantly. I much appreciate that I could have this unique and wonderful experience as a chemical experimentalist.

I want to thank my committee professor, Professor Ilan Benjamin and Professor Nader Pourmand for generously offering their time throughout the oral qualifying exam, seminars and dissertation.

I also thank Dr. Peter Weiss, Dr. Randa Roland and Dr. Alegra Eroy-Reveles for directing my work as teaching assistant. Thank Ms. Karen Meece, Ms. Katie Cramton and Ms. Janet Jones for their great help. I would like to thank all professors and staff in our department who provides advice and help for me.

I would like to thank our lab members, students and visiting scholars, who provided a lot of help for my research and my life during these years. Especially, I would like to thank Dr. Peiguang Hu, Dr. Limei Chen, Dr. Lin Guo, Dr. Samantha Sweeney and Prof. Xiongwu Kang for their teaching me a lot of knowledge of chemistry and experiments. Thank Dr. Yi Peng, Dr. Ting He and Mr. Qiming Liu for help me a lot in my research. We constructively discussed about the research idea and had many successful collaborate projects together. Thank Dr. Christopher Deming, Dr. Jia En

Lu, Mr. Rene Mercado, and Mr. Forrest Nichols for help me measure my samples. Thank Ms. Carolin Wahl for constructive discussion about the science. Thank Mr. Re Mercado, Mr. Gustavo Chata and Ms. Carolin Wahl for teaching me driving and provide a lot of help of my life. We have a very good time in these years. Also Thank Mr. Rene Mercado, Mr. Gustavo Chata, Mr. John Diniz and Dr. Mauricio D. Rojas-Andrade taught me a lot of knowledge about American culture.

I would like to thank lab members of Ping lab for providing me great assistance about theoretical calculations. Especially, I would like to thank Dr. Feng Wu and Mr. Tyler Smart for their great help and collaboration in a series of critical projects.

I thank all of collaborator and expert who provide resources and advices to my work. Especially, I would like to thank Prof. Peng Zhang and Mr. David Morris for XAS measurement; thank Prof. Peng Gao, Prof. Jun Luo, Prof. Zhiming Zhang and Mr. Ning Li for TEM measurement; thank my father, Prof. Xiaoquan Lu who provides a lot of help about my research; thank Prof. Shaojun Guo, Prof. Sen Zhang, Prof. Liang Wang provides constructive suggestions for my research project.

I also would like to thank my friends in our neighbor labs, and we have a good time in the same department for these years. Especially I would like to thank Dr. Bin Yao, Dr. Jing Zhang for their great help in my life. We had a wonderful time living together for 4 years. Thanks Dr. Longbo Li, Dr. Tianyi Kou and Ms. Ke Xu for their help in these years.

Finally, I would like to thank my parents and family who always supporting me. And thank my girlfriend for her great support during the nearest two years.

I also thank the funding source for my research, including UCSC chancellors' dissertation year fellowship, Natural Science Foundation and Sigma Xi. Thank computational time provided by XSEDE and Brookhaven National Lab, thank XAS measurement from Argonne Nation Lab and sample characterization from Berkeley National Lab.

The text of this dissertation includes reprints of the following previously published material:

Bingzhang Lu, Tyler J. Smart, Dongdong Qin, Jia En Lu, Nan Wang, Limei Chen, Yi Peng, Yuan Ping, and Shaowei Chen, "Nitrogen and Iron-Codoped Carbon Hollow Nanotubules as High-Performance Catalysts Towards Oxygen Reduction Reaction: A Combined Experimental and Theoretical Study", Chem. Mater., 2017, 29, 5617.

Ting He, Bingzhang Lu, Yang Chen, Yong Wang, Yaqiang Zhang, John L. Davenport, Alan P. Chen, Chih-Wen Pao, Min Liu, Zhifang Sun, Alexander Stram, Alexander Mordaunt, Jairo Velasco Jr., Yuan Ping, Yi Zhang, Shaowei Chen, "Nanowrinkled Carbon Aerogels Embedded with FeNx Sites as Effective Oxygen Electrodes for Rechargeable Zinc-Air Battery", Research, 2019, 6813585.

Bingzhang Lu, Lin Guo, Feng Wu, Yi Peng, Jia En Lu, Tyler J. Smart, Nan Wang, Y. Zou Finfrock, David Morris, Peng Zhang, Ning Li, Peng Gao, Yuan Ping, and Shaowei Chen, "Ruthenium atomically dispersed in carbon outperforms platinum toward hydrogen evolution in alkaline media", Nat. Commun., 2019, 10, 631.

Yi Peng, Bingzhang Lu, Limei Chen, Nan Wang, Jia En Lu, Yuan Ping, and Shaowei Chen, "Hydrogen evolution reaction catalyzed by ruthenium ion-complexed graphitic-like carbon nitride nanosheets", J. Mater. Chem. A, 2017, 5, 18261.

Bingzhang Lu, Qiming Liu, Forrest Nichols, Rene Mercado, David Morris, Ning Li, Peng Zhang, Peng Gao, Yuan Ping, and Shaowei Chen "Oxygen Reduction Reaction Catalyzed by Carbon-Supported Platinum Few-Atom Clusters: Significant Enhancement by Doping of Atomic Cobalt", Research, 2020, 9167829.

Bingzhang Lu, Bin Yao, Graham Roseman, Christopher P. Deming, Jia En Lu, Glenn L. Millhauser, Yat Li and Shaowei Chen, "Ethanol oxidation reaction catalyzed by palladium nanoparticles supported on hydrogen-treated TiO2 nanobelts: Impacts of oxygen vacancies", ChemElectroChem, 2017, 4, 2211

Yi Peng, Bingzhang Lu, Nan Wang, Jia En Lu, Chunhong Li, Yuan Ping, Shaowei Chen, "Oxygen Reduction Reaction Catalyzed by Black Phosphorus-Supported Metal Nanoparticles: Impacts of Interfacial Charge Transfer", ACS Appl. Mater. Interfaces, 2019, 11, 24707.

Yi Peng, Bingzhang Lu, Feng Wu, Fengqi Zhang, Jia En Lu, Xiongwu Kang, Yuan Ping, and Shaowei Chen, "Point of Anchor: Impacts on Interfacial Charge Transfer of Metal Oxide Nanoparticles", J. Am. Chem. Soc., 2018, 140, 15290.

The corresponding author, Professor Shaowei Chen, listed in the publications, directed and supervised the research which forms the basis for the dissertation.

Chapter 1 Introduction

1.1. Background and overview

The rapid increase of energy consumption and the increasing impacts on the environment are emerging challenges for the development of human society.[1-3] It has been recognized that traditional fossil fuels, a non-sustainable energy source, will be depleted in the foreseeable future.[4] Moreover, significant greenhouse gas emission arising from the exploitation, transportation and consumption has caused great environmental problems.[5] For example, the leakages of oil have caused long-time ecological disaster in many areas, and the high consumption of fossil fuels leads to significant air pollution and increasing CO2 concentration to the highest level of history.[6, 7] To resolve these issues, developing sustainable, high efficiency and clean energy technologies is one of the urgent missions for modern chemistry. Towards this end, extensive studies have been carried out focusing on the development of new energy conversion and storage technologies, such as lithium ion/air batteries,[8, 9] photovoltaic,[10, 11] solar cell,[12-14] etc.

Among these, proton exchange membrane fuel cells (PEMFC) have shown unique advantages, owing to their high energy conversion efficiency, high power density, low or zero CO_2 emission and ease of operation.[15-17] The main component of a fuel cell includes three parts: anode, cathode and electrolyte (Figure 1). The anode and cathode are the places where reactions happen, while the membrane separates the electrolyte into the

anode and cathode compartments. The performance of the fuel cell is largely dependent upon the electrocatalysts loaded on the two electrodes. Thus this dissertation is focused on the rational design of effective nanocomposites as high-performance electrocatalysts for fuel cell technologies.

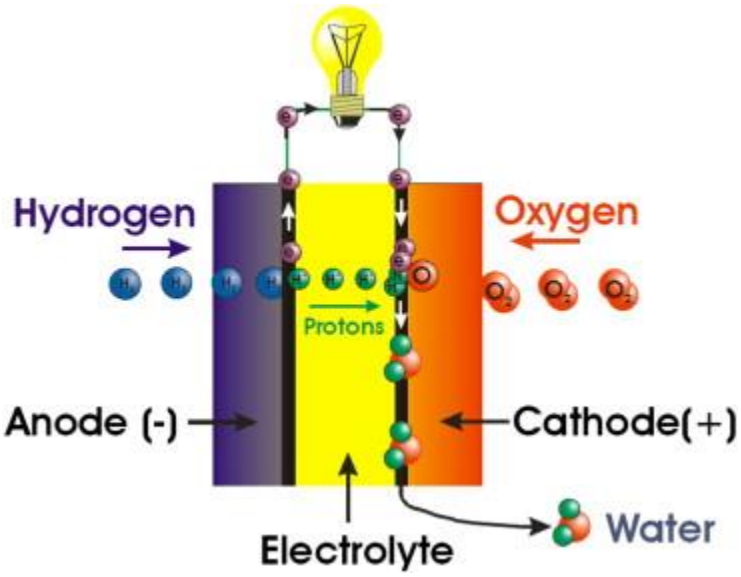

Figure 1. Schematic design of the PEM fuel cell, copyright from reference[18]

1.2. Electrochemistry reactions of fuel cells and water electrolyzers

1.2.1 Oxygen reduction reaction

Oxygen reduction reaction (ORR) occurs at the cathodes of fuel cells, water electrolyzers, and metal-air batteries, via either the four-electron pathway,

$$O_2 + 4H^+ + 4e^- = 2H_2O \quad \text{(acidic electrolyte)} \qquad (1)$$

$$O_2 + 2H_2O + 4e^- = 4OH^- \quad \text{(alkaline electrolyte)} \qquad (2)$$

or the two-electron pathway,

$$O_2 + 2H^+ + 2e^- = H_2O_2 \text{ (acidic electrolyte)} \quad (3)$$

or $$O_2 + 2e^- + 2H_2O = H_2O_2 + 2OH^- \text{ (alkaline electrolyte)} \quad (4)$$

For ORR in fuel cell, the 4e pathway is favored, with a minimal production of H_2O_2.[19]

Due to its complicated pathway and sluggish electron-transfer kinetics, ORR has been recognized as a major bottleneck that limits the fuel cell performance. Therefore, development of high-efficiency, high-durability, and low-cost catalysts represents a most important task for fuel cell technology. In an experimental test, the on-set potential (E_{onset}), half-wave potential ($E_{1/2}$), diffusion-limited current and H_2O_2 yield are the commonly used parameters in the evaluation of the electrocatalytic activity. In general, commercial Pt/C is used as the benchmark which can reach an E_{onset} of arounc +0.98 V vs reversible hydrogen electrode (RHE), $E_{1/2}$ of +0.83 to +0.85 V, a limited current density of 5-6 mA/cm^2, and a charge transfer number of ca. 4.

At shown, platinum loaded on carbon (Pt/C) is considered as the best catalyst. However, platinum-based catalysts have great limitation that hampers the industrialization of fuel cells: firstly, despite apparent activity, the performance remains unsatisfactory and cannot meet the requirement for the commercial setting. The electron-transfer kinetics of the cathode is ca. 10,000 times more sluggish than that of the anode and has been recognized as a bottleneck of the overall reaction. Secondly, the scarcity of Pt leads to an unfavorable cost for fuel cells. In fact, the cost of Pt accounts for about 50% of the overall cost of the fuel cell stack.[20] Moreover, platinum-based materials suffer from a

relatively poor durability, easy deactivation by CO poisoning, and strong fuel crossover effect.[21]

To mitigate these issues, a variety of ORR catalyst have been developed in recent years, which mainly focus on the following three groups of materials: noble metals, non-noble metals, and metal-free composites. For a noble metal catalyst, the most successful catalyst is Pt alloy, which shows great ORR activity, low Pt loading and high stability, such as Pt_3Ni,[22-24] Pt_3Co,[25, 26] Pt_3Fe,[27, 28] etc. In the development of single atom catalysis, even isolated atoms of noble metals have been attempted for ORR electrocatalysus; yet the activity is not satisfying in acidic media,[29-31] with a very few exceptions.[32-34] For the non-noble metal catalysts, the most representative one is based on Fe/N/C composites, which show great electrochemical activity due to the Fe-N_x sites.[35-37] Nitrogen-doped carbon is another class of important ORR catalysts.[38, 39] Some of these catalyst shows great activity in alkaline media, great CO resistance and high stability; however, the activity in acid remains a major challenge.

1.2.2 anode reaction: fuel oxidation

The anode reaction is the fuel oxidation reaction. The most common fuel is hydrogen gas, which can be adopted in PEMFC, alkaline fuel cell (AFC), solid oxide fuel cell (SOFC), etc. Other regular fuels include formic acid, methanol and ethanol, correspond to direct formic acid fuel cell (DFAFC), direct methanol fuel cell (DMFC), and direct ethanol fuel cell (DEFC). The respective anodic reaction is hydrogen oxidation reaction (HOR),

formic acid oxidation reaction (FAOR), methanol oxidation reaction (MOR), and ethanol oxidation reaction (EOR).

Specifically, for a hydrogen fuel cell, HOR at the anode can be shown as follows:

$$H_2 = 2H^+ + 2e^- \text{ (acidic electrolyte)} \quad (5)$$

Or $$H_2 + 2OH^- = 2H_2O + 2e^- \text{ (alkaline electrolyte)} \quad (6)$$

H_2 gas, having a very high power density of 140 MJ/Kg, 3 times as much as that of gasolines, is considered as the best fuel.[40] In PEMFC, HOR is generally considered as a facile reaction, with relatively fast kinetics even with a very low loading of platinum catalysts.[41] The major problem for HOR is the sluggish kinetics in an alkaline electrolyte, which is two orders of magnitude slower than that in an acidic electrolyte, even with a much higher Pt loading. To solve this problem, much cheaper and more stable Fe/N/C ORR catalysts are needed as the electrode catalyst. Indeed, substantial efforts have been devoted to enhancing the activity of noble metals-based material or developing non-noble metal-based catalysts.[42, 43]

Formic acid is another commonly used fuel, due to ease of transportation, nonflammability, and low crossover effect.[44, 45] The disadvantage of formic acid fuel is that the power output is relatively lower than that of H_2 and methanol, and DFAFC can produce only a limited energy. The FAOR can be expressed as

$$HCOOH = CO_2 + 2H^+ + 2e^- \text{ (acidic electrolyte)} \quad (7)$$

or $$HCOOH + OH^- = CO_2 + H_2O + 2e^- \text{ (alkaline electrolyte)} \quad (8)$$

Most research focuses on the improvement of the electron-transfer kinetics of Pt and Pd based nanocatalysts as the leading catalysts for this reaction.[46] Despite substantial progress so far, the toxicity and serious CO poisoning effect for Pt catalyst remains a major challenge.

With a high energy conversion efficiency, low pollution and convenience of storage,[47] DMFC is widely recognized as an important power source for portable electronics and electrical vehicles.[48] The power can be 15 times greater than that of lithium-ion battery in the same volume.[49] The disadvantage is that methanol can easily penetrate the membrane, short-circuit the electrodes and reduce the power output, the so-called crossover effect.[50] Another disadvantage is that CO may be generated during the reaction and poison the Pt catalyst.[51] The MOR can be expressed as

$$CH_3OH + H_2O = CO_2 + 6H^+ + 6e^- \text{ (acidic electrolyte)} \quad (9)$$

Or $$CH_3OH + 6\ OH^- = CO_2 + 5H_2O + 6e^- \text{ (alkaline electrolyte)} \quad (10)$$

Compare to other fuels, ethanol has unique advantages, although DEFC is not studied as much as other fuel cells. The major advantage of DEFL is the easy harvesting of ethanol from biomass and the mature supply chains.[52] Moreover, ethanol has a high boiling point, safe transportation, low toxicity, and minimal crossover effect.[53] Also, ethanol contains a higher energy density (24 MJ/L) than methanol (15.6 MJ/L). EOR is shown as

$$C_2H_5OH + 3H_2O = 2CO_2 + 12H^+ + 12e^- \text{ (acidic electrolyte)} \quad (11)$$

Or $$C_2H_5OH + 12OH^- = 2CO_2 + 9H_2O + 12e^- \text{ (alkaline electrolyte)} \quad (12)$$

Yet electrochemical oxidation of ethanol involves a significant energy barrier, due to the strong C-C bond. Up to now, there is no known efficient EOR catalyst to complete the 12-electron electrooxidation to form CO2 at ambient temperature.[54] Even for most active systems, the incomplete 2 or 4 electron transfer can slow the EOR and renders the DEFCs economically unviable.[55]

For the fuel oxidation reaction, the most common indicator is the current density and position of the forward peak and the ratio of the forward/backward peak heights in a cyclic voltammetry (CV) scan. A good catalyst should have a negative peak potential, a large peak height (high current density), and a high forward/backward peak ratio for a complete oxidation process. As shown above, most of the fuel oxidation reactions highly rely on noble metal catalysts, whose high costs greatly hamper the commercialization of fuel cell technologies. Except for HOR in acid, other reaction needs substantial improvement of the reaction kinetics, even if Pt is adopted as the catalyst.

1.2.3 water electrolyzer

As a reverse device of hydrogen fuel cell, water electrolyzer plays an important role in H_2 and O2 generation. H_2 is essential as a sustainable and clean energy; however, so far, 95% of H_2 is produced by the water gas shift reaction based on fossil fuels.[56, 57] For instance, the 2015 hydrogen levelized cost from water electrolysis is 4 USD/kg, which is 2 times higher than that from water gas shift or natural gas steam reforming, according to the report from the US Department of Energy (DOE Technical Targets for Hydrogen Production from Electrolysis). The main problem is the high price and sluggish kinetics

of catalysts, especially for OER in an acid electrolyte. Therefore, research of hydrogen evolution reaction (HER) and oxygen evolution reaction (OER) electrocatalysis has drawn a great deal of attention lately.

HER takes place at the negative electrode,

$$2H^+ + 2e^- = H_2 \text{ (acidic electrolyte)} \quad (13)$$

Or $$2H_2O + 2e^- = H_2 + 2OH^- \text{ (alkaline electrolyte)} \quad (14)$$

The most common factor for evaluating the HER activity is the overpotential (η_{10}) at 10 mA/cm^2. As the benchmark, commercial Pt/C can reach an η_{10} of -10 to -30 mV in 0.5 M H_2SO_4 and -50 mV in 1 M KOH.[58] Other important factors include Tafel slope, charge transfer resistance, faradaic efficiency and turnover frequency.[59] Platinum-based materials have long been considered as the most efficient HER catalyst, and reducing the Pt loading and finding low-cost substitutes for HER has become an important mission in the field. Many materials have shown remarkable activity in acid electrolytes, such as oxides, chalcogenides, phosphides and nitrides of nickel,[60, 61] cobalt[62, 63] and molybdenum[64], and heteroatom-doped carbon.[65-67] Another major problem of HER is the sluggish kinetics in alkaline electrolytes. This is because the water dissociation process is required which includes a sluggish H-O bond breaking process.[68] In fact, the electron-transfer kinetics in alkaline media on Pt is two orders of magnitude slower than that in acid.[69] Developing alkaline HER catalysts is therefore important, due to the extremely difficult counter reaction (OER) in an acid electrolyte. We developed ruthenium-based materials which exhibited a much better activity than Pt, with a much lower price. This

will be detailed in Chapter 3. Yet, many studies need to be carried out for non-noble materials.

The positive electrode is the place where oxygen evolution happens, as shown below,

$$2H_2O = O_2 + 4H^+ + 4e^-(\text{acid electrolyte}) \qquad (15)$$

$$4OH^- = O_2 + 2H_2O + 4e^- \text{ (alkaline electrolyte)} \quad (16)$$

This is a 4-electron transfer reaction with very sluggish kinetics. The reaction kinetics and catalyst stability have been studied extensively in recent years. The best catalysts are RuO_2 and IrO_2, but neither reaction kinetics nor the stability is satisfying. RuO_2 and IrO_2 can be easily oxidized into RuO_4 and IrO_3 and dissolved in the solution and lose activity during the reaction.[70] At present, many kinds of metal (hydro)oxides has been applied to catalyze OER in alkaline media, such as perovskite (ABO_3) spinel (AB_2O_4), double layer hydroxide (e.g., $Fe_xNi_{1-x}OOH$).[70, 71] Moreover, a variety of metal sulfides, selenides, nitrides and carbon materials have shown obvious activity in alkaline electrolyte.[70] The most challenge task is to develop OER catalyst in acid electrolyte. Except for RuO_2 and IrO_2, very few catalysts can reach an η_{10} under -750 mV (activity normalized by surface area of oxide).[72] Except for water splitting, OER also plays an important part in rechargeable metal-air batteries and artificial photosynthesis.

1.3. Nanomaterial design and synthesis for electrocatalysis

As mentioned, nanomaterial have served as the best class of catalysts. Nanoparticles, clusters and even single atom loaded on different support materials are effective catalysts

for ORR, OER, HER and other electrochemical reactions. The most commonly used materials are carbon-based nanocomposites, noble metal alloys, metal oxides, metal phosphides, metal sulfides and ligand functionalized materials.

1.3.1 Noble metal electrocatalysts

For most electrochemical reactions, noble metal-based materials are the catalysts of choice. Yet some of the catalytic activity and/or stability remains unsatisfying. For example, as mentioned above, Pt catalysts cannot achieve a satisfying ORR activity; RuO_2 and IrO_2 are generally considered as best OER catalysts; however, the activity and stability remains subpar for practical applications. There are two major goals for developing noble metal-based electrocatalyst: enhanced activity and reduced loading.

The enhancement of the electrocatalytic activity towards ORR, HER and fuel oxidation reactions by Pt, Pd, Ru or other noble metals has been widely reported, involving several strategies, such as alloying with a secondary metal to enhance the intrinsic activity, engineering surface to increase accessibility of active sites, and selective morphology for maximal exposure of active sites. Among these, noble metal alloy nanoparticles are widely used as leading ORR, HER and fuel oxidation electrocatalysts. For example, Stamenkovic et al.[73] discovered that Pt_3Ni alloy nanoparticles with dominant exposure of the (111) surfaces can reach a half-wave potential ($E_{1/2}$) 100 mV more positive than that of commercial Pt/C, with a 90-fold specific activity enhancement. Chen et al.[74] showed that Pt_3Ni 3-D nanoframe achieved a great activity enhancement of ORR and HER (Figure 2). Luo et al.[75] synthesized PdMo alloy nanosheets (width 100 nm and height 0.8

nm) “PdMo bimetallene”, where an enormous amount of Pd active sites were exposed and a ultrahigh mass activity of ORR was achieved that was 107 times higher than that of commercial Pd/C. PtCu,[76] PtNi,[77, 78] RuCo,[79] RuCu[80] and IrCo[81] nanoparticles have also been prepared and exhibited a much greater activity of HER than commercial Pt/C. As for the fuel oxidation reaction, PdCu, PtRu and PtSn nanostructures serve as leading catalysts for FAOR,[82, 83] MOR,[84, 85] EOR,[86, 87] respectively.

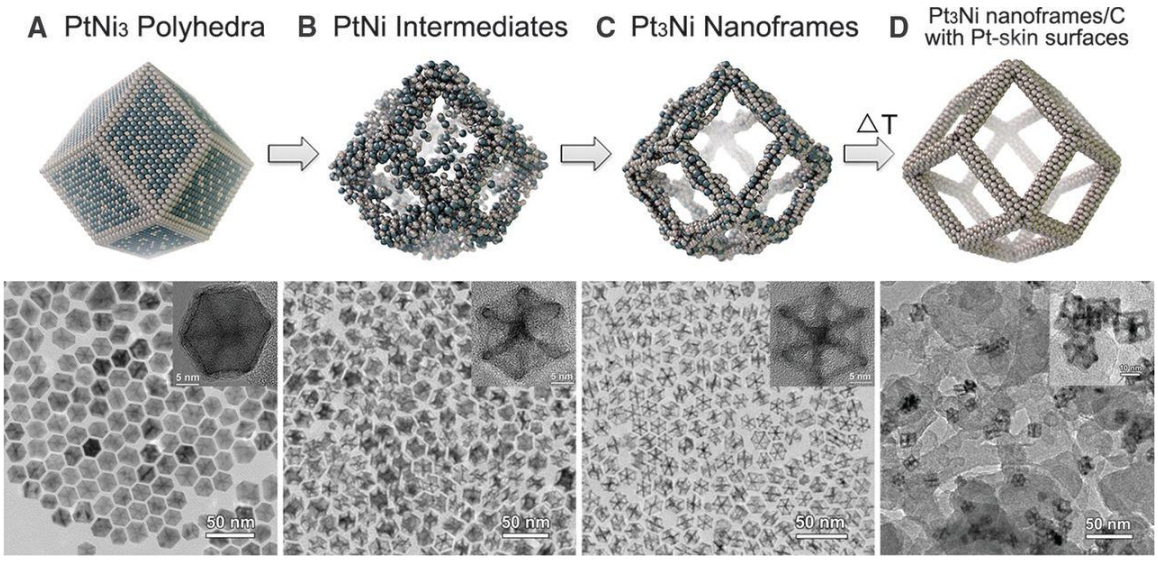

Figure 2 Schematic illustrations and corresponding TEM images of the samples obtained at four representative stages during the evolution process from polyhedra to nanoframes. Copyright from ref[74].

For OER, structural modification of IrO2 or RuO2 is a typical strategy to enhance the activity and stability. For instance, SrIrO3 shows an ultrahigh specific activity and durability as the leading catalyst.[72] Moreover, the 6H phase of SrIrO3 is found to be more active than 3C phase, can reach a low $\eta_{10,OER}$ of only 248 mV in an acid electrolyte.[88]

Ruthenium oxide-based OER catalysts also show great activity. For example, $Cr_{0.4}Ru_{0.6}O_2$ shows an $\eta_{10,OER}$ 178 mV in an acid electrolyte.[89] In another study, a Cu-doped RuO_2 polyhedral catalyst exhibits an $\eta_{10,OER}$ of 188 mV in an acid electrolyte.[90]

To reduce noble metal loading, the size of the noble metal nanoparticles needs to be reduced as much as possible. For example, Chong et al.[91] synthesized 2 nm Pt_3Co nanoparticles on a Co-N doped carbon substrate by a pyrolysis method. The sample showed an ultralow Pt loading at a mass ratio at 2.7 wt% and a record high ORR mass activity at 1.77 A/mg in a fuel cell. In addition, noble metal single atoms have also been widely studied and shown great activity in HER, ORR and OER. Among them, Pt and Ru single atoms has been the most successful HER catalysts and water splitting catalysts, respectively. For example, coordinated by nitrogen, oxygen or sulfur atoms, Pt single atoms show great HER activity when supported on a substrate of carbon,[92] metal oxide,[93] metal sulfide,[94] metal phosphide,[95] selenide,[96] MXene,[97] etc. In other examples, Ru single atoms show great HER activity when they are loaded on nitrogen-doped carbon,[98] nitride imide nanotubes,[99] MXene[100] and MoS_2;[100] as well as great OER activity when loaded on FeCo hydroxide to form a Ru-O-Fe(Co) bond.[101]

1.3.2 non-noble materials

Non-noble materials are another class of important electrocatalysts, due to their low costs, high stability and poison resistance. Some of these even surpass noble materials in certain reactions. For example, Fe/N/C catalysts usually show a better ORR activity than commercial Pt/C in an alkaline electrolyte.[37] It has been found that pyrolysis of a mixture

of an iron precursor and a nitrogen-containing carbon precursor can produce Fe/N/C catalysts with great ORR activity;[102] yet their active sites and mechanism have been under active debates.[103] Until recently, it is verified that Fe-N_x single atom sites play a dominant role.[35, 37] In recent studies, it has been found that the activity also varies with the coordination configuration of Fe-N_x.[31, 104] Similarly, Co-N_x also has significant ORR activity.[105] Yet, a non-noble ORR catalyst that can suppress Pt/C in acid has been rare.

As discussed earlier, leading non-noble material catalysts for HER include metal oxides, phosphides, sulfides and selenides. Many of the catalyst are prepared by hydrothermal methods and can reach a very low $\eta_{10,HER}$ under -100 mV in an acidic or alkaline electrolyte.[106] For example, Chen et al.[107] synthesized Mo-Ni oxide nanorod arrays by a solvothermal process, and treated the samples with H_2 at a high temperature to form oxygen vacancies. This material showed an ultrahigh HER activity, with an $\eta_{10,HER}$ of only -17 mV. In another study, Tian et al.[108] prepared CoP nanowire arrays by a hydrothermal method, and observed a high HER activity in a wide range of pH. MoS2 has also been studied extensively towards HER. Liu et al[109] doped P into MoS_2 nanosheets by a hydrothermal process, and the resulting catalyst showed an $\eta_{10,HER}$ of only -43 mV in 0.5 M H_2SO_4.

FeNi hydroxide is generally considered as the best OER catalyst in alkaline electrolytes. This is usually prepared by a hydrothermal process, can reach a current density of 1 A/cm^2 at 1.6 V vs RHE,[110] and show great stability, a performance greatly suppressing that of Ir or Ru oxides. In addition, a variety of metal oxides (perovskite, spinel, etc) have

also been extensively studied. These are usually prepared by high temperature calcination, solid-phase combustion, pulsed laser deposition, precipitation, etc.[111] For example, Schafer et al.[112] prepared a Co_3O_4-based metal-ceramic composite and observed a great OER activity, with an $\eta_{10,OER}$ of only 220 mV. Yet, due to the instability in acid, none of these oxides can be used in acid electrolytes.

1.3.3 Carbon based materials

Carbon-based materials have found extensive applications in electrocatalysis. Carbon materials provide a wide potential window and good electrical conductivity, due to structural diversity and flexibility for the manipulation of the catalytic performance, such as morphology (0-D quantum dots, 1-D nanowires/nanotubes, 2-D graphene and 3-D network, nano/meso/microporous nanostructures, etc), phase (graphene, amorphous, graphdiyne, etc), and heteroatom dopants (nitrogen, sulfur, oxygen, metal single atom, etc). Moreover, the carbon materials provide great support for the loading of a variety of nanostructures with strong metal-support interactions.[31, 104, 113] The design, synthesis and activity adjustment of carbon-based materials have shown a great outlook for electrocatalysis.

Indeed, a number of catalysts towards a variety of electrochemical reactions have been prepared. Of these, N-doped carbon has shown significant activity as metal-free catalysts for ORR;[38, 114] Fe single atoms embedded in carbon materials also show apparent ORR activity which may suppress that of Pt/C in alkaline electrolytes.[115] PtCo nanoparticles derived from ZIF-67 have been used as ORR catalysts in PEMFC.[91] In addition, HER can

be catalyzed by C_3N_4,[116] N,S-codoped graphene,[117] and a variety of nanostructures derived from pyrolyzed carbon.[58, 118, 119] Figure 3 shows the main procedures for preparation of carbon-based single atom catalysts.

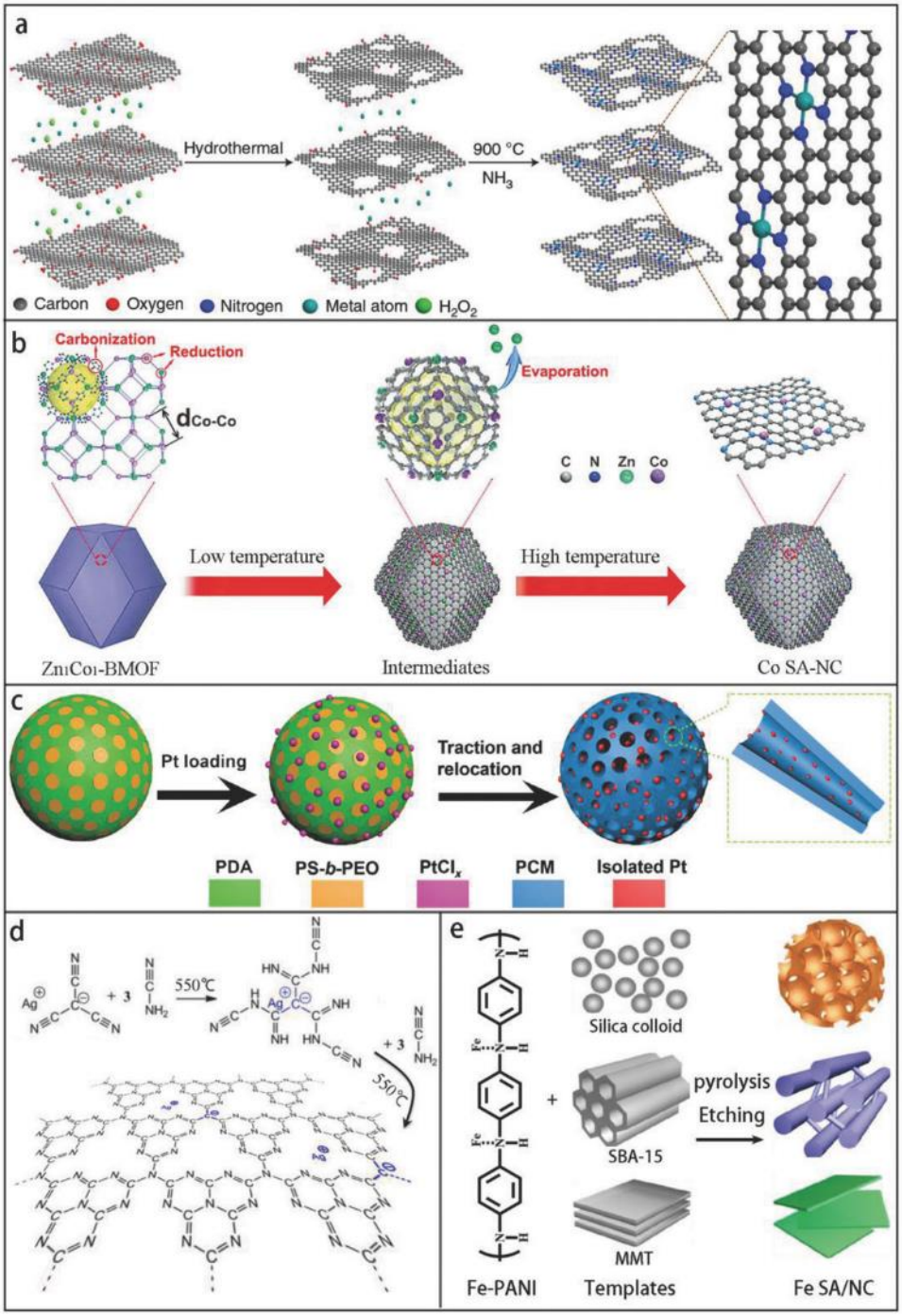
a
Hydrothermal
900 °C
NH3
Carbon
Oxygen
Nitrogen
Metal atom
H2O2
b
Carbonization
Reduction
dCo-Co
Evaporation
C
N
Zn
Co
Low temperature
High temperature
Zn1Co1-BMOF
Intermediates
Co SA-NC
c
Pt loading
Traction and relocation
PDA
PS-b-PEO
PtClx
PCM
Isolated Pt
d
550℃
+ 3
e
Silica colloid
pyrolysis
Etching
SBA-15
MMT
Templates
Fe-PANI
Fe SA/NC

Figure 3 Representative examples of metal SACs supported on a carbon matrix through a pyrolysis route with various precursors. a) Preparation of M-NG (M = Fe, Co, Ni) with MN4C4 moieties in which the precursors are metal ions adsorbed on a 3D graphene hydrogel. b) Preparation of Co-NG from a Zn1Co1-BMOF precursor. c) Synthesis of Pt-PCM starting with polydopamine. d) Ag-C3N4 derived from silver tricynomethanide and cyanamide. e) Synthesis of Fe-NC with the assistance of various templates. Copyright to ref [104]

1.4. Catalytic active sites

1.4.1 Material characterization

In typical characterization, the elemental composition of the nanomaterials is a critical parameter. For example, the morphology, lattice and elemental distribution can be analyzed by various microscopic techniques, such as transmission electron microscopy (TEM), scanning electron microscopy (SEM), high-angle annular dark-field scanning transmission electron microscopy (HAADF-STEM), atomic force microscopy (AFM), etc. The lattice structure of a material can be identified by X-ray diffraction (XRD). The contents of elements can be quantitatively identified by inductively coupled plasma optical emission spectrometry (ICP-OES) measurements. The valence state and charge transfer properties can be characterized by X-ray photoelectron spectroscopy (XPS) measurements. Optical properties can be measured by UV-vis spectroscopy and fluorescence spectroscopy. The organic material, carbon material and organic ligand can be characterized by Raman spectra, nuclear magnetic resonance (NMR), infrared

spectroscopy (IR) and thermogravimetric analysis (TGA), etc. The porosity and surface area of carbon materials can be measured by gas adsorption technique, such as the Brunauer–Emmett–Teller method (BET).

The detailed structure can be identified more clearly by some specific and advanced characterization methods. For instance, high-resolution TEM (HRTEM) can be used to identify the lattice distortion, phase segregation and edge structure of a nanoparticle. Moreover, aberration-corrected STEM (AC-STEM) with a sub-angstrom resolution can be used to identify the single atom distribution. In addition, high-resolution electron energy loss spectroscopy (EELS) can be used to identify the element of a single atom or a cluster in the material. To understand the electronic structure and atomic level geometric structure of a material, X-ray absorption spectroscopy (XAS) plays a very important role. XAS includes two parts, X-ray adsorption near edge structure (XANES) and extended X-ray absorption fine structure (EXAFS). The XANES data includes accurate information about the detailed electronic structure of an element, such as oxidation states, ligand field, etc. The EXAFS data contains information about the coordination structure, such as bond length, coordination numbers, etc. Electron paramagnetic resonance (EPR) is a sensitive technique to identify unpaired electrons, transitional metal d-electrons, oxygen vacancies and free radical reaction intermediates. Mossbauer spectroscopy is usually carried out to identify the coordination structure of magnetically active atoms.

1.4.2 Experiments to understand the active sites and reaction mechanism

In addition to systematic characterization, control experiments are the keys to understanding the active sites and reaction mechanism.

For understanding the active sites of a catalyst, poisoning tests are a common method. The main idea of this test is to apply a strong blocking agent to terminate proposed target sites, then compare the activity before and after so as to identify the source of the difference. Sulfur compounds are commonly applied to block the metal sites. For example, Niu et al.[120] synthesized a Fe,N-codoped carbon ORR catalyst, with Fe-N_x sites embedded in the carbon matrix. To identify whether the active site is Fe-N_x, CN- was applied to block the Fe sites. They then tested the ORR activity in the presence of 10 mM KCN and found that $E_{1/2}$ exhibited a negative shift of only 18 mV. Thus, they argued that the contribution of Fe-Nx moieties was minor, and the key active sites were likely the carbon sites, instead of Fe (Figure 4). In another study, Thorum et al.[121] examine the ORR activity of carbon-supported Cu (II) with 3,5-diamino-1,2,3-triazole (CuDAT) in the presence of fluoride, thiocyanate, ethanethiol and cyanide. The activity of CuDAT significantly decreased upon the addition of these poisonous agents, indicating that the Cu complex was the active sites for ORR.

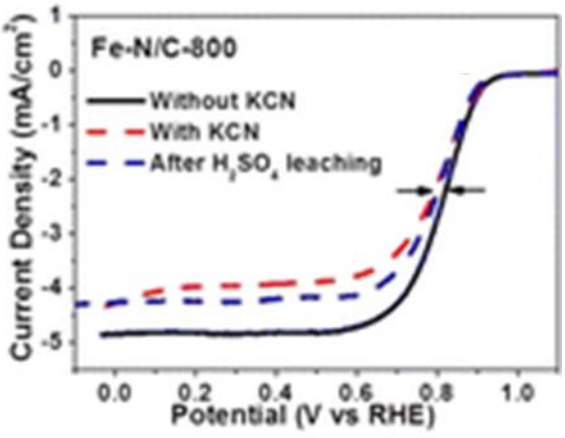

Figure 4 LSV curves of Fe-N/C-800 before (black) and after (blue) H2SO4 leaching treatments, and in 0.1 M KOH aqueous solution with 10 mM KCN (red). Copyright to ref [120]

Moreover, control experiment with chelating agents, such as EDTA[98], can be adopted to identify the activity of single atoms. For example, Liu et al.[122] synthesized a carbon-based material with Pd nanoparticle and Pd single atoms (Pd-N species). To identify the ORR activity of Pd-N species, they tested the activity with the addition of EDTA. A significant decrease of the ORR activity was observed in the presence of EDTA, indicating that Pd-N species played an important role in ORR.

Other than catalysts poisoning tests, the characterization of catalyst after electrochemical performance test can be helpful in understanding the active sites. For example, to identify which kind of nitrogen dopants (pyridinic, graphitic or pyrrolic) are in charge of ORR performance in nitrogen-doped carbon materials (note this is a highly debated research topic), Wang et al.[123] carried out XPS studies to examine the concentration change of different types of nitrogen species along with a variety of CV cycles. It is noticed that the ORR activity decay was highly correlated with the concentration decrease of graphitic nitrogen, while other nitrogen species showed no such correlation. By this, it is proposed that the graphitic nitrogen was the key sites of ORR. In another study, Seitz et al.[72] found that the roughness of $SrIrO_3$ was significantly increased after 30 h of OER tests, along with an increasing activity and identified that the dissolution of Sr^{2+} and exposure of IrO_x moieties played an important role in OER electrocatalysis.

Furthermore, operando measurements provide an opportunity to monitor the material structural change during the reactions. This is considered as one of the most powerful characterization methods. For example, to understand the activity and stability of an OER catalyst with Ru single atoms on CoFe layered double hydroxides, Li et al.[124] carried out a systematic operando XAS measurement, and found that the Ru single atoms became oxidized at 1.6 V, but not over-oxidized into a high valence state over +4 which is dissolvable in solution. Meanwhile, the oxidation state and coordination of Ru atoms were reversely recovered when the bias potential was switched off. Moreover, they found that the Co-O-Ru and Fe-O-Ru bond shrank during OER, which further enhanced the stability of Ru atoms. That is, the OER reaction process can be clearly understood by operando XAS measurements.

Isotope tracing is another unique method to understand reaction mechanism. For example, Grimaud et al.[125] used ^{18}O labeling with in-situ mass spectrometry and discovered a new OER reaction mechanism catalyzed by high-covalence cobaltate perovskite (Figure 5). $LaCoO_3$ were labeled by ^{18}O and no ^{18}O was detected in the O_2 gas after OER, indicate $LaCoO_3$ follows the traditional concerted proton electron transfer pathway. However, $^{34}O_2$ and $^{36}O_2$ were detected when an ^{18}O labeled $SrCoO_{3-\delta}$ and other cobaltate perovskites were used as the OER catalyst. This important evidence shows that lattice oxygen atoms are involved in the reaction process. They also proposed new reaction mechanism based on this discovery, which is important for further theoretical works.

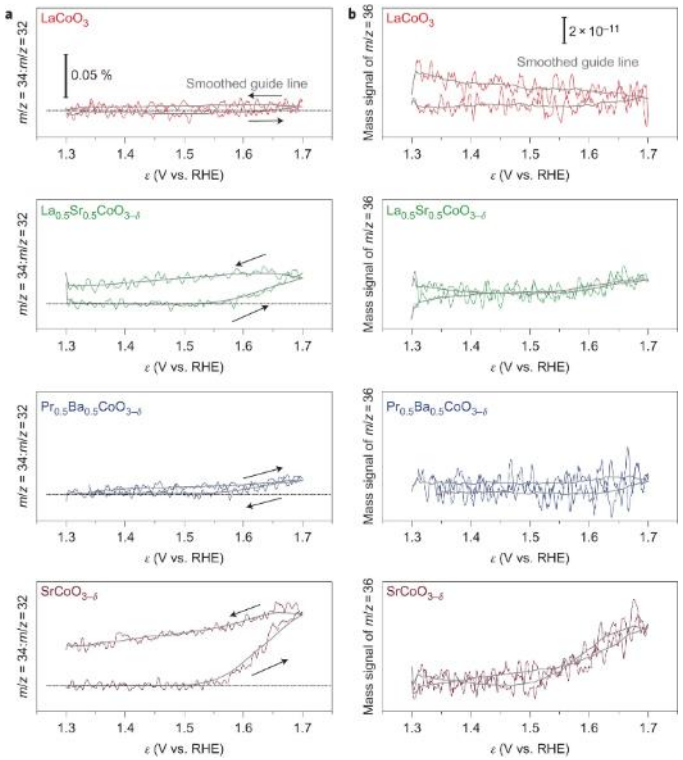

Figure 5 Data were measured in 0.1 M KOH by OLEMS at a scan rate of 2 mV s^{-1} (no gas bubbling). **a**, $^{34}O_2/^{32}O_2$ ratios, where the straight lines correspond to the natural abundance of ^{18}O of 0.2%. The arrows indicate forward and backward scans. **b**, $^{36}O_2$ signal. All data were taken from the first cycle. Copyright to ref [125].

1.4.3 Theoretical studies of electrocatalytic reactions

1.4.3.1 Three important strategies for first principles calculations of electrocatalytic reactions

First principles calculations are a very important method for understanding and explaining the electrocatalytic activity. The most straightforward purpose of the calculations is to acquire the energy diagram, which shows free energies of different reaction steps. With this energy diagram, one can evaluate the activity of different sites,

identify the most active sites and understand the rate determine step. In this level of theory work, there are mainly three strategies of implementing the calculations.

In the first strategy (with the best accuracy), the calculations will be carried out by building structural models based on a systematic experimental characterization of the materials on the atomic or lattice level. Certain reactions can be simulated on the model by calculating the energy of a series of reaction intermediates. Finally, the reaction energies are used to compare with experiment results. If the theoretical results are consistent with the experimental data, the reaction process simulation is reliable, and reaction intermediates information (e.g., reaction energies, atomic geometry, active site, etc.) can be fully discovered. This strategy can be regarded as using theory to explain experiments".

In the second strategy, theoretical calculations are used to go over all possible structures and predict the most probable active sites and reaction pathways. In many cases, the material system is very complex and contains a variety of components. Thus, a clear and detailed atomic level characterization is impossible. For example, it is common that a variety of FeN_x moieties coexist in the Fe/N/C material (e.g., FeN_4, FeN_3C, FeN_2, etc). And sometimes XAS studies cannot distinguish the Fe-C/ Fe-N bond due to the similar bond length, or the coordination number is not very clear. In this situation, the screening of all possible structures is necessary, which can be carried out by formation energy calculations, within the range of results from experimental characterization. The important structures with the lowest formation energy or a certain property closest to experimental results (e.g., charge transfer property close to the XPS results; band gap

close to the result of UV-vis and photoluminescence measurements, etc.) can be selected for further calculations. Finally, the catalytic activity can be compared to experimental results, and the most possible active sites can be obtained. This strategy can be called "mutual input of theory and experiments".

The third one is to carry out systematic calculations at first and obtain useful information to synthesize materials, and then implement experimental work to verify the theoretical prediction. This strategy has the highest level of difficulty among the three strategies and must be based on a plentiful accumulation of experience and knowledge in the field. For example, as one of the earliest and most important reports of ORR catalysis on Pt-based catalysts, Greeley et al.[126] brought forward the descriptor of ORR and carried out systematic screening calculations for a wide range of Pt alloys. They then carried out experimental measurements and successfully confirmed that Pt_3Sc and Pt_3Y alloy exhibited a much better ORR activity than Pt, consistent with theoretical predictions. This strategy can be considered as using theory to guide experiments.

1.4.3.2 Models of calculation

Building a suitable model is the first step and the foundation of a calculation study. As mentioned above, in general, one should have sufficient information from structural characterization of the material. For instance, from the analysis of TEM and XRD measurements, one can obtain key information such as the matter, phase, size, lattice, surface, etc. From XAS and XPS analysis, one can acquire information about the atomic configuration, coordination number, etc. For a metal-ligand system, from NMR and IR

studies, one can obtain accurate organic structures; and from TGA, one can assess the ratio and density of the organic ligands on the metal surface. For a material within a certain pH and potential, one should build the model referred to the Pourbaix diagram.

The most common model of a nanoparticle (quantum dot) is the slab model. This model is made within the supercell and has several layers and an infinite 2D structure in X and Y directions, enough vacuum in the Z direction to avoid interactions and periodic boundary condition. In principle, if the nanoparticle or quantum dot is much smaller than their Bohr excitation radius, they must be calculated with an actual size cluster model instead of slab model, due to the quantum confine effect.

To build a slab model, the correct crystal structure should be calculated at first. For this, a suitable pseudopotential should be selected, and a series of parameters are tested until a minimum or lowest energy can be reached, such as lattice constant, k-point sampling, and cutoff energy. A suitable smearing method and parameter also should be adopted for a metallic system. After that, the size of the supercell can be selected and a correlated lattice can be cut out, according to the TEM analyses. For example, if in TEM studies show that the Pt nanoparticle surface is dominated by the (110) facets, a slab with the Pt(110) surface will be cut out from the Pt lattice. The thickness is another key factor to build the slab model, and the distance between each slab should be tested to make sure that there is no interaction between the periodic images. Finally, the slab model will be relaxed and ready for further calculations, where fixing the bottom layer is an important method to keep a correct surface relaxation.

Except for the slab model for nanoparticles, single-layer graphene, C_3N_4, black phosphors, boron nitride and other models are widely used to calculate the related materials; and a cluster model can be adopted to simulate actual cluster materials.

1.4.3.3 Catalytic process and mechanism

The main idea to evaluate the catalytic activity from theory is to calculate the energy of intermediate species and/or critical descriptors.

For HER, the reaction mechanism is[127]

$$H^+ + e^- = H^* \text{ (Volmer step)} \quad (17)$$

$$H^* + H^+ + e^- = H_2 \text{ (Heyrovsky step)} \quad (18)$$

$$2\,H^* = H_2 \text{ (Tafel step)} \quad (19)$$

In this reaction, the adsorption free energy of H* (ΔG_{H^*}) is usually used as an important descriptor to evaluate the activity of an active site. Generally, $\Delta G_{H^*} < 0$ indicates that the desorption of H is too difficult (Heyrovsky step/Tafel step controlled), while $\Delta G_{H^*}>0$ suggests that adsorption of H is too difficult (Volmer step controlled). The best site should have a ΔG_{H^*} close to 0 eV, as shown in Figure 6. This descriptor is considered valid in both acidic and alkaline electrolyte.

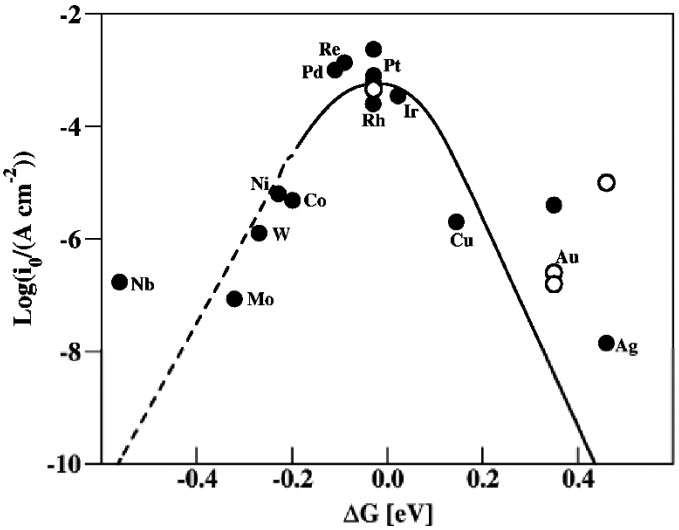

Figure 6. A volcano plot. The data points are measured exchange current density plotted versus the calculated free energy of H adsorption at U > 0 V. The metals on the left side of the volcano have high H coverage (1 ML) and the metals on the right side low H coverage (0.25 ML). The line is a prediction by a kinetic model in which all input parameters are taken from DFT calculations. The dashed line indicates that the metals which bind H stronger than 0.2 eV/H usually form oxides at U > 0 V. The open circles are (111) data whereas the filled circles are polycrystalline. Copyright from the reference[128].

For ORR, the reaction mechanism is[127]

$$* + O_2 + H^+ + e^- = OOH* \qquad (20)$$

$$OOH* + H^+ + e^- = O* + H_2O \quad (21)$$

$$O^* + H^+ + e^- = OH^* \qquad (22)$$

$$OH^* + H^+ + e^- = H_2O + * \qquad (23)$$

Theoretical studies can be carried out to calculate the binding energy of OOH*, O* and OH* and the reaction free energy, so as to construct the energy diagram. In most of the cases, the first step -oxygen adsorption or the last step -OH desorption is the rate determine step (largest up-hill step). Moreover, it has been found that the free energy of these two steps has a universal linear relationship:[129] that is, a stronger O_2 adsorption will cause a stronger OH adsorption and a weaker O_2 adsorption will cause a weaker OH adsorption. For a carbon-based material, the carbon atom can act as an active site, but O_2 adsorption remains difficult, and desorption of OH is favorable. So, the OOH* or OH* binding energy should be strengthened. In opposite, Pt nanoparticle surface exhibits too strong O2 adsorption, rendering it difficult for the desorption of OH*, such that the OOH* and OH* binding energy should be weakened.[130] Therefore, an optimal site should have equal energies of these two steps to minimize the overall reaction energy. The intercept of the ΔG_{OOH^*} vs ΔG_{OH^*} line is different with different catalytic sites, which can determine the optimal reaction energy.[131]

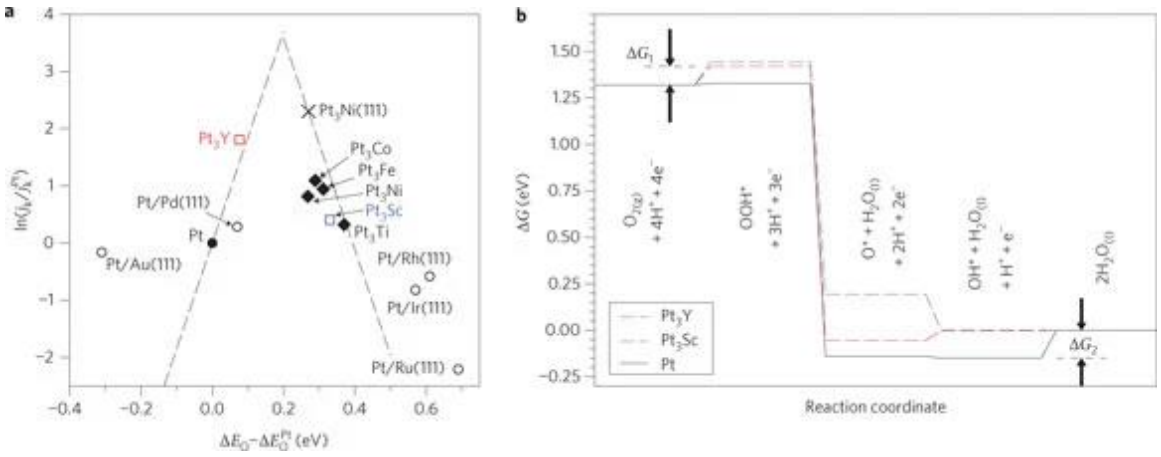

Figure 7. (a) Measured kinetic current density as reported in the literature for a range of alloy electrocatalysts with Pt 'skins' plotted as a function of the calculated oxygen adsorption energy, ΔE_O. All data are shown relative to Pt. (b) Calculated free energy diagram for the oxygen reduction reaction at 0.9 V with respect to the reversible hydrogen electrode (RHE) under standard conditions for Pt(111) (solid line) and for Pt overlayers on the $Pt_3Sc(111)$ and $Pt_3Y(111)$ surfaces (dashed). The free energy changes for the formation of OOH (ΔG_1) and the removal of OH (ΔG_2) are indicated. Copyright to reference [130].

Moreover, the adsorption energy of O* (or referenced to that of Pt) can be used as a descriptor to roughly estimate the ORR activity (Figure 7). However, ΔG_{O*} cannot reflect the free energy change of rate determine step and it does not always have a strong connection with ΔG_{OOH*} and ΔG_{OH*}.[131, 132] So although it is an easy way of estimation, the accuracy is not always satisfying.

For OER, the reaction mechanism is proposed as [127]

$$H_2O + * = OH* + H^+ + e^- \quad (24)$$

$$OH* = O* + H^+ + e^- \quad (25)$$

$$O* + H_2O = OOH* + H^+ + e^- \quad (26)$$

$$OOH* = * + O_2 + H^+ + e^- \quad (27)$$

Generally, the OER mechanism is much more complicated than ORR. Firstly, it has been found that different catalysts, or a catalyst under different potentials, may have different rate determine steps.[133] This greatly increases the complexity of calculations and difficulty for making a conclusion. For example, Haschke et al. showed that Fe_2O_3 catalysts displayed a rate determine step at O-O formation by ^{18}O labeling, consistent with results from theoretical studies,[134] whereas Exner et al. argued that for the IrO_2 catalyst, the rate determine step was the formation or decomposition of OOH intermediates at different potentials.[135] In addition, Ping et al. discovered that when considering the energy barrier and transition states, water dissociation became the rate-determine step, and the reaction was highly dependent on the potential, transition state and surface oxygen vacancy.[136] Moreover, as shown above, lattice oxygen may take part in OER, and some catalysts follow a reaction mechanism different from surface intermediate adsorption (e.g., $SrCoO_{3-\delta}$),[125] and some catalyst are proved not having lattice oxygen involved (eg. RuO2, $LaCoO_3$).[137] Determination of the mechanism of OER is a challenging work and more research in this field is in urgent need. The most useful descriptor of this reaction is ΔG_{O*}-ΔG_{OH*}, which can have best evaluations (Figure 8).

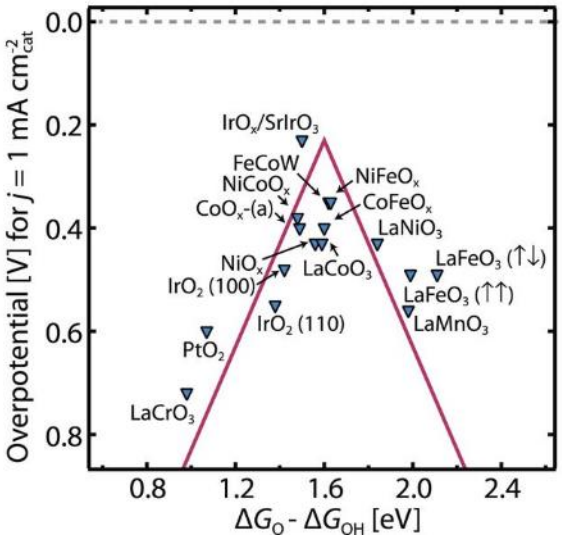

Figure 8, OER volcano plot for metal oxides, with the indicator of ΔG_{O*}-ΔG_{OH*}. The best catalyst is IrO_x synthesized by the leaching out Sr^{2+} from $SrIrO_3$. Copyright from ref [127].

1.4.3.4 Modification items

After calculation of the energy of reaction intermediate species, the adsorption energy can be calculated by equation

$$E = E_{ads*} - E_{*} - E_{ads} \quad (28)$$

where * indicates a catalytic active site and ads is the adsorbents. In some cases, van der Waals correction is required in the calculation.

To calculate reaction free energy, the modification item should be added. For instance, phonon calculation is usually applied to calculate the vibration frequencies, follows by deriving the zero-point energy (ZPE) and entropy. Moreover, a solvation energy should

be applied as implicit water molecules, to correct the solvation effect. For example, the charge-asymmetric non-locally determined local electric (CANDLE) solvation model is widely used for this purpose.[138] In addition, sometimes a cluster of water are placed in the supercell, or molecular dynamic calculations can be used to simulate the movement of a large volume of water molecules and diffusion situations.

In summary, the reaction energy can be calculated in the following equation[139]

$$\Delta G = \Delta E + \Delta ZPE - T\Delta S + \Delta E_{solvation} + k_b T \ln 10 * pH - eU \quad (29)$$

There are also mechanisms proposed for fuel oxidation reactions, CO_2 reduction reaction, nitrogen reduction reaction, etc. These mechanisms can be adopted for the simulation of the related electrocatalysts.

1.4.3.5 Transition state

As shown above, the reaction energy can be estimated from the adsorption energy of intermediate species with some modifications. In fact, the Bell–Evans–Polanyi (BEP) principle is introduced for this calculation strategy. The energy barrier is assumed to be linearly correlated to the enthalpy of the reaction. However, sometimes this is not enough to obtain an accurate result. For example, in alkaline solution, HER is not only influenced by the hydrogen binding energy, but also affected by a significant water dissociation process which does not exist in acid electrolyte.[98] In this case, the water dissociation barrier and transition state should be calculated to better understand the catalytic process. The most common method is Nudged Elastic Band (NEB) method and Climb Image Nudged Elastic Band (CINEB) method. The CINEB calculation should be

implemented based on NEB calculation, which can provide more accurate transition state and energy barrier.

1.5. Understand the origin of electrocatalytic activity

After an active site is identified, the mechanistic origin of the electrocatalytic activity can be further discussed. The direct reason of the activity is the moderate binding energy.

1.5.1 Energy band and density of states (DOS)

Energy band calculations are important for understanding the electronic structure. Firstly, the energy band can be used to identify if the material is a metal, a semiconductor or an insulator. This point is important because a metallic system has high conductivity, which is essential for an electrocatalyst. Moreover, the energy band can be used to explain the photoluminescence property of a material. For example, Peng et al. found that the fluorescents of C_3N_4 can be quenched by the chelation of ruthenium ions. From calculations, it was discovered that ruthenium centers induced a spin down state inside of the band gap and transformed the semiconducting C_3N_4 into a metallic structure. Therefore, the activity of HER became significantly enhanced. This will be discussed in more detail in Chapter 3. In addition, for a semiconductor material, the band gap, direct or indirect electron transition can be identified, and the doping effect can be characterized.

Compared to energy band calculation, density of state (DOS) can be carried out in a low-symmetric system, which is more commonly used. The binding energy of intermediate

species is highly related to the DOS around the Fermi level, where the activated electrons and empty states are located. For example, in ORR electrocatalysis, nitrogen-doped carbon has difficulty in O_2 adsorption, while O_2 adsorption on Fe sites of FeN_4 structure is much easier. This is partly because there are few states around the Fermi level of a N-doped carbon structure, while there are a large number of spin down states in the FeN_4 center. This work will be detailed in Chapter 2. Moreover, the higher DOS on the Fermi level indicates easier electron donation/withdrawal, which is essential for an electrocatalytic reaction.

In addition, the position of the d-band center, with referrence to the Fermi level, is highly correlated to the binding energy of intermediate species and influenced by the charge transfer process on the material. This is the foundation of manipulating the electronic structure and the activity of the electrocatalysts. For example, from the Figure 9, one can clearly see that a down shift of the d-band center can weaken the adsorption of O2 and CO on a platinum or a gold surface.

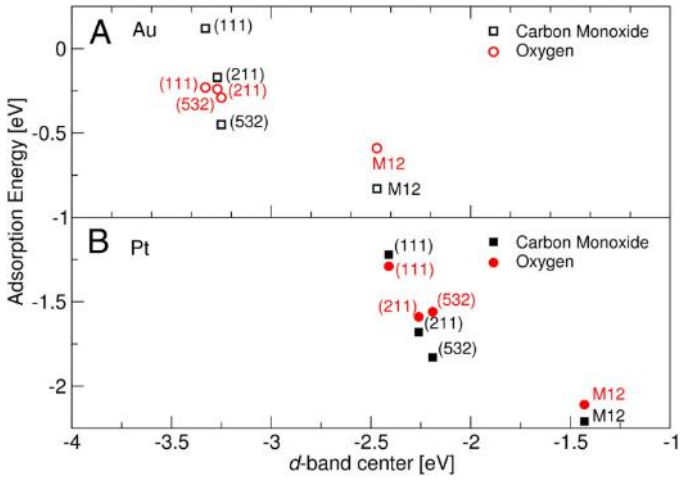

Figure 9. Illustration of the extent of the *d*-band model. Calculated CO and O adsorption energies for a range of different Au (*A*) and Pt (*B*) surfaces including 12 atom clusters are seen to correlate with the calculated *d*-band center (ε_d), copyright from ref [140].

It should be note that there are several intrinsic defects in DFT calculations, such as the exchange correlation potential of the Kohn-Sham equation that cannot be accurately described, the electron self-interaction error, etc. These will result in errors of the electronic structure (e.g., severe underestimation of the band gap). To minimize the error, DFT+U should be applied to all heavy atoms. Moreover, if a more accurate electronic structure is required, the PBE level of calculation is not enough. Instead, a hybrid functional calculation (PBE0, HSE06, B3LYP, etc)[141] or a GW calculation is needed.[142] These calculations will consume much more computational time but can provide more accurate results.

1.5.2 Charge transfer

In principle, all chemical properties of an atom can be determined by its charge density. So, a charge transfer process can change the charge density of certain sites, which is essential to adjust the activity of an electrocatalyst. From calculations, the charge density distribution can be plotted and charge of each atoms of the material can be obtained by Bader charge or Lowdin charge analyses. Moreover, the results of theory can be examined by experimental characterization, such as the binding energy shift in XPS, a white line intensity shift in XAS, etc. Extensive studies have shown how charge density

can influence the binding energy of intermediates. For example, carbon atoms of a nitrogen-doped graphene work as active sites of ORR. The activity of these carbon atoms comes from electron transfer to nearby nitrogen atoms. This generates a spin density and partial single atoms on the carbon sites, leading to binding of oxygen species.[37]

Because of this, manipulating charge transfer has great significance in adjusting the electrocatalytic activity. Both theory and experimental work should focus more on this topic.

1.6. Charge density for manipulation of electrocatalytic activity

As shown above, charge transfer plays an important role in manipulating the electrocatalytic activity. The activity change is due to donation or withdrawal of electron of the activity sites, which influences the binding energy of critical reaction intermediates. Many experimental studies have shown that the electrocatalytic activity is highly correlated to charge transfer within the material.[143] The most significant work are the studies about metal-metal charge transfer (MMCT), metal-ligand charge transfer (MLCT), metal-support charge transfer and electron gain of high electronegative atom. As an example of MMCT, Chen et al.[144] discovered that charge transfer effect from gold to silver can enhance the ORR activity of silver site in an Au-Ag Janus nanoparticle. In another work, MLCT has been confirmed to significantly influence the ORR of Pt nanoparticles. Zhou et al.[145] functionalized Pt nanoparticles (2.0 to 2.5 nm in diameter) with *para*-substituted R-phenyl derivatives (R = CH_3, F, Cl, OCF_3 and CF_3) and found the ORR activity consistently increased with increasing strength of electro-withdrawing

groups (Figure 10). This enhancement was caused by the decrease of Pt electron density, which reduced the ability for Pt surface to adsorb oxygen species.

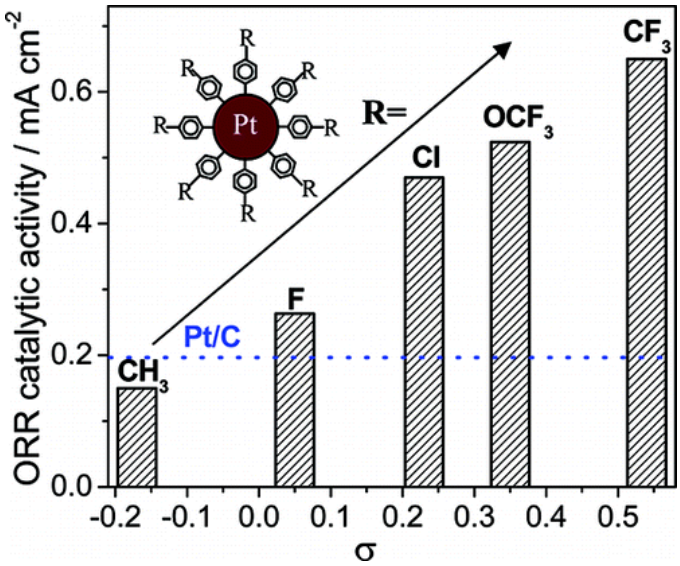

Figure 10 ORR activity of Pt nanoparticle can be adjusted by electron withdraw from the ligand. Copyright from ref [145].

More research has confirmed that the activity can also be enhanced by select metal-support charge transfer. For example, in a series of studies, GQD or NGQD substrates can significantly withdraw electrons from Pt or Pd nanoparticles, leading to enhancement of the ORR activity.[146-149] By contrast, black phosphorus substrate can donate electrons to Pt, Au and Ag nanoparticles, which diminishes the ORR activity decay of Pt but enhances the activity of Au and Ag.[150] In addition, oxygen vacancy doped TiO_2 can donate electrons to Pd nanoparticles and enhance the activity of ethanol oxidation reaction[151] (These two works will be detailed in chapter 5). Moreover, for single atom catalysts, the metal-support interaction will be maximized. In this case, coordination with

high electronegativity atoms can significantly diminish the electron density of the single metal atom site, as manifested in Pt and Ru single atom HER electrocatalysts.[152]

Moreover, developing new methods to manipulating charge transfer is also important. In Chapter 6, a novel and strong charge transfer effect from ligand to metal oxide is introduced.[153] In this study, alkyne-functioned TiO2 can spontaneously transfer electrons from the conjugated organic groups to TiO2 surface through a unique C≡C-O bond. This charge transfer can also be found with other metal oxides.

1.7. Central dogma and ways of rational synthesis of catalysts and manipulation of the activity

From the above analyses, one can see a central dogma of the electrocatalytic performance. That is, charge density of the active site influences the binding energy of critical intermediate, and binding energy determine the activity of the active sites. The active sites determine the overall activity, as shown in Figure 11. In addition, this dogma separates the activity adjustment in these four levels, each of which has different questions to answer and missions to achieve.

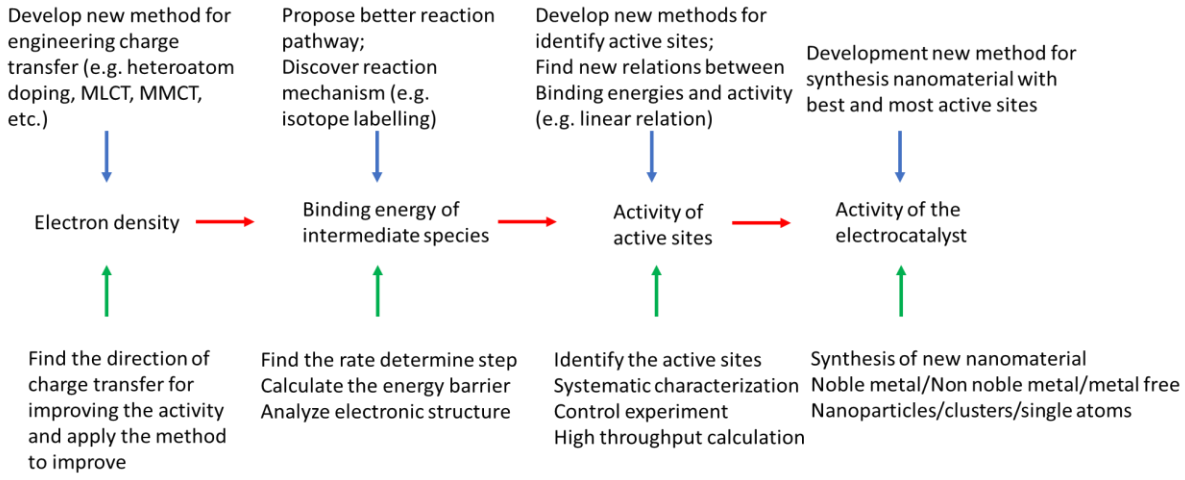

Figure 11. Central dogma of electrocatalyst with best activity. The question and main task for each level of study.

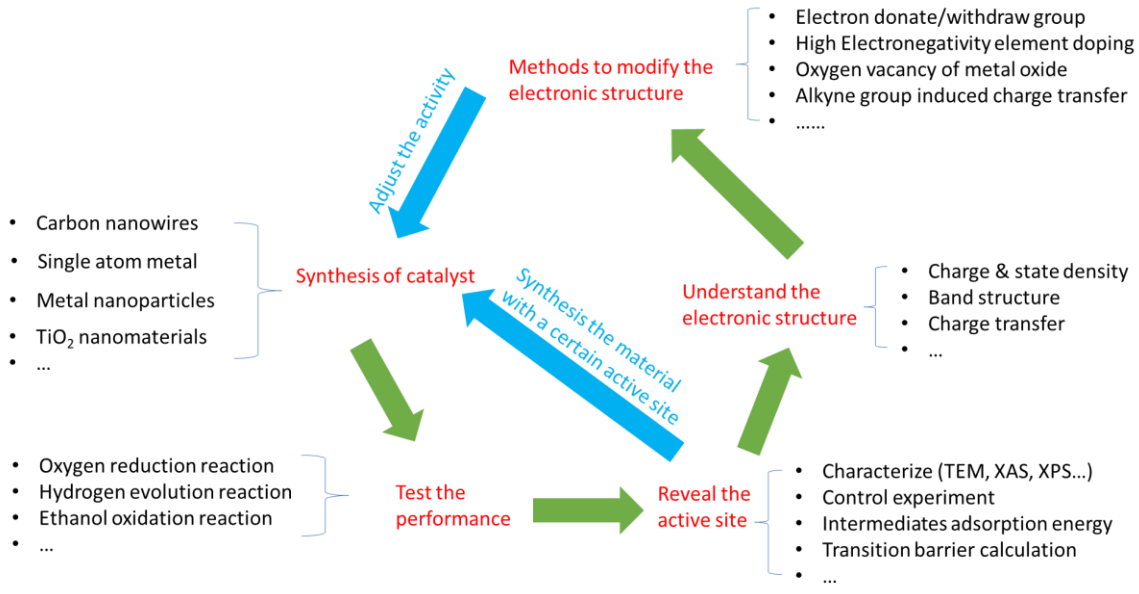

Figure 12. Strategy loop for the rational design of electrocatalysts

For understanding and manipulating each component of this dogma, a cycle loop of rational synthesis of materials is built from both experimental and theoretical perspectives (Figure 12). Five important elements are included in this loop, synthesis of nanomaterial, activity test, identification of active structure, electronic structure analyses, and modification of electronic structure. For one specific work, from the experimental and/or theory sides, one to five of these aspects will be addressed. For example, a material can be synthesized and have some activity in a reaction, then careful characterization and control experiment will be carried out, followed by models building for simulations of the electrocatalytic activity. Then the activity sites are revealed, and this knowledge can further help direct the material synthesis to increase exposure of active sites. Furthermore, the electronic structure can be characterized, and the donation or withdrawal of electrons will be revealed to enhance the activity. A method of manipulation will be adopted and have feedback for structural engineering of the materials. Alternatively, experimental intermediates can be used to modify the theoretical methods. In other words, experiment and theory will be integrated to influence each other so as to push forward the development of the electrocatalysts.

Within this context, this dissertation includes a series of studies that employ such a design loop for the development of effective electrocatalysts for a range of important reactions in electrochemical energy technologies.

Chapter 2 introduces nitrogen and iron-based carbon nanowires with a focus on the synthesis, ORR activity, active site identification and mechanistic understanding of the activity.

Chapter 3 discusses nitrogen and ruthenium codoped carbon nanowires for HER electrocatalysis.

Chapter 4 combines theoretical and experimental studies to identify the ORR activity of platinum-cobalt single atom/clusters supported on nitrogen-doped carbon.

Chapter 5 examines the impacts of metal-supported electron transfer involved oxygen-defected TiO_2 and black phosphorus on the electrocatalytic activity of Pd and other metal nanoparticles.

Chapter 6 introduces a unique method for the modification of the optical and electronic properties of metal oxide nanoparticles and implications in the photocatalytic activity.

1.8. References

1. Cook, T. R.; Dogutan, D. K.; Reece, S. Y.; Surendranath, Y.; Teets, T. S.; Nocera, D. G., Solar Energy Supply and Storage for the Legacy and Nonlegacy Worlds. *Chem Rev* **2010,** *110* (11), 6474-6502.

2. Nitopi, S.; Bertheussen, E.; Scott, S. B.; Liu, X.; Engstfeld, A. K.; Horch, S.; Seger, B.; Stephens, I. E. L.; Chan, K.; Hahn, C.; Nørskov, J. K.; Jaramillo, T. F.; Chorkendorff, I., Progress and Perspectives of Electrochemical CO2 Reduction on Copper in Aqueous Electrolyte. *Chem Rev* **2019,** *119* (12), 7610-7672.

3. Wolf, S.; Keenan, T. F.; Fisher, J. B.; Baldocchi, D. D.; Desai, A. R.; Richardson, A. D.; Scott, R. L.; Law, B. E.; Litvak, M. E.; Brunsell, N. A.; Peters, W.;

van der Laan-Luijkx, I. T., Warm spring reduced carbon cycle impact of the 2012 US summer drought. *Proc. Natl. Acad. Sci. U. S. A.* **2016,** *113* (21), 5880-5885.

4. Anantharaj, S.; Ede, S. R.; Sakthikumar, K.; Karthick, K.; Mishra, S.; Kundu, S., Recent Trends and Perspectives in Electrochemical Water Splitting with an Emphasis on Sulfide, Selenide, and Phosphide Catalysts of Fe, Co, and Ni: A Review. *Acs Catal* **2016,** *6* (12), 8069-8097.

5. Jernelöv, A., How to defend against future oil spills. *Nature* **2010,** *466* (7303), 182-183.

6. Wang, L. M.; Chen, W. L.; Zhang, D. D.; Du, Y. P.; Amal, R.; Qiao, S. Z.; Bf, J. W.; Yin, Z. Y., Surface strategies for catalytic CO2 reduction: from two-dimensional materials to nanoclusters to single atoms. *Chem Soc Rev* **2019,** *48* (21), 5310-5349.

7. Li, X.; Yu, J. G.; Jaroniec, M.; Chen, X. B., Cocatalysts for Selective Photoreduction of CO2 into Solar Fuels. *Chem Rev* **2019,** *119* (6), 3962-4179.

8. Manthiram, A.; Fu, Y. Z.; Chung, S. H.; Zu, C. X.; Su, Y. S., Rechargeable Lithium-Sulfur Batteries. *Chem Rev* **2014,** *114* (23), 11751-11787.

9. Liu, T.; Vivek, J. P.; Zhao, E. W.; Lei, J.; Garcia-Araez, N.; Grey, C. P., Current Challenges and Routes Forward for Nonaqueous Lithium-Air Batteries. *Chem Rev* **2020,** *120* (14), 6558-6625.

10. Bottari, G.; de la Torre, G.; Guldi, D. M.; Torres, T., Covalent and Noncovalent Phthalocyanine-Carbon Nanostructure Systems: Synthesis, Photoinduced Electron Transfer, and Application to Molecular Photovoltaics. *Chem Rev* **2010,** *110* (11), 6768-6816.

11. Hedley, G. J.; Ruseckas, A.; Samuel, I. D. W., Light Harvesting for Organic Photovoltaics. *Chem Rev* **2017,** *117* (2), 796-837.

12. Wadsworth, A.; Moser, M.; Marks, A.; Little, M. S.; Gasparini, N.; Brabec, C. J.; Baran, D.; McCulloch, I., Critical review of the molecular design progress in non-fullerene electron acceptors towards commercially viable organic solar cells. *Chem Soc Rev* **2019,** *48* (6), 1596-1625.

13. Vasilopoulou, M.; Fakharuddin, A.; Coutsolelos, A. G.; Falaras, P.; Argitis, P.; Yusoff, A. R. B.; Nazeeruddin, M. K., Molecular materials as interfacial layers and additives in perovskite solar cells. *Chem Soc Rev* **2020,** *49* (13), 4496-4526.

14. Pan, Z. X.; Rao, H. S.; Mora-Sero, I.; Bisquert, J.; Zhong, X. H., Quantum dot-sensitized solar cells. *Chem Soc Rev* **2018,** *47* (20), 7659-7702.

15. He, Y. H.; Liu, S. W.; Priest, C.; Shi, Q. R.; Wu, G., Atomically dispersed metal-nitrogen-carbon catalysts for fuel cells: advances in catalyst design, electrode performance, and durability improvement. *Chem Soc Rev* **2020,** *49* (11), 3484-3524.

16. Wang, Y. J.; Qiao, J. L.; Baker, R.; Zhang, J. J., Alkaline polymer electrolyte membranes for fuel cell applications. *Chem Soc Rev* **2013,** *42* (13), 5768-5787.

17. Zhang, H. W.; Shen, P. K., Advances in the high performance polymer electrolyte membranes for fuel cells. *Chem Soc Rev* **2012,** *41* (6), 2382-2394.

18. Peighambardoust, S. J.; Rowshanzamir, S.; Amjadi, M., Review of the proton exchange membranes for fuel cell applications. *International Journal of Hydrogen Energy* **2010,** *35* (17), 9349-9384.

19. Jung, E.; Shin, H.; Hooch Antink, W.; Sung, Y.-E.; Hyeon, T., Recent Advances in Electrochemical Oxygen Reduction to H2O2: Catalyst and Cell Design. *Acs Energy Lett* **2020,** *5* (6), 1881-1892.

20. Wang, Y. J.; Zhao, N. N.; Fang, B. Z.; Li, H.; Bi, X. T. T.; Wang, H. J., Carbon-Supported Pt-Based Alloy Electrocatalysts for the Oxygen Reduction Reaction in Polymer Electrolyte Membrane Fuel Cells: Particle Size, Shape, and Composition Manipulation and Their Impact to Activity. *Chem Rev* **2015,** *115* (9), 3433-3467.

21. Zhou, M.; Wang, H. L.; Guo, S. J., Towards high-efficiency nanoelectrocatalysts for oxygen reduction through engineering advanced carbon nanomaterials. *Chem Soc Rev* **2016,** *45* (5), 1273-1307.

22. Huang, X.; Zhao, Z.; Cao, L.; Chen, Y.; Zhu, E.; Lin, Z.; Li, M.; Yan, A.; Zettl, A.; Wang, Y. M.; Duan, X.; Mueller, T.; Huang, Y., High-performance transition metal–doped Pt₃Ni octahedra for oxygen reduction reaction. *Science* **2015,** *348* (6240), 1230-1234.

23. Gong, M.; Deng, Z.; Xiao, D.; Han, L.; Zhao, T.; Lu, Y.; Shen, T.; Liu, X.; Lin, R.; Huang, T.; Zhou, G.; Xin, H.; Wang, D., One-Nanometer-Thick Pt3Ni Bimetallic Alloy Nanowires Advanced Oxygen Reduction Reaction: Integrating Multiple Advantages into One Catalyst. *Acs Catal* **2019,** *9* (5), 4488-4494.

24. Becknell, N.; Kang, Y.; Chen, C.; Resasco, J.; Kornienko, N.; Guo, J.; Markovic, N. M.; Somorjai, G. A.; Stamenkovic, V. R.; Yang, P., Atomic Structure of Pt3Ni Nanoframe Electrocatalysts by in Situ X-ray Absorption Spectroscopy. *J Am Chem Soc* **2015,** *137* (50), 15817-15824.

25. Xiong, Y.; Xiao, L.; Yang, Y.; DiSalvo, F. J.; Abruña, H. D., High-Loading Intermetallic Pt3Co/C Core–Shell Nanoparticles as Enhanced Activity Electrocatalysts toward the Oxygen Reduction Reaction (ORR). *Chemistry of Materials* **2018,** *30* (5), 1532-1539.

26. Wang, D.; Xin, H. L.; Hovden, R.; Wang, H.; Yu, Y.; Muller, D. A.; DiSalvo, F. J.; Abruña, H. D., Structurally ordered intermetallic platinum–cobalt core–shell nanoparticles with enhanced activity and stability as oxygen reduction electrocatalysts. *Nature Materials* **2013,** *12* (1), 81-87.

27. Zhang, S.; Zhang, X.; Jiang, G.; Zhu, H.; Guo, S.; Su, D.; Lu, G.; Sun, S., Tuning Nanoparticle Structure and Surface Strain for Catalysis Optimization. *J Am Chem Soc* **2014,** *136* (21), 7734-7739.

28. Chung, D. Y.; Jun, S. W.; Yoon, G.; Kwon, S. G.; Shin, D. Y.; Seo, P.; Yoo, J. M.; Shin, H.; Chung, Y.-H.; Kim, H.; Mun, B. S.; Lee, K.-S.; Lee, N.-S.; Yoo, S. J.; Lim, D.-H.; Kang, K.; Sung, Y.-E.; Hyeon, T., Highly Durable and Active PtFe Nanocatalyst for Electrochemical Oxygen Reduction Reaction. *J Am Chem Soc* **2015,** *137* (49), 15478-15485.

29. Li, T.; Liu, J.; Song, Y.; Wang, F., Photochemical Solid-Phase Synthesis of Platinum Single Atoms on Nitrogen-Doped Carbon with High Loading as Bifunctional Catalysts for Hydrogen Evolution and Oxygen Reduction Reactions. *Acs Catal* **2018,** *8* (9), 8450-8458.

30. Song, X.; Li, N.; Zhang, H.; Wang, H.; Wang, L.; Bian, Z., Promotion of hydrogen peroxide production on graphene-supported atomically dispersed platinum:

Effects of size on oxygen reduction reaction pathway. *Journal of Power Sources* **2019,** *435*, 226771.

31. Lu, B.; Liu, Q.; Chen, S., Electrocatalysis of Single-Atom Sites: Impacts of Atomic Coordination. *Acs Catal* **2020,** *10* (14), 7584-7618.

32. Liu, J.; Jiao, M.; Lu, L.; Barkholtz, H. M.; Li, Y.; Wang, Y.; Jiang, L.; Wu, Z.; Liu, D.-j.; Zhuang, L.; Ma, C.; Zeng, J.; Zhang, B.; Su, D.; Song, P.; Xing, W.; Xu, W.; Wang, Y.; Jiang, Z.; Sun, G., High performance platinum single atom electrocatalyst for oxygen reduction reaction. *Nat Commun* **2017,** *8* (1), 15938.

33. Liu, J.; Jiao, M.; Mei, B.; Tong, Y.; Li, Y.; Ruan, M.; Song, P.; Sun, G.; Jiang, L.; Wang, Y.; Jiang, Z.; Gu, L.; Zhou, Z.; Xu, W., Carbon-Supported Divacancy-Anchored Platinum Single-Atom Electrocatalysts with Superhigh Pt Utilization for the Oxygen Reduction Reaction. *Angewandte Chemie International Edition* **2019,** *58* (4), 1163-1167.

34. Xiao, M.; Zhu, J.; Li, G.; Li, N.; Li, S.; Cano, Z. P.; Ma, L.; Cui, P.; Xu, P.; Jiang, G.; Jin, H.; Wang, S.; Wu, T.; Lu, J.; Yu, A.; Su, D.; Chen, Z., A Single-Atom Iridium Heterogeneous Catalyst in Oxygen Reduction Reaction. *Angewandte Chemie International Edition* **2019,** *58* (28), 9640-9645.

35. Zhang, H.; Hwang, S.; Wang, M.; Feng, Z.; Karakalos, S.; Luo, L.; Qiao, Z.; Xie, X.; Wang, C.; Su, D.; Shao, Y.; Wu, G., Single Atomic Iron Catalysts for Oxygen Reduction in Acidic Media: Particle Size Control and Thermal Activation. *J Am Chem Soc* **2017,** *139* (40), 14143-14149.

36. Wu, G.; More, K. L.; Johnston, C. M.; Zelenay, P., High-Performance Electrocatalysts for Oxygen Reduction Derived from Polyaniline, Iron, and Cobalt. *Science* **2011,** *332* (6028), 443-447.

37. Lu, B.; Smart, T. J.; Qin, D.; Lu, J. E.; Wang, N.; Chen, L.; Peng, Y.; Ping, Y.; Chen, S., Nitrogen and Iron-Codoped Carbon Hollow Nanotubules as High-Performance Catalysts toward Oxygen Reduction Reaction: A Combined Experimental and Theoretical Study. *Chemistry of Materials* **2017,** *29* (13), 5617-5628.

38. Gong, K.; Du, F.; Xia, Z.; Durstock, M.; Dai, L., Nitrogen-Doped Carbon Nanotube Arrays with High Electrocatalytic Activity for Oxygen Reduction. *Science* **2009,** *323* (5915), 760-764.

39. Liang, H.-W.; Zhuang, X.; Brüller, S.; Feng, X.; Müllen, K., Hierarchically porous carbons with optimized nitrogen doping as highly active electrocatalysts for oxygen reduction. *Nat Commun* **2014,** *5* (1), 4973.

40. Kanan, M. W.; Surendranath, Y.; Nocera, D. G., Cobalt–phosphate oxygen-evolving compound. *Chem Soc Rev* **2009,** *38* (1), 109-114.

41. Sheng, W. C.; Gasteiger, H. A.; Shao-Horn, Y., Hydrogen Oxidation and Evolution Reaction Kinetics on Platinum: Acid vs Alkaline Electrolytes. *J Electrochem Soc* **2010,** *157* (11), B1529-B1536.

42. Qiu, Y.; Xin, L.; Li, Y. W.; McCrum, I. T.; Guo, F. M.; Ma, T.; Ren, Y.; Liu, Q.; Zhou, L.; Gu, S.; Janik, M. J.; Li, W. Z., BCC-Phased PdCu Alloy as a Highly Active Electrocatalyst for Hydrogen Oxidation in Alkaline Electrolytes. *J Am Chem Soc* **2018,** *140* (48), 16580-16588.

43. Sheng, W. C.; Bivens, A. P.; Myint, M.; Zhuang, Z. B.; Forest, R. V.; Fang, Q. R.; Chen, J. G.; Yan, Y. S., Non-precious metal electrocatalysts with high activity for hydrogen oxidation reaction in alkaline electrolytes. *Energ Environ Sci* **2014,** *7* (5), 1719-1724.

44. Rees, N. V.; Compton, R. G., Sustainable energy: a review of formic acid electrochemical fuel cells. *Journal of solid state electrochemistry* **2011,** *15* (10), 2095-2100.

45. Zhang, L.; Wu, W.; Jiang, Z.; Fang, T., A review on liquid-phase heterogeneous dehydrogenation of formic acid: recent advances and perspectives. *Chemical Papers* **2018,** *72* (9), 2121-2135.

46. Luo, S. P.; Chen, W.; Cheng, Y.; Song, X.; Wu, Q. L.; Li, L. X.; Wu, X. T.; Wu, T. H.; Li, M. R.; Yang, Q.; Deng, K. R.; Quan, Z. W., Trimetallic Synergy in Intermetallic PtSnBi Nanoplates Boosts Formic Acid Oxidation. *Adv Mater* **2019,** *31* (40).

47. Du, X. W.; Luo, S. P.; Du, H. Y.; Tang, M.; Huang, X. D.; Shen, P. K., Monodisperse and self-assembled Pt-Cu nanoparticles as an efficient electrocatalyst for the methanol oxidation reaction. *J Mater Chem A* **2016,** *4* (5), 1579-1585.

48. Cui, X.; Xiao, P.; Wang, J.; Zhou, M.; Guo, W. L.; Yang, Y.; He, Y. J.; Wang, Z. W.; Yang, Y. K.; Zhang, Y. H.; Lin, Z. Q., Highly Branched Metal Alloy Networks with Superior Activities for the Methanol Oxidation Reaction. *Angew Chem Int Edit* **2017,** *56* (16), 4488-4493.

49. Joghee, P.; Malik, J. N.; Pylypenko, S.; O'Hayre, R., A review on direct methanol fuel cells – In the perspective of energy and sustainability. *MRS Energy & Sustainability* **2015,** *2*, E3.

50. Ahmed, M.; Dincer, I., A review on methanol crossover in direct methanol fuel cells: challenges and achievements. *International Journal of Energy Research* **2011,** *35* (14), 1213-1228.

51. Chung, D. Y.; Kim, H.-i.; Chung, Y.-H.; Lee, M. J.; Yoo, S. J.; Bokare, A. D.; Choi, W.; Sung, Y.-E., Inhibition of CO poisoning on Pt catalyst coupled with the reduction of toxic hexavalent chromium in a dual-functional fuel cell. *Scientific Reports* **2014,** *4* (1), 7450.

52. Akhairi, M. A. F.; Kamarudin, S. K., Catalysts in direct ethanol fuel cell (DEFC): An overview. *International Journal of Hydrogen Energy* **2016,** *41* (7), 4214-4228.

53. Du, W. X.; Mackenzie, K. E.; Milano, D. F.; Deskins, N. A.; Su, D.; Teng, X. W., Palladium-Tin Alloyed Catalysts for the Ethanol Oxidation Reaction in an Alkaline Medium. *Acs Catal* **2012,** *2* (2), 287-297.

54. Piwowar, J.; Lewera, A., On the absence of a beneficial role of Rh towards CC bond cleavage during low temperature ethanol electrooxidation on PtRh nanoalloys. *Journal of Electroanalytical Chemistry* **2020**, 114229.

55. Chang, Q.; Kattel, S.; Li, X.; Liang, Z.; Tackett, B. M.; Denny, S. R.; Zhang, P.; Su, D.; Chen, J. G.; Chen, Z., Enhancing C–C Bond Scission for Efficient Ethanol Oxidation using PtIr Nanocube Electrocatalysts. *Acs Catal* **2019,** *9* (9), 7618-7625.

56. Shi, Y.; Zhang, B., Recent advances in transition metal phosphide nanomaterials: synthesis and applications in hydrogen evolution reaction. *Chem Soc Rev* **2016,** *45* (6), 1529-1541.

57. Navarro, R. M.; Peña, M. A.; Fierro, J. L. G., Hydrogen Production Reactions from Carbon Feedstocks: Fossil Fuels and Biomass. *Chem Rev* **2007,** *107* (10), 3952-3991.

58. Lu, B.; Guo, L.; Wu, F.; Peng, Y.; Lu, J. E.; Smart, T. J.; Wang, N.; Finfrock, Y. Z.; Morris, D.; Zhang, P.; Li, N.; Gao, P.; Ping, Y.; Chen, S., Ruthenium atomically dispersed in carbon outperforms platinum toward hydrogen evolution in alkaline media. *Nat Commun* **2019,** *10* (1), 631.

59. Zhu, J.; Hu, L. S.; Zhao, P. X.; Lee, L. Y. S.; Wong, K. Y., Recent Advances in Electrocatalytic Hydrogen Evolution Using Nanoparticles. *Chem Rev* **2020,** *120* (2), 851-918.

60. Gong, M.; Zhou, W.; Tsai, M.-C.; Zhou, J.; Guan, M.; Lin, M.-C.; Zhang, B.; Hu, Y.; Wang, D.-Y.; Yang, J.; Pennycook, S. J.; Hwang, B.-J.; Dai, H., Nanoscale nickel oxide/nickel heterostructures for active hydrogen evolution electrocatalysis. *Nat Commun* **2014,** *5* (1), 4695.

61. Zhao, L.; Zhang, Y.; Zhao, Z.; Zhang, Q.-H.; Huang, L.-B.; Gu, L.; Lu, G.; Hu, J.-S.; Wan, L.-J., Steering elementary steps towards efficient alkaline hydrogen evolution via size-dependent Ni/NiO nanoscale heterosurfaces. *National Science Review* **2019,** *7* (1), 27-36.

62. Hu, G.; Tang, Q.; Jiang, D.-e., CoP for hydrogen evolution: implications from hydrogen adsorption. *Phys Chem Chem Phys* **2016,** *18* (34), 23864-23871.

63. Zhang, J.; Xiao, W.; Xi, P.; Xi, S.; Du, Y.; Gao, D.; Ding, J., Activating and Optimizing Activity of CoS2 for Hydrogen Evolution Reaction through the Synergic Effect of N Dopants and S Vacancies. *Acs Energy Lett* **2017,** *2* (5), 1022-1028.

64. Ding, Q.; Song, B.; Xu, P.; Jin, S., Efficient Electrocatalytic and Photoelectrochemical Hydrogen Generation Using MoS2 and Related Compounds. *Chem* **2016,** *1* (5), 699-726.

65. Peng, Y.; Lu, B.; Chen, L.; Wang, N.; Lu, J. E.; Ping, Y.; Chen, S., Hydrogen evolution reaction catalyzed by ruthenium ion-complexed graphitic carbon nitride nanosheets. *J Mater Chem A* **2017,** *5* (34), 18261-18269.

66. Peng, Y.; Pan, W.; Wang, N.; Lu, J.-E.; Chen, S., Ruthenium Ion-Complexed Graphitic Carbon Nitride Nanosheets Supported on Reduced Graphene Oxide as High-Performance Catalysts for Electrochemical Hydrogen Evolution. *ChemSusChem* **2018,** *11* (1), 130-136.

67. Qu, K.; Zheng, Y.; Zhang, X.; Davey, K.; Dai, S.; Qiao, S. Z., Promotion of Electrocatalytic Hydrogen Evolution Reaction on Nitrogen-Doped Carbon Nanosheets with Secondary Heteroatoms. *ACS Nano* **2017,** *11* (7), 7293-7300.

68. Zheng, Y.; Jiao, Y.; Vasileff, A.; Qiao, S.-Z., The Hydrogen Evolution Reaction in Alkaline Solution: From Theory, Single Crystal Models, to Practical Electrocatalysts. *Angewandte Chemie International Edition* **2018,** *57* (26), 7568-7579.

69. Durst, J.; Siebel, A.; Simon, C.; Hasché, F.; Herranz, J.; Gasteiger, H. A., New insights into the electrochemical hydrogen oxidation and evolution reaction mechanism. *Energ Environ Sci* **2014,** *7* (7), 2255-2260.

70. Suen, N. T.; Hung, S. F.; Quan, Q.; Zhang, N.; Xu, Y. J.; Chen, H. M., Electrocatalysis for the oxygen evolution reaction: recent development and future perspectives. *Chem Soc Rev* **2017,** *46* (2), 337-365.

71. Zhao, Q.; Yan, Z. H.; Chen, C. C.; Chen, J., Spinels: Controlled Preparation, Oxygen Reduction/Evolution Reaction Application, and Beyond. *Chem Rev* **2017,** *117* (15), 10121-10211.

72. Seitz, L. C.; Dickens, C. F.; Nishio, K.; Hikita, Y.; Montoya, J.; Doyle, A.; Kirk, C.; Vojvodic, A.; Hwang, H. Y.; Norskov, J. K.; Jaramillo, T. F., A highly active and stable IrOx/SrIrO3 catalyst for the oxygen evolution reaction. *Science* **2016,** *353* (6303), 1011-1014.

73. Stamenkovic, V. R.; Fowler, B.; Mun, B. S.; Wang, G. F.; Ross, P. N.; Lucas, C. A.; Markovic, N. M., Improved oxygen reduction activity on Pt3Ni(111) via increased surface site availability. *Science* **2007,** *315* (5811), 493-497.

74. Chen, C.; Kang, Y. J.; Huo, Z. Y.; Zhu, Z. W.; Huang, W. Y.; Xin, H. L. L.; Snyder, J. D.; Li, D. G.; Herron, J. A.; Mavrikakis, M.; Chi, M. F.; More, K. L.; Li, Y. D.; Markovic, N. M.; Somorjai, G. A.; Yang, P. D.; Stamenkovic, V. R., Highly Crystalline Multimetallic Nanoframes with Three-Dimensional Electrocatalytic Surfaces. *Science* **2014,** *343* (6177), 1339-1343.

75. Luo, M. C.; Zhao, Z. L.; Zhang, Y. L.; Sun, Y. J.; Xing, Y.; Lv, F.; Yang, Y.; Zhang, X.; Hwang, S.; Qin, Y. N.; Ma, J. Y.; Lin, F.; Su, D.; Lu, G.; Guo, S. J., PdMo bimetallene for oxygen reduction catalysis. *Nature* **2019,** *574* (7776), 81-+.

76. Tymoczko, J.; Calle-Vallejo, F.; Schuhmann, W.; Bandarenka, A. S., Making the hydrogen evolution reaction in polymer electrolyte membrane electrolysers even faster. *Nat Commun* **2016,** *7*.

77. Wang, P. T.; Zhang, X.; Zhang, J.; Wan, S.; Guo, S. J.; Lu, G.; Yao, J. L.; Huang, X. Q., Precise tuning in platinum-nickel/ nickel sulfide interface nanowires for synergistic hydrogen evolution catalysis. *Nat Commun* **2017,** *8*.

78. Cao, Z. M.; Chen, Q. L.; Zhang, J. W.; Li, H. Q.; Jiang, Y. Q.; Shen, S. Y.; Fu, G.; Lu, B. A.; Xie, Z. X.; Zheng, L. S., Platinum-nickel alloy excavated nano-multipods with hexagonal close-packed structure and superior activity towards hydrogen evolution reaction. *Nat Commun* **2017,** *8*.

79. Su, J. W.; Yang, Y.; Xia, G. L.; Chen, J. T.; Jiang, P.; Chen, Q. W., Ruthenium-cobalt nanoalloys encapsulated in nitrogen-doped graphene as active electrocatalysts for producing hydrogen in alkaline media. *Nat Commun* **2017,** *8*.

80. Wu, Q. L.; Luo, M.; Han, J. H.; Peng, W.; Zhao, Y.; Chen, D. C.; Peng, M.; Liu, J.; de Groot, F. M. F.; Tan, Y. W., Identifying Electrocatalytic Sites of the Nanoporous Copper-Ruthenium Alloy for Hydrogen Evolution Reaction in Alkaline Electrolyte. *Acs Energy Lett* **2020,** *5* (1), 192-199.

81. Jiang, P.; Chen, J. T.; Wang, C. L.; Yang, K.; Gong, S. P.; Liu, S.; Lin, Z. Y.; Li, M. S.; Xia, G. L.; Yang, Y.; Su, J. W.; Chen, Q. W., Tuning the Activity of Carbon

for Electrocatalytic Hydrogen Evolution via an Iridium-Cobalt Alloy Core Encapsulated in Nitrogen-Doped Carbon Cages. *Adv Mater* **2018,** *30* (9).

82. Shen, T.; Zhang, J.; Chen, K.; Deng, S.; Wang, D., Recent Progress of Palladium-Based Electrocatalysts for the Formic Acid Oxidation Reaction. *Energy & Fuels* **2020,** *34* (8), 9137-9153.

83. Yang, N. L.; Zhang, Z. C.; Chen, B.; Huang, Y.; Chen, J. Z.; Lai, Z. C.; Chen, Y.; Sindoro, M.; Wang, A. L.; Cheng, H. F.; Fan, Z. X.; Liu, X. Z.; Li, B.; Zong, Y.; Gu, L.; Zhang, H., Synthesis of Ultrathin PdCu Alloy Nanosheets Used as a Highly Efficient Electrocatalyst for Formic Acid Oxidation. *Adv Mater* **2017,** *29* (29).

84. Huang, L.; Zhang, X. P.; Wang, Q. Q.; Han, Y. J.; Fang, Y. X.; Dong, S. J., Shape-Control of Pt-Ru Nanocrystals: Tuning Surface Structure for Enhanced Electrocatalytic Methanol Oxidation. *J Am Chem Soc* **2018,** *140* (3), 1142-1147.

85. Kakati, N.; Maiti, J.; Lee, S. H.; Jee, S. H.; Viswanathan, B.; Yoon, Y. S., Anode Catalysts for Direct Methanol Fuel Cells in Acidic Media: Do We Have Any Alternative for Pt or Pt-Ru? *Chem Rev* **2014,** *114* (24), 12397-12429.

86. Antolini, E.; Gonzalez, E. R., Effect of synthesis method and structural characteristics of Pt-Sn fuel cell catalysts on the electro-oxidation of CH3OH and CH3CH2OH in acid medium. *Catal Today* **2011,** *160* (1), 28-38.

87. Ma, Y.; Wang, H.; Ji, S.; Linkov, V.; Wang, R., PtSn/C catalysts for ethanol oxidation: The effect of stabilizers on the morphology and particle distribution. *Journal of Power Sources* **2014,** *247*, 142-150.

88. Yang, L.; Yu, G.; Ai, X.; Yan, W.; Duan, H.; Chen, W.; Li, X.; Wang, T.; Zhang, C.; Huang, X.; Chen, J.-S.; Zou, X., Efficient oxygen evolution electrocatalysis in acid by a perovskite with face-sharing IrO6 octahedral dimers. *Nat Commun* **2018,** *9* (1), 5236.

89. Lin, Y. C.; Tian, Z. Q.; Zhang, L. J.; Ma, J. Y.; Jiang, Z.; Deibert, B. J.; Ge, R. X.; Chen, L., Chromium-ruthenium oxide solid solution electrocatalyst for highly efficient oxygen evolution reaction in acidic media. *Nat Commun* **2019,** *10*.

90. Su, J. W.; Ge, R. X.; Jiang, K. M.; Dong, Y.; Hao, F.; Tian, Z. Q.; Chen, G. X.; Chen, L., Assembling Ultrasmall Copper-Doped Ruthenium Oxide Nanocrystals into Hollow Porous Polyhedra: Highly Robust Electrocatalysts for Oxygen Evolution in Acidic Media. *Adv Mater* **2018,** *30* (29).

91. Chong, L.; Wen, J. G.; Kubal, J.; Sen, F. G.; Zou, J. X.; Greeley, J.; Chan, M.; Barkholtz, H.; Ding, W. J.; Liu, D. J., Ultralow-loading platinum-cobalt fuel cell catalysts derived from imidazolate frameworks. *Science* **2018,** *362* (6420), 1276-+.

92. Liu, D.; Li, X.; Chen, S.; Yan, H.; Wang, C.; Wu, C.; Haleem, Y. A.; Duan, S.; Lu, J.; Ge, B.; Ajayan, P. M.; Luo, Y.; Jiang, J.; Song, L., Atomically dispersed platinum supported on curved carbon supports for efficient electrocatalytic hydrogen evolution. *Nature Energy* **2019,** *4* (6), 512-518.

93. Liu, W.; Xu, Q.; Yan, P.; Chen, J.; Du, Y.; Chu, S.; Wang, J., Fabrication of a Single-Atom Platinum Catalyst for the Hydrogen Evolution Reaction: A New Protocol by Utilization of HxMoO3−x with Plasmon Resonance. *ChemCatChem* **2018,** *10* (5), 946-950.

94. Guan, Y.; Feng, Y.; Wan, J.; Yang, X.; Fang, L.; Gu, X.; Liu, R.; Huang, Z.; Li, J.; Luo, J.; Li, C.; Wang, Y., Ganoderma-Like MoS2/NiS2 with Single Platinum Atoms Doping as an Efficient and Stable Hydrogen Evolution Reaction Catalyst. *Small* **2018,** *14* (27), 1800697.

95. Zhang, L.; Han, L.; Liu, H.; Liu, X.; Luo, J., Potential-Cycling Synthesis of Single Platinum Atoms for Efficient Hydrogen Evolution in Neutral Media. *Angewandte Chemie International Edition* **2017,** *56* (44), 13694-13698.

96. Jiang, K.; Liu, B.; Luo, M.; Ning, S.; Peng, M.; Zhao, Y.; Lu, Y.-R.; Chan, T.-S.; de Groot, F. M. F.; Tan, Y., Single platinum atoms embedded in nanoporous cobalt selenide as electrocatalyst for accelerating hydrogen evolution reaction. *Nat Commun* **2019,** *10* (1), 1743.

97. Zhang, J.; Zhao, Y.; Guo, X.; Chen, C.; Dong, C.-L.; Liu, R.-S.; Han, C.-P.; Li, Y.; Gogotsi, Y.; Wang, G., Single platinum atoms immobilized on an MXene as an efficient catalyst for the hydrogen evolution reaction. *Nature Catalysis* **2018,** *1* (12), 985-992.

98. Lu, B. Z.; Guo, L.; Wu, F.; Peng, Y.; Lu, J. E.; Smart, T. J.; Wang, N.; Finfrock, Y. Z.; Morris, D.; Zhang, P.; Li, N.; Gao, P.; Ping, Y.; Chen, S. W., Ruthenium atomically dispersed in carbon outperforms platinum toward hydrogen evolution in alkaline media. *Nat Commun* **2019,** *10*.

99. Yang, J.; Chen, B.; Liu, X.; Liu, W.; Li, Z.; Dong, J.; Chen, W.; Yan, W.; Yao, T.; Duan, X.; Wu, Y.; Li, Y., Efficient and Robust Hydrogen Evolution:

Phosphorus Nitride Imide Nanotubes as Supports for Anchoring Single Ruthenium Sites. *Angewandte Chemie International Edition* **2018,** *57* (30), 9495-9500.

100. Zhang, J.; Xu, X.; Yang, L.; Cheng, D.; Cao, D., Single-Atom Ru Doping Induced Phase Transition of MoS2 and S Vacancy for Hydrogen Evolution Reaction. *Small Methods* **2019,** *3* (12), 1900653.

101. Li, P.; Wang, M.; Duan, X.; Zheng, L.; Cheng, X.; Zhang, Y.; Kuang, Y.; Li, Y.; Ma, Q.; Feng, Z.; Liu, W.; Sun, X., Boosting oxygen evolution of single-atomic ruthenium through electronic coupling with cobalt-iron layered double hydroxides. *Nat Commun* **2019,** *10* (1), 1711.

102. Bezerra, C. W. B.; Zhang, L.; Lee, K.; Liu, H.; Marques, A. L. B.; Marques, E. P.; Wang, H.; Zhang, J., A review of Fe–N/C and Co–N/C catalysts for the oxygen reduction reaction. *Electrochimica Acta* **2008,** *53* (15), 4937-4951.

103. Jiang, W.-J.; Gu, L.; Li, L.; Zhang, Y.; Zhang, X.; Zhang, L.-J.; Wang, J.-Q.; Hu, J.-S.; Wei, Z.; Wan, L.-J., Understanding the High Activity of Fe–N–C Electrocatalysts in Oxygen Reduction: Fe/Fe3C Nanoparticles Boost the Activity of Fe–Nx. *J Am Chem Soc* **2016,** *138* (10), 3570-3578.

104. Peng, Y.; Lu, B.; Chen, S., Carbon-Supported Single Atom Catalysts for Electrochemical Energy Conversion and Storage. *Adv Mater* **2018,** *30* (48), 1801995.

105. Wang, X.; Li, Z.; Qu, Y.; Yuan, T.; Wang, W.; Wu, Y.; Li, Y., Review of Metal Catalysts for Oxygen Reduction Reaction: From Nanoscale Engineering to Atomic Design. *Chem* **2019,** *5* (6), 1486-1511.

106. Zhu, J.; Hu, L.; Zhao, P.; Lee, L. Y. S.; Wong, K.-Y., Recent Advances in Electrocatalytic Hydrogen Evolution Using Nanoparticles. *Chem Rev* **2020,** *120* (2), 851-918.

107. Chen, Y.-Y.; Zhang, Y.; Zhang, X.; Tang, T.; Luo, H.; Niu, S.; Dai, Z.-H.; Wan, L.-J.; Hu, J.-S., Self-Templated Fabrication of MoNi4/MoO3-x Nanorod Arrays with Dual Active Components for Highly Efficient Hydrogen Evolution. *Adv Mater* **2017,** *29* (39), 1703311.

108. Tian, J.; Liu, Q.; Asiri, A. M.; Sun, X., Self-Supported Nanoporous Cobalt Phosphide Nanowire Arrays: An Efficient 3D Hydrogen-Evolving Cathode over the Wide Range of pH 0–14. *J Am Chem Soc* **2014,** *136* (21), 7587-7590.

109. Liu, P.; Zhu, J.; Zhang, J.; Xi, P.; Tao, K.; Gao, D.; Xue, D., P Dopants Triggered New Basal Plane Active Sites and Enlarged Interlayer Spacing in MoS2 Nanosheets toward Electrocatalytic Hydrogen Evolution. *Acs Energy Lett* **2017,** *2* (4), 745-752.

110. Liu, Y.; Liang, X.; Gu, L.; Zhang, Y.; Li, G.-D.; Zou, X.; Chen, J.-S., Corrosion engineering towards efficient oxygen evolution electrodes with stable catalytic activity for over 6000 hours. *Nat Commun* **2018,** *9* (1), 2609.

111. Zhao, Q.; Yan, Z.; Chen, C.; Chen, J., Spinels: Controlled Preparation, Oxygen Reduction/Evolution Reaction Application, and Beyond. *Chem Rev* **2017,** *117* (15), 10121-10211.

112. Schäfer, H.; Chevrier, D. M.; Kuepper, K.; Zhang, P.; Wollschlaeger, J.; Daum, D.; Steinhart, M.; Heß, C.; Krupp, U.; Müller-Buschbaum, K.; Stangl, J.;

Schmidt, M., X20CoCrWMo10-9//Co3O4: a metal–ceramic composite with unique efficiency values for water-splitting in the neutral regime. *Energ Environ Sci* **2016,** *9* (8), 2609-2622.

113. Zhu, C. Z.; Li, H.; Fu, S. F.; Du, D.; Lin, Y. H., Highly efficient nonprecious metal catalysts towards oxygen reduction reaction based on three-dimensional porous carbon nanostructures. *Chem Soc Rev* **2016,** *45* (3), 517-531.

114. Zhang, J.; Xia, Z.; Dai, L., Carbon-based electrocatalysts for advanced energy conversion and storage. *Science Advances* **2015,** *1* (7), e1500564.

115. He, T.; Lu, B.; Chen, Y.; Wang, Y.; Zhang, Y.; Davenport, J. L.; Chen, A. P.; Pao, C.-W.; Liu, M.; Sun, Z.; Stram, A.; Mordaunt, A.; Velasco, J.; Ping, Y.; Zhang, Y.; Chen, S., Nanowrinkled Carbon Aerogels Embedded with FeN Sites as Effective Oxygen Electrodes for Rechargeable Zinc-Air Battery. *Research* **2019,** *2019*, 6813585.

116. Duan, J.; Chen, S.; Jaroniec, M.; Qiao, S. Z., Porous C3N4 Nanolayers@N-Graphene Films as Catalyst Electrodes for Highly Efficient Hydrogen Evolution. *ACS Nano* **2015,** *9* (1), 931-940.

117. Zhou, W.; Zhou, Y.; Yang, L.; Huang, J.; Ke, Y.; Zhou, K.; Li, L.; Chen, S., N-doped carbon-coated cobalt nanorod arrays supported on a titanium mesh as highly active electrocatalysts for the hydrogen evolution reaction. *J Mater Chem A* **2015,** *3* (5), 1915-1919.

118. Mahmood, J.; Li, F.; Jung, S.-M.; Okyay, M. S.; Ahmad, I.; Kim, S.-J.; Park, N.; Jeong, H. Y.; Baek, J.-B., An efficient and pH-universal ruthenium-based catalyst for the hydrogen evolution reaction. *Nature Nanotechnology* **2017,** *12* (5), 441-446.

119. Zhou, W.; Jia, J.; Lu, J.; Yang, L.; Hou, D.; Li, G.; Chen, S., Recent developments of carbon-based electrocatalysts for hydrogen evolution reaction. *Nano Energy* **2016,** *28*, 29-43.

120. Niu, W. H.; Li, L. G.; Liu, X. J.; Wang, N.; Liu, J.; Zhou, W. J.; Tang, Z. H.; Chen, S. W., Mesoporous N-Doped Carbons Prepared with Thermally Removable Nanoparticle Templates: An Efficient Electrocatalyst for Oxygen Reduction Reaction. *J Am Chem Soc* **2015,** *137* (16), 5555-5562.

121. Thorum, M. S.; Hankett, J. M.; Gewirth, A. A., Poisoning the Oxygen Reduction Reaction on Carbon-Supported Fe and Cu Electrocatalysts: Evidence for Metal-Centered Activity. *J Phys Chem Lett* **2011,** *2* (4), 295-298.

122. Liu, Q. M.; Peng, Y.; Li, Q. X.; He, T.; Morris, D.; Nichols, F.; Mercado, R.; Zhang, P.; Chen, S. W., Atomic Dispersion and Surface Enrichment of Palladium in Nitrogen-Doped Porous Carbon Cages Lead to High-Performance Electrocatalytic Reduction of Oxygen. *Acs Appl Mater Inter* **2020,** *12* (15), 17641-17650.

123. Wang, N.; Lu, B. Z.; Li, L. G.; Niu, W. H.; Tang, Z. H.; Kang, X. W.; Chen, S. W., Graphitic Nitrogen Is Responsible for Oxygen Electroreduction on Nitrogen-Doped Carbons in Alkaline Electrolytes: Insights from Activity Attenuation Studies and Theoretical Calculations. *Acs Catal* **2018,** *8* (8), 6827-6836.

124. Li, P. S.; Wang, M. Y.; Duan, X. X.; Zheng, L. R.; Cheng, X. P.; Zhang, Y. F.; Kuang, Y.; Li, Y. P.; Ma, Q.; Feng, Z. X.; Liu, W.; Sun, X. M., Boosting oxygen evolution of single-atomic ruthenium through electronic coupling with cobalt-iron layered double hydroxides. *Nat Commun* **2019,** *10*.

125. Grimaud, A.; Diaz-Morales, O.; Han, B. H.; Hong, W. T.; Lee, Y. L.; Giordano, L.; Stoerzinger, K. A.; Koper, M. T. M.; Shao-Horn, Y., Activating lattice oxygen redox reactions in metal oxides to catalyse oxygen evolution. *Nat Chem* **2017,** *9* (5), 457-465.

126. Greeley, J.; Stephens, I. E. L.; Bondarenko, A. S.; Johansson, T. P.; Hansen, H. A.; Jaramillo, T. F.; Rossmeisl, J.; Chorkendorff, I.; Norskov, J. K., Alloys of platinum and early transition metals as oxygen reduction electrocatalysts. *Nat Chem* **2009,** *1* (7), 552-556.

127. Seh, Z. W.; Kibsgaard, J.; Dickens, C. F.; Chorkendorff, I.; Nørskov, J. K.; Jaramillo, T. F., Combining theory and experiment in electrocatalysis: Insights into materials design. *Science* **2017,** *355* (6321), eaad4998.

128. Skúlason, E.; Tripkovic, V.; Björketun, M. E.; Gudmundsdóttir, S.; Karlberg, G.; Rossmeisl, J.; Bligaard, T.; Jónsson, H.; Nørskov, J. K., Modeling the Electrochemical Hydrogen Oxidation and Evolution Reactions on the Basis of Density Functional Theory Calculations. *The Journal of Physical Chemistry C* **2010,** *114* (42), 18182-18197.

129. Viswanathan, V.; Hansen, H. A.; Rossmeisl, J.; Nørskov, J. K., Universality in Oxygen Reduction Electrocatalysis on Metal Surfaces. *Acs Catal* **2012,** *2* (8), 1654-1660.

130. Greeley, J.; Stephens, I. E. L.; Bondarenko, A. S.; Johansson, T. P.; Hansen, H. A.; Jaramillo, T. F.; Rossmeisl, J.; Chorkendorff, I.; Nørskov, J. K., Alloys of platinum and early transition metals as oxygen reduction electrocatalysts. *Nat Chem* **2009,** *1* (7), 552-556.

131. Chai, G.-L.; Hou, Z.; Shu, D.-J.; Ikeda, T.; Terakura, K., Active Sites and Mechanisms for Oxygen Reduction Reaction on Nitrogen-Doped Carbon Alloy Catalysts: Stone–Wales Defect and Curvature Effect. *J Am Chem Soc* **2014,** *136* (39), 13629-13640.

132. Li, M.; Zhang, L.; Xu, Q.; Niu, J.; Xia, Z., N-doped graphene as catalysts for oxygen reduction and oxygen evolution reactions: Theoretical considerations. *Journal of Catalysis* **2014,** *314*, 66-72.

133. Mavros, M. G.; Shepherd, J. J.; Tsuchimochi, T.; McIsaac, A. R.; Van Voorhis, T., Computational Design Principles of Two-Center First-Row Transition Metal Oxide Oxygen Evolution Catalysts. *The Journal of Physical Chemistry C* **2017,** *121* (29), 15665-15674.

134. Haschke, S.; Mader, M.; Schlicht, S.; Roberts, A. M.; Angeles-Boza, A. M.; Barth, J. A. C.; Bachmann, J., Direct oxygen isotope effect identifies the rate-determining step of electrocatalytic OER at an oxidic surface. *Nat Commun* **2018,** *9* (1), 4565.

135. Exner, K. S.; Over, H., Beyond the Rate-Determining Step in the Oxygen Evolution Reaction over a Single-Crystalline IrO2(110) Model Electrode: Kinetic Scaling Relations. *Acs Catal* **2019,** *9* (8), 6755-6765.

136. Ping, Y.; Nielsen, R. J.; Goddard, W. A., The Reaction Mechanism with Free Energy Barriers at Constant Potentials for the Oxygen Evolution Reaction at the IrO2 (110) Surface. *J Am Chem Soc* **2017,** *139* (1), 149-155.

137. Stoerzinger, K. A.; Diaz-Morales, O.; Kolb, M.; Rao, R. R.; Frydendal, R.; Qiao, L.; Wang, X. R.; Halck, N. B.; Rossmeisl, J.; Hansen, H. A.; Vegge, T.;

Stephens, I. E. L.; Koper, M. T. M.; Shao-Horn, Y., Orientation-Dependent Oxygen Evolution on RuO2 without Lattice Exchange. *Acs Energy Lett* **2017,** *2* (4), 876-881.

138. Sundararaman, R.; Goddard, W. A., The charge-asymmetric nonlocally determined local-electric (CANDLE) solvation model. *J Chem Phys* **2015,** *142* (6).

139. Norskov, J. K.; Rossmeisl, J.; Logadottir, A.; Lindqvist, L.; Kitchin, J. R.; Bligaard, T.; Jonsson, H., Origin of the overpotential for oxygen reduction at a fuel-cell cathode. *J Phys Chem B* **2004,** *108* (46), 17886-17892.

140. Nørskov, J. K.; Abild-Pedersen, F.; Studt, F.; Bligaard, T., Density functional theory in surface chemistry and catalysis. *Proceedings of the National Academy of Sciences* **2011,** *108* (3), 937-943.

141. Pacchioni, G., First Principles Calculations on Oxide-Based Heterogeneous Catalysts and Photocatalysts: Problems and Advances. *Catalysis Letters* **2015,** *145* (1), 80-94.

142. Wu, F.; Galatas, A.; Sundararaman, R.; Rocca, D.; Ping, Y., First-principles engineering of charged defects for two-dimensional quantum technologies. *Physical Review Materials* **2017,** *1* (7), 071001.

143. Peng, Y.; Lu, B. Z.; Wang, N.; Li, L. G.; Chen, S. W., Impacts of interfacial charge transfer on nanoparticle electrocatalytic activity towards oxygen reduction. *Phys Chem Chem Phys* **2017,** *19* (14), 9336-9348.

144. Chen, L. M.; Deming, C. P.; Peng, Y.; Hu, P. G.; Stofan, J.; Chen, S. W., Gold core@silver semishell Janus nanoparticles prepared by interfacial etching. *Nanoscale* **2016,** *8* (30), 14565-14572.

145. Zhou, Z. Y.; Kang, X. W.; Song, Y.; Chen, S. W., Ligand-Mediated Electrocatalytic Activity of Pt Nanoparticles for Oxygen Reduction Reactions. *J Phys Chem C* **2012,** *116* (19), 10592-10598.

146. Chen, L.; Peng, Y.; Lu, J.-E.; Wang, N.; Hu, P.; Lu, B.; Chen, S., Platinum nanoparticles encapsulated in nitrogen-doped graphene quantum dots: Enhanced electrocatalytic reduction of oxygen by nitrogen dopants. *International Journal of Hydrogen Energy* **2017,** *42* (49), 29192-29200.

147. Deming, C. P.; Mercado, R.; Lu, J. E.; Gadiraju, V.; Khan, M.; Chen, S. W., Oxygen Electroreduction Catalyzed by Palladium Nanoparticles Supported on Nitrogen-Doped Graphene Quantum Dots: Impacts of Nitrogen Dopants. *Acs Sustain Chem Eng* **2016,** *4* (12), 6580-6589.

148. Deming, C. P.; Mercado, R.; Gadiraju, V.; Sweeney, S. W.; Khan, M.; Chen, S. W., Graphene Quantum Dots-Supported Palladium Nanoparticles for Efficient Electrocatalytic Reduction of Oxygen in Alkaline Media. *Acs Sustain Chem Eng* **2015,** *3* (12), 3315-3323.

149. He, G. Q.; Song, Y.; Liu, K.; Walter, A.; Chen, S.; Chen, S. W., Oxygen Reduction Catalyzed by Platinum Nanoparticles Supported on Graphene Quantum Dots. *Acs Catal* **2013,** *3* (5), 831-838.

150. Peng, Y.; Lu, B. Z.; Wang, N.; Lu, J. E.; Li, C. H.; Ping, Y.; Chen, S. W., Oxygen Reduction Reaction Catalyzed by Black-Phosphorus-Supported Metal Nanoparticles: Impacts of Interfacial Charge Transfer. *Acs Appl Mater Inter* **2019,** *11* (27), 24707-24714.

151. Lu, B.; Yao, B.; Roseman, G.; Deming, C. P.; Lu, J. E.; Millhauser, G. L.; Li, Y.; Chen, S., Ethanol Oxidation Reaction Catalyzed by Palladium Nanoparticles Supported on Hydrogen-Treated TiO2 Nanobelts: Impact of Oxygen Vacancies. *ChemElectroChem* **2017,** *4* (9), 2211-2217.

152. Lu, B. Z.; Liu, Q. M.; Chen, S. W., Electrocatalysis of Single-Atom Sites: Impacts of Atomic Coordination. *Acs Catal* **2020,** *10* (14), 7584-7618.

153. Peng, Y.; Lu, B. Z.; Wu, F.; Zhang, F. Q.; Lu, J. E.; Kang, X. W.; Ping, Y.; Chen, S. W., Point of Anchor: Impacts on Interfacial Charge Transfer of Metal Oxide Nanoparticles. *J Am Chem Soc* **2018,** *140* (45), 15290-15299.

Chapter 2 Heteroatom-doped carbon for oxygen reduction: impact of nitrogen dopants, FeN4 sites and Stone-Wales FeNx sites.

2.1 Abstract

Heteroatom-doped carbons represent a unique class of low-cost, effective catalysts for the electroreduction of oxygen, with a performance that may rival that of commercial Pt/C catalysts. In the present study, Fe and N codoped porous carbon nanotubules were prepared by controlled pyrolysis of tellurium nanowire-supported melamine formaldehyde polymer core–sheath nanofibers at elevated temperatures. Electron microscopic studies showed the formation of hollow carbon nanotubules with the outer diameter of 35–40 nm, inner diameter of 5–10 nm, and length of several hundred nanometers. Elemental mapping and spectroscopic measurements confirmed the doping of the carbon nanotubules with N and Fe including the formation of FeN4 moieties. Electrochemical studies showed that the resulting Fe,N-codoped carbons exhibited much enhanced electrocatalytic activity toward oxygen reduction in alkaline media as compared to the counterparts doped with nitrogen alone and prepared in a similar fashion, and the one prepared at 800 °C stood out as the best among the series, with an activity even better than that of commercial Pt/C. Such a remarkable performance was ascribed to the FeN4 moieties that facilitated the binding of oxygen species. This is further supported by results from DFT

calculations, where relevant atomistic models were built based on experimental results and reaction free energies on various possible active sites were computed by first-principles calculations. The computational results suggested that for N-doped carbons, the active sites were the carbon atoms adjacent to nitrogen dopants, while for Fe,N-codoped carbon, the FeN_4 moieties were most likely responsible for the much enhanced electrocatalytic activity, in excellent agreement with experimental results. Significantly, from the electronic structure studies, it was found that the high density of states close to the Fermi level and high spin density played a critical role in determining the electrocatalytic activity. Moreover, a more detailed study discovered the FeN_x sites in the Stone-Wales configurations induced by the nanowrinkles of the hierarchical porous carbon aerogels show a much lower free energy than the normal counterparts. The resulting iron and nitrogen-codoped carbon aerogels show excellent activity of oxygen reduction reaction.

2.2 Introduction

Polymer electrolyte membrane fuel cells (PEMFC) have been attracting extensive interest as a viable energy technology for portable electronics as well as transportation, because of the high efficiency in converting chemical energy in small organic fuel molecules to electricity.[1-6] During fuel cell operation, oxygen reduction reaction (ORR) at the cathode is a critical process that has been recognized as a major bottleneck limiting the fuel cell performance, due to the complex reaction pathways and sluggish electron-transfer kinetics. To produce current density sufficiently high

for practical applications, Pt-based nanoparticles have been used extensively as the catalysts of choice for ORR. Nevertheless, wide applications of PEMFCs based on Pt catalysts have been hampered by the low natural abundance, high costs and lack of long-term stability of platinum.[7-9] Lately, carbon-based materials have been found to exhibit apparent ORR activity and may serve as a promising candidate to replace Pt for ORR catalysis.[10-13] These carbon catalysts are generally doped with heteroatoms, such as N,[14] P,[15] B[16] and S[17], and the activity may be further enhanced by the incorporation of various transition metals, such as Fe,[18] Co,[19] Ni[20] and Cu[21]. Among these, Fe,N-codoped carbons have stood out because of their remarkable ORR activity that may even rival that of commercial Pt/C catalysts.[22-31] Such carbon-based catalysts are generally prepared by controlled pyrolysis of selected precursors. Of these, template-assisted synthesis has been used rather extensively,[32] where the ORR activity has been found to be dependent on various structural parameters, such as the concentrations and molecular configurations of the dopants, and porosity, surface accessibility and electrical conductivity of the carbon materials. For instance, Wei et al.[33] coated cellulose with an iron tannin framework ink, and prepared Fe_3C/Fe-N-C nanocomposites by controlled pyrolysis at elevated temperatures with the addition of dicyandiamide. The materials exhibited a high onset potential of +0.98 V vs RHE as well as high kinetic current density of 6.4 mA/cm^2 at +0.8 V. Ferrero et al.[18] exposed $FeCl_3$-impregnated silica particles to pyrrole vapors to produce Fe-polypyrrole nanoparticles; and pyrolysis of the resulting polymer hybrids led to the formation of Fe and N codoped porous carbons which exhibited apparent ORR activity in both

acid and base solutions. Yang et al.[34] pyrolyzed L-cysteine decorated C_3N_4 nanosheets and synthesized N-doped graphene nanoribbons as metal-free ORR catalysts which exhibited a high onset potential +0.92 V and half-wave potential of +0.84 V vs RHE. Sa et al.[35]{Sa, 2016 #5070} prepared Fe-N/C catalysts by pyrolysis of Fe(III)-porphyrin and carbon nanotube complexes with a SiO_2 coating, which displayed a high half-wave potential of +0.88 V along with good durability.

Despite the progress, the mechanistic origin, in particular, the role of the various N dopant configurations in ORR has remained a matter of heated debate.[34, 36] In addition, in Fe,N-codoped carbons, FeN_x, Fe_3C and/or even carbon atoms have been proposed as the active centers for ORR.[37-40] In fact, a series of studies based on density functional theory (DFT) calculations have been carried out to resolve these issues;[41, 42] yet it remains a challenge to correlate the structural models in DFT calculations to the experimental systems. This is the primary motivation of the present study where we combine experimental and theoretical approaches to unravel the catalytically active sites of Fe,N-codoped carbons for ORR in alkaline media.

In the present study, by controlled pyrolysis of core-sheath nanofibers with melamine-formaldehyde polymers supported on tellurium nanowire (Te NW) surfaces as the precursors, we successfully synthesized one-dimensional, porous, Fe,N-codoped carbon nanotubules, which exhibited apparent ORR activity in alkaline media, with a performance comparable/superior to that of state-of-art Pt-free catalysts reported in recent literature.[18, 33, 40, 43-45] The Te NWs were used as thermally removable nanowire templates,[46, 47] largely because of the ease of preparation,[48, 49]

and low boiling point of tellurium (449 °C).[50] The formation of one-dimensional nanotubular structures is anticipated to facilitate both electron-transfer kinetics and mass-transfer of reaction intermediates, as compared to the random porous carbons in most prior research.[51] Computationally, relevant atomistic models were built where N-doped carbon was embedded with FeN_4 moieties based on experimental data from XPS and electron microscopic measurements. First-principles calculations were carried out in the presence of implicit solvents to estimate the reaction free energies of each intermediate on various possible sites and overpotentials that showed excellent agreement with experimental data. The results suggest that the FeN_4 moieties were mostly likely the ORR active sites and played a major role in determining the observed ORR activity.

In a continues study, the activity of normal FeNx site (flat surface) and Stone-Wales FeNx (with nanowrinkle) is further compared. The result show the Stone-Wales FeN4 site has best activity for oxygen reduction. Such unique coordination structure was confirmed in a 3-dimensional material with nanowrinkled carbon aerogel embedded with FeNx sites. Such material has ultrahigh ORR activity, with an ultrahigh high onset and halfwave potential at 1.10 V and 0.90 V, respectively.

2.3 Result and Discussion

In the present study, Te NWs were synthesized by a facile hydrothermal method and used as the structural templates for the synthesis of Fe,N-codoped porous carbon nanotubules. This mainly involved two steps: (a) polymerization of melamine and

formaldehyde at 90 C in the presence of Te NWs led to the deposition of the polymers on the nanowire surface, forming core-sheath nanofibers (Te-MF); and (b) pyrolysis of the obtained Te-MF nanofibers at controlled temperatures, with the addition of a calculated amount of $FeCl_3$ as activating reagent, produced Fe,N-codoped porous carbon nanotubules (MF-Fe-T). In this procedure, melamine was selected as the carbon and nitrogen sources, and formaldehyde as a second carbon source and linking agent. The structures of the produced carbon nanotubules were first characterized by TEM measurements. Figure 1a depicts a representative TEM image of the Te-MF nanofiber precursors, where the core-sheath structures can be clearly observed. The nanofibers exhibited a length of several hundred nanometers and a diameter of 35 - 40 nm, and formed a three-dimensional network structure. In addition, the diameter of the Te nanowires can be identified at 5 to 10 nm. No well-defined lattice fringes were observed in high-resolution TEM measurements (Figure 2a), indicating amorphous nature of the melamine-formaldehyde polymer. After pyrolysis at 900 C, whereas the fibrous structures were retained, the dark-contrast tellurium nanowires vanished altogether, leading to the formation of a hollow nanotubular structure (MF-900) with the inner diameter consistent with that of the original Te NWs, as shown in Figure 1b. This may be ascribed to the thermal evaporation of the tellurium templates at elevated temperatures. Due to its large atomic radius, the evaporation of the tellurium nanowires might facilitate the formation of a porous structure of the carbon nanotubules and hence a high surface area. Consistent hollow nanotubular structures were obtained when a calculated

amount of $FeCl_3$ was mixed with Te-MF prior to pyrolysis at various temperatures (600 to 900 °C), as manifested in Figure 1c-f for the MF-Fe-T series.

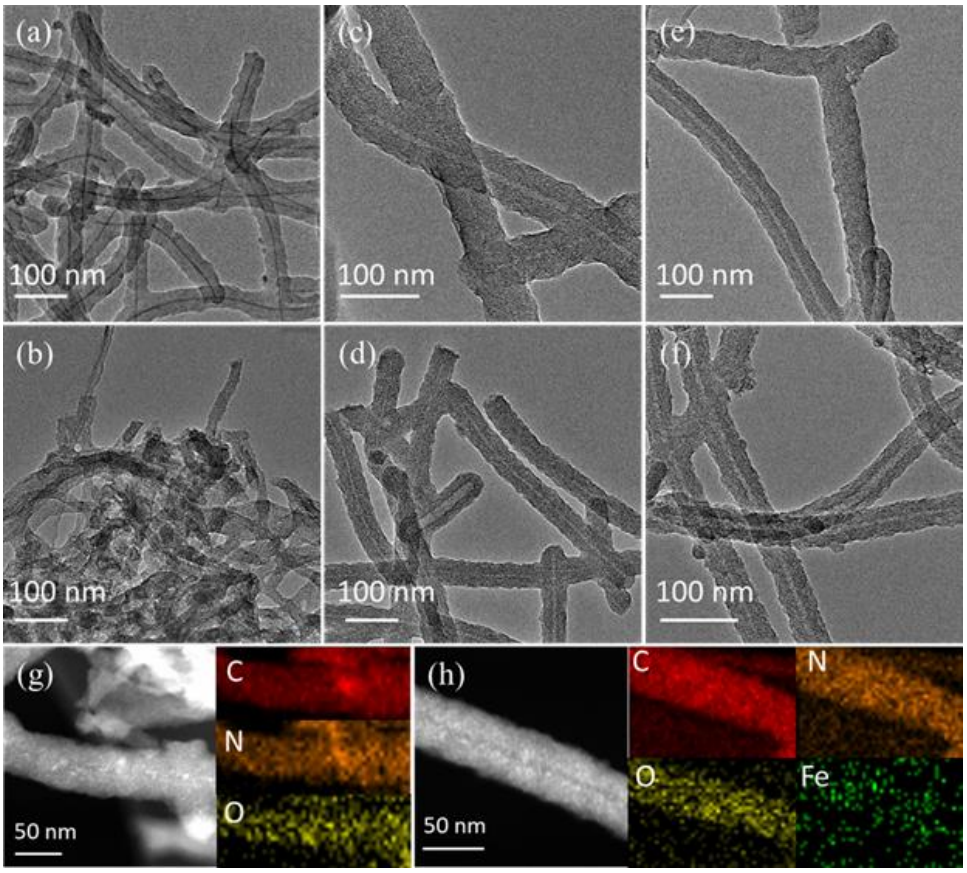

Figure 1. Representative TEM images of (a) Te-MF, (b) MF-900, (c) MF-Fe-600, (d) MF-Fe-700, (e) MF-Fe-800, and (f) MF-Fe-900. HAADF-STEM and elemental mapping images of (g) MF-900 and (h) MF-Fe-800.

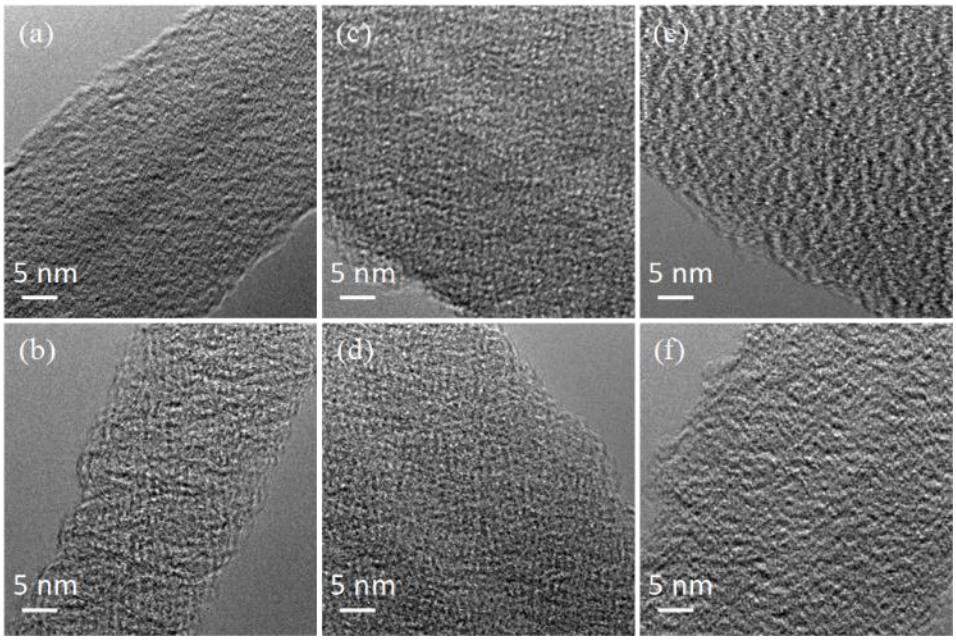

Figure 2. High-resolution TEM images of (a) Te-MF, (b) MF-900, (c) MF-Fe-600, (d) MF-Fe-700, (e) MF-Fe-800, and (f) MF-Fe-900. No well-defined lattice fringes can be seen, indicating the formation of largely amorphous structures.

The elemental compositions of the hollow nanotubules were then examined by HAADF-STEM measurements and elemental mapping analysis. From Figure 1g, one can see that in the MF-900 sample, the elements of carbon, nitrogen and oxygen were all readily identified and distributed rather homogeneously throughout the nanotubules, suggesting the formation of nitrogen-doped carbons. When pyrolysis of Te-MF was carried out in the presence of $FeCl_3$, in addition to carbon, nitrogen and oxygen, the Fe signals were also found across the nanotubule samples, as exemplified by the MF-Fe-800 sample (Figure 1h). This suggests that both nitrogen and iron were doped into the carbon molecular skeletons.

The elemental compositions and valence states were then examined by XPS measurements. From the survey spectra in Figure 3, one can see that both Te-MF and MF-900 samples exhibited three well-defined peaks at 285 eV, 400 eV, and 531 eV, which may be ascribed to the C 1s, N 1s and O 1s electrons, respectively. For the MF-Fe-T series (T = 600, 700, 800, and 900) of Fe,N-codoped carbon nanotubules, the Fe 2p electrons can also be identified at ca. 710 eV. The high-resolution scans of the C 1s electrons were depicted in Figure 5a. One can see that deconvolution of the Te-MF spectrum yields two peaks at 284.43 eV and 286.43 eV, due to the sp^2 and sp^3 C in the melamine-formaldehyde polymer (Figure 4), respectively.[52] After pyrolysis at elevated temperatures, all samples exhibited a major C 1s peak at ca. 284.6 eV, which can be assigned to graphitic sp^2 C, signifying successful carbonization of the melamine-formaldehyde polymer at elevated temperatures, despite the lack of long-range lattice fringes in high-resolution TEM measurements (Figure 5b-f).[53] There are also two minor peaks at 285.6-286.0 eV and 286.6-288.0 eV. The former is most likely due to the combined contributions of sp^3 carbon and N-bonded carbon (Figure 4),[53-55] whereas the latter may be ascribed to oxidized carbon. Notably, based on the integrated peak areas, the content of graphitic sp^2 C was found to increase markedly with pyrolysis temperature (Table 1), 38.2% for MF-Fe-600, 42.1% for MF-Fe-700, 52.7% for MF-Fe-800, and 66.6% for MF-Fe-900, indicating enhanced graphitization of the polymer precursors (for the minor carbon species, the contents were much lower at 10-20%). For comparison, the content of graphite sp^2 C for MF-900 (56.2%)

was lower than that of MF-Fe-900, which might be ascribed to the promoting effect of Fe species in the formation of graphitic carbons.[40, 56]

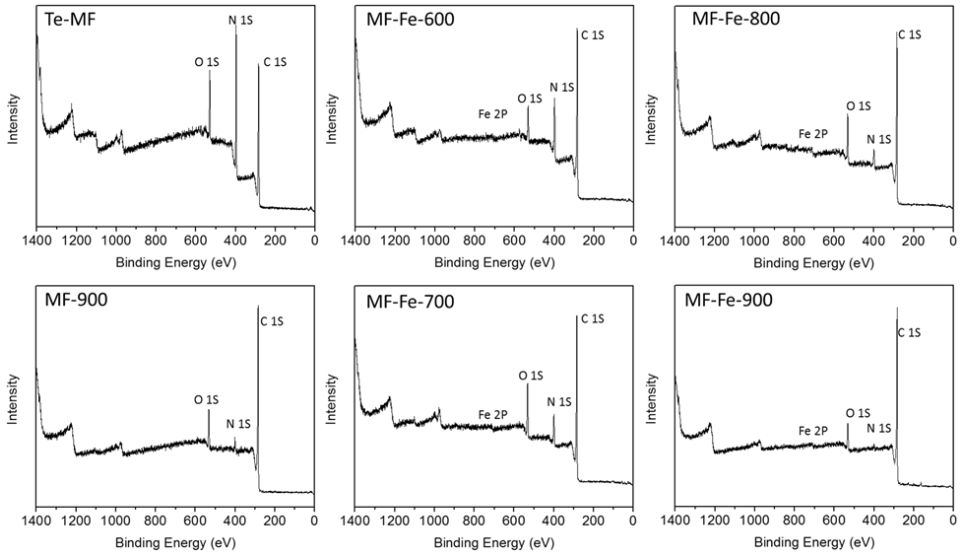

Figure 3. XPS survey spectra of Te-MF, MF-900, MF-Fe-600, MF-Fe-700, MF-Fe-800 and MF-Fe-900.

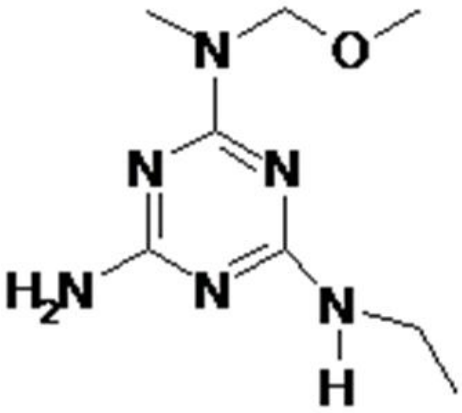

Figure 4. possible melamine-formaldehyde resin structure, the amino group of melamine molecule can be linked by (-CH_2-O-CH_2-) or (-CH_2-) or no linkage[52].

Sample	Fe-N	Pyridinic N	Pyrrolic N	Graphitic N	Oxidized N

s	BE (eV)	Conc (at%)	BE (eV)	Conc (at%)	BE (eV)	Conc (at%)	BE (eV)	Conc (at%)	BE (eV)	Conc (at%)
MF-900			398.24	1.2	400.35	1.5	401	1.5	402.55	1.4
MF-Fe-600	399.3	0.48	398.41	10.1	400.00	2.8	400.94	3.8	402.44	1.3
MF-Fe-700	399.38	0.52	398.3	5.6	400.00	2.1	400.75	2.9	402.10	1.5
MF-Fe-800	399.30	0.64	398.11	2.7	400.00	1.6	400.65	1.8	402.50	2.2
MF-Fe-900	399.10	0.25	398.06	0.35	399.90	0.23	400.71	0.96	402.03	0.81

Table 1. Summary of the binding energy (BE) and concentration of various nitrogen dopants in carbon nanotubules

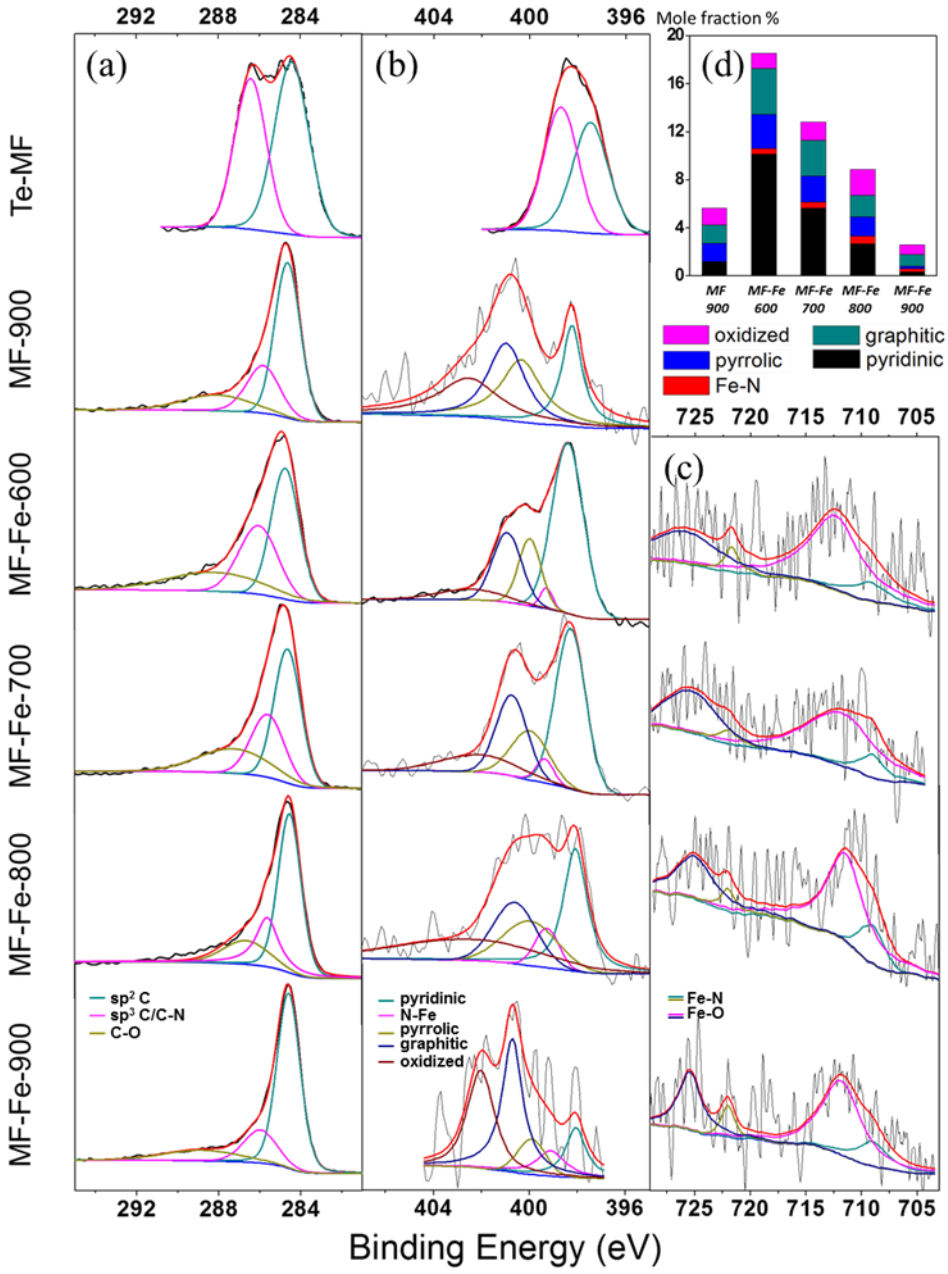

Figure 5. High-resolution XPS scans of (a) C1s, (b) N 1s and (C) Fe 2p electrons in the series of nanofiber precursors and doped carbon nanotubules. Grey curves are experimental data and colored curves are deconvolution fits. (d) Content distributions of various types of nitrogen dopants in the samples.

The N 1s spectra are depicted in Figure 5b. For Te-MF, two peaks were resolved at 397.5 eV and 398.7 eV at almost equal concentration, and may be assigned to the sp^2 N in C=N and sp^3 N in N-H (Figure 4), respectively. By contrast, deconvolution of the MF-900 spectrum yielded four nitrogen species at 398.24, 400.35, 401.00 and 402.55 eV, consistent with the binding energies of pyridinic, pyrrolic, graphitic and oxidized nitrogens, respectively,[57] indicating that nitrogen was indeed incorporated into the graphitic molecular skeletons by high-temperature pyrolysis. For the series of MF-Fe-T samples, these four types of nitrogen dopants remained well resolved at consistent binding energies. Furthermore, one additional nitrogen species may be resolved at 399.3 eV, which may be ascribed to N in Fe-N moieties.[29, 35, 40, 58] The nitrogen contents were then quantified, where one can see that the overall nitrogen concentration decreased with increasing pyrolysis temperature (Table 1), 18.5 at% for MF-Fe-600, 12.9 at% for MF-Fe-700, 8.9 at% for MF-Fe-800 and 2.6 at% for MF-Fe-900 (note that it was somewhat higher at 5.6 at% for MF-900). Figure 5d depicts the concentrations of the various nitrogen dopants within each sample. One can see that pyridinic nitrogen accounted for ca. 50% of the nitrogen dopants in the MF-Fe-600 and MF-Fe-700 samples, but for the samples prepared at higher temperatures (MF-Fe-800 and MF-Fe-900), (oxidized) graphitic nitrogen became the dominant species, indicating enhanced thermal stability of the latter as compared to the former (Table 2).[59]

Samples	C	N	Fe	sp^2 C	N (Fe-N)	Fe (Fe-N)	x (FeN_x)
MF-900	94.36 %	5.64%		56.17 %			
MF-Fe-600	80.65 %	18.54 %	0.81 %	38.16 %	0.48%	0.12%	4.00
MF-Fe-700	86.17 %	12.91 %	0.92 %	42.10 %	0.53%	0.13%	4.08
MF-Fe-800	90.10 %	8.89%	1.01 %	52.67 %	0.64%	0.16%	4.00
MF-Fe-900	96.73 %	2.60%	0.68 %	66.60 %	0.25%	0.15%	1.67

Table 2. Summary of elemental compositions in the various carbon nanotubules by XPS measurements

The Fe 2p data are depicted in Figure 5c. One can see that the series of MF-Fe-T samples all exhibited two pairs of peaks. The first doublet can be identified at ca. 709 and 722 eV, most likely due to Fe atoms bonded to N,[58, 60] whereas the other at ca. 712 and 725 eV, arising from Fe in iron oxides such as Fe_3O_4, Fe_2O_3 and Fe-O-C.[61, 62] {Turcu, 2015 #4898} Notably, the total Fe content was found to be ca. 1 at%, increasing slightly from 0.81% for MF-Fe-600 to 0.92% for MF-Fe-700, reaching a maximum at 1.01% for MF-Fe-800, but then diminishing to 0.68% for MF-Fe-900 (Table 1), most probably due to the thermal volatility of the iron species at elevated temperatures.[40, 56] Remarkably, the atomic ratio of Fe and N in Fe-N bonds was found

to be 4.0 for MF-Fe-600, MF-Fe-700, and MF-Fe-800, but only 1.67 for MF-Fe-900, indicating the formation of FeN_4 moieties in the first three samples whereas in the last one, Fe was highly under-coordinated probably because of the low overall concentration of the nitrogen dopants (Table 1).

Further structural insights were obtained in Raman measurements. Figure 6 depicts the Raman spectra of the series of carbon nanotubules, which all exhibited a well-defined D band at ca. 1350 cm^{-1} and a G band at ca. 1577 cm^{-1}, again, confirming the formation of graphitic carbons by pyrolysis of the polymer precursors. In addition, one can see that the ratio of the D and G band intensity decreased slightly with increasing pyrolysis temperature, at 2.93 for MF-Fe-600, 2.77 for MF-Fe-700, and 2.57 for MF-Fe-800, and but then increased somewhat to 2.95 for MF-Fe-900 (Table 3), indicating an initial increase of the degree graphitization with pyrolysis temperature; yet at too high a temperature, the porous graphitic framework might collapse, leading to the formation of an increasingly defective structure. That is, within the present experimental context, 800 °C represented an optimal pyrolysis temperature, corresponding to the lowest concentration of structural defects in the resulting hollow carbon nanotubules.

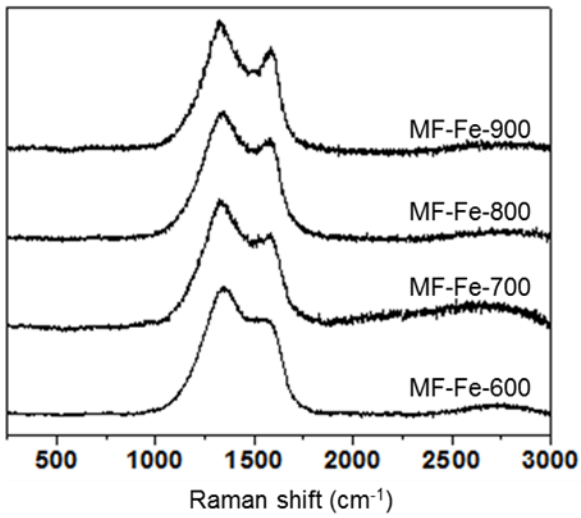

Figure 6. Raman spectra of the Fe,N-codoped carbon (MF-Fe-T) nanotubules.

Samples	D band (cm ^{1})	G band (cm ^{1})	I_D/I_G ratio
MF-Fe-600	1351	1575	2.93
MF-Fe-700	1343	1577	2.77
MF-Fe-800	1347	1577	2.57
MF-Fe-900	1342	1578	2.95

Table 3. Summary of results in Raman measurements of Fe,N-codoped carbon nanafibers

Significantly, the obtained doped carbon nanotubules exhibited apparent electrocatalytic activity towards ORR. Figure 7a depicts the RRDE voltammograms of a glassy carbon electrode modified with a calculated amount of the carbon nanotubules prepared above. One can see that as the electrode potential was swept negatively, nonzero current started to emerge, indicating oxygen reduction catalyzed by these doped carbon nanotubules. Yet, a closer analysis shows that the performance actually varied among the series of samples. For instance, the onset potential (E_{onset}) was found to increase in the order of MF-900 (+0.85 V) < MF-Fe-600 (+0.86 V) < MF-Fe-700 (+0.92 V) < MF-Fe-900 (+0.97 V) < MF-Fe-800 (+0.98 V). These are also summarized in Table 4 (a similar variation can also be observed with the half-wave potential, $E_{½}$). In fact, the onset potential of MF-Fe-800 was even slightly more positive than that (+0.97 V) of commercial Pt/C. In addition, one can see that the onset potential of MF-900 was comparable to that of metal-free carbon catalysts for ORR reported in the literature;[63-65] however, the fact that it was markedly more negative than those of the MF-Fe-T series indicates the significant role of Fe dopants (most likely FeN_4 moieties) in the enhancement of the ORR performance, as detailed below.

Furthermore, one can see that all carbon nanotubule catalysts showed a very low ring current density with the ring potential set at +1.5 V, indicating the production of only a minimal amount of peroxide species during oxygen reduction. This is clearly illustrated in Figure 4b, which shows the number of electron transfer (n) involved in ORR within the potential range of +1.0 to +0.2 V, with $n = \frac{4I_D}{I_D + \frac{I_R}{N}}$, where I_D and I_R

are the voltammetric currents at the disk and ring electrodes, respectively, and N is the collection efficiency (40%).[66] One can see that at all samples the n values are over 3.9, indicating almost complete reduction of oxygen to OH through the four-electron pathway. Yet, small discrepancy can be observed. For instance, at +0.70 V, n increased slightly in the order of MF-Fe-600 (3.92) < MF-Fe-700 (3.98) < MF-Fe-900 ⊕ MF-Fe-800 ⊕ Pt/C (3.99), as shown in Table 4.

Further comparison can be made with the Tafel plots (Figure 7c). One can see that the kinetic current density increased with increasing overpotentials, and within the wide range of electrode potential from +1.0 to +0.6 V, the MF-Fe-800 samples exhibited the highest kinetic current density among the series. For instance, at +0.90 V, the kinetic current density was found to be less than 0.05 mA/cm^2 for MF-900 and MF-Fe-600, 0.08 mA/cm^2 for MF-Fe-700, 0.63 mA/cm^2 for MF-Fe-800, and 0.33 mA/cm^2 for MF-Fe-900. Significantly, the performance of MF-Fe-800 was even better than that of Pt/C (0.53 mA/cm^2). Furthermore, the Tafel slope may also be quantified and compared, which was 101 mV/dec for MF-900 and 111 mV/dec for MF-Fe-600, but decreased markedly to 76 mV/dec for MF-Fe-700, 81 mV/dec for MF-Fe-800 and 78 mV/dec for MF-Fe-900, all close to that of (89 mV/dec) for commercial Pt/C (Table 4). This suggests that with increasing pyrolysis temperature, the resulting Fe,N-codoped carbon nanotubules behaved analogous to Pt/C, where the rate-determining step was likely the first electron-reduction of oxygen.

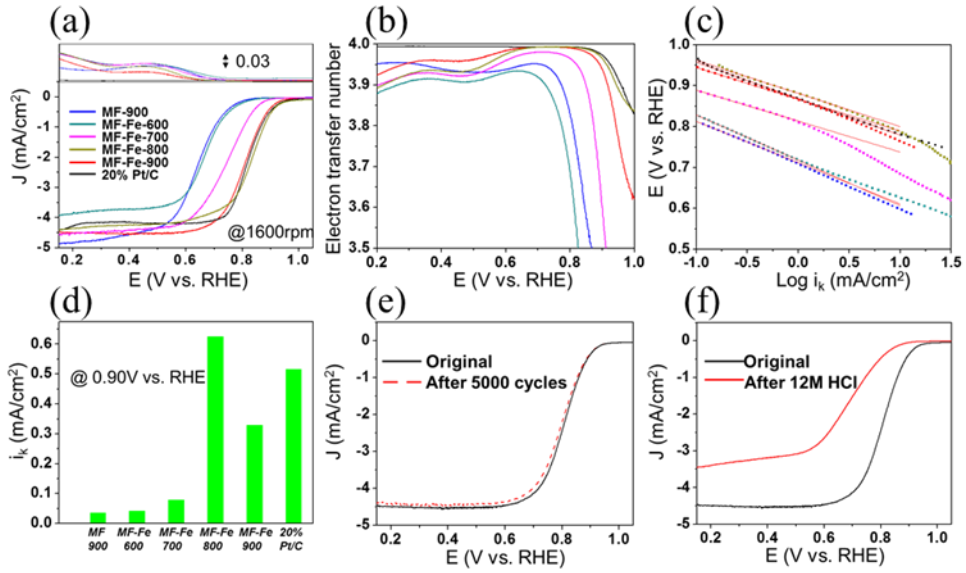

Figure 7. ORR performance of N and Fe N doped carbon nanofibers. (a) RRDE voltammograms at the rotation rate of 1600 rpm and potential scan rate of 10 mV/s in an oxygen-saturated 0.1 M KOH solution. The upper panel is ring current density with a scale bar at 0.03 mA/cm^2, and the lower panel is disk panel. (b) Variation of the number of electron transfer (n) with electrode potential. (c) Tafel plot for the series of samples. The legends of (b) and (c) are the same as in (a). (d) Comparison of the kinetic current density at +0.9 V vs. RHE. (e) RDE voltammograms of MF-Fe-800 before and after 5,000 cycles of potential scans at the scan rate of 500 mV/s. (f) RDE voltammograms of MF-Fe-800 before and after acid etching with 12 M HCl.

Sample	E_{onset}	$E_{½}$	n at +0.7	J_k at +0.9	Tafel

	(V vs RHE)	(V vs RHE)	V	V (mA/cm^2)	slope (mV/dec)
MF-900	0.85	0.64	3.95	0.05	101
MF-Fe-600	0.86	0.67	3.92	0.05	111
MF-Fe-700	0.92	0.75	3.98	0.08	76
MF-Fe-800	0.98	0.83	3.99	0.63	81
MF-Fe-900	0.97	0.81	3.99	0.33	78
20% Pt/C	0.97	0.82	3.99	0.53	89

Table 4. Summary of ORR performance of the series of carbon nanotubules

The series of MF-Fe-T catalysts also showed excellent durability. Take MF-Fe-800 as the example, the half-wave potential ($E_{½}$) exhibited a negative shift of less than 7 mV after 5,000 cycles of potential scans (Figure 7e). In addition, after the carbon nanotubules were subject to chemical etching with 12 M HCl, one can see that the activity diminished markedly, with a negative shift of about 100 mV of the onset potential and a 30% decrease of the limiting currents (Figure 7f). These observations indicate that Fe species played an indispensable role in the ORR activity, most likely through the FeN_4 moieties in the Fe,N-codoped carbon nanotubules. Such a remarkable performance is highly comparable or even superior to leading results reported in recent literatures with relevant carbon-based catalysts (Table 5).

Samples	Catalyst loading (mg/cm^2)	Onset potential (V vs RHE)	n @ +0.7 V	Limit current density (mA/cm^2)	Reference s
MF-Fe-800	0.041	0.98	3.99	4.22	This work
FP-Fe-N-850	0.3	0.98	~3.9	5	[67]
Fe–N–CC	0.1	0.94	3.7	~4	[68]
Fe3-NG	0.5	0.965	3.78-3.97	7.2	[43]
Fe-N/C-800	0.079	0.98	3.97	4.81	[69]
Fe-N/G	0.058	0.874	3.77	5.21	[70]
Fe/C/N	0.2	0.94	3.90	~5	[44]

Table 5. Comparison of ORR activity with literature results in 0.1 M KOH

Taken together, these experimental results indicate that the MF-Fe-800 sample stood out as the best catalyst among the series. In addition, whereas apparent ORR activity was observed with carbons doped with nitrogen alone, the performance was markedly improved with additional doping of Fe-containing compounds. That is, the Fe species, rather than the N dopants, played a dominant role in determining the ORR activity. First-principles calculations were then carried out to shed light on the contributions of nitrogen dopants and FeN_4 moieties to the electrocatalytic activity. It was observed that pyrrolic and oxidized nitrogen dopants had only minimal contributions to the ORR activity, and pyridinic nitrogen was mostly inactive in binding oxygeneous species (Figure 8), consistent with earlier results.[36, 42, 71] Therefore, the calculations were focused mainly on graphitic nitrogen dopants and FeN_4 moieties, with several representative models depicted in Figure 9 which were based upon experimental data presented above in Figure 5 and Table 1. For the

graphitic nitrogen, two scenarios were examined: (a) one isolated N dopant in the graphene supercells such that there is no interaction between the N dopants (Graphene 1N, Figure 9), and (b) two N dopants in the same hexatomic ring in the supercell, where interactions between the two N dopants are possible (only negligible interactions between N dopants from different hexatomic rings), at three different configurations, the ortho (Graphene 2No, Figure 9), meso (Graphene 2Nm, Figure 9), and para (Graphene 2Np, Figure 9) structures. In addition, as XPS studies suggest the formation of FeN_4 moieties in the carbon structure, two FeN_4 doped graphene structures were also studied with the normal FeN_4 and Stone-Wales defect FeN_4 (Figure 9).[72-74]

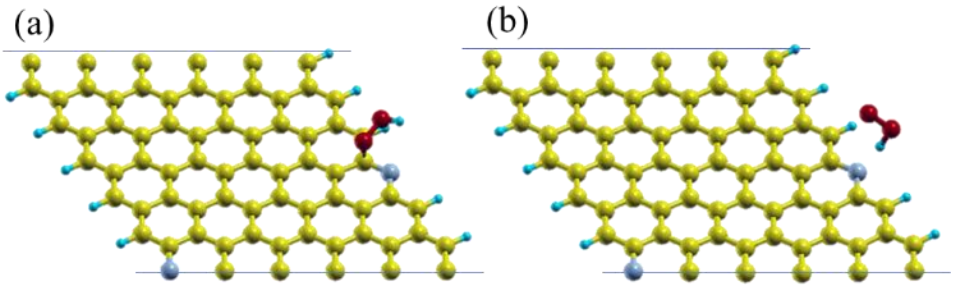

Figure 8. The configuration of OOH species on neighbor carbon of pyridinic N a) before and b) after relax calculation. The OOH species can not be stably attached to the carbon.

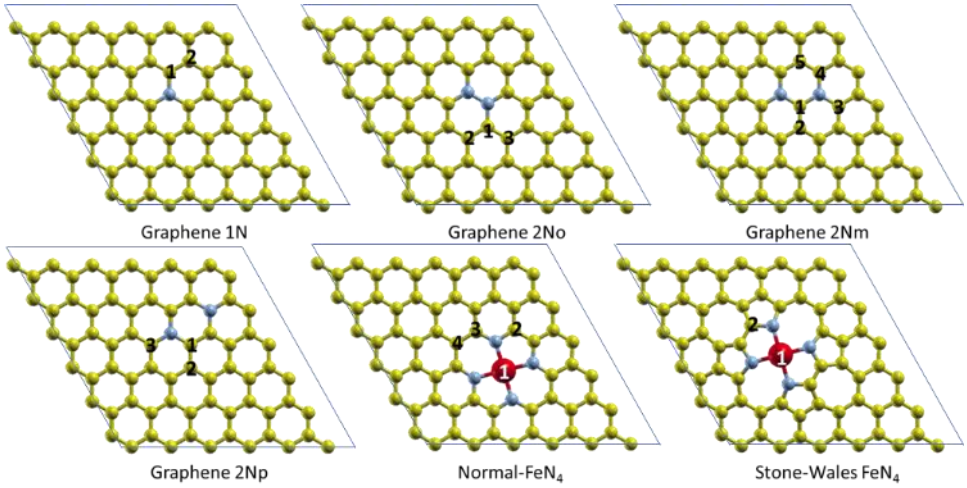

Figure 9. Atomistic models of N and FeN_4-doped graphene. The numbers indicate tested candidate active sites for ORR activity. The atoms are shown as blue (N), red (Fe), and yellow (C) spheres.

In the electrochemical measurements (Figure 7), the n values were found to be close to 4, indicating that the ORR process mostly followed the 4-electron reduction pathway, which involves the following steps,

$$* + O_2 + H^+ + e^- = OOH* \quad (1) \quad \Delta G_1$$

$$OOH* + H^+ + e^- = O* + H_2O \quad (2) \quad \Delta G_2$$

$$O* + H^+ + e^- = OH* \quad (3) \quad \Delta G_3$$

$$OH* + H^+ + e^- = H_2O + * \quad (4) \quad \Delta G_4$$

where * is the active site, and the ORR activity has been argued to be most likely limited by two reactions, the first electron reduction of oxygen (eq. 1) and reduction of adsorbed hydroxy to water and its desorption from the catalyst surface (eq. 4).[12, 42, 75] That is, the binding of the catalytic active sites to oxygen species can not be too strong or too weak. In fact, within this mechanistic model, the overall reaction will be

optimized with a smallest reaction free energy of the limiting step when $\Delta G_1 = \Delta G_4$. As $\Delta G_2 + \Delta G_3 = \Delta E_{OH^*} - \Delta E_{OOH^*}$ (where ΔG is reaction free energy and ΔE is adsorption energy), and based on the Faraday's law, the total energy $\Delta G^0 = \Sigma \Delta G_i = -4E^0 = -4.92$ eV with E^0 being the formal potential (+1.23 V) of oxygen reduction. Thus, the smallest possible free energy for reactions (1) and (4) is $\Delta G_{ave} = \Delta G_1 = \Delta G_4 = \frac{1}{2}(\Delta G_1 + \Delta G_4) = \frac{1}{2}[\Delta G^0 - (\Delta E_{OH^*} - \Delta E_{OOH^*})]$. It has been observed that there is a linear relationship between ΔE_{OOH^*} and ΔE_{OH^*}. Thus, $\Delta E_{OOH^*} - \Delta E_{OH^*}$ is a constant, which is defined as b, and the optimal potential is obtained as

$$U = -\Delta G_{ava}/2e = -(-4.92 + b)/2 \qquad (5)$$

Figure 10 depicts the linear relationship between the calculated binding energies of OOH and OH intermediates at the various carbon active sites, including carbon atoms in the FeN4 structures (Figure 9). Linear regression yields a slope of 1.03 which is within 3% of the theoretical value of 1, and the intercept of 3.24 eV is in the typical range of 3.0 – 3.4 eV that has been observed previously.[75, 76] From equation (5), the optimal potential for the carbon sites was estimated to be 0.84 V, in good agreement with the experimental onset potential of 0.85 eV observed above for nitrogen-doped carbon, MF-900. Notably, one can see from Figure 10 that for both FeN_4 structures (Figure 9) the iron centers have a more optimal potential than the carbon sites. Using a slope of 1 we estimated the intercepts of 3.01 eV for Fe in the normal FeN_4 structure and 2.96 eV for Fe in the Stone-Wales FeN_4 structure. Thus, from equation (5), the corresponding optimal potentials can be estimated to be 0.96 and 0.98 V for these Fe-N co-doped structures, in excellent agreement with the experimental onset

potential (+0.98 V) observed for Fe,N-codoped carbon nanotubules, MF-Fe-800 (Figure 7). This strongly suggests that indeed the Fe centers played a more significant role in determining the ORR than the carbon sites, as the theoretical onset potential of the latter is 120-140 mV more positive than that of the former (Table 4).

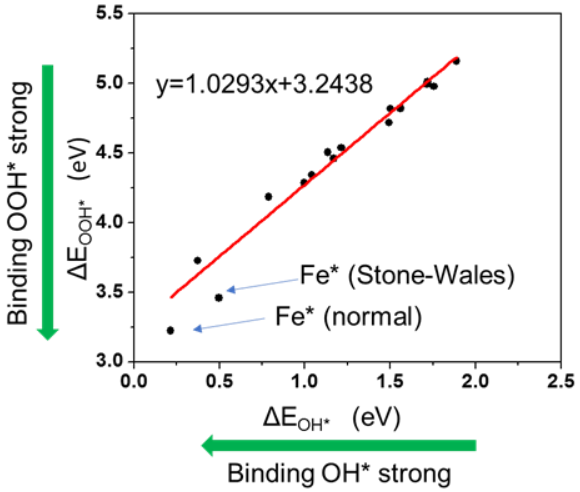

Figure 10. Correlation between the adsorption energies of the OOH and OH intermediate species. The two data points at the bottom are for the Fe sites in Normal FeN4 and Stone-Wales FeN4 as showed in Figure 9. Other data points represent results for the various carbon sites from the structures shown in Figure 9, and the red line is the linear regression of these data. The green arrows are to indicate the direction of increasing binding energies.

It should be noted that in the above calculations the following two factors are neglected: (a) reactions (1) and (4) are assumed to be the rate-determining steps with the activity optimized at $\Delta G_1 = \Delta G_4$. However, this ideal situation is difficult to reach, as step (3) is also an "uphill" reaction and may be involved in controlling the overall reaction kinetics; and (b) the ZPE correction, entropy correction and solvation energy

correction were ignored. Thus, in order to make more accurate predictions and correlations with experimental data, we carefully calculated all four steps of ORR reactions for each candidate active site at the potential at +0.9 V vs RHE. ZPE correction, entropy correction and solvation energy corrections were all included in the reaction free energy calculations, as showed explicitly in Table 6 and graphically in Figure 11. It can be seen that nearly all carbon sites showed a very high ΔG_1, signifying that carbon sites experienced difficulty in adsorbing OOH* intermediate. In addition, whereas at some sites the third step showed the highest energies, the first step remained energetically unfavorable. Correspondingly, the reaction energy of the last step on all carbon sites was negative, suggesting that the OH species might be easily released from the carbon sites. On the contrast, for the Fe sites in the FeN_4 structures, step (3) or (4) can be identified as the rate-determining step, signifying favorable binding with oxygen species. Hence, adsorption of O_2 is energetically favorable while the release of OH is unfavorable, consistent with results from recent studies.[77] From Table 6, one can also see that the most active structures are Graphene 2Nm-3, where the two nitrogen dopants are in a meso configuration, with a reaction free energy of the limiting step of only 0.61 eV; and such a number diminished further to 0.51 eV for the Fe sites of normal FeN_4 and 0.39 eV for Stone-Wales FeN_4. From these calculations, we can then estimate the minimal reaction current density,

$$J = J_o e^{-\frac{\Delta G}{k_B T}} \qquad (6)$$

where J is the current density, k_B is the Boltzmann constant and T is temperature.[75] Thus, the ratio between the current density of the Fe,N-codoped graphene over N-doped graphene can be estimated to be

$$\frac{J_{Fe,N}}{J_N} = e^{\frac{-\Delta G_{Fe,N-max}+\Delta G_{N-min}}{k_B T}} \qquad (7)$$

where $\Delta G_{Fe,N\text{-}max}$ and $\Delta G_{N\text{-}min}$ denote the largest free energy of Fe sites and lowest free energy of N-doped C sites. At room temperature (298 K), this current density ratio was estimated to be 36.14, implying that the Fe sites of FeN_4 in Fe,N-codpoed carbons are over 36 times more active than carbon with N doping alone. Experimentally, the kinetic current density of MF-Fe-800 was calculated to be about 20 times higher than that of MF-900 (Figure 11 and Table 4), in rather good agreement with this theoretical prediction.

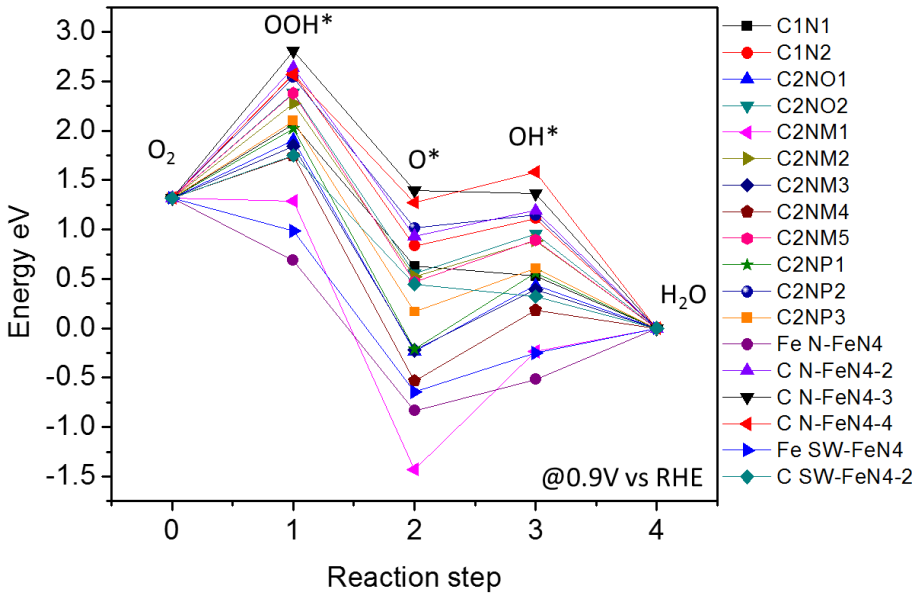

Figure 11. Reaction free energy diagram of reaction steps (1) – (4) in ORR at the various atomistic sites that are defined in Figure 9. In the figure legends, C1N1 and C1N2 refer to the C1 and C2 sites in Graphene 1N, respectively. C2NM1, C2NM3, and C2NM4 refer to the C1, C3 and C4 sites in Graphene 2Nm, respectively. Fe N-FeN4 and C N-FeN4-2 refer to the Fe site and C2 site in normal-FeN4, respectively. Fe SW-FeN4 and C SW-FeN4-2 refer to the Fe site and C2 site in Stone-Wales FeN4, respectively.

Series	Sites (Figure 9)	Reactions	ΔG_1	ΔG_2	ΔG_3	ΔG_4	Maximum

1	Graphene 1N	1	0.746704	-1.43633	-0.10291	-0.52746	0.746704
	Graphene 1N	2	1.251549	-1.73955	0.280898	-1.11289	1.251549
2	Graphene 2No	1	0.584959	-2.14171	0.672337	-0.43558	0.672337
	Graphene 2No	2	1.061605	-1.8252	0.396898	-0.9533	1.061605
3	Graphene 2Nm	1	-0.03097	-2.71732	1.194689	0.233605	1.194689
	Graphene 2Nm	2	0.956986	-1.75124	0.361012	-0.88676	0.956986
	Graphene 2Nm	3	0.525793	-2.06723	0.610438	-0.389	0.610438
	Graphene 2Nm	4	0.424411	-2.27648	0.714486	-0.18242	0.714486
	Graphene 2Nm	5	1.058495	-1.90931	0.425957	-0.89515	1.058495
4	Graphene 2Np	1	0.702391	-2.23442	0.775594	-0.56357	0.775594
	Graphene 2Np	2	1.218355	-1.52393	0.133904	-1.14833	1.218355
	Graphene 2Np	3	0.779295	-1.93295	0.441376	-0.60773	0.779295
5	Normal-FeN4	1	-0.63258	-1.52169	0.315965	0.518311	0.518311

	Normal-FeN4	2	1.318813	-1.71032	0.261827	-1.19032	1.318813
	Normal-FeN4	3	1.483572	-1.40708	-0.03281	-1.36368	1.483572
	Normal-FeN4	4	1.247679	-1.29418	0.310938	-1.58444	1.247679
6	Stone-Wales FeN4	1	-0.33785	-1.62667	0.393209	0.251312	0.393209
	Stone-Wales FeN4	2	0.43166	-1.30276	-0.12577	-0.32313	0.43166

Table 6. Calculated reaction energies of various active sites at +0.9 V vs RHE. The numbers highlighted in red correspond to the rate-determining steps. Numbers highlighted in blue correspond to the lowest reaction free energy (most active sites) of the structure. The reaction energy is calculated by $\Delta G_i = \Sigma E(product) - \Sigma E(reactant) + \Delta ZPE - T\Delta S + \Delta E_{sol} + q(U\text{-}NHE) - K_b T \ln[H^+]$, where ΔG is the reaction free energy, E is final energy of each configuration, ΔZPE is the zero-point energy correction, ΔS is entropy correction and ΔE_{sol} is solvation energy correction, q is charge of single electron, U is the potential of electrode, K_b is the Boltzmann constant.

Furthermore, from Table 6, one can see that the carbon atoms adjacent to a nitrogen dopant are more active than the next nearest neighbors. For example, the nearest-

neighbor carbons in Graphene 1N-1, 2No-1, 2Nm-3, 2Nm-4, 2Np-1 and 2Np-3 (Figure 9) exhibited a reaction free energy of the limiting step of 0.75, 0.67, 0.61, 0.71, 0.78 and 0.78 eV, respectively, all much lower than those in the second nearest neighbor configurations, Graphene 1N-2 (1.25 eV), 2No-2 (1.06 eV), 2Nm-2 (0.96 eV), 2Nm-5 (1.06 eV) and 2Np-2 (1.22 eV), consistent with results reported previously.[78] Note that the carbon site of Stone-Wales FeN_4 exhibited a reaction free energy of the limiting step of only 0.43 eV, much lower than those of carbon sites in other configurations. This indicates that some carbon atoms can also contribute to the activity in Fe,N-codoped graphene. In fact, in a previous study[40] we observed that despite a low Fe concentration (~1%), Fe,N-codoped carbon exhibited a remarkable ORR activity.

We selected two representative systems, Graphene 2Nm and Normal FeN_4 (Figure 9), for a more comprehensive study of their electronic structures in order to identify the critical factors that determine the different activities between Fe,N-codoped graphene and N-doped graphene. From the reaction free energy calculations of these systems (Figure 11), one can see that it is difficult for carbon to adsorb oxygen species in N-doped graphene while it is much easier for Fe in FeN_4-doped graphene. In fact, the binding of oxygen is more favorable when a high density of states exists right below the Fermi level. For example, we plotted both the total density of states (DOS) along with the projected density of states of potentially active sites in Figure 12 to determine which atoms have states near the Fermi level. For the N-doped graphene system the carbon atoms which are nearest to nitrogen contributed the most to the

DOS near the Fermi level. However, their DOS near the Fermi level (Figure 12b) is still much smaller than that of FeN_4 (Figure 12c), indicating a lower probability to donate electrons and reduce O_2. Moreover, although carbon sites 3 and 4 had the largest contributions to the states, none of them had a dominant contribution (projected DOS in Figure 12b). From Figure 12c we see that FeN_4 has one order of magnitude higher density of state below the Fermi level composed predominantly of the Fe 3d orbitals.

Furthermore, it can be found that the spin density is also critical to the ORR activity because the atoms with unpaired spins have radical characters, which are highly reactive and may easily attack O_2 molecules. Figure 12d and e depict the spin density distributions. Since Fe takes a high spin configuration in FeN_4, it has a large distribution in the spin density plot from its unpaired 3d orbitals. Meanwhile the carbon near nitrogen (along with the nitrogen itself) are shown to have some unpaired electron distribution as well. Yet the spin density distribution on carbon is clearly less than the dominating cloud associated with Fe. Therefore, Fe's unpaired 3d orbitals along with their position near the Fermi level may explain why iron binds so favorably to oxygen species. This also coincides with results in a previous study,[72] where the Fe 3d unpaired electrons may cause strong interactions with O_2 for the initial step of ORR. On the contrast, we see the opposite for N, i.e., there are fewer states near the fermi level and a much smaller distribution of unpaired electrons in N-doped graphene. In fact, from Table 7, one can see that the active sites have higher unpaired spin: in N-doped graphene, only the C atoms with unpaired spins (small

compared with Fe) are active (site 3 and 4), whereas in Fe,N-codoped graphene, Fe has nearly two unpaired spins leading to a highly active site.

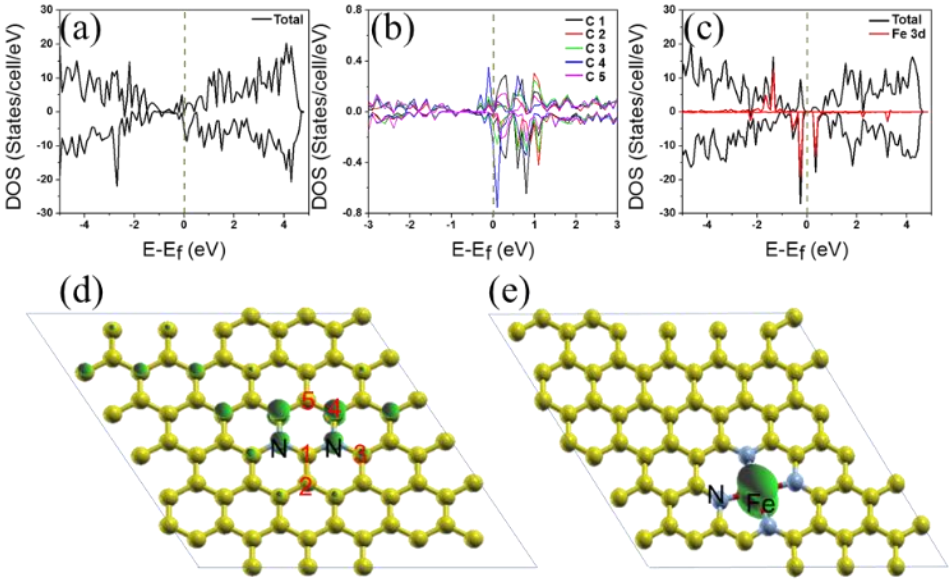

Figure 12 Density of state (DOS), projected density of states and spin density distribution in N doped and Fe-N4 doped graphene systems. DOS plots of (a) Graphene 2Nm, (b) Zoom-in around the Fermi level of panel (a) showing the DOS contribution of various carbon sites (Figure 9), and (c) Normal FeN_4. The yellow broken lines show the location of the Fermi level. Spin density distribution plots of (d) Graphene 2Nm and (e) Normal FeN_4. The green isosurface is the unpaired electron distribution (spin up-spin down). The isovalue is the same at 0.004 e/au^3 for (d) and (e).

2Nm-4	Lowdin	Spin	Spin	Active

	charge	up	down	?
1	3.7506	1.8763	1.8743	n
2	3.9836	1.9907	1.9929	n
3	3.8701	1.9470	1.9231	y
4	3.8938	1.9895	1.9044	y
5	3.9853	1.9875	1.9977	n
Normal-FeN4				
1	15.7875	8.9471	6.8405	y
2	3.8619	1.9343	1.9276	n
3	3.8419	1.9143	1.9275	n
4	4.0111	2.0107	2.0004	n
graphene C	3.9571			

Table 7. Lowdin charge of the various atom sites in Graphene 2Nm and Normal-FeN4 in Figure 9

2.4 Discussion about Stone-Wales FeNx sites with nanowrinkle in FeNx embedded carbon.

First-principles calculations were then carried out to shed light on the contribution of FeN_4 and FeN_3 moieties to the electrocatalytic activity. It is likely that the interlaced 3D structure of the hydrogel networks and the tortuous CS chains will lead to the formation of abundant wrinkles onto the obtained porous carbon aerogels. Therefore,

the electrocatalytic activity of Stone-Wales (SW)-defect FeN_4 (FeN_4 SW) and FeN_3 (FeN_3 SW) moieties, which can be formed by the nanowrinkles of carbon matrices, are examined by theoretical calculation. Figure 13a-b, 14 and 15 show the side view and top view of the atomic models of the four kinds of Fe-N centers. From the atomic models, one can see that the normal FeN_4 and normal FeN_3 moieties exhibit a planar structure in the carbon matrices, while FeN_4 SW and FeN_3 SW shows a distorted non-planar structure. The simulated scanning tunneling microscopic (STM) mages of the FeN_4 and FeN_4 SW moieties are presented in Figure 13c and 13d. As compared to normal FeN_4, the SW defects cause significant redistribution of electron densities of FeN_4 and adjacent carbon atoms. Figure 13e displays the total density of states (DOS) of normal and SW Fe-N centers. According to Figure 13f, for the FeN_4 SW on a graphene sheet, the Fe atom makes the largest contributions to the DOS near the Fermi level (red peak), which is similar to that (black line) of normal FeN_4. Apparently, the DOS near the Fermi level of FeN_4 SW is much closer to Fermi energy than that of normal FeN_4, indicating a higher probability of donating electrons and reducing oxygen. To evaluate the ORR activity of these Fe-N metal centers, the reaction free energy is calculated at the applied potential of +0.9 V vs RHE and plotted in Figure 13g. One can see that except for the fourth electron-transfer step, the first three electron-transfer steps are exothermic at +0.9 V, indicating that the rate determining step (RDS) is most likely the fourth electron-transfer step. In comparison with normal FeN_4 and FeN_3, both FeN_4 SW and FeN_3 SW show much lower endothermic energies (0.179 eV and 0.228 eV), implying a lower reaction

overpotential. These results suggest that the nanowrinkles can enhance the electrocatalytic activity of Fe-N centers on the carbon matrices by forming SW defects, as manifested below in electrochemical tests.

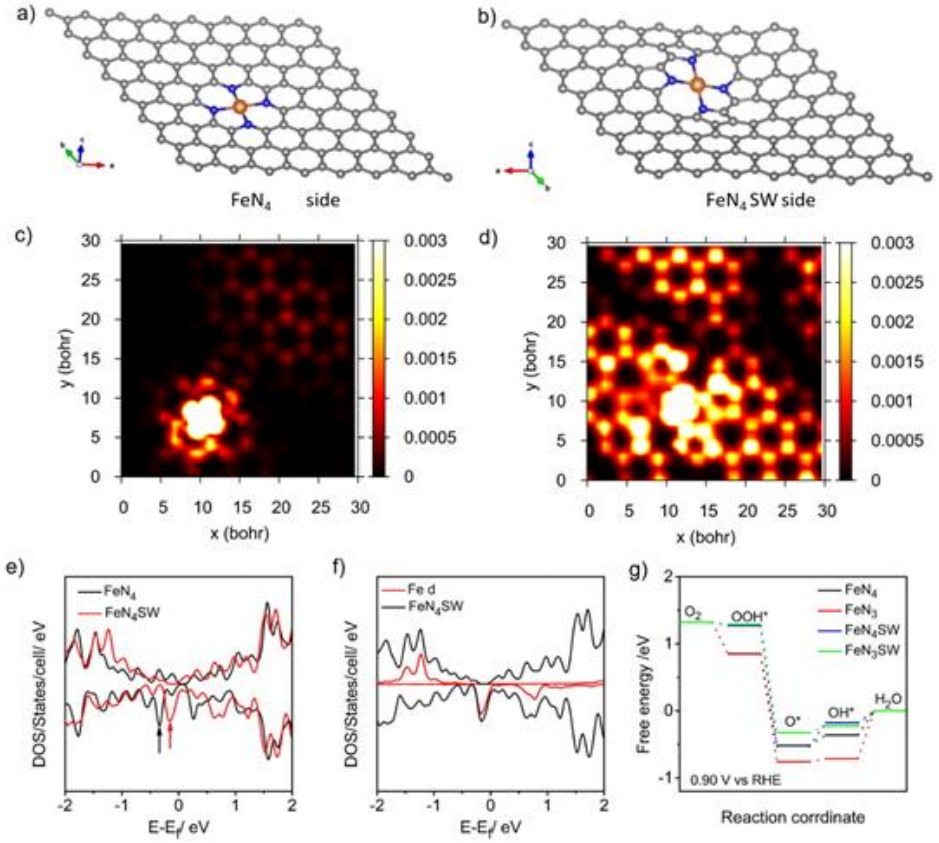

Figure 13 (a, c) Side view and simulated STM image of normal FeN_4 doped graphene sheets. (b, d) Side view and simulated STM image of Stone-Wales FeN_4 (FeN_4 SW) doped graphene sheets. (e) Density of state (DOS) of normal FeN_4 and FeN_4 SW doped graphene sheets. (f) DOS of FeN_4 SW and Fe 3d. (g) Free energy diagrams of ORR processes on normal FeN_4, normal FeN_3, FeN_4SW and FeN_3SW at the applied of 0.9 V.

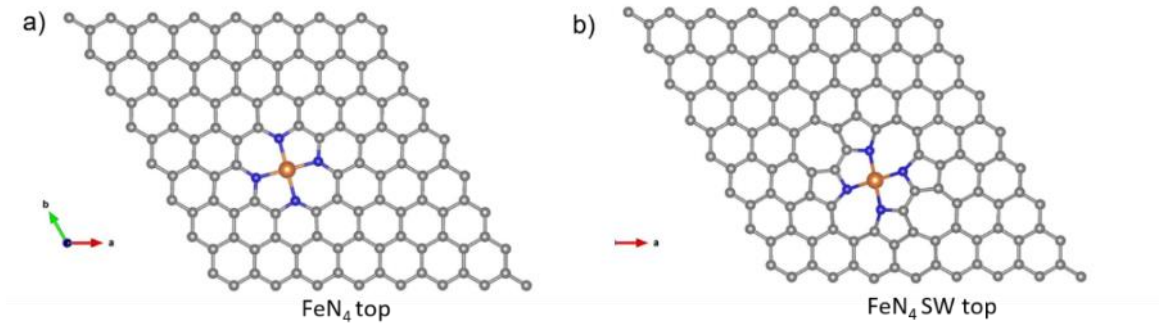

Figure 14 Top view of normal FeN_4 and FeN_4 SW moieties in graphene.

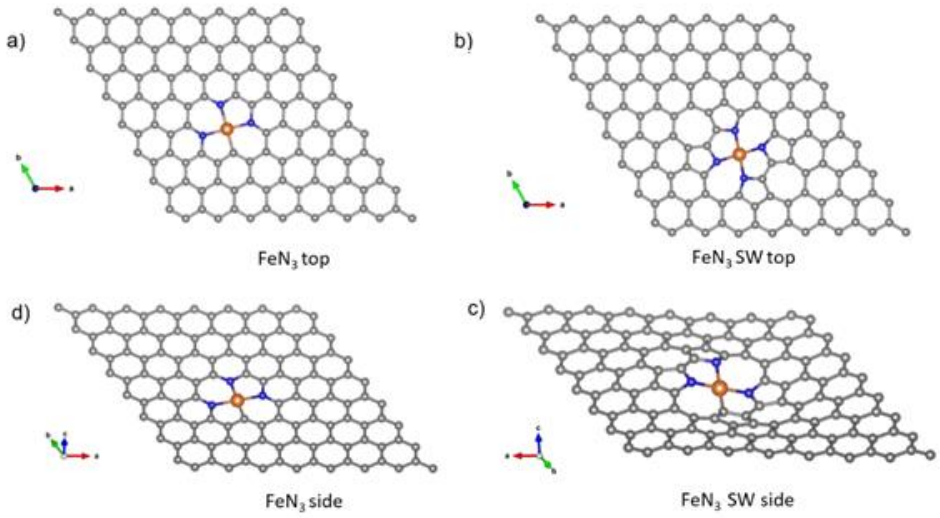

Figure 15 Top view and side view of normal and SW FeN_3 and FeN_4 moieties in graphene.

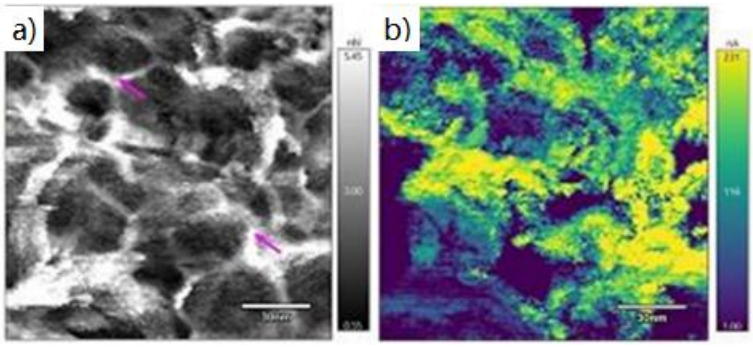

Figure 16 Identification of nanowrinkle in the sample of the $NCA_{C\text{-}Zn}$/Fe carbon aerogel. AFM images of $NCA_{C\text{-}Zn}$/Fe aerogels: (a) adhesion force image and (b) current flow image.

The material synthesis and electrochemical measurement were carried out by co-workers in this work. In short, the freeze-dried $CS_{Si\text{-}Zn}$/FePM hydrogel was then used as a 3D reactor to synthesize metal-doped carbon aerogels by controlled pyrolysis, which was then subject to HF etching to remove the SiO_2 templates, producing $NCA_{C\text{-}Zn}$/Fe. The $NCA_{C\text{-}Zn}$/Fe sample displays a highly porous, nanowrinkled structure with rich mesopores of ca. 10 nm in diameter. Fast Force Mapping (FFM) measurements were carried out to examine the nanowrinkle in carbon. The data presented in Figure 16 exhibit a ca. 10 nm variation in the mechanical and electrical properties of the porous carbon, confirming the formation of nanowrinkled carbon. Domains dictated by round features in topography are outlined by prominent changes in max force and an increase in the adhesion force (Figure 16(a)). Notably, the adhesion force, which represents the bulk modulus or stiffness of the sample, indicates that these round regions are stiffer in the center and softer around the edges. Typically, sp^2-hybridized carbon exhibits hydrophobic characteristics, whereas defective carbons are more hydrophilic. With an AFM tip that consists of a hydrophilic silicon oxide layer, a high adhesion force corresponds to a hydrophilic domain. This implies that the metal centers are most likely situated within the high

adhesion force areas. Interestingly, from Figures 16 (a) and (b), one can see that the soft nodes correspond to high electrical conductance. Taken together, these results suggest that the metal sites are mostly located in the high adhesion and high conductivity areas of the porous carbon aerogel. Both features are conducive to oxygen electrocatalysis.

The electrocatalytic activity of the carbon aerogels obtained above was then investigated in 0.1 M KOH. **Figure 17a-b** shows the ORR polarization curves and H_2O_2 yields of carbon aerogels, in comparison to commercial Pt/C (20 wt%). As a metal-free catalyst, the CA_C sample shows a rather apparent electrocatalytic activity with an onset potential (E_{onset}) of +0.94 V and half-wave potential ($E_{1/2}$) of +0.79 V, much positive than those of other carbon substrates reported in recent literature.[79-81] This suggests that biomass alone may be exploited as a carbon source to fabricate metal-free ORR electrocatalysts. Notably, doping of FePM complex in the CS_{Zn} hydrogel led to a marked enhancement of the catalytic performance with E_{onset} = +1.10 V and $E_{1/2}$ = +0.90 V ($NCA_{C\text{-}Zn}$/Fe), which is even better than those of commercial Pt/C (+0.99 V and +0.83 V).[82] Likewise, the $NCA_{C\text{-}Zn}$/Fe single atom catalyst shows a lowest average H_2O_2 yield (1.45%) within the potential range of +0.2 V to +0.9 V, signifying a high-efficiency $4e^-$ reduction pathway.

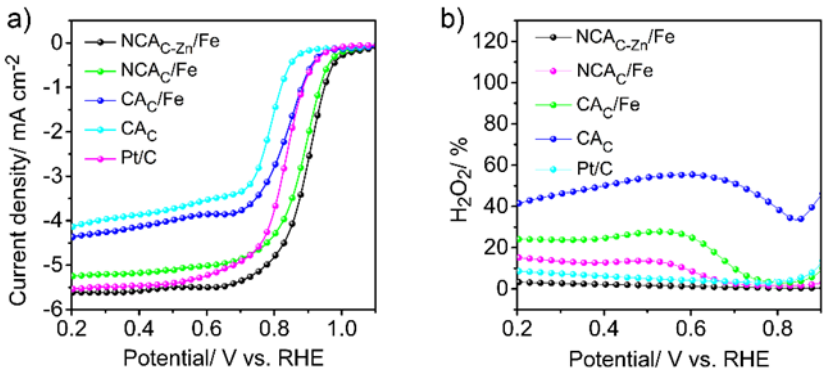

Figure 17 ORR performance in alkaline media. (a) ORR polarization curves of CA_C, CA_C/Fe, NCA_C/Fe and $NCA_{C\text{-}Zn}$/Fe, as well as the Pt/C at 1600 rpm in 0.1 M KOH at the potential sweep rate of 5 mV s^{-1}. (b) H_2O_2 yield of CA_C, CA_C/Fe, NCA_C/Fe, $NCA_{C\text{-}Zn}$/Fe and Pt/C.

2.5 Experimental section

Chemicals. Sodium tellurite (Na_2TeO_3, 99.5%, Alfa Aesar), melamine (99%, Acros Organics), hydrazine hydrate (N_2H_4, 64% v/v, Acros Organics), polyvinylpyrrolidone (PVP, K30, USB), sodium hydroxide (NaOH, Fisher Scientific), formaldehyde (37% v/v, Acros Organics), ammonia (35% in water, Acros Organics), and Pt/C (20 wt.%, Alfa Aesar) were used as received. Water was supplied from a Barnstead Nanopure water system (18.3 M ohm cm).

Synthesis of Te NWs. Te NWs were synthesized by adopting a literature procedure.[83] In a typical experiment, 0.0368 g of Na_2TeO_3 and 0.4 g of PVP were dissolved in 13

mL of nanopure water under vigorous stirring to form a homogenous solution, into which were injected 1.35 mL of an ammonia solution and 0.66 mL of N_2H_4. The solution was then transferred into a 20 mL Telfon-lined autoclave container and heated at 180 °C for 3 h. The autoclave was cooled down naturally before the product was collected by centrifugation at 3000 rpm for 2 min with the addition of a small amount of acetone, and stored in a 4 °C refrigerator.

Synthesis of Te NWs-melamine formaldehyde polymer core-sheath nanofibers. In brief, 12.5 mg of Te NWs prepared above was dispersed in 5 mL of water. Separately, 0.126 g of melamine together with 15 mL of water was added in a 50 mL round-bottom flask, and the solution was heated to 90 °C under magnetic stirring, into which were then injected the Te NWs solution, 20 μL of 0.2 M NaOH and 0.53 mL of formaldehyde. The solution was heated at 90 °C for 7 h before being cooled down naturally. The product was collected by centrifugation at 5,000 rpm for 5 min, washed with water and ethanol, and dried in a vacuum chamber for 24 h, affording Te NWs-melamine formaldehyde polymer (Te-MF) core-sheath nanofibers.

Synthesis of Fe,N-codoped carbon nanotubules. In a typical synthesis, 50 mg of the Te-MF nanofibers obtained above was dispersed in 1 mL of ethanol, along with 1 mg of $FeCl_3$. The mixture was sonicated for 1 h to form a homogeneous dispersion, which was then dried by a nitrogen flow and kept in a vacuum chamber for 12 h before being placed in a tube furnace and heated at a controlled temperature (600, 700, 800, or 900 °C) for 3 h at a heating rate of 5 °C/min. The nitrogen flow was maintained at 200 cc/min. The obtained samples were washed with water and ethanol

for 3 times, and referred to as MF-Fe-T with T = 600, 700, 800, or 900. A control sample was also prepared in the same manner at the heating temperature of 900 °C but without the addition of $FeCl_3$, which was denoted as MF-900.

Characterization. Transmission electron microscopy (TEM) and elemental mapping studies were carried out with a FEI Tecnai TF20 microscope operated at 200 KV. X-ray photoelectron spectroscopy (XPS) measurements were acquired by using a PHI X-tool instrument. Raman spectra were collected with a micro Raman Imaging Microscope with a laser wavelength of 632.8 nm.

Electrochemistry. Electrochemical measurements were carried out with a CHI 710 electrochemical workstation in a conventional three-electrode configuration. To prepare catalyst inks, in a typical experiment, 1 mg of the samples obtained above, together with 4 mg of carbon black and 10 L of nafion, was dispersed in 1 mL of ethanol. The mixture was sonicated for at least 1 h to make a homogenous dispersion. Then, 10 μL of the ink was dropcast onto the glassy carbon disk of a rotating (gold) ring-(glassy carbon) disk electrode (RRDE, from Pine Instrument), corresponding a catalyst loading of 40.65 ug/cm^2. When the catalyst film was dry, 4 μL of 20% nafion was added on top of the catalyst before the electrode was immersed into electrolyte solutions for data acquisition. A Ag/AgCl electrode in 0.1 M KCl was used as the reference electrode and a platinum coil as the counter electrode. The reference electrode was calibrated against a reversible hydrogen electrode (RHE) and all potentials in the present study were referred to this RHE.

Computational Methods. DFT calculations were performed with the open-source planewave code, Quantum Espresso.[84] A two-dimensional supercell was built based on a 6 × 6 unit cell. The vacuum thickness was set at about 14 Å to avoid interactions between periodic images. The ultrasoft pseudopotential[85] was adopted with the kinetic cutoff energy of 40 Ry (charge density cutoff 200 Ry) and 4 × 4 × 1 Monkhorst-Pack K-point grids were sampled for the supercell to converge the total energy to the accuracy of 1 meV. The Marzari-Vanderbilt smearing[86] was adopted with a smearing of 0.002 Ry. The electronic energy was converged to 10^{-8} Ry and the force was converged to 10^{-4} a.u. Density functional perturbation theory (DFPT)[87] was employed to compute the vibrational frequencies of surface species and molecules for the zero point energy (ZPE) and entropy contribution, similar to a previous work.[88] The implicit solvation calculations were performed with the newly developed solvation model (CANDLE)[89] which has been shown to be suitable for various surfaces in open source code JDFTx.[90, 91]

2.6 Conclusion

Nitrogen and iron codoped carbon hollow nanotubules were synthesized by controlled pyrolysis of core-sheath nanofibers based on Te NWs-supported melamine formaldehyde polymer with the addition of a calculated amount of $FeCl_3$, where the Te NWs served as thermally removable templates because of its low boiling point. Electron microscopic and XPS measurements confirmed the successful incorporation

of Fe and N dopants into the carbon molecular skeletons, and electrochemical studies of the resulting nanocomposites showed apparent activity towards ORR in alkaline media that was highly comparable to leading results reported in recent literature, within the context of onset potential, number of electron transfer, and kinetic current density. Significantly, the sample prepared at 800 °C stood out as the best catalysts among the series, with a performance even better than that of commercial Pt/C. In addition, comparative studies with N-doped carbons prepared in a similar fashion suggested that Fe species, rather than nitrogen dopants, played a dominant role in dictating the ORR activity, most probably due to the formation of FeN_4 moieties. This was further supported by first principles calculations where the atomistic models were built based on the structural characteristics obtained in experimental studies. Theoretically, the optimal potential for the Fe sites was 120-140 mV more positive than that of N-doped carbon sites, and correlated well with the ORR onset potentials observed experimentally. Notably, the limited activity of N-doped carbon was ascribed to the low binding of oxygeneous species, as suggested by the low DOS below the fermi level and low spin density; in contrast, the Fe sites of the FeN_4 structure were far more active in the adsorption of oxygen intermediates, in excellent agreement with experimental results. From the combined experimental and theoretical studies, one can see that Fe species, in particular, FeN_4 moieties, likely played a dominant role in the determination of the ORR activity. This may be exploited as a fundamental framework for the rational design of high-performance ORR catalysts by deliberate engineering of the nanocomposite structures. Moreover, a Stone-Wales

FeN4 sites embedded in carbon, deriving nanowinkles in the material, shows best activity among all FeNx sites.

2.7 Reference

1. Green, M. A.; Bremner, S. P., Energy conversion approaches and materials for high-efficiency photovoltaics. *Nature materials* **2016,** *16* (1), 23-34.

2. Stamenkovic, V. R.; Strmcnik, D.; Lopes, P. P.; Markovic, N. M., Energy and fuels from electrochemical interfaces. *Nature materials* **2016,** *16* (1), 57-69.

3. Dusastre, V.; Martiradonna, L., Materials for sustainable energy. *Nature materials* **2017,** *16* (1), 15-15.

4. Ping, Y.; Goddard, W. A., 3rd; Galli, G. A., Energetics and Solvation Effects at the Photoanode/Catalyst Interface: Ohmic Contact versus Schottky Barrier. *Journal of the American Chemical Society* **2015,** *137* (16), 5264-7.

5. Wang, Y. J.; Qiao, J.; Baker, R.; Zhang, J., Alkaline polymer electrolyte membranes for fuel cell applications. *Chemical Society reviews* **2013,** *42* (13), 5768-87.

6. Zhang, H.; Shen, P. K., Recent development of polymer electrolyte membranes for fuel cells. *Chemical reviews* **2012,** *112* (5), 2780-832.

7. Li, M.; Zhao, Z.; Cheng, T.; Fortunelli, A.; Chen, C. Y.; Yu, R.; Zhang, Q.; Gu, L.; Merinov, B. V.; Lin, Z.; Zhu, E.; Yu, T.; Jia, Q.; Guo, J.; Zhang, L.; Goddard, W. A., 3rd; Huang, Y.; Duan, X., Ultrafine jagged platinum nanowires

enable ultrahigh mass activity for the oxygen reduction reaction. *Science* **2016,** *354* (6318), 1414-1419.

8. Huang, X.; Zhao, Z.; Cao, L.; Chen, Y.; Zhu, E.; Lin, Z.; Li, M.; Yan, A.; Zettl, A.; Wang, Y. M.; Duan, X.; Mueller, T.; Huang, Y., ELECTROCHEMISTRY. High-performance transition metal-doped Pt(3)Ni octahedra for oxygen reduction reaction. *Science* **2015,** *348* (6240), 1230-4.

9. Bu, L.; Zhang, N.; Guo, S.; Zhang, X.; Li, J.; Yao, J.; Wu, T.; Lu, G.; Ma, J. Y.; Su, D.; Huang, X., Biaxially strained PtPb/Pt core/shell nanoplate boosts oxygen reduction catalysis. *Science* **2016,** *354* (6318), 1410-1414.

10. Zhu, C.; Li, H.; Fu, S.; Du, D.; Lin, Y., Highly efficient nonprecious metal catalysts towards oxygen reduction reaction based on three-dimensional porous carbon nanostructures. *Chemical Society reviews* **2016,** *45* (3), 517-31.

11. Zhou, M.; Wang, H. L.; Guo, S., Towards high-efficiency nanoelectrocatalysts for oxygen reduction through engineering advanced carbon nanomaterials. *Chemical Society reviews* **2016,** *45* (5), 1273-307.

12. Peng, Y.; Lu, B.; Wang, N.; Li, L.; Chen, S., Impacts of interfacial charge transfer on nanoparticle electrocatalytic activity towards oxygen reduction. *Phys. Chem. Chem. Phys.* **2017,** *19* (14), 9336-9348.

13. Hu, P. G.; Liu, K.; Deming, C. P.; Chen, S. W., Multifunctional graphene-based nanostructures for efficient electrocatalytic reduction of oxygen. *J Chem Technol Biot* **2015,** *90* (12), 2132-2151.

14. Gong, K.; Du, F.; Xia, Z.; Durstock, M.; Dai, L., Nitrogen-doped carbon nanotube arrays with high electrocatalytic activity for oxygen reduction. *Science* **2009,** *323* (5915), 760-4.

15. Zhang, J.; Zhao, Z.; Xia, Z.; Dai, L., A metal-free bifunctional electrocatalyst for oxygen reduction and oxygen evolution reactions. *Nature nanotechnology* **2015,** *10* (5), 444-52.

16. Fei, H.; Ye, R.; Ye, G.; Gong, Y.; Peng, Z.; Fan, X.; Samuel, E. L.; Ajayan, P. M.; Tour, J. M., Boron- and nitrogen-doped graphene quantum dots/graphene hybrid nanoplatelets as efficient electrocatalysts for oxygen reduction. *ACS nano* **2014,** *8* (10), 10837-43.

17. Higgins, D. C.; Hoque, M. A.; Hassan, F.; Choi, J. Y.; Kim, B.; Chen, Z. W., Oxygen Reduction on Graphene-Carbon Nanotube Composites Doped Sequentially with Nitrogen and Sulfur. *Acs Catal* **2014,** *4* (8), 2734-2740.

18. Ferrero, G. A.; Preuss, K.; Marinovic, A.; Jorge, A. B.; Mansor, N.; Brett, D. J.; Fuertes, A. B.; Sevilla, M.; Titirici, M. M., Fe-N-Doped Carbon Capsules with Outstanding Electrochemical Performance and Stability for the Oxygen Reduction Reaction in Both Acid and Alkaline Conditions. *ACS nano* **2016,** *10* (6), 5922-32.

19. Shang, L.; Yu, H.; Huang, X.; Bian, T.; Shi, R.; Zhao, Y.; Waterhouse, G. I.; Wu, L. Z.; Tung, C. H.; Zhang, T., Well-Dispersed ZIF-Derived Co,N-Co-doped Carbon Nanoframes through Mesoporous-Silica-Protected Calcination as Efficient Oxygen Reduction Electrocatalysts. *Advanced materials* **2016,** *28* (8), 1668-74.

20. Ma, N.; Jia, Y.; Yang, X. F.; She, X. L.; Zhang, L. Z.; Peng, Z.; Yao, X. D.; Yang, D. J., Seaweed biomass derived (Ni,Co)/CNT nanoaerogels: efficient bifunctional electrocatalysts for oxygen evolution and reduction reactions. *J Mater Chem A* **2016,** *4* (17), 6376-6384.

21. Yu, H.; Fisher, A.; Cheng, D.; Cao, D., Cu,N-codoped Hierarchical Porous Carbons as Electrocatalysts for Oxygen Reduction Reaction. *ACS applied materials & interfaces* **2016,** *8* (33), 21431-9.

22. Yu, H.; Shang, L.; Bian, T.; Shi, R.; Waterhouse, G. I.; Zhao, Y.; Zhou, C.; Wu, L. Z.; Tung, C. H.; Zhang, T., Nitrogen-Doped Porous Carbon Nanosheets Templated from g-C3 N4 as Metal-Free Electrocatalysts for Efficient Oxygen Reduction Reaction. *Advanced materials* **2016,** *28* (25), 5080-6.

23. Zhang, C. L.; Wang, B. W.; Shen, X. C.; Liu, J. W.; Kong, X. K.; Chuang, S. S. C.; Yang, D.; Dong, A. G.; Peng, Z. M., A nitrogen-doped ordered mesoporous carbon/graphene framework as bifunctional electrocatalyst for oxygen reduction and evolution reactions. *Nano Energy* **2016,** *30*, 503-510.

24. Graglia, M.; Pampel, J.; Hantke, T.; Fellinger, T. P.; Esposito, D., Nitro Lignin-Derived Nitrogen-Doped Carbon as an Efficient and Sustainable Electrocatalyst for Oxygen Reduction. *ACS nano* **2016,** *10* (4), 4364-71.

25. Dai, L.; Xue, Y.; Qu, L.; Choi, H. J.; Baek, J. B., Metal-free catalysts for oxygen reduction reaction. *Chemical reviews* **2015,** *115* (11), 4823-92.

26. Shao, M.; Chang, Q.; Dodelet, J. P.; Chenitz, R., Recent Advances in Electrocatalysts for Oxygen Reduction Reaction. *Chemical reviews* **2016,** *116* (6), 3594-657.

27. Song, L. T.; Wu, Z. Y.; Zhou, F.; Liang, H. W.; Yu, Z. Y.; Yu, S. H., Sustainable Hydrothermal Carbonization Synthesis of Iron/Nitrogen-Doped Carbon Nanofiber Aerogels as Electrocatalysts for Oxygen Reduction. *Small* **2016,** *12* (46), 6398-6406.

28. Wu, Z. Y.; Xu, X. X.; Hu, B. C.; Liang, H. W.; Lin, Y.; Chen, L. F.; Yu, S. H., Iron Carbide Nanoparticles Encapsulated in Mesoporous Fe-N-Doped Carbon Nanofibers for Efficient Electrocatalysis. *Angewandte Chemie* **2015,** *54* (28), 8179-83.

29. Lin, L.; Zhu, Q.; Xu, A. W., Noble-metal-free Fe-N/C catalyst for highly efficient oxygen reduction reaction under both alkaline and acidic conditions. *Journal of the American Chemical Society* **2014,** *136* (31), 11027-33.

30. Sasan, K.; Kong, A. G.; Wang, Y.; Mao, C. Y.; Zhai, Q. G.; Feng, P. Y., From Hemoglobin to Porous N-S-Fe-Doped Carbon for Efficient Oxygen Electroreduction. *J Phys Chem C* **2015,** *119* (24), 13545-13550.

31. Wang, Y.; Kong, A. G.; Chen, X. T.; Lin, Q. P.; Feng, P. Y., Efficient Oxygen Electroreduction: Hierarchical Porous Fe-N-doped Hollow Carbon Nanoshells. *Acs Catal* **2015,** *5* (6), 3887-3893.

32. Niu, W. H.; Li, L. G.; Chen, S. W., Recent Progress in Template-Assisted Synthesis of Nitrogen-Doped Porous Carbons for Oxygen Electroreduction. *Journal of Electrochemistry* **2017,** *23*, accepted.

33. Wei, J.; Liang, Y.; Hu, Y.; Kong, B.; Simon, G. P.; Zhang, J.; Jiang, S. P.; Wang, H., A Versatile Iron-Tannin-Framework Ink Coating Strategy to Fabricate Biomass-Derived Iron Carbide/Fe-N-Carbon Catalysts for Efficient Oxygen Reduction. *Angewandte Chemie* **2016,** *55* (4), 1355-9.

34. Yang, Y.; Liu, J.-W.; Yu, S.-H., Coiling ultrathin tellurium nanowires into nanorings by Pickering emulsion. *Chem. Commun.* **2016,** *52* (52), 8091-8094.

35. Sa, Y. J.; Seo, D. J.; Woo, J.; Lim, J. T.; Cheon, J. Y.; Yang, S. Y.; Lee, J. M.; Kang, D.; Shin, T. J.; Shin, H. S.; Jeong, H. Y.; Kim, C. S.; Kim, M. G.; Kim, T. Y.; Joo, S. H., A General Approach to Preferential Formation of Active Fe-Nx Sites in Fe-N/C Electrocatalysts for Efficient Oxygen Reduction Reaction. *Journal of the American Chemical Society* **2016,** *138* (45), 15046-15056.

36. Guo, D.; Shibuya, R.; Akiba, C.; Saji, S.; Kondo, T.; Nakamura, J., Active sites of nitrogen-doped carbon materials for oxygen reduction reaction clarified using model catalysts. *Science* **2016,** *351* (6271), 361-5.

37. Lee, J. S.; Park, G. S.; Kim, S. T.; Liu, M.; Cho, J., A highly efficient electrocatalyst for the oxygen reduction reaction: N-doped ketjenblack incorporated into Fe/Fe3C-functionalized melamine foam. *Angewandte Chemie* **2013,** *52* (3), 1026-30.

38. Zhu, Y.; Zhang, B.; Liu, X.; Wang, D. W.; Su, D. S., Unravelling the structure of electrocatalytically active Fe-N complexes in carbon for the oxygen reduction reaction. *Angewandte Chemie* **2014,** *53* (40), 10673-7.

39. Zitolo, A.; Goellner, V.; Armel, V.; Sougrati, M. T.; Mineva, T.; Stievano, L.; Fonda, E.; Jaouen, F., Identification of catalytic sites for oxygen reduction in iron- and nitrogen-doped graphene materials. *Nature materials* **2015,** *14* (9), 937-42.

40. Niu, W.; Li, L.; Liu, X.; Wang, N.; Liu, J.; Zhou, W.; Tang, Z.; Chen, S., Mesoporous N-doped carbons prepared with thermally removable nanoparticle templates: an efficient electrocatalyst for oxygen reduction reaction. *Journal of the American Chemical Society* **2015,** *137* (16), 5555-62.

41. Szakacs, C. E.; Lefevre, M.; Kramm, U. I.; Dodelet, J. P.; Vidal, F., A density functional theory study of catalytic sites for oxygen reduction in Fe/N/C catalysts used in H(2)/O(2) fuel cells. *Physical chemistry chemical physics : PCCP* **2014,** *16* (27), 13654-61.

42. Chai, G. L.; Hou, Z.; Shu, D. J.; Ikeda, T.; Terakura, K., Active sites and mechanisms for oxygen reduction reaction on nitrogen-doped carbon alloy catalysts: Stone-Wales defect and curvature effect. *Journal of the American Chemical Society* **2014,** *136* (39), 13629-40.

43. Cui, X. Y.; Yang, S. B.; Yan, X. X.; Leng, J. G.; Shuang, S.; Ajayan, P. M.; Zhang, Z. J., Pyridinic-Nitrogen-Dominated Graphene Aerogels with Fe-N-C Coordination for Highly Efficient Oxygen Reduction Reaction. *Adv Funct Mater* **2016,** *26* (31), 5708-5717.

44. Zhao, Y.; Kamiya, K.; Hashimoto, K.; Nakanishi, S., Efficient Bifunctional Fe/C/N Electrocatalysts for Oxygen Reduction and Evolution Reaction. *J Phys Chem C* **2015,** *119* (5), 2583-2588.

45. Lai, Q.; Su, Q.; Gao, Q.; Liang, Y.; Wang, Y.; Yang, Z.; Zhang, X.; He, J.; Tong, H., In Situ Self-Sacrificed Template Synthesis of Fe-N/G Catalysts for Enhanced Oxygen Reduction. *ACS applied materials & interfaces* **2015,** *7* (32), 18170-8.

46. Liang, H. W.; Liu, J. W.; Qian, H. S.; Yu, S. H., Multiplex templating process in one-dimensional nanoscale: controllable synthesis, macroscopic assemblies, and applications. *Accounts of chemical research* **2013,** *46* (7), 1450-61.

47. Song, L. T.; Wu, Z. Y.; Liang, H. W.; Zhou, F.; Yu, Z. Y.; Xu, L.; Pan, Z.; Yu, S. H., Macroscopic-scale synthesis of nitrogen-doped carbon nanofiber aerogels by template-directed hydrothermal carbonization of nitrogen-containing carbohydrates. *Nano Energy* **2016,** *19*, 117-127.

48. Wang, J. L.; Liu, J. W.; Lu, B. Z.; Lu, Y. R.; Ge, J.; Wu, Z. Y.; Wang, Z. H.; Arshad, M. N.; Yu, S. H., Recycling nanowire templates for multiplex templating synthesis: a green and sustainable strategy. *Chemistry* **2015,** *21* (13), 4935-9.

49. Wang, K.; Yang, Y.; Liang, H. W.; Liu, J. W.; Yu, S. H., First sub-kilogram-scale synthesis of high quality ultrathin tellurium nanowires. *Mater Horizons* **2014,** *1* (3), 338-343.

50. Xu, J.; Xin, S.; Liu, J. W.; Wang, J. L.; Lei, Y.; Yu, S. H., Elastic Carbon Nanotube Aerogel Meets Tellurium Nanowires: A Binder- and Collector-Free Electrode for Li-Te Batteries. *Adv Funct Mater* **2016,** *26* (21), 3580-3588.

51. Cui, G.; Zhi, L.; Thomas, A.; Kolb, U.; Lieberwirth, I.; Mullen, K., One-dimensional porous carbon/platinum composites for nanoscale electrodes. *Angewandte Chemie* **2007,** *46* (19), 3464-7.

52. Semenov, A. V.; Pergament, A. L.; Pikalev, A. A., Raman spectroscopy of melamine-formaldehyde resin microparticles exposed to processing in complex plasma. *J Raman Spectrosc* **2016,** *47* (11), 1293-1297.

53. Chen, L. M.; Hu, P. G.; Deming, C. P.; Wang, N.; Lu, J. E.; Chen, S. W., Intervalence Charge Transfer of Ruthenium-Nitrogen Moieties Embedded within Nitrogen-Doped Graphene Quantum Dots. *J Phys Chem C* **2016,** *120* (24), 13303-13309.

54. Ong, W.-J.; Tan, L.-L.; Chai, S.-P.; Yong, S.-T., Heterojunction engineering of graphitic carbon nitride (gC 3 N 4) via Pt loading with improved daylight-induced photocatalytic reduction of carbon dioxide to methane. *Dalton Transactions* **2015,** *44* (3), 1249-1257.

55. Xing, Z.; Ju, Z. C.; Zhao, Y. L.; Wan, J. L.; Zhu, Y. B.; Qiang, Y. H.; Qian, Y. T., One-pot hydrothermal synthesis of Nitrogen-doped graphene as high-performance anode materials for lithium ion batteries. *Sci Rep-Uk* **2016,** *6*.

56. Niu, W.; Li, L.; Liu, J.; Wang, N.; Li, W.; Tang, Z.; Zhou, W.; Chen, S., Graphene-Supported Mesoporous Carbons Prepared with Thermally Removable

Templates as Efficient Catalysts for Oxygen Electroreduction. *Small* **2016,** *12* (14), 1900-8.

57. Liu, X. J.; Zou, S. Z.; Chen, S. W., Ordered mesoporous carbons codoped with nitrogen and iron as effective catalysts for oxygen reduction reaction. *Nanoscale* **2016,** *8* (46), 19249-19255.

58. Jiang, W. J.; Gu, L.; Li, L.; Zhang, Y.; Zhang, X.; Zhang, L. J.; Wang, J. Q.; Hu, J. S.; Wei, Z.; Wan, L. J., Understanding the High Activity of Fe-N-C Electrocatalysts in Oxygen Reduction: Fe/Fe3C Nanoparticles Boost the Activity of Fe-N(x). *Journal of the American Chemical Society* **2016,** *138* (10), 3570-8.

59. Yang, S.; Feng, X.; Wang, X.; Mullen, K., Graphene-based carbon nitride nanosheets as efficient metal-free electrocatalysts for oxygen reduction reactions. *Angewandte Chemie* **2011,** *50* (23), 5339-43.

60. Artyushkova, K.; Serov, A.; Rojas-Carbonell, S.; Atanassov, P., Chemistry of Multitudinous Active Sites for Oxygen Reduction Reaction in Transition Metal-Nitrogen-Carbon Electrocatalysts. *J Phys Chem C* **2015,** *119* (46), 25917-25928.

61. Zhou, D.; Yang, L. P.; Yu, L. H.; Kong, J. H.; Yao, X. Y.; Liu, W. S.; Xu, Z. C.; Lu, X. H., Fe/N/C hollow nanospheres by Fe(III)-dopamine complexation-assisted one-pot doping as nonprecious-metal electrocatalysts for oxygen reduction. *Nanoscale* **2015,** *7* (4), 1501-1509.

62. Meng, F. L.; Wang, Z. L.; Zhong, H. X.; Wang, J.; Yan, J. M.; Zhang, X. B., Reactive Multifunctional Template-Induced Preparation of Fe-N-Doped

Mesoporous Carbon Microspheres Towards Highly Efficient Electrocatalysts for Oxygen Reduction. *Advanced materials* **2016,** *28* (36), 7948-7955.

63. Pei, G. X.; Liu, X. Y.; Wang, A.; Lee, A. F.; Isaacs, M. A.; Li, L.; Pan, X.; Yang, X.; Wang, X.; Tai, Z.; Wilson, K.; Zhang, T., Ag Alloyed Pd Single-Atom Catalysts for Efficient Selective Hydrogenation of Acetylene to Ethylene in Excess Ethylene. *Acs Catal* **2015,** *5* (6), 3717-3725.

64. Sa, Y. J.; Park, C.; Jeong, H. Y.; Park, S. H.; Lee, Z.; Kim, K. T.; Park, G. G.; Joo, S. H., Carbon nanotubes/heteroatom-doped carbon core-sheath nanostructures as highly active, metal-free oxygen reduction electrocatalysts for alkaline fuel cells. *Angewandte Chemie* **2014,** *53* (16), 4102-6.

65. Zhang, P.; Sun, F.; Xiang, Z. H.; Shen, Z. G.; Yun, J.; Cao, D. P., ZIF-derived in situ nitrogen-doped porous carbons as efficient metal-free electrocatalysts for oxygen reduction reaction. *Energ Environ Sci* **2014,** *7* (1), 442-450.

66. Zhou, Z. Y.; Kang, X.; Song, Y.; Chen, S., Enhancement of the electrocatalytic activity of Pt nanoparticles in oxygen reduction by chlorophenyl functionalization. *Chemical communications* **2012,** *48* (28), 3391-3.

67. Wei, J.; Liang, Y.; Hu, Y. X.; Kong, B. A.; Simon, G. P.; Zhang, J.; Jiang, S. P.; Wang, H. T., A Versatile Iron-Tannin-Framework Ink Coating Strategy to Fabricate Biomass-Derived Iron Carbide/Fe-N-Carbon Catalysts for Efficient Oxygen Reduction. *Angew Chem Int Edit* **2016,** *55* (4), 1355-1359.

68. Ferrero, G. A.; Preuss, K.; Marinovic, A.; Jorge, A. B.; Mansor, N.; Brett, D. J. L.; Fuertes, A. B.; Sevilla, M.; Titirici, M. M., Fe-N-Doped Carbon Capsules

with Outstanding Electrochemical Performance and Stability for the Oxygen Reduction Reaction in Both Acid and Alkaline Conditions. *Acs Nano* **2016,** *10* (6), 5922-5932.

69. Niu, W. H.; Li, L. G.; Liu, X. J.; Wang, N.; Liu, J.; Zhou, W. J.; Tang, Z. H.; Chen, S. W., Mesoporous N-Doped Carbons Prepared with Thermally Removable Nanoparticle Templates: An Efficient Electrocatalyst for Oxygen Reduction Reaction. *J Am Chem Soc* **2015,** *137* (16), 5555-5562.

70. Lai, Q. X.; Su, Q.; Gao, Q. W.; Liang, Y. Y.; Wang, Y. X.; Yang, Z.; Zhang, X. G.; He, J. P.; Tong, H., In Situ Self-Sacrificed Template Synthesis of Fe-N/G Catalysts for Enhanced Oxygen Reduction. *Acs Appl Mater Inter* **2015,** *7* (32), 18170-18178.

71. Xing, T.; Zheng, Y.; Li, L. H.; Cowie, B. C.; Gunzelmann, D.; Qiao, S. Z.; Huang, S.; Chen, Y., Observation of active sites for oxygen reduction reaction on nitrogen-doped multilayer graphene. *ACS nano* **2014,** *8* (7), 6856-62.

72. Kattel, S.; Atanassov, P.; Kiefer, B., A density functional theory study of oxygen reduction reaction on non-PGM Fe-Nx-C electrocatalysts. *Physical chemistry chemical physics : PCCP* **2014,** *16* (27), 13800-6.

73. Zhang, J.; Wang, Z.; Zhu, Z. P.; Wang, Q., A Density Functional Theory Study on Mechanism of Electrochemical Oxygen Reduction on FeN4-Graphene. *J Electrochem Soc* **2015,** *162* (7), F796-F801.

74. Kattel, S.; Wang, G., A density functional theory study of oxygen reduction reaction on Me–N4 (Me = Fe, Co, or Ni) clusters between graphitic pores. *J Mater Chem A* **2013,** *1* (36), 10790.

75. Viswanathan, V.; Hansen, H. A.; Rossmeisl, J.; Norskov, J. K., Universality in Oxygen Reduction Electrocatalysis on Metal Surfaces. *ACS Catal.* **2012,** *2* (8), 1654-1660.

76. Li, M. T.; Zhang, L. P.; Xu, Q.; Niu, J. B.; Xia, Z. H., N-doped graphene as catalysts for oxygen reduction and oxygen evolution reactions: Theoretical considerations. *J. Catal.* **2014,** *314*, 66-72.

77. McClure, J. P.; Borodin, O.; Olguin, M.; Chu, D.; Fedkiw, P. S., Sensitivity of Density Functional Theory Methodology for Oxygen Reduction Reaction Predictions on Fe-N-4-Containing Graphitic Clusters. *J Phys Chem C* **2016,** *120* (50), 28545-28562.

78. Yu, L.; Pan, X. L.; Cao, X. M.; Hu, P.; Bao, X. H., Oxygen reduction reaction mechanism on nitrogen-doped graphene: A density functional theory study. *J Catal* **2011,** *282* (1), 183-190.

79. Deng, Y.; Chi, B.; Li, J.; Wang, G.; Zheng, L.; Shi, X.; Cui, Z.; Du, L.; Liao, S.; Zang, K.; Luo, J.; Hu, Y.; Sun, X., Atomic Fe-Doped MOF-Derived Carbon Polyhedrons with High Active-Center Density and Ultra-High Performance toward PEM Fuel Cells. *Adv. Energy Mater.* **2019,** *0* (0), 1802856.

80. Wan, G.; Yu, P.; Chen, H.; Wen, J.; Sun, C.-j.; Zhou, H.; Zhang, N.; Li, Q.; Zhao, W.; Xie, B.; Li, T.; Shi, J., Engineering Single-Atom Cobalt Catalysts toward Improved Electrocatalysis. *Small* **2018,** *14* (15), 1704319.

81. Jiang, R.; Li, L.; Sheng, T.; Hu, G.; Chen, Y.; Wang, L., Edge-Site Engineering of Atomically Dispersed Fe–N4 by Selective C–N Bond Cleavage for Enhanced Oxygen Reduction Reaction Activities. *Journal of the American Chemical Society* **2018,** *140* (37), 11594-11598.

82. Xia, W.; Mahmood, A.; Liang, Z. B.; Zou, R. Q.; Guo, S. J., Earth-Abundant Nanomaterials for Oxygen Reduction. *Angew. Chem. Int. Ed.* **2016,** *55* (8), 2650-2676.

83. Qian, H. S.; Yu, S. H.; Gong, J. Y.; Luo, L. B.; Fei, L. F., High-quality luminescent tellurium nanowires of several nanometers in diameter and high aspect ratio synthesized by a poly (vinyl pyrrolidone)-assisted hydrothermal process. *Langmuir : the ACS journal of surfaces and colloids* **2006,** *22* (8), 3830-5.

84. Giannozzi, P.; Baroni, S.; Bonini, N.; Calandra, M.; Car, R.; Cavazzoni, C.; Ceresoli, D.; Chiarotti, G. L.; Cococcioni, M.; Dabo, I.; Dal Corso, A.; de Gironcoli, S.; Fabris, S.; Fratesi, G.; Gebauer, R.; Gerstmann, U.; Gougoussis, C.; Kokalj, A.; Lazzeri, M.; Martin-Samos, L.; Marzari, N.; Mauri, F.; Mazzarello, R.; Paolini, S.; Pasquarello, A.; Paulatto, L.; Sbraccia, C.; Scandolo, S.; Sclauzero, G.; Seitsonen, A. P.; Smogunov, A.; Umari, P.; Wentzcovitch, R. M., QUANTUM ESPRESSO: a modular and open-source software project for quantum simulations of

materials. *Journal of physics. Condensed matter : an Institute of Physics journal* **2009,** *21* (39), 395502.

85. Garrity, K. F.; Bennett, J. W.; Rabe, K. M.; Vanderbilt, D., Pseudopotentials for high-throughput DFT calculations. *Comp Mater Sci* **2014,** *81*, 446-452.

86. Marzari, N.; Vanderbilt, D.; De Vita, A.; Payne, M. C., Thermal contraction and disordering of the Al(110) surface. *Phys Rev Lett* **1999,** *82* (16), 3296-3299.

87. Baroni, S.; de Gironcoli, S.; Dal Corso, A.; Giannozzi, P., Phonons and related crystal properties from density-functional perturbation theory. *Rev Mod Phys* **2001,** *73* (2), 515-562.

88. Ping, Y.; Nielsen, R. J.; Goddard, W. A., 3rd, The Reaction Mechanism with Free Energy Barriers at Constant Potentials for the Oxygen Evolution Reaction at the IrO(2) (110) Surface. *Journal of the American Chemical Society* **2017,** *139* (1), 149-155.

89. Sundararaman, R.; Goddard, W. A., 3rd, The charge-asymmetric nonlocally determined local-electric (CANDLE) solvation model. *The Journal of chemical physics* **2015,** *142* (6), 064107.

90. Petrosyan, S. A.; Briere, J. F.; Roundy, D.; Arias, T. A., Joint density-functional theory for electronic structure of solvated systems. *Phys Rev B* **2007,** *75* (20), 205105.

91. Ping, Y.; Sundararaman, R.; Goddard, W. A., 3rd, Solvation effects on the band edge positions of photocatalysts from first principles. *Physical chemistry chemical physics : PCCP* **2015,** *17* (45), 30499-509.

Chapter 3 Ruthenium single atoms as efficient catalyst for hydrogen evolution reaction

3.1 Abstract

Hydrogen evolution reaction (HER) is an important process in electrochemical energy conversion and storage. Herein, we report the design and synthesis of effective HER catalysts based on Ru,N-codoped carbon nanowires. The catalytic performance is markedly better than that of commercial Pt/C catalyst, with an overpotential of only −12 mV to reach the current density of 10 mV/cm^2 in 1 M KOH and −47 mV in 0.1 M KOH. Comparison with control experiments suggest that the remarkable activity is mainly ascribed to individual ruthenium atoms embedded within the carbon matrix, with minimal contributions from ruthenium nanoparticles. Consistent results are obtained in first-principles calculations, where RuC_xN_y moieties are found to show a much lower H binding energy than ruthenium nanoparticles, and a lower kinetic barrier for water dissociation than platinum. Among these, RuC_2N_2 stands out as the most active catalytic center, where both ruthenium and adjacent carbon atoms are possible active sites. Consistently, in another our study, the Ru single atom in C3N4 matrix also show great HER activity, the active sites can be Ru and neighboring nitrogen sites.

3.2 Introduction

Hydrogen evolution reaction (HER) plays a significant role in electrochemical water splitting for clean and sustainable hydrogen energy[1, 2]. In practice, room-temperature

water electrolysis can be performed in both acid and alkaline electrolytes, where platinum-based nanoparticles generally serve as the catalysts of choice. Whereas numerous studies have been carried out in acid, the high costs of proton exchange membranes[3] as well as the sluggish electron-transfer kinetics of oxygen evolution reaction in acidic media[4] have greatly hampered the wide-spread applications of acidic water electrolyzers. Such issues can be mitigated when the reactions are carried out in alkaline media, where HER involves three key steps[5, 6],

$$H_2O + * + e- = H* + OH^- \text{ (Volmer)} \quad (1)$$

$$H* + H_2O + e- = H_2 + OH^- \text{ (Heyrovsky)} \quad (2)$$

$$2H* = H_2 \text{ (Tafel)} \quad (3)$$

with * being the active site. The HER performance is generally discussed within the context of the Volmer-Heyrovsky or Volmer-Tafel pathway. Interestingly, whereas alkaline HER entails water dissociation, a unique step that is unseen in acid HER, the adsorption free energy of H to the catalyst surface (G_{H*}) remains an effective descriptor[7-11]. In conjunction with the calculations of the energy barrier of water dissociation[12], the active sites as well as the reaction pathways can be resolved.

Nevertheless, alkaline water electrolysis come with a significant disadvantage of its own, which is the markedly diminished HER electron-transfer kinetics catalyzed by platinum (about two orders of magnitude lower than that in acid)[13]. Thus, it is of both fundamental and technological significance to improve the performance of Pt-based HER catalysts[6] or develop viable alternatives that are low-costs and high-performance for HER electrocatalysis in alkaline electrolytes (e.g., transition metal oxides,

chalcogenides and phosphides)[14-17]. Towards this end, non-platinum noble metals, such as ruthenium, rhodium, palladium and iridium,[18-21] have also been attracting particular attention because of their apparent performances. Of these, ruthenium, in the forms of nanoparticles, alloys, and oxides, has been found to display a HER activity that is comparable to that of commercial platinum catalysts in alkaline solutions[22-29]. For instance, Mahmood et al.[18] reduced $RuCl_3$ onto nitrogen-doped 2D frameworks by $NaBH_4$, and the composite was then pyrolyzed producing ruthenium nanoparticles of 1.6 nm in diameter dispersed in the carbon matrix. The sample exhibited an apparent HER activity with an overpotential (η_{10}) of only -25 mV to reach the current density of 10 mA/cm^2 in 1 M KOH. In another study[30], Zheng et al. prepared a composite with ruthenium nanoparticles (dia. 2nm, consisting of a mixture of face-centered cubic (*fcc*)and hexagonal close-packed (*hcp*) ruthenium) and carbon nitride (C_3N_4) by annealing the product at elevated temperatures. The catalyst showed an η_{10} of -79 mV in 0.1 M KOH. In these studies, the HER activity was generally ascribed to ruthenium nanoparticles[18, 30, 31]. In a more recent study[32], Zhang et al. immersed a polyaniline-coated graphite foam into a Ru^{3+} solution, and after pyrolysis at controlled temperatures, TEM measurements showed that Ru nanoparticles (2.1-8.3 nm in diameter) and atomic species were formed and dispersed on the carbon surface. The resulting sample showed an η_{10} of -21 mV in 1 M KOH. Based on results of a poisoning experiment with KSCN, the activity was attributed to atomically dispersed Ru in the nitrogen-doped carbon matrix instead of the Ru nanoparticles; yet the detailed structures of the atomic species and hence the catalytic active centers

remained unresolved. In a series of other studies[27, 28, 33], ruthenium ions were embedded into the C_3N_4 skeleton by complexation to the pyridinic N moieties of the tri-s-triazine units, forming a structure with isolated Ru metal centers; yet the corresponding HER activity, while remarkable, remained subpar as compared to that of Pt/C. This raises an interesting question: will ruthenium single atom catalysts ever rival commercial Pt/C in HER electrocatalysis? This is the primary motivation of the present study.

Herein, we prepared a nanocomposite based on ruthenium and nitrogen co-doped carbons and examined the impacts of both ruthenium nanoparticles and atomic ruthenium sites on the HER performance. Experimentally, melamine-formaldehyde polymer was coated onto tellurium nanowires (Te NWs), and the core-sheath nanowires were pyrolyzed at controlled temperature, with the addition of a calculated amount of ruthenium(III) chloride, leading to the formation of Ru,N-codoped carbon nanowires where both ruthenium nanoparticles and ruthenium single atoms were embedded within the carbon matrix. Significantly, the sample exhibited a remarkable HER activity in alkaline media, a performance even significantly better than that of commercial Pt/C. Control experiments showed that the HER activity was primarily due to atomically dispersed Ru coordinated to N and C, with minor contributions from ruthenium nanoparticles. Consistent results were obtained in computational studies based on first principles calculations, where the HER active sites were most likely the ruthenium atomic centers involved in (undersaturated) coordination with N and C (RuC_xN_y). Carbon atoms adjacent to the Ru center were also the possible active

sites based on favorable H binding energies and relatively low formation energies. The corresponding energy barriers for water dissociation (Volmer reaction) were then evaluated by using the climbing-image nudged elastic band (CI-NEB) method[12, 34], which were found to be even lower than that on Pt[35], indicating a faster kinetic process.

3.3 Result and discussion

3.3.1 Synthesis and characterization

One-dimensional Ru,N-codoped carbon nanowires were synthesized by using Te NWs as sacrificial templates[36-39]. The procedure includes four major steps (**Figure 1a**): (a) hydrothermal synthesis of Te NWs, (b) formation of a melamine-formaldehyde resin shell on Te NWs (Te@MF), (c) reaction of Te with $RuCl_3$ to incorporate Ru precursors into Te@MF (Ru-MF); and (d) pyrolysis of the Ru-MF nanowires at elevated temperatures to produce Ru,N-codoped carbon nanofibers (Ru-NC-T, with T being the pyrolysis temperature). In this procedure (details in the Method section), melamine serves as a carbon and nitrogen source, and formaldehyde as a second carbon source and linking agent.

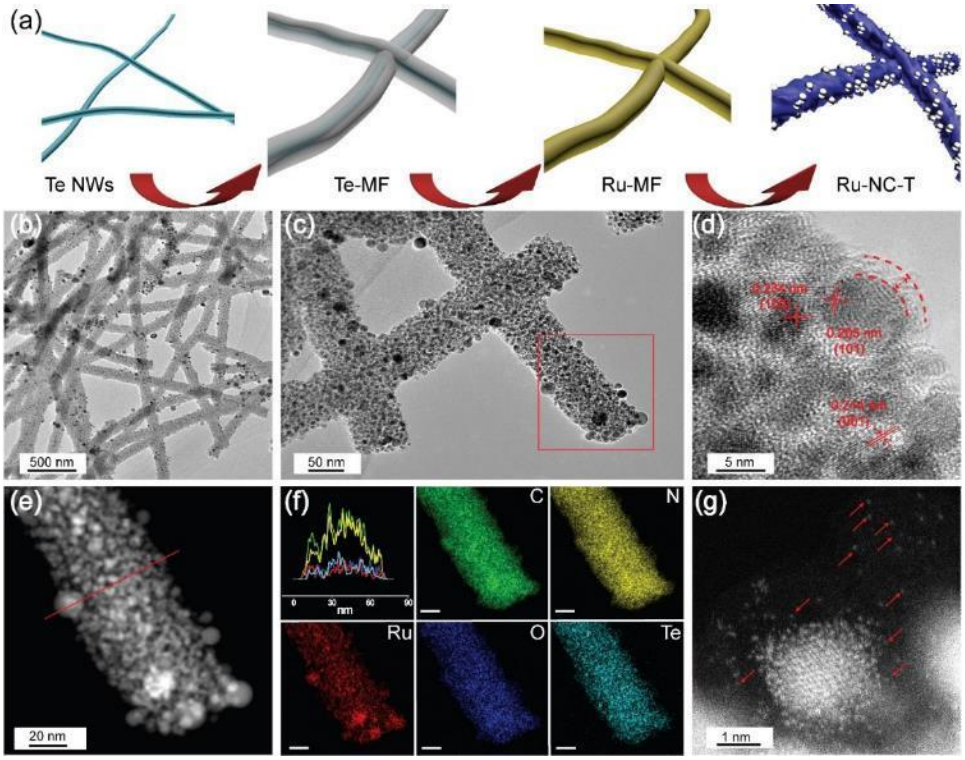

Figure 1. Schematic of the synthesis of Ru-NC-T samples and TEM studies of Ru-NC-800. (a) Synthetic procedure of the Ru-NC-T samples. (b)-(d) Representative TEM images at different magnifications. Scale bars are (b) 500 nm, (c) 100 nm, and (d) 5 nm. (e) HAADF-STEM image of the red area of figure 1c. (f) Cross-sectional elemental distributions by line scans along the red line in figure 1e. The colors of the elemental maps of C, N, O, Te and Ru correspond to those in the line scan spectra. Scale bars are all 20 nm. (g) A zoom-in of figure 1e, where red arrows signify ruthenium single atoms.

When $RuCl_3$ was added into the Te NW dispersion, the solution color was found to change from blue to dark brown, indicative of reaction between Te and Ru^{3+} forming

$RuTe_x$ complexes. From the TEM image in **figure 2a**, one can see that the resulting nanowires are 80-100 nm in diameter and several microns in length, and the surface is decorated with a number of dark spots which are most likely the $RuTe_x$ complexes. This can be better observed at higher magnifications (**figure 2b**). Yet, no well-defined lattice fringes can be seen (**figure 2c**), suggesting amorphous characteristics of the resin and the complexes. Elemental mapping analysis shows that the elements of C, N, O, Te and Ru are distributed rather evenly throughout the nanowires (**figure 2d-f**). After pyrolysis at elevated temperatures, dark-contrast objects were formed and embedded within the carbon matrix (**figure 1b-d** and **3**), which exhibited well-defined lattice fringes (**figure 1d**), with interplanar spacings of 0.234, 0.214, and 0.205 nm that are characteristic of the (100), (001) and (101) planes of *hcp* Ru (JCPDS-ICDD card No. 06-0663). This indicates the formation of Ru nanoparticles, which were encapsulated within a thin carbon layer of 2-3 nm (**figure 1d**). The ruthenium nanoparticles showed a marked increase of the diameter with increasing pyrolysis temperature, ca. 1.0 nm for Ru-NC-500, 2-3 nm for Ru-NC-600, 5.0 nm for Ru-NC-700, and 10 nm for Ru-NC-800 (**figure 3**). The formation of ruthenium nanoparticles is likely due to reduction of the $RuTe_x$ complex in Ru-MF by carbon at high temperatures, which also facilitated the migration and Ostwald ripening of the nanoparticles, leading to an increase of the nanoparticle size. Furthermore, one can see that the nanowire morphologies did not change appreciably after pyrolysis, though with a somewhat smaller cross-sectional diameter (ca. 60 nm) than that of Ru-MF, likely due to partial decomposition of the MF resin during the carbonization

process (**figure 1b-d** and **3**). Elemental mapping based on EDX analysis shows that all elements of C, N, O, Te, and Ru remained readily visible (**figure 1e-f**); and whereas the distributions of C, N, O and Te were rather uniform (no other element was detected, **figure 4**), ruthenium exhibited apparent clustering, coincident with the formation of ruthenium nanoparticles. Remarkably, in addition to Ru nanoparticles, a number of Ru single atoms can also be readily identified within the carbon matrix, as manifested in double aberration-corrected HAADF-STEM measurements and highlighted by red arrows in **figure 1g** and **5**.

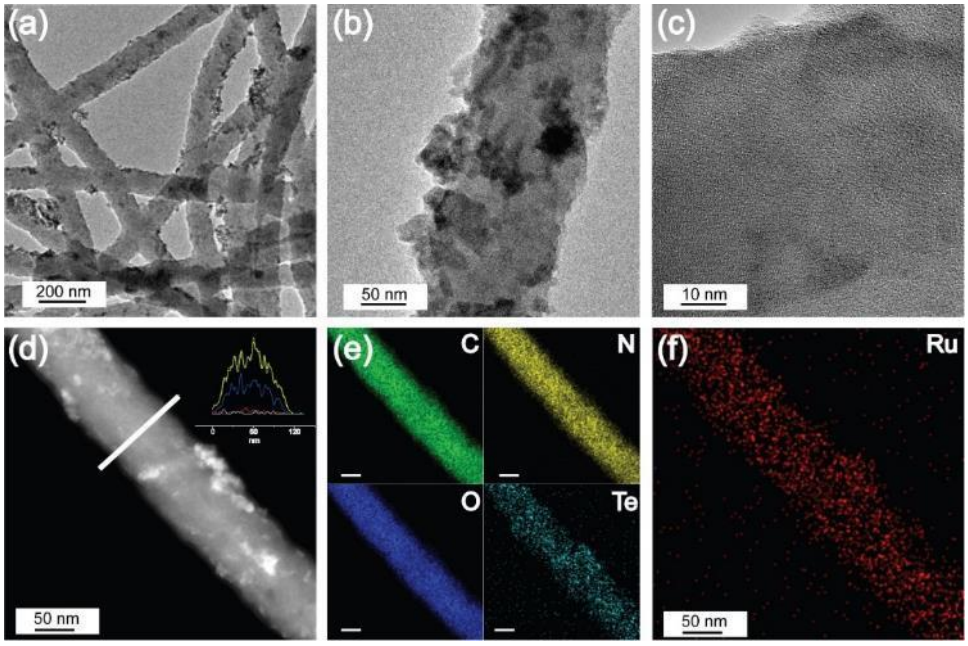

Figure 2. TEM studies of Ru-MF. (a)-(c) Representative TEM images. (d) HAADF-STEM image. Inset is elemental line scans for C, N, O, Te and Ru, where the colors coincide with those in panels (e)-(f).

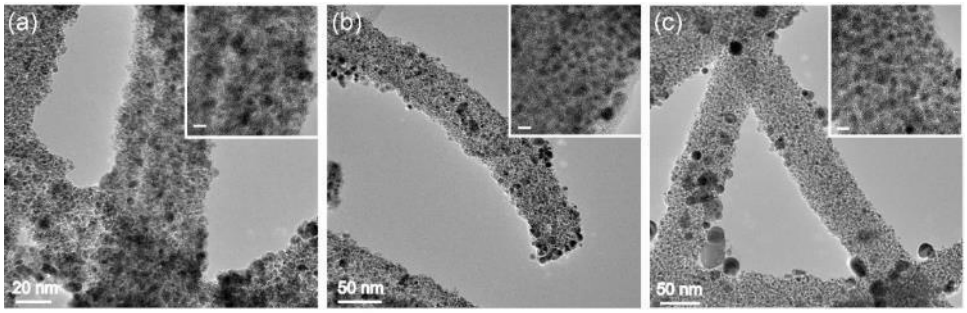

Figure 3. **Representative TEM images** of (a) Ru-NC-500, (b) Ru-NC-600, and (c) Ru-NC-700. Scale bars are (a) 20 nm, (b) 50 nm and (c) 50 nm. The insets are the corresponding images at higher magnification. Scale bars are all 5 nm

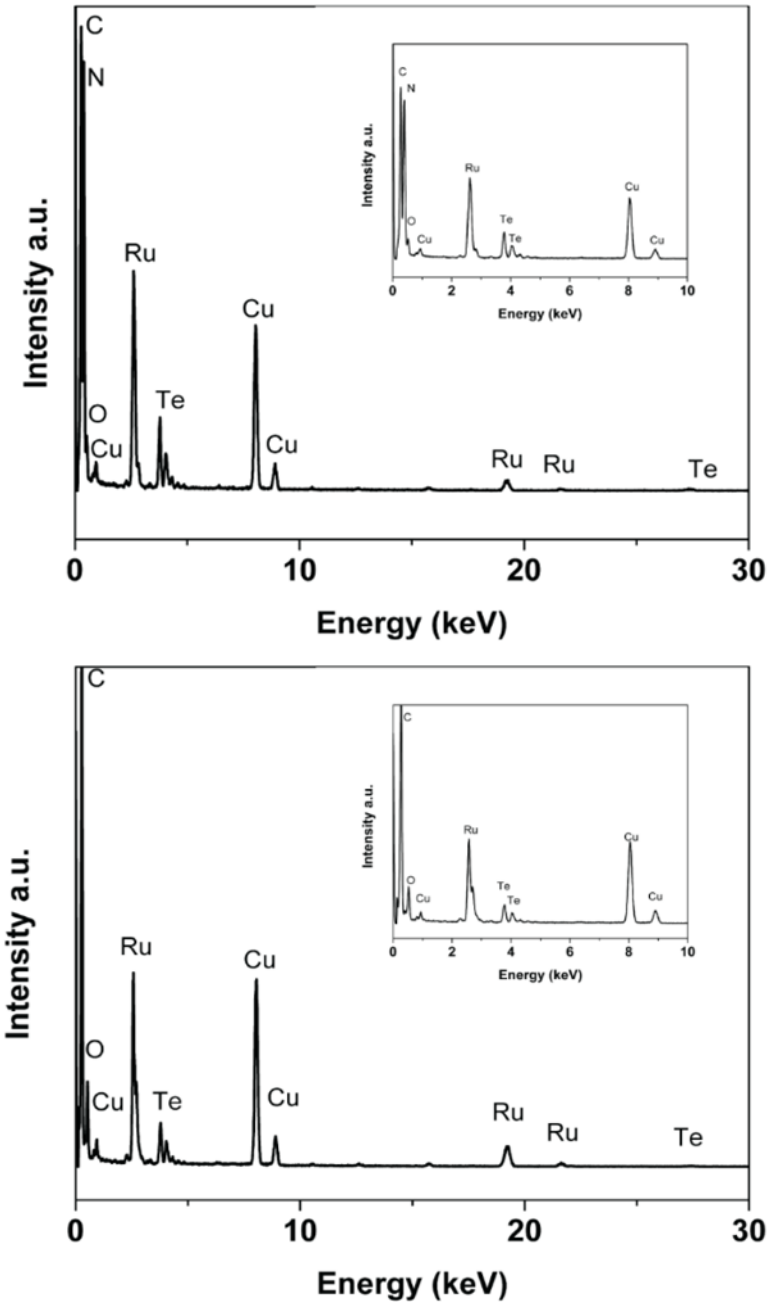

Figure 4. **EDX spectra** of (top) Ru-MF and (bottom) Ru-NC-800. Insets is the zoom in of the regions between 0 and 10 eV. In both samples, the Cu peaks are from the TEM grids.

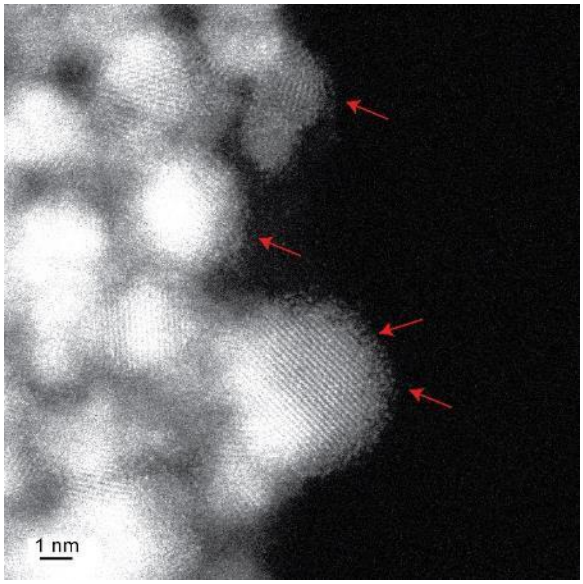

Figure 5. **Representative 2AC-HAADF-STEM image** of Ru-NC-700 of Ru nanoparticles and Ru single atoms. The arrows point out the carbon shell around Ru nanoparticles where Ru single atoms dispersed.

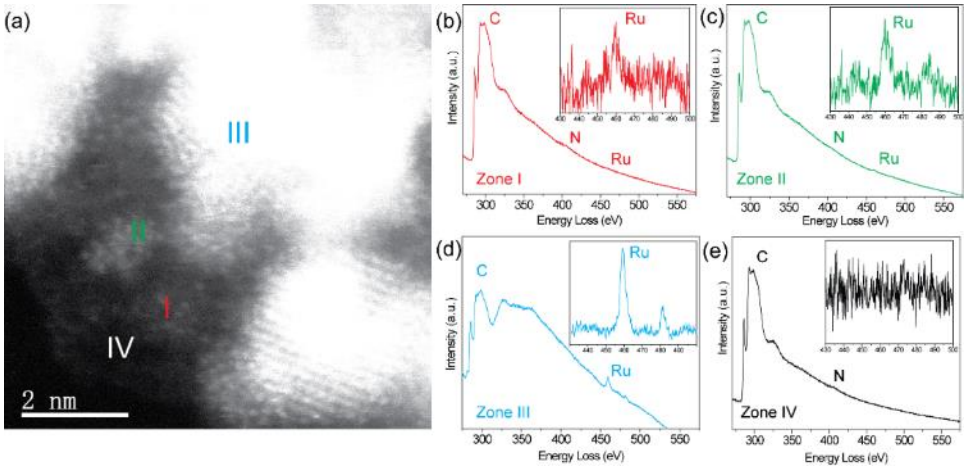

Figure 6. HAADF-STEM and EELS data of Ru-NC-700. (a) Representative HAADF-STEM image of Ru-NC-700; and EELS spectra of zones (I) to (IV) in panel (a) that correspond to ruthenium single atoms, ruthenium nanoclusters, ruthenium

nanoparticles, and ruthenium-free carbon matrix, respectively. The insets are the respective zoom-in within the energy range of 430-500 eV.

To further confirm the formation of Ru single atoms and to examine the structure of the various forms of ruthenium in the carbon matrix, electron energy loss spectroscopic (EELS) measurements were carried out at the edge of a Ru-NC nanowire, where four zones I – IV were selected (**figure 6a**): (I) ruthenium single atoms, (II) ruthenium nanoclusters, (III) ruthenium nanoparticles, and (IV)

ruthenium-free carbon matrix. From the EELS spectra in **figure 6b-e**, one can see that both C (ca. 300 eV) and N (ca. 400 eV) were rather visible in all four zones, whereas Ru (ca. 460 eV, insets to **figure 6b-e**) appeared only in zones I – III but was absent in zone IV, and in comparison to the spectral background, the Ru signals became intensified from single atoms (zone I) to nanoclusters (zone II) and further to

nanoparticles (zone III). This suggests that ruthenium was most likely stabilized by coordination to nitrogen and/or carbon in the matrix. Furthermore, the fact that no oxygen signal (ca. 523 eV) was detected indicates that the Ru-NC samples were largely unoxidized.

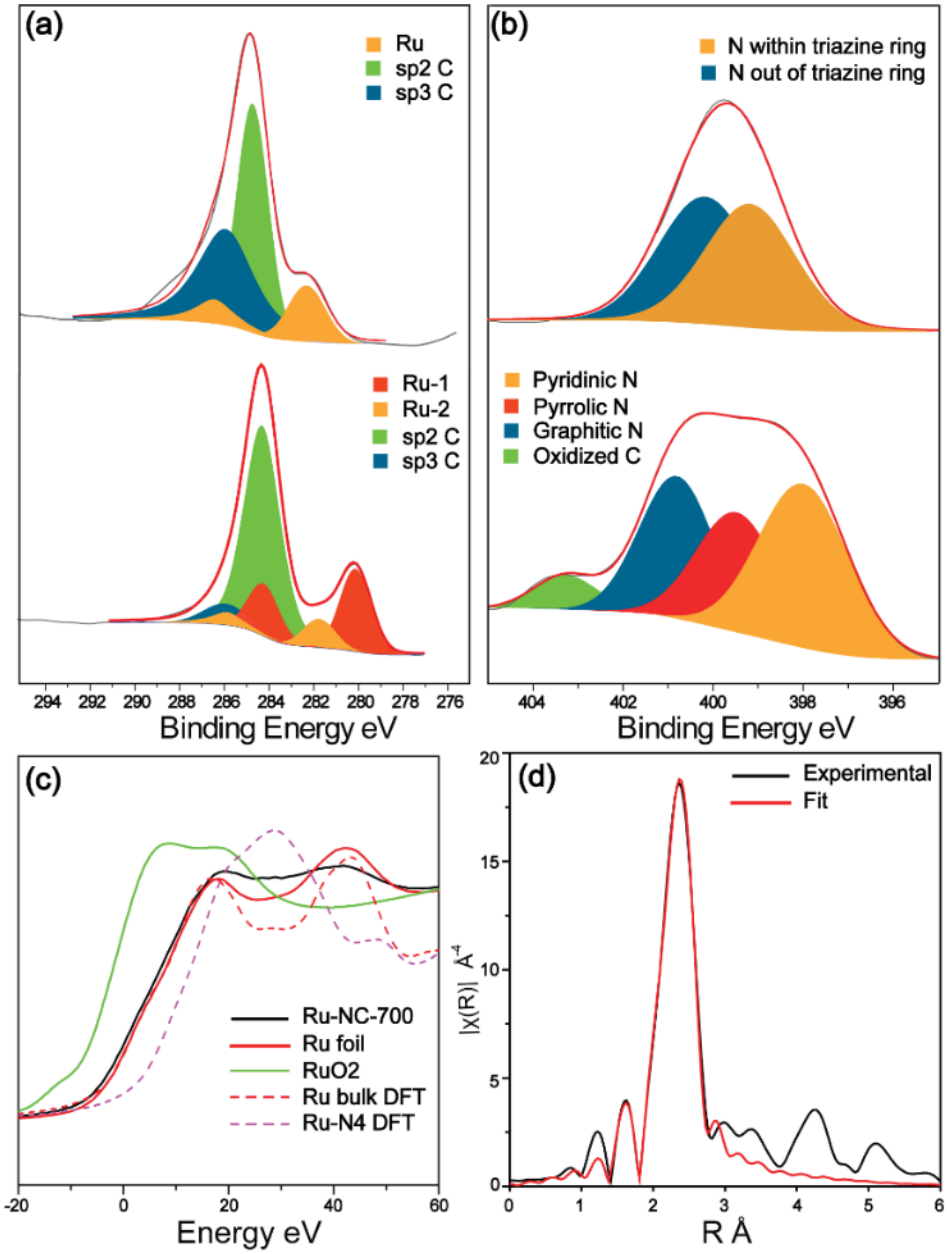

Figure 7. XPS data of Ru-MF and Ru-NC-700, and XAS analysis of Ru-NC-700. (a) C 1s and Ru 3d spectra of Ru-MF (upper panel) and Ru-NC-700 (lower panel). (b) N 1s spectra of Ru-MF (upper panel) and Ru-NC-700 (lower panel). Black curves are experimental data, shaded peaks are deconvolution fits, and red curves are the sum of the fits. (c) Normalized XANES data for Ru-NC-700, solid lines are experimental data and dash lines are simulated data by DFT calculations. (d) FT-EXAFS data for Ru-NC-700, where black curve is experimental data and red curve is the best fit.

Elemental analysis of the Ru-NC-T samples was then carried out by XPS measurements (**figure 7a,b and 8-11**). The atomic ratio of Csp^2/Csp^3 increased markedly from ca. 1:1 for Ru-MF to 4.74:1 for Ru-NC-500, 4.22:1 for Ru-NC-600, 9.2:1 for Ru-NC-700, and 16.98:1 for Ru-NC-800, suggesting increasing graphitization with increasing pyrolysis temperature (**table 1**). In addition, two ruthenium species are resolved for the Ru-NC samples, the first one (red, Ru-1) can be ascribed to metallic Ru(0), whereas the other one (yellow, Ru-2) are at somewhat higher energies, very close to Ru(II) in Ru-N coordination that was observed previously[27]. This is consistent with the formation of both ruthenium nanoparticles and ruthenium atomic species embedded within the carbon matrix, as manifested in TEM measurements (**figure 1f, 2a** and **5**); and the atomic ratio of Ru-2/Ru-1 was found to decrease with increasing pyrolysis temperature, 0.45 for Ru-NC-500, 0.36 for Ru-NC-600, 0.35 for Ru-NC-700, and 0.31 for Ru-NC-800 (**table 2**). As the overall ruthenium content remained almost unchanged at ca. 4 at% among the Ru-NC-T series (**table 3**) and the nanoparticle core size increased from Ru-NC-500 to

Ru-NC-800 (**figure 1**), this suggests that apparent nanoparticle sintering occurred with increasing pyrolysis temperature, whereas the number of atomic Ru species varied at a much lower rate. Nitrogen was also found to be doped into the carbon matrix of the Ru-NC samples (**Figure 7b and 11)** in the forms of pyridinic, pyrrolic, graphitic, and oxidized N[40-42], and with increasing pyrolysis temperature, the overall nitrogen content decreased accordingly, 5.24 at.% for Ru-NC-500, 3.44 at.% for Ru-NC-600, 2.04 at.% for Ru-NC-700, 0.96 at.% for Ru-NC-800 (**table 4**). Additional data can be found in **table 5**, and more detailed discussion is included under **figure 11**.

Sample	**Csp^2**	**Csp^3**	**Csp^2/Csp^3 atomic ratio**
Ru-MF	284.64	285.84	1
Ru-NC-500	284.20	285.80	4.71
Ru-NC-600	284.16	285.80	4.22
Ru-NC-700	284.17	285.84	9.20
Ru-NC-800	284.20	285.80	16.98

Table 1. C 1s binding energy and atomic ratio of sp^2 and sp^3 carbons by XPS measurements

Sample	Ru-1 ($3d_{5/2}$)	Ru-1 ($3d_{3/2}$)	Ru-2 ($3d_{5/2}$)	Ru-2 ($3d_{3/2}$)	Ru-2/Ru-1
Ru-MF	282.24	286.33	0	0	
Ru-NC-500	280.18	284.28	281.87	285.97	0.45
Ru-NC-600	280.06	284.16	281.75	285.75	0.36
Ru-NC-700	280.04	284.14	281.66	285.76	0.35
Ru-NC-800	280.00	284.10	281.50	285.60	0.31

Table 2. Summary of Ru 3d binding energy (eV) by XPS measurements

Sample	Ru	C	N	Te
Ru-MF	1.48	88.56	9.61	0.34
Ru-NC-500	4.02	87.69	5.24	3.05
Ru-NC-600	4.66	89.38	3.44	2.51
Ru-NC-700	3.85	92.12	2.04	1.98
Ru-NC-800	3.89	93.03	0.96	2.11

Table 3. Elemental composition (at%) by XPS measurements

Sample	Pyridinic		Pyrrolic		Graphitic		Oxidized	
	BE (eV)	Content (%)	BE (eV)	Content (%)	BE (eV)	Content (%)	BE (eV)	Content (%)
Ru-MF	399.16 (triazine ring)				400.16 (non-triazine ring)			
Ru-NC-500	398.27	53.1	399.62	19.0	400.66	11.8	402.11	16.1

Ru-NC-600	398.06	49.3	399.47	23.4	400.84	17.1	402.50	10.1
Ru-NC-700	398.00	39.5	399.47	26.2	400.80	28.5	403.27	5.8
Ru-NC-800	398.00	25.9	399.50	29.8	400.80	37.3	402.50	6.9

Table 4. N 1s binding energy (BE) and content by XPS measurements

Sample	**$3d_{5/2}$**	**$3d_{3/2}$**
Ru-MF	576.32	586.74
Ru-NC-500	575.75	586.09
Ru-NC-600	575.58	586.04
Ru-NC-700	575.60	586.04
Ru-NC-800	575.59	586.04

Table 5. Te 3d binding energy (eV) by XPS measurements

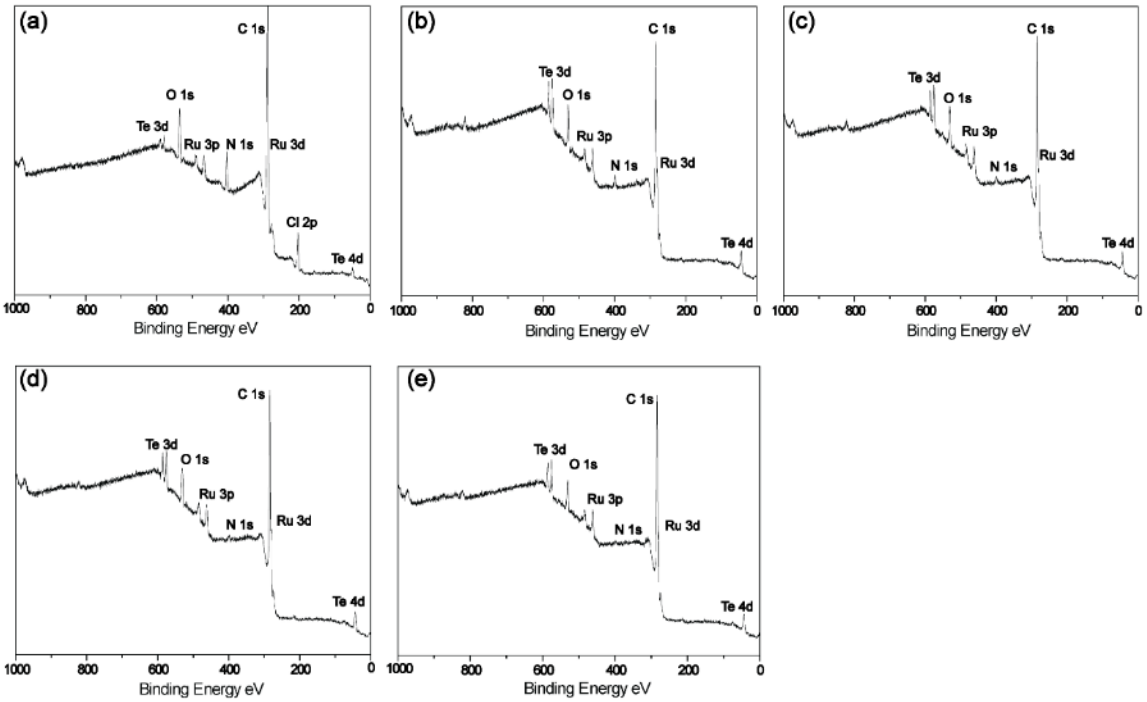

Figure 8. **XPS full survey spectra** of (a) Ru-MF, (b) Ru-NC-500, (c) Ru-NC-600, (d) Ru-NC-700, and (e) Ru-NC-800.

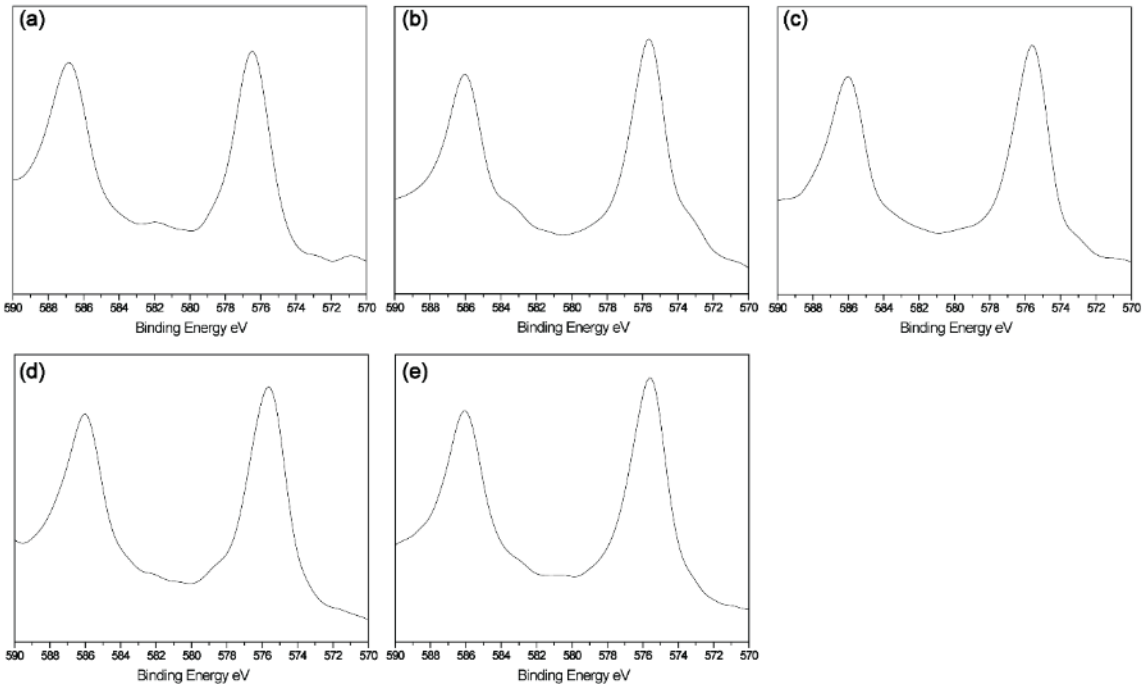

Figure 9. XPS spectra of Te 3d electrons of (a) Ru-MF, (b) Ru-NC-500, (c) Ru-NC-600, (d) Ru-NC-700, and (e) Ru-NC-800.

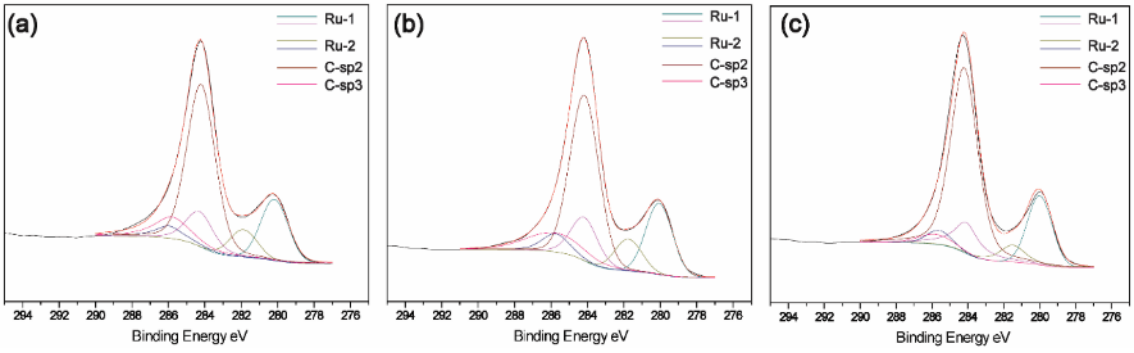

Figure 10. XPS spectra of C 1s and Ru 3d electrons of (a) Ru-NC-500, (b) Ru-NC-600, and (c) Ru-NC-800. Black curves are experimental data and colored curves are deconvolution fits.

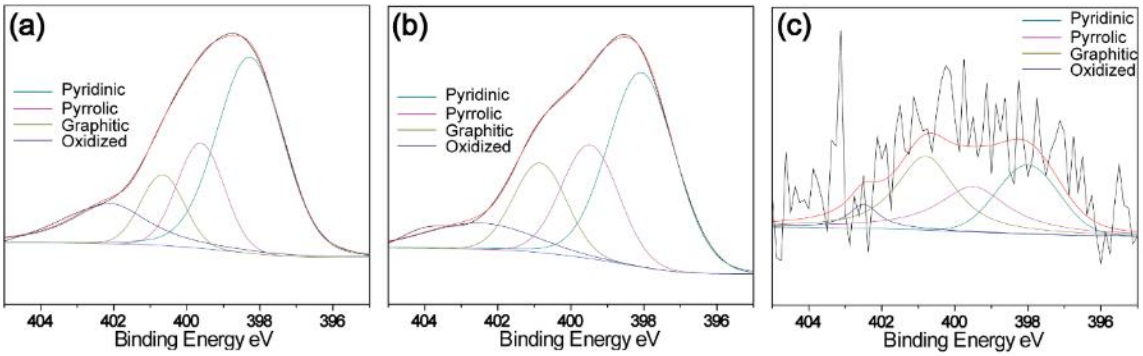

Figure 11. XPS spectra of N 1s electrons of (a) Ru-NC-500, (b) Ru-NC-600, and (c) Ru-NC-800. Black curves are experimental data and colored curves are deconvolution fits.

Further structural insights were obtained from Raman and XRD measurements. Broad D and G bands can be observed at ca. 1350 and 1550 cm^{-1} in Raman measurements (**figure 12**), indicating defective structures of the carbon matrix. In addition, the vibrational bands at 400-600 cm^{-1} can be assigned to Ru-N/Ru-C stretching[43], suggestive of the formation of RuC_xN_y moieties in the samples. In XRD measurements (**figure 13**), all Ru-NC-T samples exhibited diffraction patterns that are consistent with those of *hcp* Ru. In addition, a broad peak can be identified within 2theta = 20 to 30°, characteristic of the (002) diffraction of nanosized graphitic carbon[44].

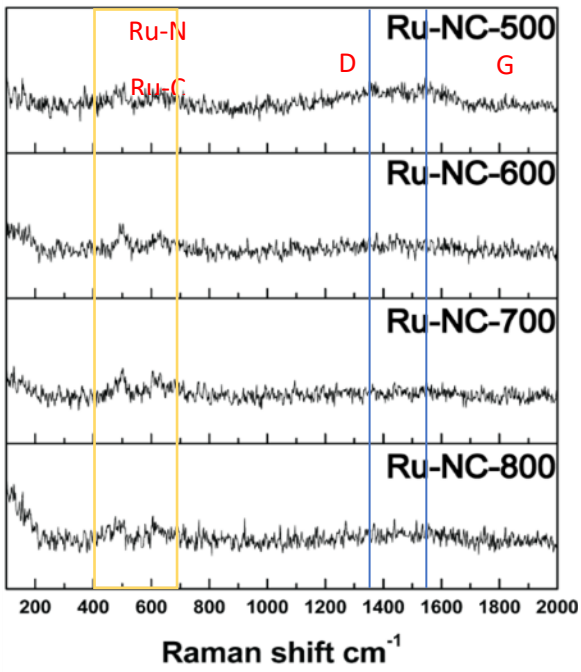

Figure 12. **Raman spectra** of the Ru-NC-T samples

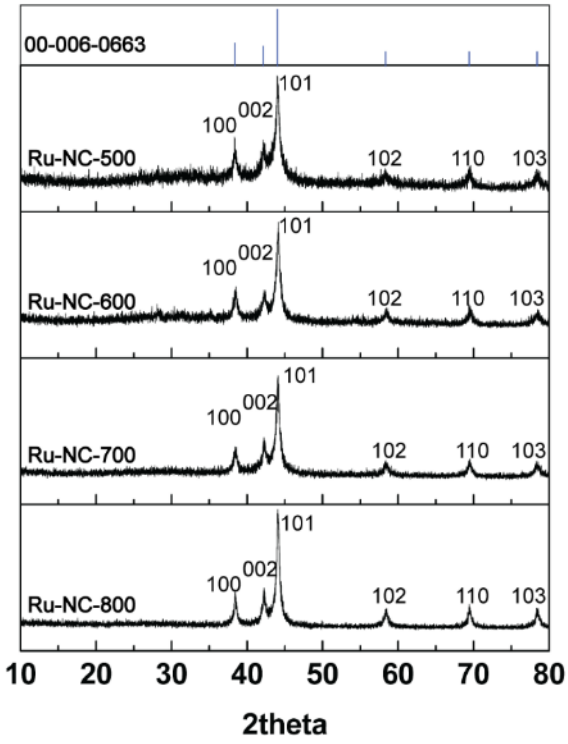

Figure 13. **XRD profiles** of Ru-NC-500, Ru-NC-600, Ru-NC-700 and Ru-NC-800. The standard profile of hcp Ru (00-006-0663) is included in the top of the figure.

Consistent results were obtained from X-ray absorption spectroscopy (XAS) measurements. **Figure 7c** shows the X-ray absorption near-edge structure (XANES) spectra of Ru-NC-700, Ru foil, and RuO_2. It can be seen that the absorption edge of Ru-NC-700 (black solid curve) is close to that of Ru foil (red solid curve) but markedly different from that of RuO_2 (green solid curve), consistent with results from EELS measurements (**figure 6**) where no oxygen signals were detected. In addition, one can see that within the range of 18-40 eV, the Ru-NC-700 sample shows an

almost flat feature. This can be attributed to the combined contributions of Ru nanoparticles and single atoms, as Ru foil displays a valley (DFT simulation of bulk Ru shows a consistent profile, red dashed curve) whereas Ru single atoms (e.g., RuN_4, purple dashed curve; more details in **figure 14**) contribute a peak from DFT XAS simulations. **Figure 7d** shows the FT-EXAFS spectrum of Ru-NC-700, along with the theoretical fit. Two main peaks can be fitted by using a Ru-Ru and Ru-N/C (C and N are indistinguishable in the fitting) shell with a bond distance of 2.68 and 2.03 Å, respectively[45, 46]. Moreover, from the fitting, the coordination number (CN) was estimated to be 6.6 for Ru-Ru, and 1.3 for Ru-N/Ru-C (**table 6**). The former is markedly lower than that (12) of bulk Ru, likely due to the formation of ruthenium nanoparticles,[47] whereas the latter is abnormally large for the size of the nanoparticles observed in **figure 1**. These are consistent with the formation of both ruthenium nanoparticles and single atoms bonded to the N and/or C in the carbon matrix, as manifested in HAADF-STEM measurements in **figure 1**. Furthermore, based on the CN[47-50], the Ru atomic ratio in single atoms vs nanoparticles was estimated to be 0.41, very close to that determined by XPS measurements (**table 2**).

	bond	**Coordination number (CN)**	**Bond length R (Å)**	**σ^2 (Å) x10^{-3}**	**E_0 (eV)**	**R factor**
Ru-NC-	Ru-N/Ru-C	1.3 (5)	2.03 (2)	4.2 (4)	-2.6 (9)	0.0021

700	Ru-Ru	6.6 (5)	2.678 (3)	4.2 (4)	-2.6 (9)	0.0021
Ru-NC-700 (1/8)	Ru-N/Ru-C	2.4 (6)	2.02 (1)	8 (2)	-2 (1)	0.0136
	Ru-Ru	6.4 (7)	2.71 (1)	8 (2)	-2 (1)	0.0136

Table 6. EXAFS fitting results of Ru-NC-700 from Figure 2c and Ru-NC-700

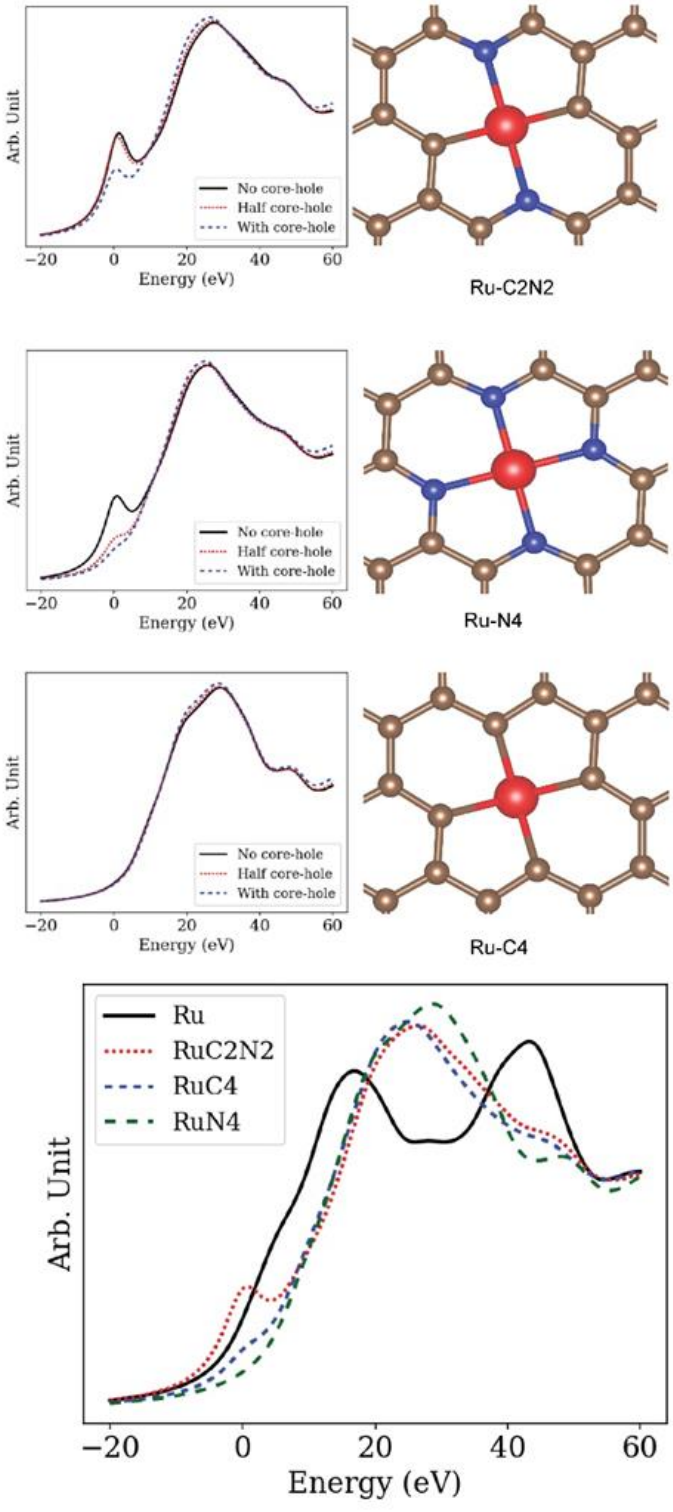

(1/8) from Figure 17g

Figure 14. Calculated XANES spectra of Ru K edge including core-hole effects for Ru NPs, Ru single atoms including RuN4, RuC2N2 and RuC4. To reduce the interactions between the absorbing Ru atoms, we use a supercell with 16 Ru atoms for Ru metal with k-point mesh 6 x 8 x 4, and a 6 x 6 graphene supercell with different defects for Ru-CN nanostructures with k-point mesh 2 x 2 x 1. The kinetic energy cutoff of wavefunction is set at 50 Ry and that of charge is 400 Ry. A smearing of 4eV is chosen to reproduce the experimental spectra linewidth.

3.3.2 HER performance

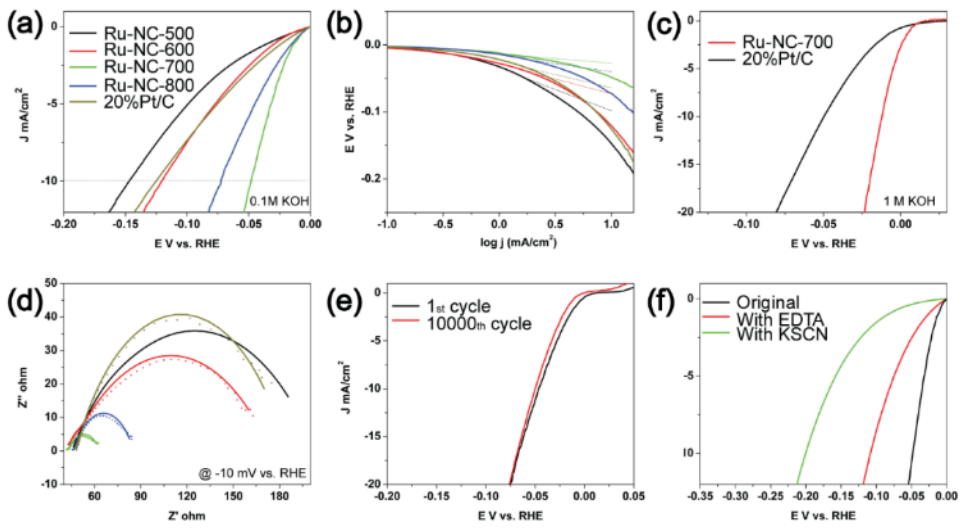

Figure 15 Electrochemical measurements. (a) Linear sweep voltammetry (LSV) curves of Ru-NC-T and commercial 20 wt% Pt/C in 0.1 M KOH. (b) Tafel plots of Ru-NC-T and 20% Pt/C. The legends are the same as those in figure 15(a). (c) LSV curves of Ru-NC-700 and 20% Pt/C in 1 M KOH. (d) Nyquist plots of Ru-NC-T and 20% Pt/C in 0.1 M KOH at -10 mV vs. RHE. The legends are the same as those in figure 15(a). Symbols are experimental data and solid curves are fits by Randles' equivalent circuit. (e) Stability test of Ru-NC-700 in 0.1 M KOH, before and after 10,000 cycles within the potential window of -0.05 V to +0.05 V vs RHE. (f) Catalysts poisoning experiment for Ru-NC-700 in 0.1 M KOH with the addition of 10 mM of EDTA (red curve) or 10 mM of KSCN (green curve).

Remarkably, in electrochemical measurements, the Ru-NC-T samples exhibited significant HER activity in alkaline media, in comparison to commercial Pt/C. From **figure 15a**, it can be seen that in 0.1 M KOH, with increasingly negative electrode potentials, all Ru-NC-T samples exhibited nonzero cathodic currents, signifying apparent HER activity, and the activity varied among the samples. For instance, η_{10}, an important parameter of the HER activity, can be identified at –146 mV for Ru-NC-500, –120 mV for Ru-NC-600, –47 mV for Ru-NC-700, and –72 mV for Ru-NC-800. Significantly, all but Ru-NC-500 showed an η_{10} that was even lower than that for commercial Pt/C (–125 mV, **table 7**). Consistent behaviors can be seen in the Tafel plots in **figure 15b**, where the Tafel slope was only 24 mV/dec for Ru-NC-800, 14 mV/dec for Ru-NC-700, 43 mV/dec for Ru-NC-600, and 64 mV/dec for Ru-NC-500, in comparison to 39 mV/dec for Pt/C. This suggests that Ru-NC-700 and Ru-NC-800

samples even outperformed Pt/C towards HER in alkaline media, with Ru-NC-700 standing out as the best sample among the series. In 1 M KOH (**figure 15c**), the enhancement, as compared to Pt/C, is even more pronounced, with an η_{10} of only –12 mV for Ru-NC-700, much better than that of Pt/C (–49 mV). In fact, to the best of our knowledge, the Ru-NC-700 sample outperforms any other Ru-based HER catalysts in basic media that have been reported in recent literatures (**table 8**). In addition, Ru-NC-700 also showed a remarkably high HER activity in acid, with a low η_{10} of –29 mV and Tafel slope = 28 mV/dec in 0.5 M H_2SO_4, as compared to –13 mV and 18 mV/dec for Pt/C (**figure 16**).

Sample	**R_{CT} (Ω)**	**Tafel slope (mV/dec)**	**η_{10} (mV)**
Ru-NC-500	154	64	–146
Ru-NC-600	129	43	–120
Ru-NC-700	20.7	14	–47
Ru-NC-800	38.6	24	–72
20%Pt/C	136	39	–125

Table 7. Summary of HER performances in 0.1 M KOH

catalyst	**catalyst loading (mg/cm^2)**	**Electrolyte solution**	**η_{10} (mV)**	**Reference**
Ru-NC-700 nanowires	0.2	0.1 M KOH	–47	this work
		1 M KOH	–12	
Ru@C_2N	0.285	1 M KOH	–17	*Nat Nanotechnol* 12, 441–446 (2017)
Pt-Ni nanowire	0.015	1 M KOH	–50~60	*Nat Commun* 8, 14580 (2017)
Pt-Ni alloy	~0.66	0.1 M KOH	–65	*Nat Commun* 8, 15131 (2017)
Ni_2P-Ru	0.28	1M KOH	–31	*J Am Chem Soc* 140, 2731-2734 (2018)
Ru/C_3N_4/C	0.2	0.1M KOH	–79	*J Am Chem Soc* 138, 16174–16181 (2016)
RuP2	1	1M KOH	–52	*Angew Chem Int Ed* 56, 11559-11564 (2017)
IrCo@NC	0.285	1M KOH	–45	*Adv Mater* 30, 1705324

				(2018)
RuCo@NC	0.275	1M KOH	–28	*Nat Commun* 8, 14969 (2017)
Ru/NC	0.013	1M KOH	-21	*J Mater Chem A, 2017, 5, 25314-25318*

Table 8. Comparison of HER performance with results in recent literatures

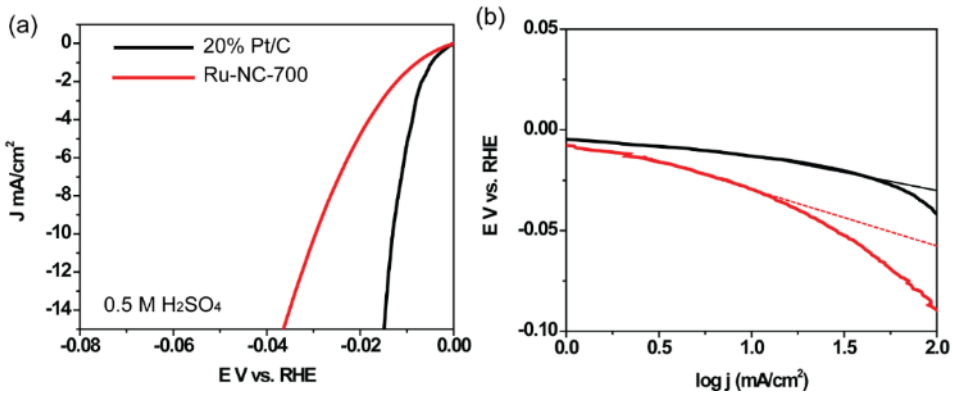

Figure 16. Electrochemical measurements in 0.5 M H_2SO_4. (a) LSV curves of Ru-NC-700 and Pt/C. Potential scan rate 10 mV/s. (b) Tafel plot of Ru-NC-700 and Pt/C, the legends are the same as (a). Dashed curves are linear fits of the Tafel regions.

The charge-transfer kinetics involved in HER were then examined by electrochemical impedance measurements. From the Nyquist plots acquired at 10 mV vs RHE (**figure 15d**), one can see that all samples exhibited a quasi-semicircle, where the diameter represents the corresponding charge-transfer resistance (R_{ct}). Interestingly, whereas R_{ct} of Ru-NC-500 (154 ohm) and Ru-NC-600 (129 ohm) was comparable to

that of commercial Pt/C (136 ohm), it was significantly lower for Ru-NC-700 (20.7 ohm) and Ru-NC-800 (38.6 ohm) (**table 7**), in good agreement with results from voltammetric measurements (**figure 15a**). The Ru-NC-700 catalysts also exhibited remarkable stability. From **figure 15e**, it can be seen that there was virtually no change of the HER polarization curves after 10,000 potential cycles.

As both Ru nanoparticles and ruthenium single atoms (likely in Ru-N/Ru-C) are present in the Ru-NC-T samples (**figure 1**), EDTA and KSCN were used as poisoning species to help differentiate their contributions. From **figure 15f**, one can see that with the addition of 10 mM KSCN, the η_{10} value shifted negatively by more than 150 mV, and the shift was much smaller (ca. 60 mV) when 10 mM EDTA was added to the solution. In fact, the HER performance of the EDTA-treated Ru-NC-700 sample was very similar to that with ruthenium nanoparticles deposited onto MF nanowires (RuNP/MF, $\eta_{10} = -124$ mV, **figure 17**). Note that SCN^- readily adsorbs onto both Ru nanoparticle surface and Ru-N/Ru-C sites, and EDTA forms coordination bonds predominantly with the latter. The different poisoning effect observed above by SCN^- and EDTA (**figure 15f**) suggests that whereas both Ru nanoparticles and Ru-N/Ru-C contributed to the HER activity, the latter likely played a dominant role. This is in sharp contrast with leading results in recent literatures where the HER activity was primarily attributed to ruthenium nanoparticles[18, 30, 31].

This is further supported by results from another control experiment (**figure 17**), where the amount of $RuCl_3$ added in sample synthesis was reduced to 1/8. The number of ruthenium nanoparticles in the resulting sample was diminished to about

1/30 of that for Ru-NC-700 (**figure 17b-c**), and XPS and XAS measurements showed a significant decrease of the Ru(0) fraction and an increase of the overall Ru oxidation states (**figure 17d-g**); yet, the HER performance (e.g., η_{10} = –50 mV) was almost identical to that of Ru-NC-700 (**figure 17a**). This implies only minimal contributions from ruthenium nanoparticles to the observed HER activity, and it is the ruthenium single atoms that dominated the HER performance (note that without the addition of $RuCl_3$, the resulting N-doped carbon nanowires, MF-700, essentially showed zero activity, **figure 17a**).

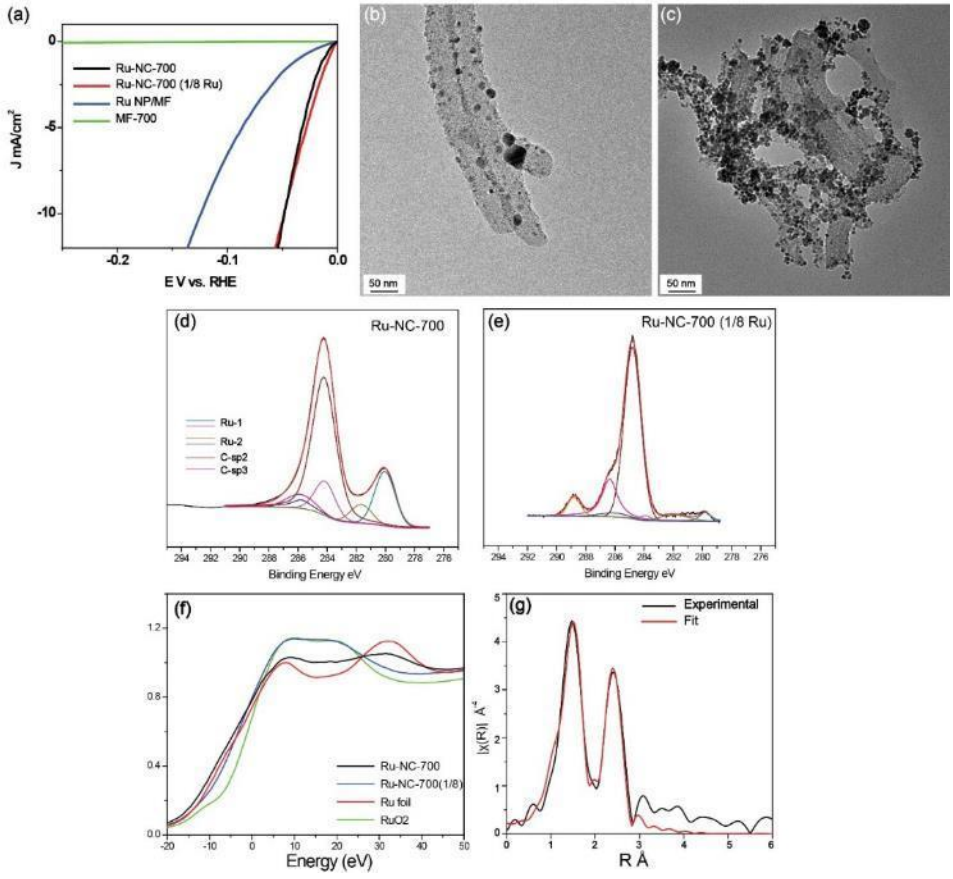

Figure 17. Control experiments with Ru-NC-700 (1/8) and Ru NP/MF. (a) LSV curve of Ru-NC-700, Ru-NC-700 (1/8 Ru), Ru NP/MF, and MF-700 at the same loading in 0.1 M KOH. Potential scan rate 10 mV/s. Representative TEM images of (b) Ru-NC-700 (1/8 Ru) and (c) Ru NP/MF. Scale bars are both 50 nm. (d) XPS of Ru-NC-700. (e) XPS of Ru-NC-700 with 1/8 Ru precursors. (f) XANES data for Ru-NC-700 and Ru-NC-700 (1/8). (g) EXAFS spectrum and its fit of Ru-NC-700 (1/8).

3.3.3 HER active sites

Results from the above experimental studies showed that Ru-N/Ru-C moieties (i.e., single atom sites) played a dominant role in the HER performance, while Ru nanoparticles made only minor contributions. To identify the chemical configurations of the Ru-N/Ru-C moieties, we examined and compared the hydrogen binding energy with a range of RuC_xN_y structures (x + y ″ 4) involving 2, 3 or 4 coordinates (**figure 19-20** and **table 9**)[28, 32, 51, 52]. Among these, the data points of select stable structures for H binding are shown in **figure 18,** and unstable configurations are labelled in red color in **table 9**. From **figure 18**, one can see that the optimal configurations are those located in the upper portion of the dark blue region that corresponds to a low formation energy, and close to zero $|\Delta G_{H^*}|$. It is interesting to note that whereas the RuN_4 moiety exhibits the lowest formation energy among the possible structural configurations of RuC_xN_{4-x} **(figure 19-20 and table 9-14**)[32, 51, 53], ca. 3 eV lower than

that of RuC_4 (**figure 18**), the large $|\Delta G_{H^*}|$ of the Ru and N sites suggest that neither of these is likely the catalytic active site (**figure 21**). By contrast, RuC2N2-1 (**figure 18**) represents the optimal structure for HER, featuring a relatively low formation energy and close to zero $|\Delta G_{H^*}|$ (< 0.2 eV) for both Ru and adjacent C, suggesting that both of these atomic sites might serve as the catalytic active sites (more discussion can be found under **figure 19 and 22**). For comparison, the ΔG_{H^*} was much higher at –0.5 to –0.6 eV for all facets of Ru nanoparticles[54]. This is consistent with the results presented above that atomically dispersed ruthenium was the dominant contributor to the observed HER activity, whereas only minimal contributions from ruthenium nanoparticles.

Table 9. Hydrogen binding free energy at various candidate active sites. The legends are the same as those in Figure 20. 'Transferred to P-Ru' means that H is transferred to P-Ru spontaneously during geometrical optimization.

Ru Coordination number	**Model**	**Candidate Active Site**	**Hydrogen binding free energy (eV)**
4	RuN4	P-Ru	-0.582943083
4	RuN4	1-N	transferred to P-Ru
4	RuN4	2-C	1.270275969
4	RuN4	3-C	1.013356014
4	RuC1N3	P-Ru	-0.703733128
4	RuC1N3	1-N	transferred to P-Ru

4	RuC1N3	2-N	0.97141363
4	RuC1N3	3-N	1.19205208
4	RuC1N3	4-C	transferred to P-Ru
4	RuC1N3	5-C	1.040701092
4	RuC1N3	6-C	1.083474449
4	RuC1N3	7-C	0.947660424
4	RuC1N3	8-C	1.124005844
4	RuC1N3	9-C	0.926125809
4	RuC1N3	10-C	0.959837379
4	RuC2N2-1	P-Ru	0.033324738
4	RuC2N2-1	1-N	1.109348832
4	RuC2N2-1	2-C	0.910202129
4	RuC2N2-1	3-C	1.303215362
4	RuC2N2-1	4-C (next to Ru)	0.151619207
4	RuC2N2-1	5-C	1.35433012
4	RuC2N2-2	P-Ru	-0.562833968
4	RuC2N2-2	1-N	0.875459835
4	RuC2N2-2	2-C	1.0208236
4	RuC2N2-2	3-C	0.932096317
4	RuC2N2-2	4-C	0.987377088
4	RuC2N2-2	5-C (next to Ru)	0.082477116
4	RuC2N2-3	P-Ru	-0.609100653

4	RuC2N2-3	1-N	0.9531818
4	RuC2N2-3	2-C	1.120259527
4	RuC2N2-3	3-C	1.11597711
4	RuC2N2-3	4-C	0.930818312
4	RuC2N2-3	5-C (next to Ru)	0.248898807
4	RuC2N2-3	6-C	1.034132029
4	RuC3N1	P-Ru	-0.505320715
4	RuC3N1	1-N	0.606394933
4	RuC3N1	2-C (next to Ru)	0.249474165
4	RuC3N1	3-C (next to Ru)	0.096627094
4	RuC3N1	4-C (next to Ru)	0.210464709
4	RuC3N1	5-C	1.033313894
4	RuC3N1	6-C	1.389703657
4	RuC3N1	7-C	1.351560007
4	RuC3N1	8-C	0.839902045
4	RuC3N1	9-C	1.429662348
4	RuC3N1	10-C	1.229403111
4	RuC4	P-Ru	0.38393673
4	RuC4	1-C (next to Ru)	0.243745845
4	RuC4	2-C	1.331248877
4	RuC4	3-C	1.54465848
3	RuN3	P-Ru	-0.679875991

3	RuN3	S-Ru	0.174130811
3	RuN3	1-N	transferred to P-Ru
3	RuN3	2-N	transferred to P-Ru
3	RuN3	3-N	transferred to P-Ru
3	RuN3	4-C	1.633488252
3	RuN3	5-C	1.032694415
3	RuN3	6-C	1.331064723
3	RuC1N2-1	P-Ru	-0.66372827
3	RuC1N2-1	S-Ru	-0.075077231
3	RuC1N2-1	1-C (next to Ru)	transferred to P-Ru
3	RuC1N2-1	2-N	1.155161478
3	RuC1N2-1	3-N	transferred to P-Ru
3	RuC1N2-1	4-C	0.971755881
3	RuC1N2-2	P-Ru	-0.638631289
3	RuC1N2-2	S-Ru	transferred to P-Ru
3	RuC1N2-2	1-N	transferred to P-Ru
3	RuC1N2-2	2-C (next to Ru)	transferred to P-Ru
3	RuC1N2-2	3-N	transferred to P-Ru
3	RuC1N2-3	P-Ru	-0.594901548
3	RuC1N2-3	S-Ru	transferred to P-Ru
3	RuC1N2-3	1-N	transferred to P-Ru
3	RuC1N2-3	2-N	transferred to P-Ru

3	RuC1N2-3	3-C (next to Ru)	transferred to P-Ru
3	RuC2N1-1	P-Ru	-0.447719616
3	RuC2N1-1	S-Ru	transferred to P-Ru
3	RuC2N1-1	1-N	0.639547772
3	RuC2N1-1	2-C (next to Ru)	transferred to P-Ru
3	RuC2N1-1	3-C (next to Ru)	transferred to P-Ru
3	RuC2N1-2	P-Ru	0.190764095
3	RuC2N1-2	S-Ru	0.167072966
3	RuC2N1-2	1-C (next to Ru)	0.157875539
3	RuC2N1-2	2-N	1.257627564
3	RuC2N1-2	3-C (next to Ru)	0.124481709
3	RuC2N1-3	P-Ru	-0.524735766
3	RuC2N1-3	S-Ru	transferred to P-Ru
3	RuC2N1-3	1-C (next to Ru)	-0.231514096
3	RuC2N1-3	2-C (next to Ru)	transferred to P-Ru
3	RuC2N1-3	3-N	0.590215326
3	RuC3	P-Ru	-0.1792363
3	RuC3	S-Ru	-0.089116372
3	RuC3	1-C (next to Ru)	0.049455235
3	RuC3	2-C (next to Ru)	0.04675622
3	RuC3	3-C (next to Ru)	transferred to P-Ru
2	RuN2	P-Ru	-0.722423256

2	RuN2	S-Ru	-0.300078452
2	RuN2	1-N	transferred to P-Ru
2	RuN2	2-C	1.549525339
2	RuN2	3-C	1.025811475
2	RuC1N1	P-Ru	-0.79196364
2	RuC1N1	S1-Ru	-0.18466765
2	RuC1N1	S2-Ru	transferred to P-Ru
2	RuC1N1	1-C (next to Ru)	transferred to P-Ru
2	RuC1N1	2-N	transferred to P-Ru
2	RuC2	P-Ru	-0.779528822
2	RuC2	S-Ru	transferred to P-Ru
2	RuC2	1-C (next to Ru)	transferred to P-Ru
2	RuN2-2	P-Ru	-0.519890686
2	RuN2-2	S-Ru	0.253072105
2	RuN2-2	1-N	transferred to P-Ru
2	RuN2-2	2-C	1.36172083
2	RuC1N1-2	P-Ru	-0.648603315
2	RuC1N1-2	S1-Ru	0.151241222
2	RuC1N1-2	S2-Ru	transferred to P-Ru
2	RuC1N1-2	1-C	transferred to P-Ru
2	RuC1N1-2	2-N	transferred to P-Ru
2	RuC2-2	P-Ru	-0.649165629

2	RuC2-2	S-Ru	transferred to P-Ru
2	RuC2-2	1-C (next to Ru)	transferred to P-Ru
N/A	N-Graphene	1-N	2.154131339
N/A	N-Graphene	2-C	1.070537906
N/A	N-Graphene	3-C	1.635290556

Table 10. Total energy, formation energy and solvation energy for various configurations.

Configuration	Total energy (eV)	Formation energy (eV)	Solvation (eV)
RuN4	-14053.88271	3.247309947	0.20206962
RuC1N3	-13934.9728	4.488247484	0.16350527
RuC2N2-1	-13816.71433	5.077748935	0.16350527
RuC2N2-2	-13816.21232	5.57975964	0.16350527
RuC2N2-3	-13816.44378	5.348291919	0.16350527
RuC3N1	-13698.07195	6.051154135	0.128220334
RuC4	-13579.73399	6.72014313	0.077945429
RuN3	-21830.68115	4.76550164	0.335250349
RuC1N2-1	-21711.82635	5.951330658	0.303315424
RuC1N2-2	-21712.55747	5.220210396	0.303315424
RuC1N2-3	-21711.9603	5.817383243	0.303315424
RuC2N1-1	-21593.88655	6.222157749	0.226661151
RuC2N1-2	-21593.87565	6.233056448	0.226661151
RuC2N1-3	-21593.57644	6.53226737	0.226661151
RuC3	-21475.47719	6.962544987	0.235213439
RuN2	-20821.07624	6.25112943	0.29231618
RuC1N1	-20703.06705	6.591348372	0.29231618
RuC2	-20584.72876	7.260671085	0.29231618

RuN2-2	-20680.27857	6.566522776	0.230167793
RuC1N1-2	-20562.16202	7.014099644	0.230167793
RuC2-2	-20443.96974	7.537415627	0.230167793
Graphene-N	-11373.10418	0.648133417	0.183929655

Table 11. Total energy of configuration with H binding, phonon energy and solvation energy for the active site candidates that bind H stably.

Ru Coordination number	Model	Active Site Candidate	Sites-H Total energy (eV)	Phonon (eV)	Solvation (eV)
4	RuN4	P-Ru	-14070.4849	0.194106971	0.174993926
4	RuN4	2-C	-14068.7693	0.326344503	0.180415417
4	RuN4	3-C	-14069.0263	0.326344503	0.180415417
4	RuC1N3	P-Ru	-13951.734	0.166932401	0.20181984
4	RuC1N3	2-N	-13950.1782	0.352093487	0.136053296
4	RuC1N3	3-N	-13949.9576	0.352093487	0.136053296
4	RuC1N3	5-C	-13950.1283	0.326344503	0.181138457
4	RuC1N3	6-C	-13950.0855	0.326344503	0.181138457
4	RuC1N3	7-C	-13950.2213	0.326344503	0.181138457
4	RuC1N3	8-C	-13950.045	0.326344503	0.181138457
4	RuC1N3	9-C	-13950.2429	0.326344503	0.181138457
4	RuC1N3	10-C	-13950.2092	0.326344503	0.181138457

4	RuC2N2-1	P-Ru	-13832.7385	0.166932401	0.20181984
4	RuC2N2-1	1-N	-13831.7818	0.352093487	0.136053296
4	RuC2N2-1	2-C	-13831.9921	0.326344503	0.172939105
4	RuC2N2-1	3-C	-13831.5991	0.326344503	0.172939105
4	RuC2N2-1	4-C (next to Ru)	-13832.74	0.307417048	0.181138457
4	RuC2N2-1	5-C	-13831.548	0.326344503	0.172939105
4	RuC2N2-2	P-Ru	-13832.8326	0.166932401	0.20181984
4	RuC2N2-2	1-N	-13831.5137	0.352093487	0.136053296
4	RuC2N2-2	2-C	-13831.3795	0.326344503	0.172939105
4	RuC2N2-2	3-C	-13831.4682	0.326344503	0.172939105
4	RuC2N2-2	4-C	-13831.4129	0.326344503	0.172939105
4	RuC2N2-2	5-C (next to Ru)	-13832.3071	0.307417048	0.181138457
4	RuC2N2-3	P-Ru	-13833.1103	0.166932401	0.20181984
4	RuC2N2-3	1-N	-13831.6675	0.352093487	0.136053296
4	RuC2N2-3	2-C	-13831.5115	0.326344503	0.172939105
4	RuC2N2-3	3-C	-13831.5158	0.326344503	0.172939105
4	RuC2N2-3	4-C	-13831.701	0.326344503	0.172939105
4	RuC2N2-3	5-C	-13832.3721	0.307417048	0.181138457

		(next to Ru)			
4	RuC2N2-3	6-C	-13831.5976	0.326344503	0.172939105
4	RuC3N1	P-Ru	-13714.6291	0.166932401	0.160896703
4	RuC3N1	1-N	-13713.6156	0.352093487	0.073998014
4	RuC3N1	2-C (next to Ru)	-13714.027	0.307417048	0.173092876
4	RuC3N1	3-C (next to Ru)	-13714.1798	0.307417048	0.173092876
4	RuC3N1	4-C (next to Ru)	-13714.066	0.307417048	0.173092876
4	RuC3N1	5-C	-13713.2621	0.326344503	0.173092876
4	RuC3N1	6-C	-13712.9057	0.326344503	0.173092876
4	RuC3N1	7-C	-13712.9438	0.326344503	0.173092876
4	RuC3N1	8-C	-13713.4555	0.326344503	0.173092876
4	RuC3N1	9-C	-13712.8657	0.326344503	0.173092876
4	RuC3N1	10-C	-13713.066	0.326344503	0.173092876
4	RuC4	P-Ru	-13595.4882	0.15078184	0.213056832
4	RuC4	1-C	-13595.7051	0.314131392	0.126477587

		(next to Ru)			
4	RuC4	2-C	-13594.6298	0.326344503	0.126477587
4	RuC4	3-C	-13594.4164	0.326344503	0.126477587
3	RuN3	P-Ru	-21847.3803	0.205576313	0.29675007
3	RuN3	S-Ru	-21846.6078	0.207182634	0.37662551
3	RuN3	4-C	-21845.2068	0.326344503	0.315834858
3	RuN3	5-C	-21845.8076	0.326344503	0.315834858
3	RuN3	6-C	-21845.5092	0.326344503	0.315834858
3	RuC1N2-1	P-Ru	-21728.5221	0.15078184	0.332371602
3	RuC1N2-1	S-Ru	-21727.9899	0.207182634	0.332371602
3	RuC1N2-1	2-N	-21726.7905	0.352093487	0.218317583
3	RuC1N2-1	4-C	-21726.9937	0.326344503	0.263878667
3	RuC1N2-2	P-Ru	-21729.2443	0.166932401	0.332371602
3	RuC1N2-3	P-Ru	-21728.6034	0.166932401	0.332371602
3	RuC2N1-1	P-Ru	-21610.483	0.166932401	0.356206262
3	RuC2N1-1	1-N	-21609.3843	0.352093487	0.159613935
3	RuC2N1-2	P-Ru	-21609.8336	0.166932401	0.356206262
3	RuC2N1-2	S-Ru	-21609.8843	0.207182634	0.34301345
3	RuC2N1-2	1-C (next to Ru)	-21609.9554	0.314131392	0.297967137

3	RuC2N1-2	2-N	-21608.7553	0.352093487	0.159613935
		3-C			
3	RuC2N1-2	(next to Ru)	-21609.9888	0.314131392	0.297967137
3	RuC2N1-3	P-Ru	-21610.2499	0.166932401	0.356206262
		1-C			
3	RuC2N1-3	(next to Ru)	-21610.0456	0.314131392	0.297967137
3	RuC2N1-3	3-N	-21609.1235	0.352093487	0.159613935
3	RuC3	P-Ru	-21491.722	0.15078184	0.297813969
3	RuC3	S-Ru	-21491.5601	0.219606873	0.157180457
		1-C			
3	RuC3	(next to Ru)	-21491.5544	0.303445414	0.206186346
		2-C			
3	RuC3	(next to Ru)	-21491.5571	0.303445414	0.206186346
2	RuN2	P-Ru	-20837.8146	0.205576313	0.250417096
2	RuN2	S-Ru	-20837.5044	0.207182634	0.361031572
2	RuN2	3-C	-20835.648	0.326344503	0.235069265
2	RuC1N1	P-Ru	-20836.1717	0.326344503	0.235069265
2	RuC1N1	S1-Ru	-20719.8363	0.166932401	0.250417096

2	RuC1N1	S2-Ru	-20719.3798	0.207182634	0.361031572
2	RuC2	S-Ru	-20601.4694	0.15078184	0.250417096
2	RuN2-2	S-Ru	-20696.997	0.205576313	0.370923384
2	RuN2-2	1-N	-20696.2257	0.207182634	0.370923384
2	RuC1N1-2	P-Ru	-20695.0382	0.326344503	0.235069265
2	RuC1N1-2	S1-Ru	-20578.9705	0.166932401	0.370923384
2	RuC1N1-2	S2-Ru	-20578.2109	0.207182634	0.370923384
2	RuC2-2	S-Ru	-20460.7627	0.15078184	0.370923384
N/A	N-doped graphene	1-N	-11386.9734	0.352093487	0.002929768
N/A	N-doped graphene	2-C	-11388.216	0.326344503	0.187725371
N/A	N-doped graphene	3-C	-11387.6512	0.326344503	0.187725371

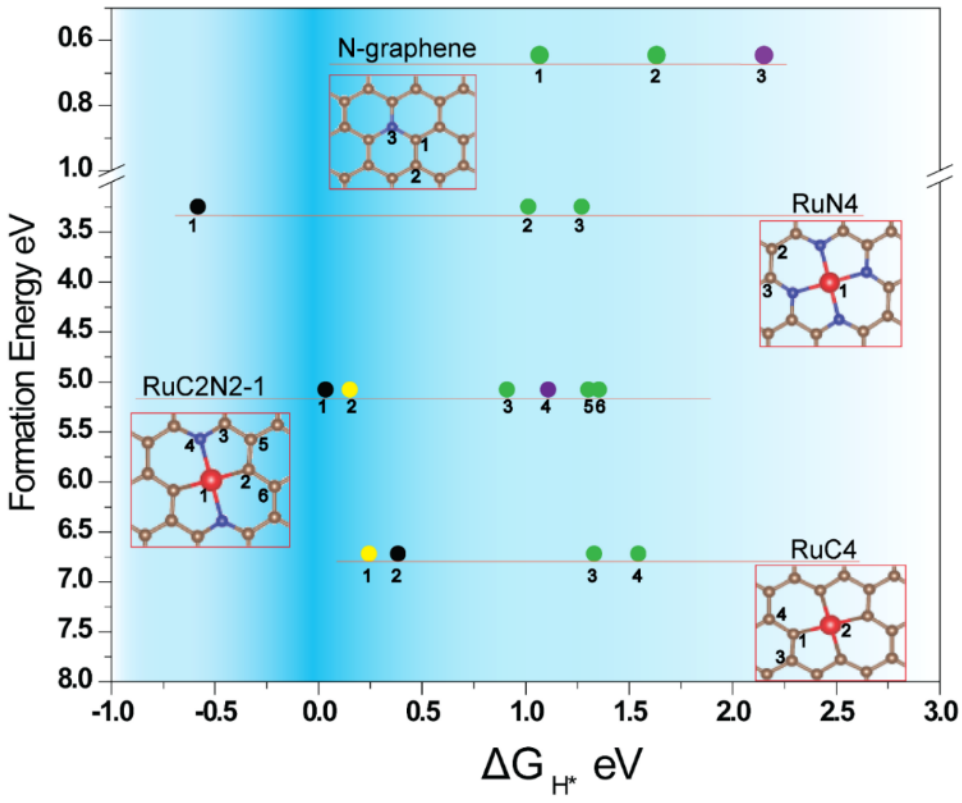

Figure 18. Energy diagram of different RuC_xN_y structures from first principles calculations. The X-axis is reaction free energy of hydrogen binding, the negative values indicate strong binding while positive values indicate weak binding. The dark blue range indicates the candidate active sites with the best activity. Y-axis is formation energy of each configuration, where a more positive value signifies a structure that is more difficult to form. The colors denote candidate active sites: H binds to ruthenium atom along the perpendicular direction to the plane (black), carbon atom next to the ruthenium (yellow), carbon atom next to nitrogen (green), or carbon atom far away from ruthenium and nitrogen atom (purple), respectively. The

note records the data point from certain structure, number records the possible active site. The version with complete RuC_xN_y configurations can be found in figure 19 and the structures can be found in figure 20.

From **Figure 18 and 19**, there are two points that warrant special attention here: (a) structural stability increases in the order of 2-coordinate< 3-coordinate< 4-coordinate; and (b) N-coordination leads to a lower formation energy than C-coordination. Note that whereas the RuN_4 moiety exhibits the lowest formation energy, ca. 3 eV lower than that of RuC_4, among the possible structural configurations of RuC_xN_{4-x}[32, 51, 55] the large | G_{H^*}| of the Ru and N sites suggest that it is unlikely the catalytic active site (**figure 21**).

However, one can see from **figure 18** that none of the RuN_4 sites is located in the dark blue region, where hydrogen adsorption free energy (ΔG_{H^*}) is close to 0 ($|\Delta G_{H^*}|$<0.5 eV), a condition favored for HER. For RuN_4, the Ru site shows a ΔG_{H^*} of –0.58 eV, suggesting strong binding of H such that hydrogen intermediates are difficult to remove from the catalyst surface, whereas H binding to the nitrogen sites of RuN_4 is not stable, and the neighboring carbons to the RuN_4 sites exhibit a very high ΔG_{H^*} of +1.0 to +1.3 eV, also energetically unfavorable for H binding. Meanwhile, this result also consistent with Choi et al.'s work, which agreed with that neither RuN4 nor RuC4 could be the active site.[55]

More favorable coordination configurations can be identified for HER from **figure 18**. First of all, when H binds to Ru in the 4-coordinated system of $RuC_{4-x}N_x$, H can only bind to Ru along the perpendicular direction (black) and the binding energy is

too negative for most of the configurations. However, for the undersaturated $RuC_{3-x}N_x$and $RuC_{2-x}N_x$ systems, the low-coordinated Ru affords space for H binding to Ru in an in-plane fashion (red), where the ΔG_{H^*} values are favorable for HER (the perpendicular and in-plan binding of H to Ru can be seen in **figure 22**). Second, the N sites can not only reduce the formation energy, but also stabilize in-plane H binding in the 2- and 3-coordinated systems, in particular, when H binds to the vacancy site opposite to N (e.g., S1 in RuC1N1-1 and RuC1N1-2 verses S2 in RuC1N1-1 and RuC1N1-2) (**figure 20** and **table 9**). Interestingly, it is unlikely that N is the active site, because it either binds H too weakly or cannot have stable binding (purple). Third, it can be seen that some carbons adjacent to Ru may have good activity (yellow). However, such active sites are stable only when the coordination number is 3 or 4, e.g., RuC2N2-1, RuC2N2-2, and RuC1N2-1, but not for the 2-coordinate systems. Other C sites show only weak H binding and are unlikely to be the HER active sites (green). Lastly, for Ru-free nitrogen-doped graphene (**figure 18**), it can be seen that both the N and C sites bind H too weakly, corresponding to low HER activity, in good agreement with experimental results (**figure 17**). In summary, for Ru,N-codoped carbons, the HER active sites are most likely the Ru atoms and/or adjacent C atoms.

From the candidate active sites (green in **table 9**), one can see that some even exhibit a binding energy close to zero, indicating that such configurations might contribute significantly to the high HER performance observed experimentally (**figure 15**). Among these, we can see that RuC2N2-1(**figure 18**) represents the optimal structure

for high HER activity, considering a combination of low formation energy and close to zero ΔG_{H^*}. Notably, in a recent study[54], ΔG_{H^*} was estimated to be –0.5 to –0.6 eV for all facets of Ru nanoparticles, which is much less favorable for HER than the active sites of RuC_xN_y structures discussed above where $|\Delta G_{H^*}| < 0.2$ eV (**figure 18).**

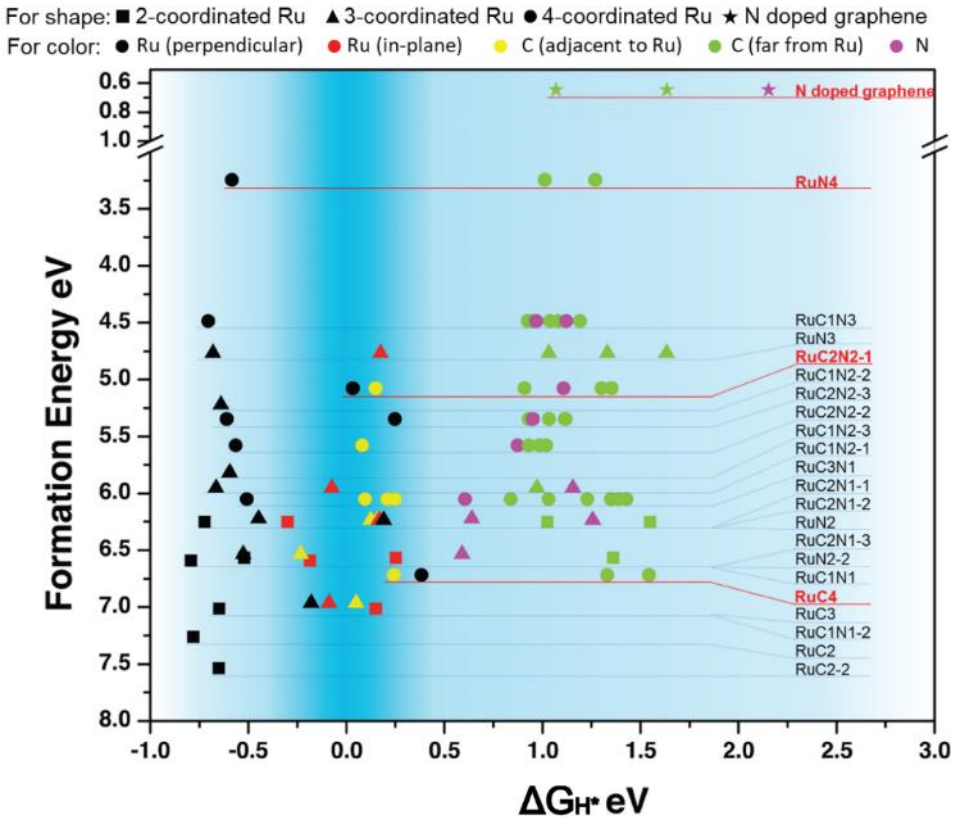

Figure 19. Energy diagram from first principles calculations of all possible RuC_xN_y structures depicted in Figure 20. The X-axis is reaction free energy of hydrogen binding, the negative values indicate strong binding while positive values indicate weak binding. The dark blue range indicates the candidate active sites with the best activity. Y-axis is formation energy of each configuration, where a more

positive value signifies a structure that is more difficult to form. The square, triangle and circle symbols represent the 2-coordinate, 3-coordinate and 4-coordinate structures, while star represents the nitrogen doped carbon. The colors denote candidate active sites: H binds to ruthenium atom along the perpendicular direction to the plane (black), in the plane (red), carbon atom next to the ruthenium (yellow), carbon atom next to nitrogen (green), or carbon atom far away from ruthenium and nitrogen atom (purple), respectively.

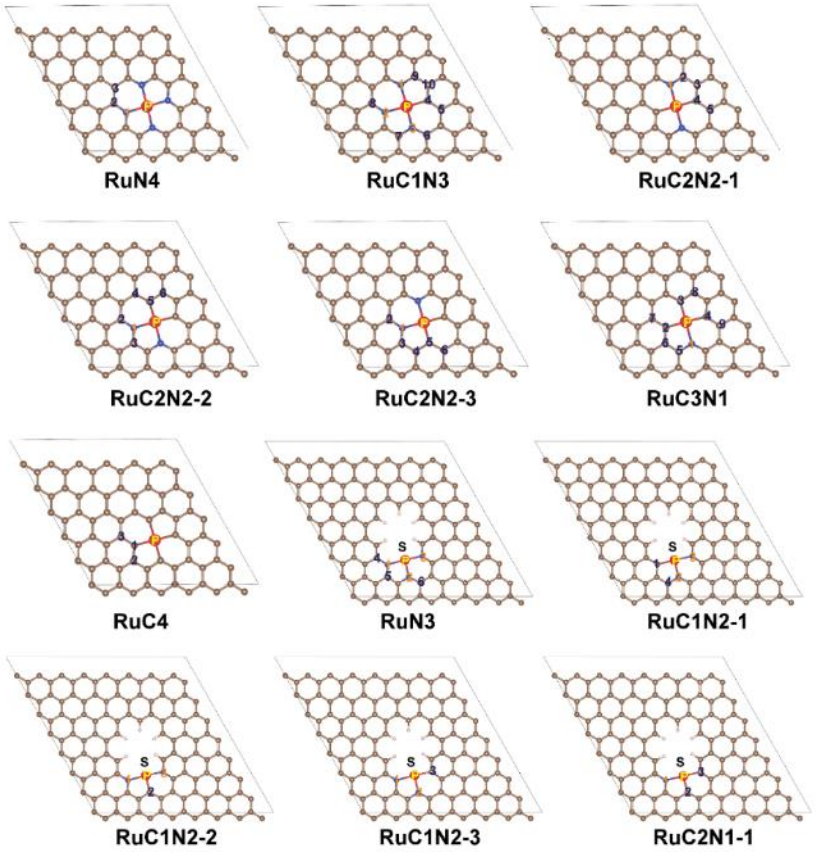

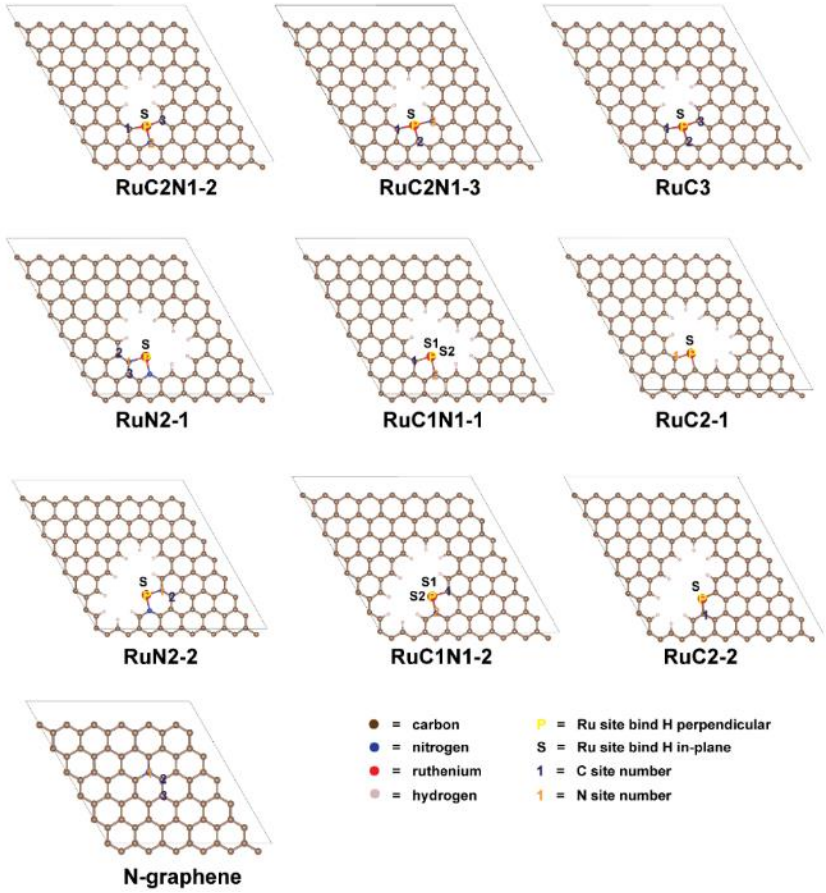

Figure 20. Computational models of Ru-N/Ru-C moieties.

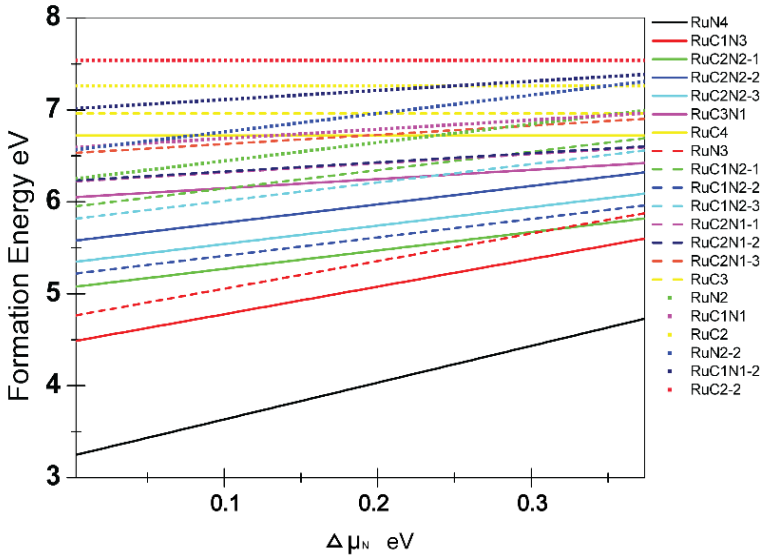

Figure 21. Formation energies of different Ru-N/Ru-C moieties as a function of N elemental chemical potentials. The range of N chemical potentials is from N in N_2 (N rich) to N in melamine (N poor).

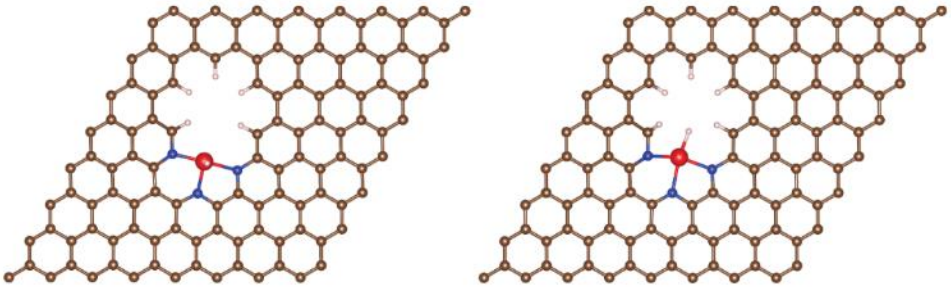

Figure 22. Optimized geometric structures of RuN3-P and RuN3-S. RuN3-P and RuN3-S refer to H binding to Ru in a perpendicular and in-plane configuration, respectively.

In addition, in previous studies[6, 13, 30], it has shown that the water dissociation process (Volmer reaction, step 1) is the rate-determining step for HER in alkaline media

(**figure 6**). Therefore, understanding the reaction pathway and kinetic barriers is critical for uncovering the reaction mechanism. We computed the reaction barrier and transition state of the water dissociation step through the CI-NEB method[34], as shown in **Figure 23**. Two possible pathways from the Volmer's step are identified, with hydrogen binding to ruthenium or the carbons adjacent to ruthenium, respectively. The corresponding reaction barriers along the configuration coordinates are shown in **figure 24**. In the initial state, after geometric optimization, the oxygen atom of H_2O points to ruthenium at a distance of 2.29Å (**figure 6a**). Then, in pathway 1, oxygen binds to the ruthenium atom, and one of the O-H bonds becomes elongated from 0.98 Å to 1.39Å, as a transition state that has an energy 0.90 eV higher than the initial state (**figure 6b**). After entropy correction, zero-point energy correction, and solvation energy correction[56], this pathway shows an energy barrier of 0.68 eV referenced to bulk water(details in **table 12-13**). Finally, the OH group settles onto the Ru atom, while H binds to an adjacent carbon atom (**figure 6c**). This structure shows an energy 0.18 eV higher than that of the initial state, indicating that pathway 1 is slightly unfavorable for H binding. In pathway 2, oxygen approaches the ruthenium site, and one of the hydrogen atoms also turns to bind. This transition state is shown in **figure 6d**. The total energy is 0.88 eV higher than that of the initial state; after corrections, the reaction barrier is only 0.59 eV, suggesting a favorable process for HER. Consistently, with OH and H binding to the same ruthenium site, the final state (**figure 6e**) is –0.23 eV lower than that of the initial state, indicative of favorable of H binding. Taken together, we can see that these two pathways exhibit similar reaction

barriers and hence similar kinetic rates, and both the ruthenium and neighboring carbon most likely serve as the active sites, consistent with results from calculations discussed above. Remarkably, the reaction barrier of the structure is comparable to results in previous studies with Pt single atom catalysts (0.5-0.8 eV),but lower than that for Pt nanoparticles (0.8-1.0 eV)[30, 57], indicating competitive HER activity by such carbon-based catalysts, as manifested in experimental studies. We also computed the grand free energy under cathodic condition at a constant negative electrochemical potential along with the implicit solvation model[57] (see the computational method section for details). We found neither the barriers nor the reaction energies varied appreciably ($< \sim 0.1$ eV), as compared to the results obtained under the constant charge condition (**table 14**), and the optimized geometry remained virtually identical.

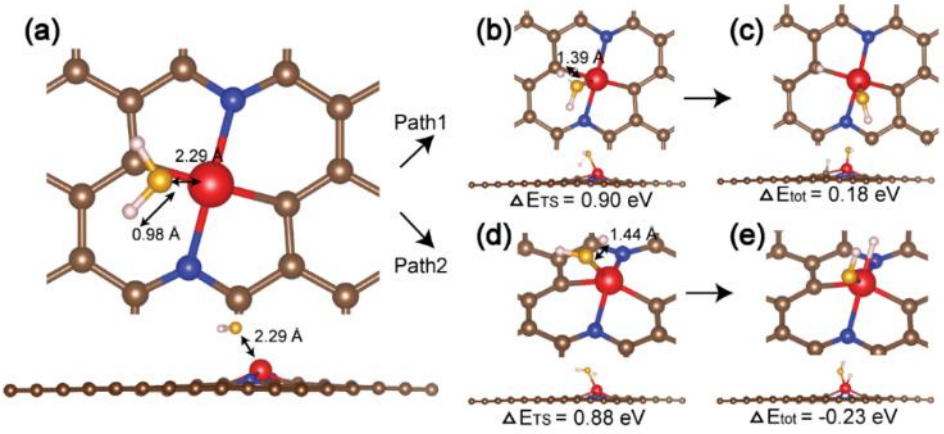

Figure 23. Reaction barriers and reaction pathways of Volmer's step at the RuC2N2-1 structure calculated by the CI-NEB method. Note that the values in

Fig.6 are before solvation and entropy corrections to the free energies. Top view and side view of (a) initial state, (b, c) transition state and final state of reaction pathway 1, (d, e) transition state and final state of reaction pathway 2. The brown, blue, red, yellow and white sphere represent C, N, Ru, O and H atoms, respectively.

	Total energy (eV)	**Solvation (eV)**	**Phonon (eV, 298K)**	**A(H_2O) (eV)**
Bare surface	-13820.76847	0.17839527	0	
Transition state	-14292.21325	0.103716834	0.540467398	
H_2O	-471.6674915			0.012411
Barrier	0.676089643			

Table 12. Correction of energy barrier of pathway-1

	Total energy (eV)	**Solvation (eV)**	**Phonon (eV, 298K)**	**A(H_2O) eV**
Bare surface	-13820.76847	0.17839527	0	
Transition state	-14292.22949	0.091087131	0.484105673	
H_2O	-471.6674915			0.012411

Barrier 0.590852615

Table 13. Correction of energy barrier of pathway-2 A(H_2O) is (free energy-total energy) of one water, including the entropy of rotation, translation, and vibration, and solvation energy of liquid water

	potential at -10 mV		**potential not considered**	
	Barrier eV	**Reaction Energy eV**	**Barrier eV**	**Reaction energy eV**
Path1	0.94	0.25	0.9	0.18
Path2	1.05	-0.06	0.88	-0.23

Table 14 Result of constant potential calculation of barrier and reaction energy in

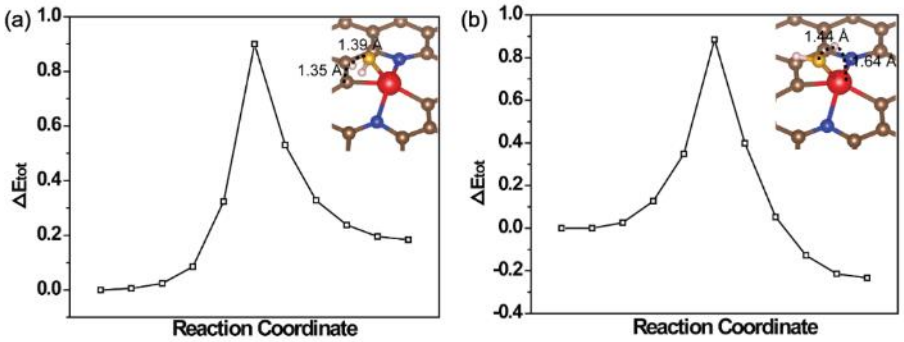

Figure 24. Water dissociation barrier for (a) reaction pathway-1 and (b) reaction pathway-2. The insets are the structure of the corresponding transition state. The colors of elements are: brown for C, blue for N, red for Ru, yellow for O and white for H.

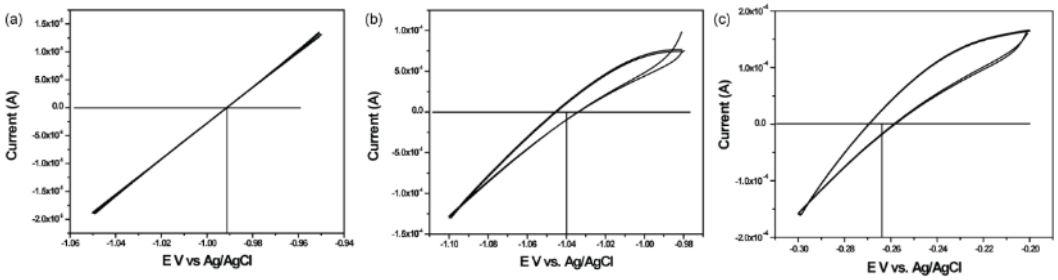

Figure 25. Calibration of Ag/AgCl reference electrode in (a) 0.1 M KOH, (b) 1 M KOH, and (c) 0.5 M H_2SO_4. Potential scan rate 1 mV/s.

3.4 Discussion about Ru single atom embedded in C3N4 for hydrogen evolution

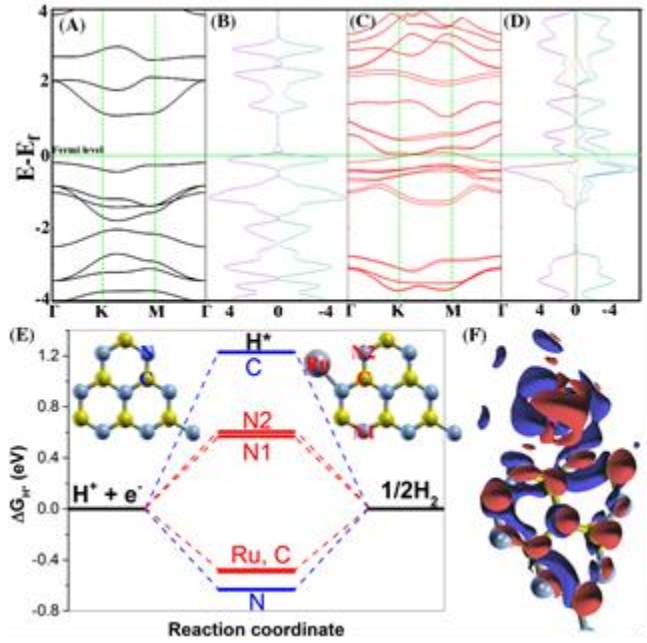

Figure 26. (A) Band structures and (B) projected density of states of C3N4. (C) Band structures and (D) projected density of states of C3N4-Ru. Contributions of Ru 4d and 5s orbitals to the PDOS are labeled. (E) Calculated Gibbs free-energy (ΔG_{H*}) of HER at the equilibrium potential for C3N4 (blue) and C3N4-Ru (red) at various bonding sites as labeled in the panel inset. (F) Schematic of interfacial charge transfer in C3N4-Ru. Red signals are positive charge and blue signals are negative charge.

DFT calculations were conducted to examine the effect of the incorporation of ruthenium ions into the C3N4 matrix on the band structures and Gibbs free energy of hydrogen adsorption and reduction. 2 × 2 cells of C3N4 and C3N4-Ru were used for the calculations (Figure 27), where a ruthenium ion was bonded to two nitrogen sites, as suggested by experimental results. The calculated band structure of C3N4 (Figure

26A) suggests an indirect band gap of about 1.3 eV, which is in good agreement with results from previous studies.[58, 59] In contrast with the semiconducting nature of C3N4, the band structure of C3N4-Ru (Figure 26B) shows no band gap, most probably because the embedment of ruthenium ions into the C3N4 matrix caused a charge transfer between C3N4 and ruthenium ions, as observed in XPS measurments.[60] This may also explain the quenching of C3N4 photoluminescence. In addition, PDOS calculations also show an apparent band gap for C3N4 while it vanished for C3N4-Ru (Figure 26C). Obviously, the incorporation of ruthenium ions into C3N4 led to redistribution of the electrons, the crossing of the Fermi level with the conduction band, and hence enhanced charge mobility and electrical conductivity, consistent with electrochemical impedance measurements. These are critical in the determination of the electrocatalytic activity.[61-63]

Notably, HER typically involves a three-state process, an initial H+ state, an intermediate H* state, and ½H2 state as the final product (Figure 26D), and the Gibbs free-energy of the formation of the intermediate H* state, $|\Delta G_H^*|$, can be used as the descriptor of the HER performance for different electrocatalysts.[64] For an ideal HER electrocatalyst, $|\Delta G_{H^*}|$ should be zero. In the present study, C3N4 was found to exhibit a Gibbs free energy of $\Delta G_{CH}^* = +1.16$ eV and $\Delta G_{NH}^* = -0.74$ eV for the labeled carbon and nitrogen bonding sites (Figure 26D inset), respectively. This suggests that pyridinic nitrogen possessed much better HER activity than the carbon site. When ruthenium ions were incorporated into the C3N4 matrix, interestingly, the Gibbs free-energy of these labeled bonding sites becomes $\Delta G_{CH^*} = -0.49$ eV, ΔG_{N1H^*}

= +0.57 eV, ΔG_{N2H*} = +0.56 eV and ΔG_{RuH*} = −0.56 eV. Obviously, the $|\Delta G_{H*}|$ values all diminished, suggesting that all the label sites in C3N4-Ru are more active than the counterparts in C3N4. From these studies, one can see that the incorporation of ruthenium ions into C3N4 molecular skeletons drastically enhanced the electrical conductivity, and facilitated the adsorption of hydrogen to various binding sites in the composites, where the formation of Ru-N moieties played a critical role in enhancing the HER performance (Figure 28-30).

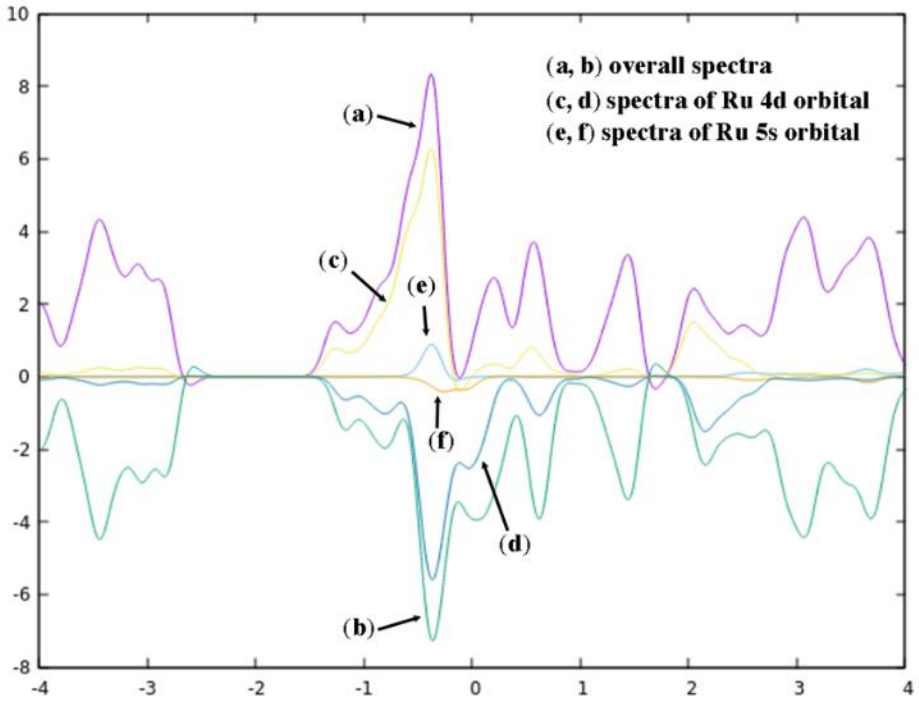

Figure 27. Projected density of state of C3N4-Ru with specific contributions from Ru 4d and 5s orbitals. x: E-EFermi, y: DOS(States/eV/cell)

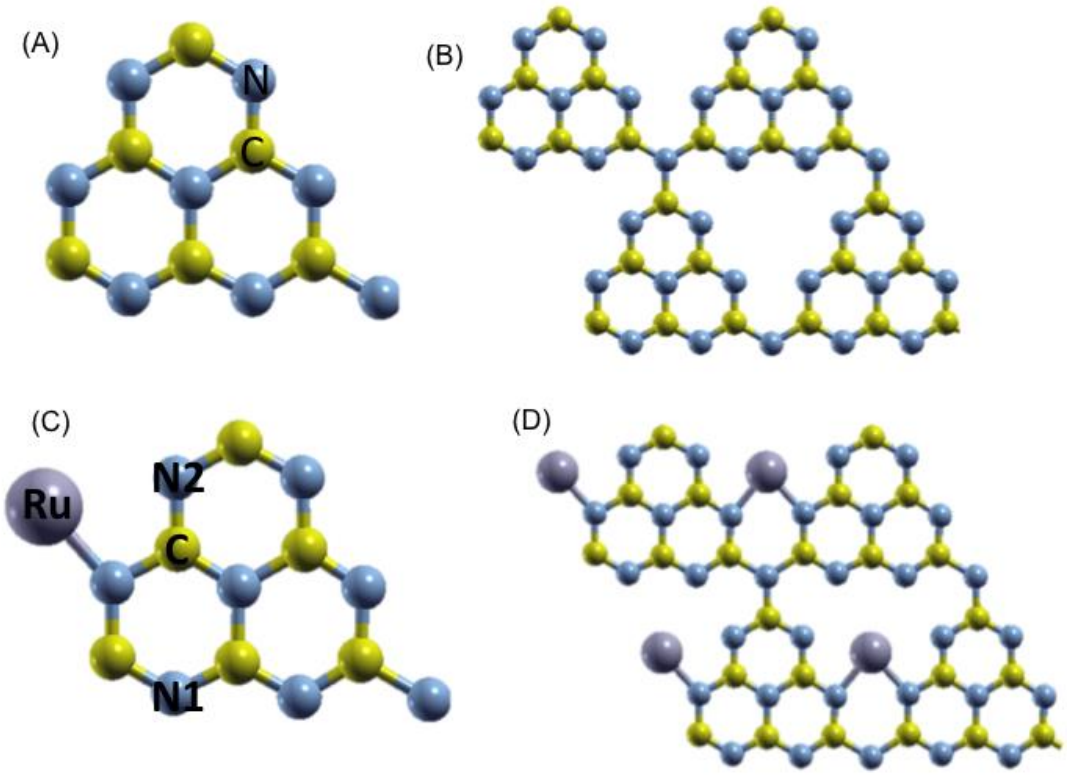

Figure 28. (A) 1×1 and (B) 2×2 cell structures of C3N4. (C) 1×1 and (D) 2×2 cell structures of C3N4-Ru. In these cell structures, the labeled atoms are the active sites candidates to calculate the Gibbs free-energy (ΔG_{H^*}).

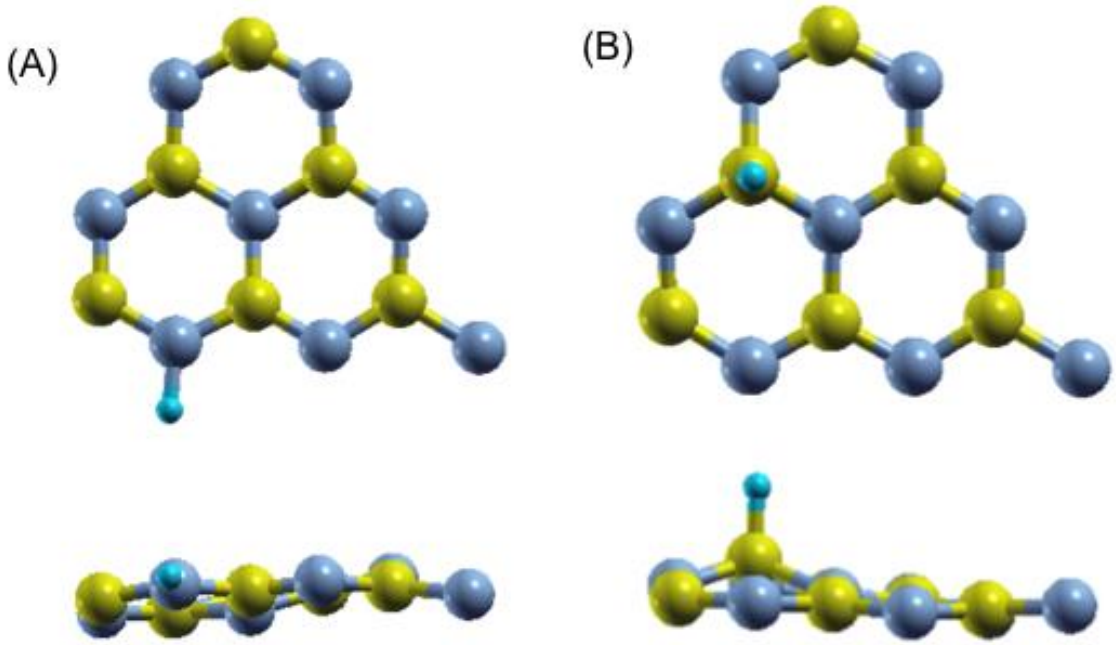

Figure 29. Stable hydrogen adsorption on (A) N and (B) C of C3N4 after relax

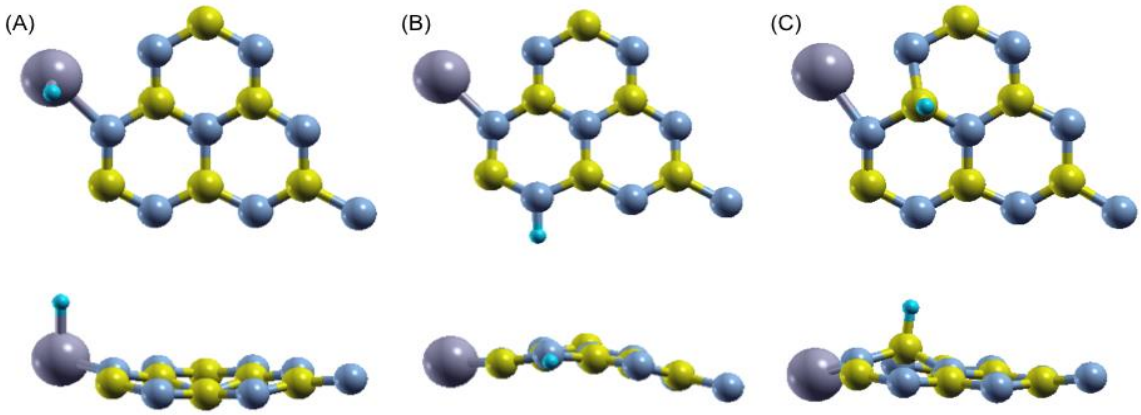

calculation. Tops are topic view and bottoms are side view.

Figure 30. Stable hydrogen adsorption on labeled (A) Ru, (B) N, and (C) C of C3N4-Ru after relaxing calculations. Tops are topic view and bottoms are side view.

3.5 Conclusion

In summary, Ru,N-codoped carbon nanowires outperforms commercial platinum towards HER in alkaline media. The remarkable performance is ascribed to the formation of RuC_xN_y moieties, where the ruthenium centers as well as the C sites likely serve as the HER active centers, with hydrogen binding facilitated by the coordinating nitrogen sites. By contrast, contributions from ruthenium nanoparticles are minor. Results from this study can be exploited for the rational design and engineering of ruthenium-based single atom catalysts towards HER in alkaline media. In addition, this study highlights the significance of structural characterization at the atomic scale in unraveling the mechanistic origin of metal, nitrogen-codoped carbons in electrocatalytic reactions. Similarly, the Ru-N configuration in Ru single atom-C3N4 structure have obvious HER activity. The Ru can be active sites, and also activate the nitrogen atoms in C3N4 structure.

3.6 Experimental section

Chemicals

Sodium tellurite (Na_2TeO_3, 99.5%, Alfa Aesar), melamine (99% Acros Organics), hydrazine hydrate (N_2H_4, 64% v/v, Acros Organics), polyvinylpyrrolidone (PVP, K30, USB), sodium hydroxide (NaOH, Fisher Scientific), formaldehyde (37% v/v, Acros Organics), ammonia (NH_3, 35% in water, Acros Organics), ruthenium chloride ($RuCl_3$, Strem Chemicals) and Pt/C (20 wt%, Alfa Aesar) were used as received

without further purification. Water was supplied from a Barnstead Nanopure Water System (18.3 MΩ cm).

Synthesis of Te nanowires. Te NWs were prepared by a literature procedure.[65] Typically, 0.18 g of Na_2TeO_3 and 2 g of PVP were dissolved in 66 mL of Nanopure water under vigorous stirring to form a homogeneous solution, into which was then injected 6.7 mL of NH_3 and 3.3 mL of N_2H_4. The solution was transferred to a 100 mL Teflon-lined autoclave container and heated at 180 °C for 3 h. The autoclave was then cooled down naturally, and the solution was stored in a 4 °C refrigerator.

Synthesis of Te NW-melamine formaldehyde polymer core-sheath nanofibers (Te-MF). The preparation of Te-MF has been described previously.[42] In brief, 10 mL of Te NWs was centrifuged at 3000 rpm for 2 min with the addition of acetone as a sinking agent. After washing by water and ethanol for 3 times, Te NWs were dispersed in 10 mL of water. Separately, 0.126 g of melamine in 10 mL of water was added into a 50 mL round-bottom flask, and the solution was heated at 90 °C under magnetic stirring, into which were then injected the Te NWs solution, 20 μL of 0.2 M NaOH, and 0.53 mL of formaldehyde. The solution was heated at 90 °C for 7 h before being cooled down naturally. The product was collected by centrifugation at 5000 rpm for 5 min, washed with water and ethanol, and dried in a vacuum chamber for 24 h.

Synthesis of ruthenium and nitrogen co-doped carbon nanowires. In a typical experiment, 50 mg of Te-MF was dissolved into 30 mL of ethanol under magnetic stirring at 350 rpm and heated at 50 °C, into which was then added 40 mg of $RuCl_3$.

The color of the solution was found to change from blue to brown. The reaction was run overnight, and the solids were collected by centrifugation and vacuum-dried. The product (Ru-MF) was placed in a tube furnace and heated at a controlled temperature (500, 600, 700 and 800 °C) for 3 h at a heating rate of 5°C/min. The nitrogen flow was maintained at 200 cc/min. The sample was denoted as Ru-NC-T with T = 500, 600, 700 or 800.

For the control experiment, 5 mg of $RuCl_3$ (1/8 of the amount used for the synthesis of the above Ru-NC-T samples) was added instead while other conditions were kept the same, and the pyrolysis was carried out at 700 °C. This sample was referred to as Ru-NC-700 (1/8 Ru). In another control experiment, 5 mg of $RuCl_3$ was reduced by an excess amount of $NaBH_4$ in the presence of 10 mg of MF-700 under vigorous stirring overnight, where MF-700 was prepared by pyrolysis of Te-MF at 700 °C. The resulting sample was denoted as Ru NP/MF.

Characterization

Transmission electron microscopy (TEM) measurements were carried out with a FEI Talos F200X high-resolution transmission electron microscope. Double aberration-corrected high-angle annular dark field-scanning transmission electron microscopic (HAADF-STEM) measurements were carried out with a modified FEI Tiatan microscope (TEAM0.5) operated at 300 KV with a HAADF detector. The STEM probe semi-angle is 30mrad, at a spatial resolution of 0.05 nm. Electron energy lose spectra (EELS) were acquired with a Nion U-HERMS200 microscope operated at 60 kV. Half convergence angle was set at 20 mrad, and a current was set at 150 pA with

dispersion of 0.166 eV/channel. The total integral time for spectral collection was 200 s. X-ray diffraction (XRD) studies were performed with a SmartLab 9KW X-ray diffraction system. Raman spectra were collected with a Thermo Electron Corporation DXR Microscope. X-ray photoelectron spectra (XPS) were acquired with a PHI-5702 XPS instrument.

X-ray absorption spectroscopy

Powder samples were measured in X-ray fluorescence mode with a ruthenium foil reference. Ru K-edge EXAFS data were collected from the CLS@APS (Sector 20-BM) beamline at the Advanced Photon Source (operated at 7.0 GeV) in Argonne National Laboratory.All EXAFS measurements were conducted at room temperature under ambient pressure. EXAFS data were normalized and then transformed into k- and R-space using the Athena program and fitted with the Artemis program with conventional procedures[66]. A k weighting of 3, k-range of 2.5–13.0 $Å^{-1}$ and a R-range of 1.4-2.8 Å was used for all the FT-EXAFS fitting analysis. In the fitting both the σ^2 and the E_0 values of the two paths were correlated to minimize the number of independent variables to ensure a reliable fitting.

Electrochemistry

Electrochemical measurements were carried out with a CHI 710 electrochemical workstation in a conventional three-electrode configuration. A Ag/AgCl electrode in 0.1 M KCl was used as the reference electrode and a graphite rod as the counter electrode. The reference electrode was calibrated against a reversible hydrogen electrode (RHE, **figure 25**) and all potentials in the present study were referred to this

RHE. To prepare catalyst inks, 4 mg of the catalysts obtained above was added into 1 mL of ethanol, 10 L of nafion solution under sonication to form a homogeneous solution. 10 L of the inks was then dropcast on a clean glassy carbon disk electrode (surface area 0.196 cm^2) at a loading of 0.20 mg/cm^2. Electrochemical impedance measurements were carried out with a Gamry Reference 600 instrument. IR-compensation was set at 85% of solution resistance in all measurements.

Computational method

Computations were carried out with an open source planewave code Quantum ESPRESSO[67]. A two-dimensional carbon matrix supercell was built on a 6 x 6 unit cell for a 4-coordinating Ru/N/C system and an 8 x 8 unit cell for other calculations. The vacuum was set as 14 Å to avoid periodic image interactions. The ultrasoft pseudopotential[68] was adopted with kinetic and charge density cutoff at 40, and 240 Ry, respectively. A 2 x 2 x 1 Monkhorst-Pack K-point grid was sampled for the supercell. The total energy was converged to the accuracy of 1 meV per atom. The Marzari Vanderbilt smearing[69] was adopted with the smearing parameter at 0.01 Ry. The electronic energy was converged to 10^{-8} Ry and the total force was converged to 10^{-4}a.u. Spin polarized calculations were considered for all systems. Density function perturbation theory (DFPT)[70] was employed to calculate the phonon frequency as inputs for entropy and zero-point energy (ZPE). The implicit solvation energy correction was applied with a newly developed solvation model (CANDLE)[71] that has been shown to be suitable for various surfaces, with the open source code JDFTx[72, 73]. The energy barrier calculation was carried out by climbing-image nudged elastic band

(CI-NEB) method[34]. The Van Der Waals correction was applied for the images with Grimme's D2 scheme[74, 75]. The calculation of XANES was performed using the XSpectra code[76] in the Quantum Espresso package. The X-ray absorption cross section is described by Fermi's Golden rule in the single particle approximation with all-electron wavefunctions. The all-electron wavefunctions are reconstructed in the framework of projected augmented wave from solutions of isolated atoms. Two projectors of each quantum number l were included in PAW to properly reconstruct the all-electron wavefunctions. The final-state effect is included by generating a half-hole or a complete hole in the core of PAW. The spin-orbit coupling in final states (bands near Fermi levels) is neglected. The constant potential calculation is performed to obtain the grand free energy at the constant electrochemical potential along with the implicit solvation model, where the charged surfaces can be effectively screened by the ionic response in solution as implemented in JDFTx. Constant potential calculation was carried out at 0.01 V vs RHE at pH = 14[56, 77].

The free energy of hydrogen binding is calculated by $\Delta G_{H^*} = \Delta E + \Delta TS - \Delta ZPE + \Delta E_{sol}$, where ΔE is the total energy difference, ΔTS is the entropy difference, ΔZPE is the zero-point energy difference and ΔE_{sol} is the solvation energy difference. The formation energy is calculated by $E_{formation} = E_{total} - \Sigma n_i \mu_i$, where n is the number of atom i, μ is the chemical potential of atom i. In this case, i can be carbon, nitrogen, ruthenium or hydrogen. The original raw data is shown in table 10 and table 11.

3.7 Reference

1. Morales-Guio, C. G.; Stern, L. A.; Hu, X. L., Nanostructured hydrotreating catalysts for electrochemical hydrogen evolution. *Chem. Soc. Rev.* **2014,** *43* (18), 6555-6569.

2. Staszak-Jirkovský, J.; Malliakas, C. D.; Lopes, P. P.; Danilovic, N.; Kota, S. S.; Chang, K.-C.; Genorio, B.; Strmcnik, D.; Stamenkovic, V. R.; Kanatzidis, M. G., Design of active and stable Co–Mo–S x chalcogels as pH-universal catalysts for the hydrogen evolution reaction. *Nat. Mater.* **2016,** *15* (2), 197.

3. Chen, L.; Dong, X.; Wang, Y.; Xia, Y., Separating hydrogen and oxygen evolution in alkaline water electrolysis using nickel hydroxide. *Nat. Commun.* **2016,** *7*, 11741.

4. Seitz, L. C.; Dickens, C. F.; Nishio, K.; Hikita, Y.; Montoya, J.; Doyle, A.; Kirk, C.; Vojvodic, A.; Hwang, H. Y.; Norskov, J. K., A highly active and stable IrOx/SrIrO3 catalyst for the oxygen evolution reaction. *Science* **2016,** *353* (6303), 1011-1014.

5. Strmcnik, D.; Lopes, P. P.; Genorio, B.; Stamenkovic, V. R.; Markovic, N. M., Design principles for hydrogen evolution reaction catalyst materials. *Nano Energy* **2016,** *29*, 29-36.

6. Subbaraman, R.; Tripkovic, D.; Strmcnik, D.; Chang, K.-C.; Uchimura, M.; Paulikas, A. P.; Stamenkovic, V.; Markovic, N. M., Enhancing Hydrogen Evolution

Activity in Water Splitting by Tailoring Li+-Ni(OH)2-Pt Interfaces. *Science* **2011,** *334* (6060), 1256-1260.

7. Xue, Y. R.; Huang, B. L.; Yi, Y. P.; Guo, Y.; Zuo, Z. C.; Li, Y. J.; Jia, Z. Y.; Liu, H. B.; Li, Y. L., Anchoring zero valence single atoms of nickel and iron on graphdiyne for hydrogen evolution. *Nat. Commun.* **2018,** *9*.

8. Fang, Z.; Peng, L.; Qian, Y.; Zhang, X.; Xie, Y.; Cha, J. J.; Yu, G., Dual Tuning of Ni–Co–A (A= P, Se, O) Nanosheets by Anion Substitution and Holey Engineering for Efficient Hydrogen Evolution. *J. Am. Chem. Soc.* **2018,** *140* (15), 5241-5247.

9. Feng, J. X.; Wu, J. Q.; Tong, Y. X.; Li, G. R., Efficient Hydrogen Evolution on Cu Nanodots-Decorated Ni3S2 Nanotubes by Optimizing Atomic Hydrogen Adsorption and Desorption. *J. Am. Chem. Soc.* **2018,** *140* (2), 610-617.

10. Tang, M. H.; Hahn, C.; Klobuchar, A. J.; Ng, J. W. D.; Wellendorff, J.; Bligaard, T.; Jaramillo, T. F., Nickel–silver alloy electrocatalysts for hydrogen evolution and oxidation in an alkaline electrolyte. *Phys. Chem. Chem. Phys.* **2014,** *16* (36), 19250-19257.

11. Sheng, W.; Myint, M.; Chen, J. G.; Yan, Y., Correlating the hydrogen evolution reaction activity in alkaline electrolytes with the hydrogen binding energy on monometallic surfaces. *Energy Environ. Sci.* **2013,** *6* (5), 1509-1512.

12. Zheng, Y.; Jiao, Y.; Qiao, S.; Vasileff, A., Hydrogen Evolution Reaction in Alkaline Solution: From Theory, Single Crystal Models, to Practical Electrocatalysts. *Angew. Chem. Int. Ed.* **2017,** *57* (26), 7568-7579.

13. Durst, J.; Siebel, A.; Simon, C.; Hasche, F.; Herranz, J.; Gasteiger, H., New insights into the electrochemical hydrogen oxidation and evolution reaction mechanism. *Energy Environ. Sci.* **2014,** *7* (7), 2255-2260.

14. Liu, L.; Jiang, Z. Q.; Fang, L.; Xu, H. T.; Zhang, H. J.; Gu, X.; Wang, Y., Probing the Crystal Plane Effect of Co3O4 for Enhanced Electrocatalytic Performance toward Efficient Overall Water Splitting. *ACS Appl. Mater. Interface* **2017,** *9* (33), 27736-27744.

15. Ma, Q. Y.; Hu, C. Y.; Liu, K. L.; Hung, S. F.; Ou, D. H.; Chen, H. M.; Fu, G.; Zheng, N. F., Identifying the electrocatalytic sites of nickel disulfide in alkaline hydrogen evolution reaction. *Nano Energy* **2017,** *41*, 148-153.

16. Liu, T. T.; Ma, X.; Liu, D. N.; Hao, S.; Du, G.; Ma, Y. J.; Asiri, A. M.; Sun, X. P.; Chen, L., Mn Doping of CoP Nanosheets Array: An Efficient Electrocatalyst for Hydrogen Evolution Reaction with Enhanced Activity at All pH Values. *ACS Catal.* **2017,** *7* (1), 98-102.

17. Sun, H. M.; Xu, X. B.; Yan, Z. H.; Chen, X.; Cheng, F. Y.; Weiss, P. S.; Chen, J., Porous Multishelled Ni2P Hollow Microspheres as an Active Electrocatalyst for Hydrogen and Oxygen Evolution. *Chem. Mater.* **2017,** *29* (19), 8539-8547.

18. Mahmood, J.; Li, F.; Jung, S. M.; Okyay, M. S.; Ahmad, I.; Kim, S. J.; Park, N.; Jeong, H. Y.; Baek, J. B., An efficient and pH-universal ruthenium-based catalyst for the hydrogen evolution reaction. *Nat. Nanotechnol.* **2017,** *12* (5), 441-446.

19. Zhu, L. L.; Lin, H. P.; Li, Y. Y.; Liao, F.; Lifshitz, Y.; Sheng, M. Q.; Lee, S. T.; Shao, M. W., A rhodium/silicon co-electrocatalyst design concept to surpass platinum hydrogen evolution activity at high overpotentials. *Nat. Commun.* **2016,** *7*.

20. Bhowmik, T.; Kundu, M. K.; Barman, S., Palladium Nanoparticle–Graphitic Carbon Nitride Porous Synergistic Catalyst for Hydrogen Evolution/Oxidation Reactions over a Broad Range of pH and Correlation of Its Catalytic Activity with Measured Hydrogen Binding Energy. *ACS Catal.* **2016,** *6* (3), 1929-1941.

21. Jiang, P.; Chen, J. T.; Wang, C. L.; Yang, K.; Gong, S. P.; Liu, S.; Lin, Z. Y.; Li, M. S.; Xia, G. L.; Yang, Y.; Su, J. W.; Chen, Q. W., Tuning the Activity of Carbon for Electrocatalytic Hydrogen Evolution via an Iridium-Cobalt Alloy Core Encapsulated in Nitrogen-Doped Carbon Cages. *Adv Mater* **2018,** *30* (9).

22. Demir, E.; Akbayrak, S.; Onal, A. M.; Ozkar, S., Nanoceria-Supported Ruthenium(0) Nanoparticles: Highly Active and Stable Catalysts for Hydrogen Evolution from Water. *Acs Applied Materials & Interfaces* **2018,** *10* (7), 6299-6308.

23. Xu, Y.; Yin, S. L.; Li, C. J.; Deng, K.; Xue, H. R.; Li, X. N.; Wang, H. J.; Wang, L., Low-ruthenium-content NiRu nanoalloys encapsulated in nitrogen-doped carbon as highly efficient and pH-universal electrocatalysts for the hydrogen evolution reaction. *J Mater Chem A* **2018,** *6* (4), 1376-1381.

24. Drouet, S.; Creus, J.; Colliere, V.; Amiens, C.; Garcia-Anton, J.; Sala, X.; Philippot, K., A porous Ru nanomaterial as an efficient electrocatalyst for the hydrogen evolution reaction under acidic and neutral conditions. *Chemical Communications* **2017,** *53* (85), 11713-11716.

25. Liu, Y.; Liu, S. L.; Wang, Y.; Zhang, Q. H.; Gu, L.; Zhao, S. C.; Xu, D. D.; Li, Y. F.; Bao, J. C.; Dai, Z. H., Ru Modulation Effects in the Synthesis of Unique Rod-like Ni@Ni2P-Ru Heterostructures and Their Remarkable Electrocatalytic Hydrogen Evolution Performance. *Journal of the American Chemical Society* **2018,** *140* (8), 2731-2734.

26. Zhang, L.; Xiong, K.; Chen, S. G.; Li, L.; Deng, Z. H.; Wei, Z. D., In situ growth of ruthenium oxide-nickel oxide nanorod arrays on nickel foam as a binder-free integrated cathode for hydrogen evolution. *Journal of Power Sources* **2015,** *274*, 114-120.

27. Peng, Y.; Lu, B. Z.; Chen, L. M.; Wang, N.; Lu, J. E.; Ping, Y.; Chen, S. W., Hydrogen evolution reaction catalyzed by ruthenium ion-complexed graphitic carbon nitride nanosheets (2017). *J. Mater. Chem. A* **2017,** *5* (36), 19499-19499.

28. Peng, Y.; Pan, W. Z.; Wang, N.; Lu, J. E.; Chen, S. W., Ruthenium Ion-Complexed Graphitic Carbon Nitride Nanosheets Supported on Reduced Graphene Oxide as High-Performance Catalysts for Electrochemical Hydrogen Evolution. *Chemsuschem* **2018,** *11* (1), 130-136.

29. Weidong, L.; Yuan, L.; Min, W.; Xiaolei, F.; T., R. S. A.; Yuan, S.; Xue, Y.; Tanglue, F.; Kaifeng, W.; Zhongyi, L.; Baojun, L.; Zhimin, C.; S., T. J.; Siyu, L.; Bai, Y., Carbon-Quantum-Dots-Loaded Ruthenium Nanoparticles as an Efficient Electrocatalyst for Hydrogen Production in Alkaline Media. *Adv. Mater. 0* (0), 1800676.

30. Zheng, Y.; Jiao, Y.; Zhu, Y. H.; Li, L. H.; Han, Y.; Chen, Y.; Jaroniec, M.; Qiao, S. Z., High Electrocatalytic Hydrogen Evolution Activity of an Anomalous Ruthenium Catalyst. *J. Am. Chem. Soc.* **2016,** *138* (49), 16174-16181.

31. Wang, J.; Wei, Z. Z.; Mao, S. J.; Li, H. R.; Wang, Y., Highly uniform Ru nanoparticles over N-doped carbon: pH and temperature-universal hydrogen release from water reduction. *Energy Environ. Sci.* **2018,** *11* (4), 800-806.

32. Zhang, J.; Liu, P.; Wang, G.; Zhang, P.; Zhuang, X.; Chen, M.; Weidinger, I.; Feng, X., Ruthenium/nitrogen-doped carbon as an electrocatalyst for efficient hydrogen evolution in alkaline solution. *J. Mater. Chem. A* **2017,** *5* (48), 25314-25318.

33. Yang, J.; Chen, B.; Liu, X.; Liu, W.; Li, Z.; Dong, J.; Chen, W.; Yan, W.; Yao, T.; Duan, X., Phosphorus Nitride Imide Nanotube as Carbon-free Support to Anchor Single Ru Sites for Efficient and Robust Hydrogen Evolution. *Angew. Chem. Int. Ed.* **2018,** *57* (30), 9495-9500.

34. Henkelman, G.; Jónsson, H., Improved tangent estimate in the nudged elastic band method for finding minimum energy paths and saddle points. *J. Chem. Phys.* **2000,** *113* (22), 9978-9985.

35. Fajin, J. L. C.; Bruix, A.; Cordeiro, M. N. D. S.; Gomes, J. R. B.; Illas, F., Density functional theory model study of size and structure effects on water dissociation by platinum nanoparticles. *J. Chem. Phys.* **2012,** *137* (3).

36. Song, L.-T.; Wu, Z.-Y.; Liang, H.-W.; Zhou, F.; Yu, Z.-Y.; Xu, L.; Pan, Z.; Yu, S.-H., Macroscopic-scale synthesis of nitrogen-doped carbon nanofiber

aerogels by template-directed hydrothermal carbonization of nitrogen-containing carbohydrates. *Nano Energy* **2016,** *19*, 117-127.

37. Xu, J.; Wang, Z.-H.; Li, H.-H.; Liu, J.-W.; Yu, S.-H., Templating synthesis of ternary PtPdTe nanowires with tunable diameter for methanol electrooxidation. *CrystEngComm* **2016,** *18* (22), 4038-4041.

38. Wang, J. L.; Liu, J. W.; Lu, B. Z.; Lu, Y. R.; Ge, J.; Wu, Z. Y.; Wang, Z. H.; Arshad, M. N.; Yu, S. H., Recycling nanowire templates for multiplex templating synthesis: a green and sustainable strategy. *Chem. Eur. J.* **2015,** *21* (13), 4935-4939.

39. Yang, Y.; Wang, K.; Liang, H.-W.; Liu, G.-Q.; Feng, M.; Xu, L.; Liu, J.-W.; Wang, J.-L.; Yu, S.-H., A new generation of alloyed/multimetal chalcogenide nanowires by chemical transformation. *Sci. Adv.* **2015,** *1* (10), e1500714.

40. Zheng, F.; Yang, Y.; Chen, Q., High lithium anodic performance of highly nitrogen-doped porous carbon prepared from a metal-organic framework. *Nat. Commun.* **2014,** *5*, 5261.

41. Zhang, J.; Qu, L.; Shi, G.; Liu, J.; Chen, J.; Dai, L., N, P-Codoped Carbon Networks as Efficient Metal-free Bifunctional Catalysts for Oxygen Reduction and Hydrogen Evolution Reactions. *Angew. Chem. Int. Ed.* **2016,** *55* (6), 2230-2234.

42. Lu, B.; Smart, T. J.; Qin, D.; Lu, J. E.; Wang, N.; Chen, L.; Peng, Y.; Ping, Y.; Chen, S., Nitrogen and Iron-Codoped Carbon Hollow Nanotubules as High-Performance Catalysts toward Oxygen Reduction Reaction: A Combined Experimental and Theoretical Study. *Chem. Mater.* **2017,** *29* (13), 5617-5628.

43. Durig, J. R.; Omura, Y.; Mercer, E. E., Far infrared and raman spectra and structure of ruthenium halogenoammine complexes. *J. Mol. Struct.* **1975,** *29* (1), 53-63.

44. Zhou, Z.; Zhang, H.; Zhou, Y.; Qiao, H.; Gurung, A.; Naderi, R.; Elbohy, H.; Smirnova, A. L.; Lu, H.; Chen, S., Binder Free Hierarchical Mesoporous Carbon Foam for High Performance Lithium Ion Battery. *Sci. Rep.* **2017,** *7* (1), 1440.

45. Adeniyi, A. A.; Ajibade, P. A., Exploring the Ruthenium-Ligands Bond and Their Relative Properties at Different Computational Methods. *J. Chem.* **2016,** *2016*.

46. Zhang, W.; Zhao, H.; Wang, L., The Simple Cubic Structure of Ruthenium Clusters. *J. Phys. Chem. B* **2004,** *108* (7), 2140-2147.

47. Kumara, L.; Sakata, O.; Kohara, S.; Yang, A.; Song, C.; Kusada, K.; Kobayashi, H.; Kitagawa, H., Origin of the catalytic activity of face-centered-cubic ruthenium nanoparticles determined from an atomic-scale structure. *Phys. Chem. Chem. Phys.* **2016,** *18* (44), 30622-30629.

48. Frenkel, A. I., Solving the structure of nanoparticles by multiple-scattering EXAFS analysis. *J. Synchrotron Radiat.* **1999,** *6* (3), 293-295.

49. Frenkel, A. I.; Yevick, A.; Cooper, C.; Vasic, R., Modeling the structure and composition of nanoparticles by extended X-ray absorption fine-structure spectroscopy. *Annu. Rev. Anal. Chem.* **2011,** *4*, 23-39.

50. Liu, F.; Zhang, P., Tailoring the local structure and electronic property of AuPd nanoparticles by selecting capping molecules. *Appl. Phys. Lett.* **2010,** *96* (4), 043105.

51. Zhang, C. H.; Sha, J. W.; Fei, H. L.; Liu, M. J.; Yazdi, S.; Zhang, J. B.; Zhong, Q. F.; Zou, X. L.; Zhao, N. Q.; Yu, H. S.; Jiang, Z.; Ringe, E.; Yakobson, B. I.; Dong, J. C.; Chen, D. L.; Tour, J. M., Single-Atomic Ruthenium Catalytic Sites on Nitrogen-Doped Graphene for Oxygen Reduction Reaction in Acidic Medium. *ACS Nano* **2017,** *11* (7), 6930-6941.

52. Wang, X.; Chen, W.; Zhang, L.; Yao, T.; Liu, W.; Lin, Y.; Ju, H.; Dong, J.; Zheng, L.; Yan, W.; Zheng, X.; Li, Z.; Wang, X.; Yang, J.; He, D.; Wang, Y.; Deng, Z.; Wu, Y.; Li, Y., Uncoordinated Amine Groups of Metal–Organic Frameworks to Anchor Single Ru Sites as Chemoselective Catalysts toward the Hydrogenation of Quinoline. *J. Am. Chem. Soc.* **2017,** *139* (28), 9419-9422.

53. Dai, L. M.; Xue, Y. H.; Qu, L. T.; Choi, H. J.; Baek, J. B., Metal-Free Catalysts for Oxygen Reduction Reaction. *Chem Rev* **2015,** *115* (11), 4823-4892.

54. Li, Y.; Zhang, L. A.; Qin, Y.; Chu, F.; Kong, Y.; Tao, Y.; Li, Y.; Bu, Y.; Ding, D.; Liu, M., Crystallinity Dependence of Ruthenium Nanocatalyst toward Hydrogen Evolution Reaction. *ACS Catal.* **2018**, 5714-5720.

55. Choi, W. I.; Wood, B. C.; Schwegler, E.; Ogitsu, T., Combinatorial Search for High-Activity Hydrogen Catalysts Based on Transition-Metal-Embedded Graphitic Carbons. *Adv. Energy Mater.* **2015,** *5* (23), 1501423.

56. Ping, Y.; Nielsen, R. J.; Goddard, W. A., The Reaction Mechanism with Free Energy Barriers at Constant Potentials for the Oxygen Evolution Reaction at the IrO2 (110) Surface. *J Am Chem Soc* **2017,** *139* (1), 149-155.

57. Cheng, N.; Stambula, S.; Wang, D.; Banis, M. N.; Liu, J.; Riese, A.; Xiao, B.; Li, R.; Sham, T.-K.; Liu, L.-M., Platinum single-atom and cluster catalysis of the hydrogen evolution reaction. *Nat. Commun.* **2016,** *7*, 13638.

58. Li, X. R.; Dai, Y.; Ma, Y. D.; Han, S. H.; Huang, B. B., Graphene/g-C3N4 bilayer: considerable band gap opening and effective band structure engineering. *Phys Chem Chem Phys* **2014,** *16* (9), 4230-4235.

59. Wang, X. C.; Maeda, K.; Thomas, A.; Takanabe, K.; Xin, G.; Carlsson, J. M.; Domen, K.; Antonietti, M., A metal-free polymeric photocatalyst for hydrogen production from water under visible light. *Nature Materials* **2009,** *8* (1), 76-80.

60. Zuo, H.-W.; Lu, C.-H.; Ren, Y.-R.; Li, Y.; Zhang, Y.-F.; Chen, W.-K., Pt 4 Clusters Supported on Monolayer Graphitic Carbon Nitride Sheets for Oxygen Adsorption: A First-Principles Study. *Acta Phys Chim Sin* **2016,** *32* (5), 1183-1190.

61. Zheng, Y.; Jiao, Y.; Zhu, Y.; Li, L. H.; Han, Y.; Chen, Y.; Du, A.; Jaroniec, M.; Qiao, S. Z., Hydrogen evolution by a metal-free electrocatalyst. *Nat. Commun.* **2014,** *5*, 3783.

62. Li, H.; Tsai, C.; Koh, A. L.; Cai, L. L.; Contryman, A. W.; Fragapane, A. H.; Zhao, J. H.; Han, H. S.; Manoharan, H. C.; Abild-Pedersen, F.; Norskov, J. K.; Zheng, X. L., Activating and optimizing MoS2 basal planes for hydrogen evolution through the formation of strained sulphur vacancies. *Nature Materials* **2016,** *15* (1), 48-+.

63. Huang, Z. F.; Song, J. J.; Li, K.; Tahir, M.; Wang, Y. T.; Pan, L.; Wang, L.; Zhang, X. W.; Zou, J. J., Hollow Cobalt-Based Bimetallic Sulfide Polyhedra for

Efficient All-pH-Value Electrochemical and Photocatalytic Hydrogen Evolution. *Journal of the American Chemical Society* **2016,** *138* (4), 1359-1365.

64. Norskov, J. K.; Bligaard, T.; Logadottir, A.; Kitchin, J. R.; Chen, J. G.; Pandelov, S.; Norskov, J. K., Trends in the exchange current for hydrogen evolution. *J Electrochem Soc* **2005,** *152* (3), J23-J26.

65. Qian, H.-S.; Yu, S.-H.; Gong, J.-Y.; Luo, L.-B.; Fei, L.-f., High-Quality Luminescent Tellurium Nanowires of Several Nanometers in Diameter and High Aspect Ratio Synthesized by a Poly (Vinyl Pyrrolidone)-Assisted Hydrothermal Process. *Langmuir* **2006,** *22* (8), 3830-3835.

66. Ravel, B.; Newville, M., ATHENA, ARTEMIS, HEPHAESTUS: data analysis for X-ray absorption spectroscopy using IFEFFIT. *Journal of Synchrotron Radiation* **2005,** *12*, 537-541.

67. Giannozzi, P.; Baroni, S.; Bonini, N.; Calandra, M.; Car, R.; Cavazzoni, C.; Ceresoli, D.; Chiarotti, G. L.; Cococcioni, M.; Dabo, I., QUANTUM ESPRESSO: a modular and open-source software project for quantum simulations of materials. *J. Phys. Condens. Matter* **2009,** *21* (39), 395502.

68. Garrity, K. F.; Bennett, J. W.; Rabe, K. M.; Vanderbilt, D., Pseudopotentials for high-throughput DFT calculations. *Comput. Mater. Sci.* **2014,** *81*, 446-452.

69. Marzari, N.; Vanderbilt, D.; De Vita, A.; Payne, M., Thermal contraction and disordering of the Al (110) surface. *Phys. Rev. Lett.* **1999,** *82* (16), 3296.

70. Baroni, S.; De Gironcoli, S.; Dal Corso, A.; Giannozzi, P., Phonons and related crystal properties from density-functional perturbation theory. *Rev. Mod. Phys.* **2001,** *73* (2), 515.

71. Sundararaman, R.; Goddard III, W. A., The charge-asymmetric nonlocally determined local-electric (CANDLE) solvation model. *J. Chem. Phys.* **2015,** *142* (6), 064107.

72. Petrosyan, S.; Briere, J.-F.; Roundy, D.; Arias, T., Joint density-functional theory for electronic structure of solvated systems. *Phys. Rev. B* **2007,** *75* (20), 205105.

73. Ping, Y.; Sundararaman, R.; Goddard III, W. A., Solvation effects on the band edge positions of photocatalysts from first principles. *Phys. Chem. Chem. Phys.* **2015,** *17* (45), 30499-30509.

74. Stefan, G., Semiempirical GGA-type density functional constructed with a long-range dispersion correction. *J. Comput. Chem.* **2006,** *27* (15), 1787-1799.

75. Vincenzo, B.; Maurizio, C.; Daniel, F.; Michele, P.; Mauro, S.; Andrea, V., Role and effective treatment of dispersive forces in materials: Polyethylene and graphite crystals as test cases. *J. Comput. Chem.* **2009,** *30* (6), 934-939.

76. Gougoussis, C.; Calandra, M.; Seitsonen, A. P.; Mauri, F., First-principles calculations of x-ray absorption in a scheme based on ultrasoft pseudopotentials: From α-quartz to high-T c compounds. *Phys. Rev. B* **2009,** *80* (7), 075102.

77. Sundararaman, R.; GoddardIII, W. A.; Arias, T. A., Grand canonical electronic density-functional theory: Algorithms and applications to electrochemistry. *J. Chem. Phys.* **2017,** *146* (11), 114104.

Chapter 4 Pt and PtCo few atom clusters for oxygen reduction reaction

4.1 abstract

Oxygen reduction reaction (ORR) plays an important role in dictating the performance of various electrochemical energy technologies. As platinum nanoparticles have served as the catalysts of choice towards ORR, minimizing the cost of the catalysts by diminishing the platinum nanoparticle size has become a critical route to advancing the technological development. Herein, first-principles calculations show that carbon-supported Pt_9 clusters represent the threshold domain size, and the ORR activity can be significantly improved by doping of adjacent cobalt atoms. This is confirmed experimentally, where platinum and cobalt are dispersed in nitrogen-doped carbon nanowires in varied forms, single atoms, few-atom clusters and nanoparticles, depending on the initial feeds. The sample consisting primarily of $Pt_{2\sim7}$ clusters doped with atomic Co species exhibits the best mass activity among the series, with a current density of 4.16 $A\,mg_{Pt}^{-1}$ at +0.85 V vs RHE that is almost 50 times higher than that of commercial Pt/C.

4.2 introduction

Oxygen reduction reaction (ORR) is an important process for a range of electrochemical energy technologies, such as fuel cells and metal-air batteries [1-3]. Currently Pt nanoparticles (Pt NPs) are the catalyst of choice towards ORR (state-of-the-art Pt/C catalysts ca. 3 nm in diameter [4]), which account for over 50% of the total device cost and significantly hamper the widespread commercialization of the technologies [5]. There are two leading strategies to reduce the catalyst cost. One is to develop platinum-free alternatives, such as heteroatom-doped carbon nanocomposites [6-9]. Yet, despite substantial progress in the alkaline media, it remains challenging to achieve a viable activity in acid, as compared to Pt/C. The other is to reduce the amount of Pt used and hence to diminish the catalyst cost but without compromising the electrocatalytic performance [10-13]. One intuitive strategy is to reduce the size of Pt NPs by taking advantage of the increasing surface-to-volume ratio and hence enhanced utilization of the Pt atoms. For instance, Pt_{12} clusters (dia. 0.9 nm) have been found to outperform Pt_{28} (1.0 nm) and Pt_{60} clusters (1.1 nm) towards ORR, with a mass activity one order of magnitude higher than that of commercial Pt/C [14]. One may argue then that Pt single atom catalysts (SACs) would be the ultimate solution, thanks to the maximal atomic utilization [15]. Yet, Pt SACs exhibit mostly a limited ORR activity, whereby O_2 undergoes 2-e reduction to H_2O_2, rather than the 4-e pathway to H_2O [16, 17]. This has been observed with Pt SACs supported on a wide range of substrate matrices, such as TiC/TiN [18, 19], reduced graphene oxide [16], S-doped carbon [17], N-doped carbon [20], etc. The limited ORR performance of Pt SACs,

in comparison to that of Pt NPs, is primarily accounted for by the isolated binding sites that render it energetically difficult to adsorb oxygen and to break the O-O bond [15, 21]. However, the mechanistic details remain under active debates, and the threshold of the Pt domain size for ORR has been largely unexplored.

Note that for conventional Pt NP catalysts, alloying with a second, non-noble metal is an effective strategy to enhance the ORR activity, primarily due to electronic and geometric effects [22, 23]. For instance, Stamenkovic et al. [24] observed that 3d transition-metals can shift the d-band center of Pt and manipulate the ORR activity. Strasser et al. [25] discovered that lattice strain of Pt alloys can significantly weaken oxygen adsorption and enhance the ORR activity. Note that alloying also leads to a reduced loading of Pt in the nanoparticle catalysts, a key factor to enhance the mass activity [26]. For instance, Strasser et al. [27] observed a significant improvement of the ORR mass activity with PtCo as compared to Pt. In another study, Liu et al. [28] synthesized a Pt_3Co alloy NP (dia. 5.6 nm) catalyst with an ultralow Pt loading of 2.7 wt%, which exhibited a mass activity several hundred times better than that of commercial 20 wt% Pt/C, due to the synergistic interaction between Pt_3Co NP and CoN_4 within the carbon matrix. Yet, to the best of our knowledge, there have been no studies of alloying at the Pt few-atom or single-atom level thus far. This is the primary motivation of the present study.

Herein, we first carried out first-principles calculations and examined and compared the ORR activities of various Pt sites in a range of domain size. The results show only limited ORR activity with subnanometer-sized Pt clusters and Pt SACs, as compared

to Pt slab, primarily due to their inability to adsorb oxygen. Yet the addition of neighboring Co atoms can significantly boost the electrocatalytic performance. These theoretical findings were indeed confirmed in experimental measurements with two sets of nanocomposite samples, Pt and Pt/Co few-atom clusters supported on nitrogen-doped carbon. Among the series, $Pt_{2\sim7}$ clusters doped with Co atomic species stood out as the optimal catalyst with a mass activity 48 times that of commercial Pt/C. This is ascribed to the synergistic interactions between Pt and adjacent Co.

4.3 Result and discussion

4.3.1 First-principles calculations.

ORR is a multiple electron reaction process, typically involving the following steps [29-31],

$$* + O_2 + H^+ + e^- \rightarrow OOH* \quad (1) \quad \Delta G1$$

$$OOH* + H^+ + e^- \rightarrow O* + H_2O \quad (2) \quad \Delta G2$$

$$O* + H^+ + e^- \rightarrow OH* \quad (3) \quad \Delta G3$$

$$OH* + H^+ + e^- \rightarrow H_2O + * \quad (4) \quad \Delta G4$$

where * represents the active site. The ORR activity has been argued to be most likely limited by two reactions, the first-electron reduction of oxygen (eq. 1) and reduction of adsorbed hydroxy to water and its desorption from the catalyst surface (eq. 4). Figure 1a depicts the calculated Gibbs free energy of the rate determine step (ΔG_{RDS}, which is defined as the highest of the four ΔG's, Table 1) in ORR, catalyzed by Pt clusters of different sizes (Pt_x, x = 1 to 9, black squares) supported on nitrogen-doped

carbon, in comparison to that of a Pt slab (Figure 2). One can see that ΔG_{RDS} decreases monotonically with increasing Pt domain size and becomes largely leveled off at Pt_9 (from 1.13 eV for Pt_1 to 0.17 eV for Pt_9, as compared to 0.14 eV for Pt slab) (Figure 2), indicating that large NPs, rather than SACs, are preferred for ORR. For a Pt single atom (Figure 1d), a high ΔG_{RDS} is observed at 1.13 eV, indicating unfavorable oxygen reduction activity. ΔG_{RDS} decreases slightly to 1.10 eV for dimeric Pt_2 (Figure 2). Yet, the addition of a third Pt atom to form trimeric Pt_3 leads to a marked decrease of ΔG_{RDS} to 0.62 eV at the central Pt atom. Further decrease of ΔG_{RDS} can be seen with a continuing increase of the Pt domain size; interestingly, ΔG_{RDS} of Pt_9 (ca. 0.9 nm in diameter, Figure 1f and Figure 2) diminishes to only 0.17 eV at the center and edge atoms, which is very comparable to that (0.14 eV) of Pt slab.

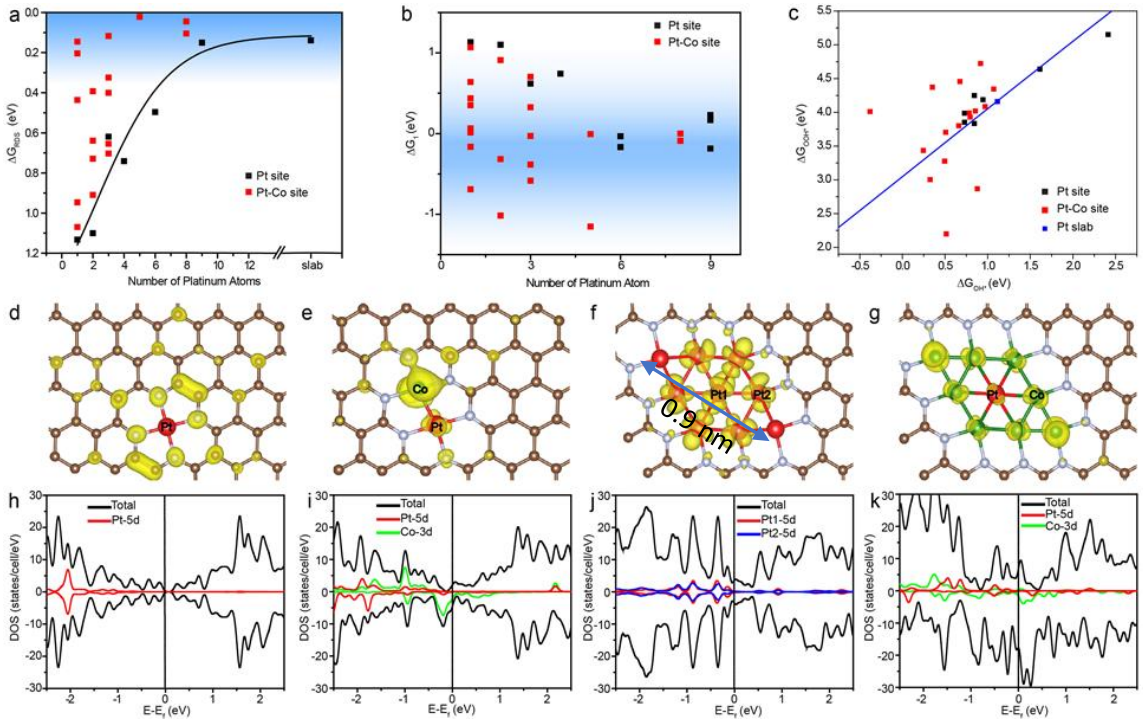

Figure 1. Results of DFT calculations of Pt and Pt-Co clusters of different sizes embedded in a nitrogen-doped carbon matrix**.** The potential is set to +0.90 V vs RHE. (a) Gibbs free energy of the rate determine step (ΔG_{RDS}) versus platinum clusters of different sizes (Pt_x). (b) Gibbs free energy of the first-electron reduction (ΔG_1) versus platinum clusters of different sizes (Pt_x). The dark blue regions in (a) and (b) indicate the range of optimal energy for ORR. (c) Correlation between adsorption free energy of OOH* and OH* intermediates on Pt sites on carbon (black squares), Pt-Co sites in carbon (red squares) and Pt slabs (blue line). (d-g) Wavefunction module square of selected configurations of Pt and Pt-Co in carbon near the Fermi level with an isosurface value of 0.001 e/au^3. (h-k) The corresponding density of states (DOS) of

configurations (d-g). The Pt, Co, N and C atom are denoted by red, green, grey and brown balls, respectively

Table 1. Gibbs free energies of each step in ORR for a range of Pt-NC and PtCo-NC configurations as shown in Figure 2 at the potential of +0.9 V. The rate determined steps (RDS) are marked as red.

# of Pt+Co	# of Pt	configuration	ΔG_1 (eV)	ΔG_2 (eV)	ΔG_3 (eV)	ΔG_4 (eV)
1	1	Pt	1.132	0.204	-1.143	-1.512
2	2	PtPt	1.10	-	-	-
2	1	PtCo	0.437	-2.407	0.425	0.226
2	1	PtCo*	1.07	-	-	-
3	3	Pt_3	0.619	-0.729	-0.498	-0.712
3	1	Pt_1Co_2	-0.165	-1.538	0.204	0.179
3	2	Pt_2Co_1	-0.316	-1.571	0.185	0.393
4	4	Pt_4	0.741	-	-	-
4	1	Pt_1Co_3	0.638	-	-	-
4	2	Pt_2Co_2	-1.821	-0.522	0.639	0.384
4	2	Pt_2Co_2	0.909	-	-	-
4	2	Pt_2Co_2*	-1.016	-1.607	0.729	0.575
4	3	Pt_3Co_1	0.703	-1.603	-0.403	-0.016
6	6	Pt_6	-0.167	-1.829	0.505	0.171
6	6	Pt_6	-0.033	-1.975	0.517	0.171
6	1	Pt_1Co_5	0.352	-3.474	1.254	0.548
6	1	Pt_1Co_5*	-0.69	-2.18	1.209	0.345
6	3	Pt_3Co_3	0.325	-1.374	-0.1	-0.171
6	3	Pt_3Co_3	-0.585	-1.87	0.479	0.655

6	3	Pt_3Co_3	-0.384	-1.711	0.401	0.375
6	3	Pt_3Co_3	-0.031	-1.248	-0.158	0.118
6	5	Pt_5Co_1	-0.008	-2.935	0.343	1.28
6	5	Pt_5Co_1*	-1.152	-0.111	-0.077	0.021
9	9	Pt_9	0.167	-1.456	0.016	-0.046
9	9	Pt_9	-0.187	-1.062	-0.128	0.057
9	1	Pt_1Co_8	0.065	-1.46	0.145	-0.071
9	5	Pt_5Co_4	-1.786	-1.534	2.1	-0.1
9	8	Pt_8Co_1	-0.091	-1.347	0.014	0.105
9	8	Pt_8Co_1*	0	-1.224	-0.14	0.044
slab	slab	Pt	0.139	-0.71	-0.535	-0.215

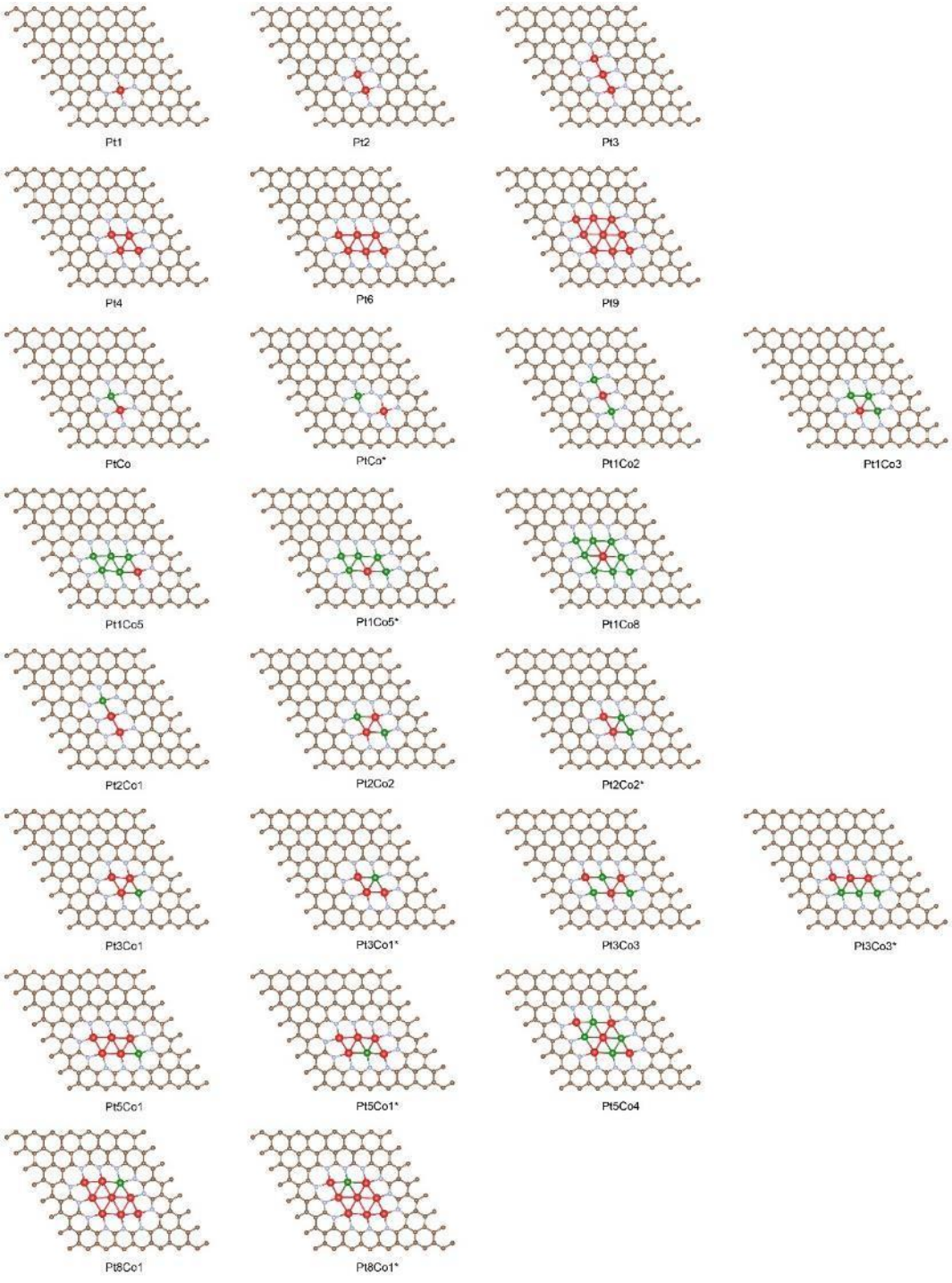
Pt1
Pt2
Pt3
Pt4
Pt6
Pt9
PtCo
PtCo*
Pt1Co2
Pt1Co3
Pt1Co5
Pt1Co5*
Pt1Co8
Pt2Co1
Pt2Co2
Pt2Co2*
Pt3Co1
Pt3Co1*
Pt3Co3
Pt3Co3*
Pt5Co1
Pt5Co1*
Pt5Co4
Pt8Co1
Pt8Co1*

Figure 2. Structural configurations of Pt and PtCo in varied domain size embedded in nitrogen-doped graphene. The red, green, grey and brown balls represent Pt, Co, N and C atoms, respectively.

This suggests that the domain size of Pt should be at least 9 atoms (ca. 0.9 nm in diameter) for optimal ORR activity. Interestingly, incorporation of an adjacent Co atom forming a Pt-Co pair significantly enhances the ORR activity. The red squares in Figure 1a are the ΔG_{RDS} of a range of configurations containing a varied number of Co and Pt (Figure 2-4). One can see that these PtCo sites all exhibit a markedly lower ΔG_{RDS} than the corresponding Pt counterparts, suggesting that the ORR activity of Pt clusters can be readily activated by neighboring Co, and the enhancement becomes drastically intensified with an increasing number of the Pt-Co pairs. For instance, for the simplest structure of a Pt-Co dimer (Pt_1Co_1, Figure 1e and Figure 2), ΔG_{RDS} is only 0.43 eV, markedly lower than those of monomeric Pt_1 (1.13 eV, Figure 1d) and dimeric Pt_2 (1.10 eV, Figure 2). For a linear trimer, Pt_1Co_2 (Figure 3) exhibits a low ΔG_{RDS} of 0.20 eV, as compared to Pt_3 (0.62 eV) and Pt_2Co_1 (0.39 eV). Notably, for an even larger cluster such as Pt_1Co_8 (Figure 1g and Figure 2), with Pt fully coordinated with Co, ΔG_{RDS} is as low as 0.14 eV, very comparable to that of a Pt slab.

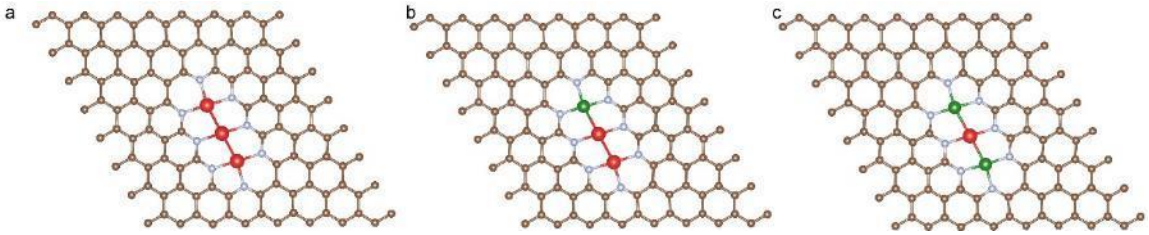

Figure 3. Linear trimers of metals in nitrogen-doped graphene: (a) Pt_3, (b) Pt_2Co_1, and (c) Pt_1Co_2. The red, green, grey and brown balls represent Pt, Co, N and C atoms, respectively.

Importantly, such activation can not only occur for Pt single atoms (Pt_1Co_y, $y \geq 1$), but also for larger Pt domains (Pt_xCo_y, $x \geq 2$ and $y \geq 1$). For example, Pt_2Co_1 (Figure 3) shows a ΔG_{RDS} of 0.39 eV, much lower than that of dimeric Pt_2 alone (1.10 eV). For larger clusters, one Pt_3Co_3 configuration shows a ΔG_{RDS} of only 0.12 eV, less than 1/5 of that (0.62 eV) of Pt_3; in the Pt_5Co_y series, the central Pt atom of Pt_5Co_1* displays a ΔG_{RDS} of only 0.02 eV, drastically below those of Pt_4 (0.74 eV) and Pt_6 (0.51 eV); and in Pt_8Co_y, the ΔG_{RDS} for the center atom of Pt_8Co_1* is 0.05 eV, also significantly lower than those of Pt_6 (0.51 eV) and Pt_9 (0.15 eV). Among these various systems, the middle Pt sites (Figure 4) of Pt_5Co_1*, Pt_1Co_8 and Pt_8Co_1* show a remarkably low ΔG_{RDS} of 0.02 eV, 0.15 eV and 0.04 eV, very close to or even lower than that of the Pt slab. In these, the Co-Pt distance is a critical parameter. For example, when the Co-Pt distance is increased from 2.27 Å (direct Pt-Co bonding) to 4.01 Å (non-direct bonding) (Figure 6), ΔG_{RDS} of the Pt site increases accordingly

from 0.43 to 1.07 eV, similar to that for Pt_1 alone (without Co, Figure 1d). These configurations can be found in Figure 2 and their activities are summarized in Table 1.

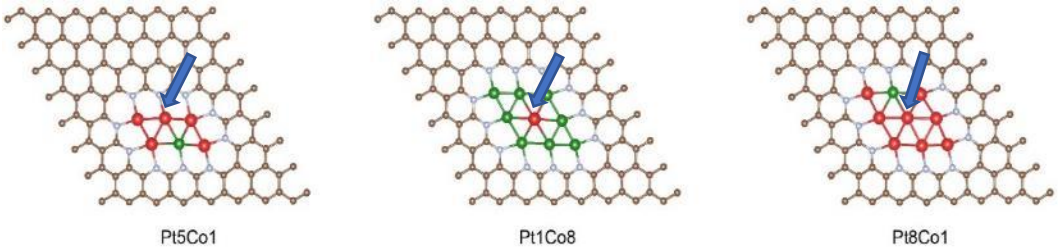

Figure 4. Structures of Pt_5Co_1*, Pt_1Co_8 and Pt_8Co_1* with the center Pt atoms highlighted by the blue arrow. The red, green, grey and brown balls represent Pt, Co, N and C atoms, respectively.

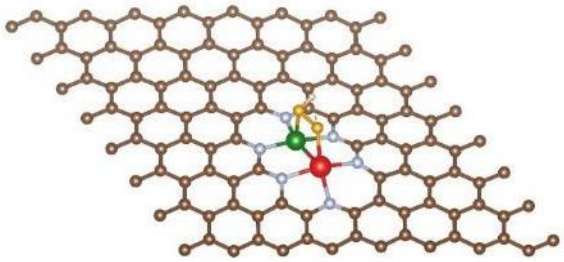

Figure 5. OOH* intermediate adopts a bridge binding fashion on a PtCo dimer.

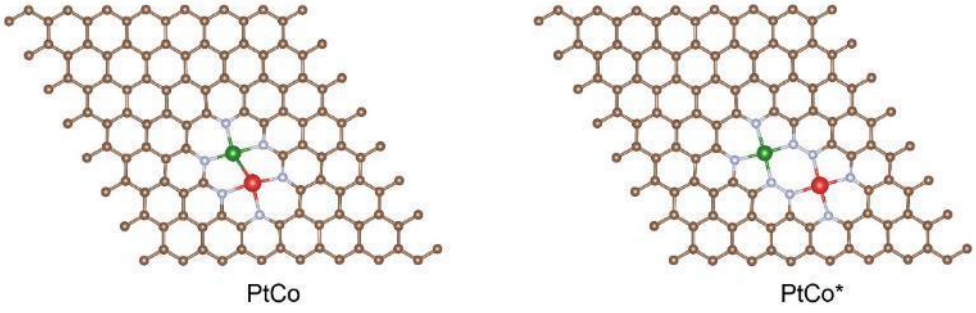

Figure 6. PtCo with or without a direct bonding linkage in a nitrogen-doped graphene matrix. The distance between Co (green) and Pt (red) is 2.27 Å for direct bonding (left) and 4.01 Å for non-direct bonding (right).

Figure 1b depicts the corresponding Gibbs free energy of the first-electron reduction of oxygen (ΔG_1, eq. 1). One can see that ΔG_1 is positive for small Pt domains ($x < 6$, black squares), far above the optimal energy of ca. -0.3 eV to 0.0 eV [32] that is highlighted in dark blue, signifying energetically unfavorable adsorption of oxygen. Yet, at any Pt domain size, the incorporation of adjacent cobalt atoms leads to a marked shift of ΔG_1, some very close to the blue region and some others even below. This is likely because of the formation of Pt-Co bonding pairs that facilitate bridge-adsorption of oxygen, which decreases the reaction energy (Figure 5); and some configurations are even so oxytropic that they can spontaneously break the O-O bond during this first-electron reduction of oxygen (e.g., Pt_3Co_3, Figure 2), leading to a negative ΔG_1. Moreover, based on the adsorption energy of the OOH* and OH* intermediates, small Pt-Co clusters can be found to deviate from the linear relationship, as shown in Figure 1c, where the energies of a number of configurations (red squares) are randomly scattered away from the line calculated for the Pt slab. Note that the linear relationship has been observed extensively in prior studies with large Pt NPs [29, 30, 33]. Breaking of the linear relationship has been reported with Pt SACs, which show unexpected ORR activity [34].

To better understand the role of cobalt and platinum in these bimetallic catalyst configurations, from the viewpoints of electronic structure and chemical bonding, the projected density of states (DOS) near the Fermi level was then calculated for several typical candidate structures (Figure 1d-g). For isolated Pt_1 embedded within N-doped carbon, the wavefunction near the Fermi level has no contribution from the Pt atom, but mainly resides at the neighboring N and C sites instead (yellow regions in Figure 1d); moreover, the DOS is low near the Fermi level, with almost no contribution from the Pt 5d orbital (Figure 1h). This indicates that isolated Pt_1 have no activated electrons to participate in reactions, in agreement with the low ORR activity observed experimentally. By contrast, for the dimeric Pt_1Co_1 pair (Figure 1e and 1i), there is an apparent contribution of the Co 3d orbital to the DOS and wavefunction near the Fermi level, and an obvious overlap between the Pt 5d and Co 3d orbitals, making the Pt site much more favorable for oxygen adsorption than Pt single atom alone. Two other extreme cases with six-coordinated Pt should also be noticed. For a Pt_9 cluster supported in N-doped carbon (Figure 1f and 1j), the activity of the central and edge Pt atoms is better than or very close to that of the platinum slab (ΔG_{RDS} = 0.06 eV and 0.17 eV, respectively, *vide ante*). The wavefunction near the Fermi level is distributed over the Pt atoms, and the Pt 5d orbital contribution to the DOS near the Fermi level leads to favorable oxygen adsorption. Pt_1Co_8 is another case (ΔG_{RDS} = 0.15 eV) with six Co-coordinated Pt. Both the platinum and cobalt atoms contribute to the large DOS near the Fermi level, which can be also seen in the wavefunction that is

distributed over Pt and Co at the Fermi level, further enhancing platinum's ability for oxygen adsorption as well as improving electrical conductivity (Figure 1g and 1k).

Bader charge is adopted to analyze the charge distribution on the individual atoms within the system. One can see a significant charge gain on the Pt atom as a result of Pt-Co direct bonding interactions. As shown in Figure 6 and Table 2, for the Pt-Co pair, the Pt charge has ca. 0.4 e $atom^{-1}$ more than that of an isolated Pt atom or a Pt atom not directly bonded with Co (PtCo* in Figure 6). This further explains that the direct bonding between Co and Pt improves the activity much more than non-direct bonding case as discussed earlier. The charge on the Co atom does not have a significant difference, as compared with isolated Co atoms in carbon. This charge gain of Pt is also confirmed by XAS and XPS measurements (vide infra).

Table 2. Bader charges of selected structures in Figure 2.

	PtCo	**PtCo***	**Pt single atom**	**Co single atom**	**Pt1Co8**
Pt	15.564	15.146	15.162		16.72
Co	16.221	16.103		16.054	16.3-16.6

Taken together, results from these calculations suggest that (a) in order to attain a reasonable ORR activity, the Pt domain must reach a minimum sizes (e.g., $x \geq 9$); and (b) neighboring Co can substantially influence the electronic structure of the Pt atoms and facilitate oxygen adsorption, but only when Pt and Co are directly bonded. Within this context, two sets of catalysts based on carbon-supported Pt and PtCo

clusters are synthesized, where the activity trends are indeed consistent with the theoretical prediction. From these, the platinum mass activity for ORR is maximized.

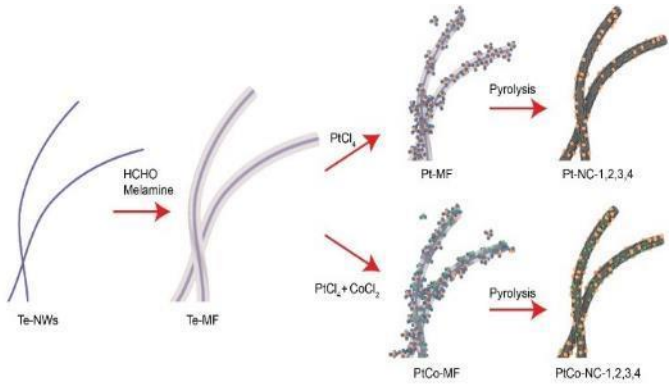

Figure 7. Schematic of the preparation of the Pt-NC and PtCo-NC samples.

4.3.2 Sample synthesis and structural characterization.

The preparation of the samples is schematically shown in Figure 7. Te NWs were used as thermally removable templates and coated with an MF resin shell that served as the carbon and nitrogen sources [35-37]. A different amount of $PtCl_4$ (and $CoCl_2$) was then added to the resulting core@shell composite (Te-MF), and subsequent pyrolysis of the mixtures at 900 °C led to the formation of nitrogen-doped carbon nanowires-supported Pt (PtCo) [32, 38]. Four samples of each series were prepared, which were denoted as Pt-NC-1, Pt-NC-2, Pt-NC-3 and Pt-NC-4 for the samples containing only Pt, and PtCo-NC-1, PtCo-NC-2, PtCo-NC-3 and PtCo-NC-4 for those containing both Pt and Co. The concentration of the $PtCl_4$ precursor was kept the same for samples

with the sample number (e.g., Pt-NC-1 and PtCo-NC-1 were prepared at the same $PtCl_4$ concentration). ICP-OES measurements show that the Pt contents in the final samples were also close, ca. 0.25 wt% for both Pt-NC-1 and PtCo-NC-1, 0.41 wt% for Pt-NC-2 and 0.50 wt% for PtCo-NC-2, 1.39 wt% for Pt-NC-3 and 0.95 wt% for PtCo-NC-3, and 4.75 wt% for Pt-NC-4 and 6.29 wt% for PtCo-NC-4 (Table 3). Note that these are all significantly lower than that in state-of-the art Pt/C (20 wt%).

Table 3. Elemental analysis of the Pt-NC and PtCo-NC samples by ICP-OES measurements

sample	Pt %wt	sample	Pt wt%	Co wt%
Pt-NC-1	0.25	**PtCo-NC-1**	0.25	0.5
Pt-NC-2	0.414	**PtCo-NC-2**	0.505	1.119
Pt-NC-3	1.391	**PtCo-NC-3**	0.954	2.638
Pt-NC-4	4.753	**PtCo-NC-4**	6.292	4.069

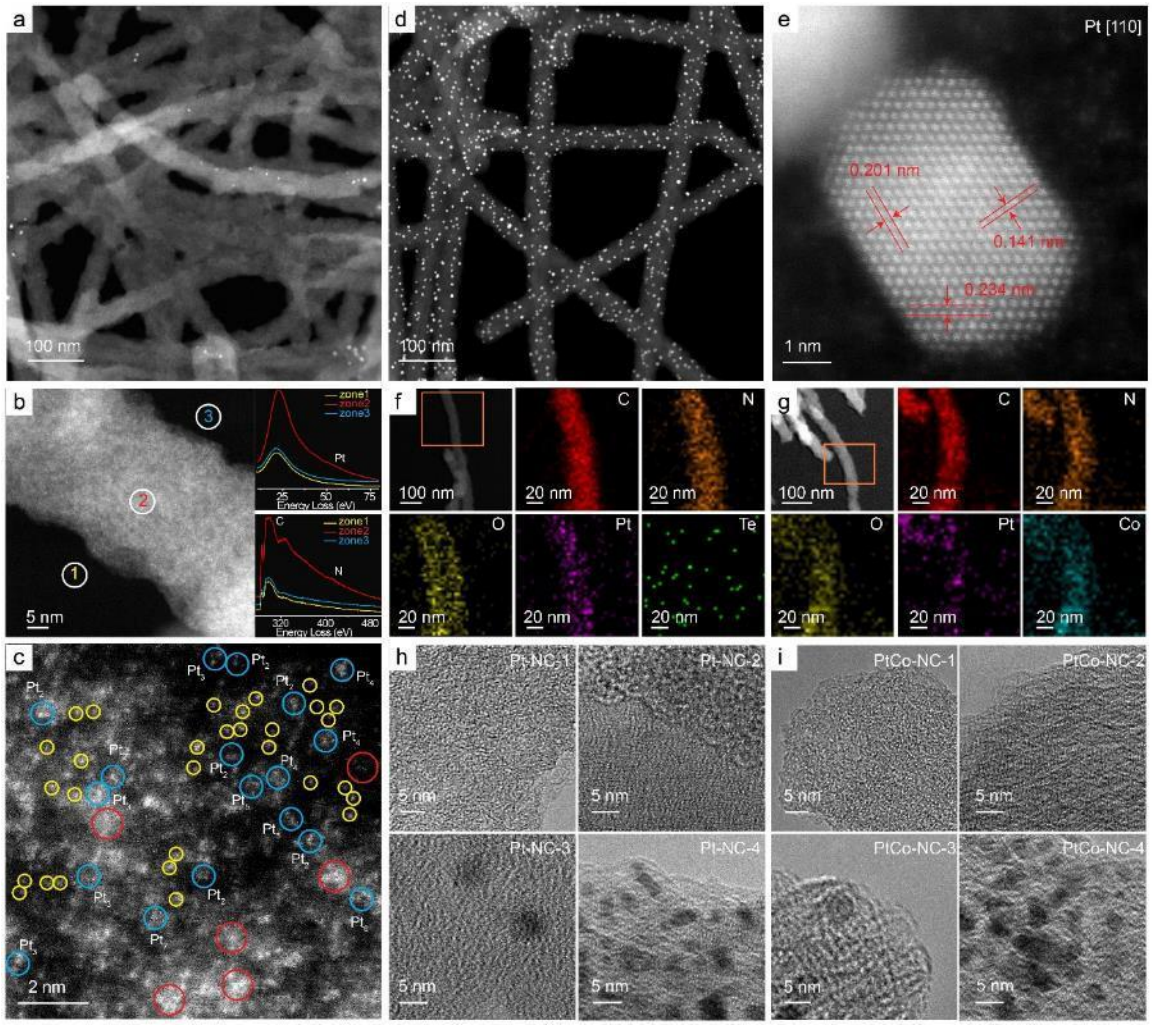

Figure 8. TEM studies of Pt-NC and PtCo-NC nanowires. (a-c) HAADF-STEM of Pt-NC-3. Insets to (b) are the EELS spectra at three selected areas. In (c), yellow circles signify Pt single atoms, blue circles highlight few-atom $Pt_{2\sim7}$ clusters, red circles denote Pt_9 or larger clusters with a diameter of ca. 0.9 nm. (d) HAADF-STEM of Pt-NC-4. (e) High-resolution TEM image of a Pt NP of Pt-NC-4. EDS elemental mapping studies of (f) Pt-NC-3 and (g) PtCo-NC-3. High-resolution TEM images of the (h) Pt-NC and (i) PtCo-NC samples

The obtained samples were first characterized by TEM measurements (Figure 8). Panel (a) shows a representative TEM image of Pt-NC-3. One can see that the nanowires have a diameter of ca. 40 nm and length of several microns, with only a handful of NPs, suggesting that Pt was mostly in the forms of few-atom clusters and single atoms. Figure 8b shows the corresponding elemental mapping analyses based on EELS measurements. It can be seen that the signals of the Pt $O_{2,3}$ edge (ca. 50 eV), C K edge (ca. 284 eV) and N K edge (ca. 401 eV) are all prominently higher on the nanowires (zone 2, red curves) than in the background (zone 1, yellow curves; and zone 3, blue curves), indicating that Pt was embedded in the nitrogen-doped carbon structure. Figure 8c is a HAADF-STEM image of Pt-NC-3, where isolated Pt atoms (yellow circles) can be found throughout the carbon matrix, along with a number of few-atom clusters ($Pt_{2\sim7}$, blue circles) and a few larger clusters ($Pt_{\geq 9}$, red circles), which are good representations of the calculation models (Pt_x) in Figure 2.

Notably, for samples prepared at lower Pt loadings (i.e., Pt-NC-1 and Pt-NC-2), no Pt NPs can be found (Figure 8h and Figure 9), suggesting that Pt is mostly dispersed within the carbon matrix as few-atom clusters and/or isolated atoms. Yet for Pt-NC-4, which was prepared with a $PtCl_4$ concentration 5 times that for Pt-NC-3, one can see that a number of Pt NPs (dia. 5 nm) were formed on the carbon nanowires (Figure 8d-e), which exhibit clearly defined lattice fringes with the interplanar spacings of 0.141, 0.201, and 0.234 nm due to the (110), (001), (111) vectors of the {110} facet of *fcc* Pt (card 00-001-1190).[39]

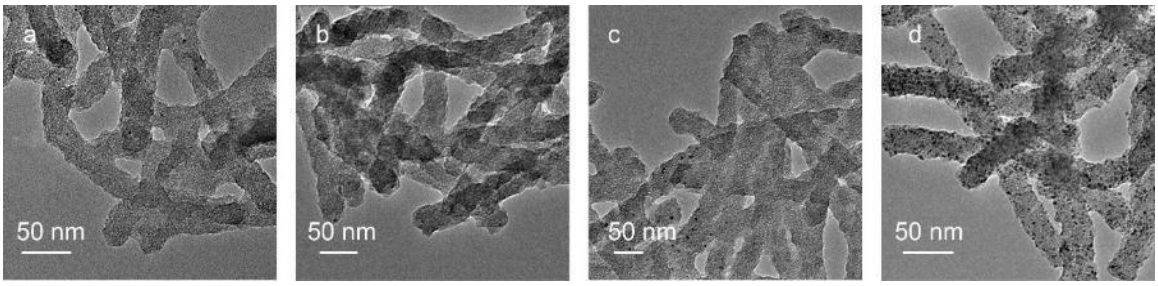

Figure 9. TEM images of the Pt-NC series: (a) Pt-NC-1, (b) Pt-NC-2, (c) Pt-NC-3 and (d) Pt-NC-4. Scale bars all 50 nm.

It is worth noting that the addition of Co did not lead to an apparent variation of the overall sample morphology. This is manifested in elemental mapping analysis of the Pt-NC-3 (Figure 8f) and PtCo-NC-3 (Figure 8g) samples, where the elements of C, N, O, and Pt can all be readily identified and dispersed in the nanowires (Co in PtCo-NC-3). Similar to the Pt-NC series, for PtCo-NC-1 and PtCo-NC-2 (Figure 8i and Figure 10), the metal species are dispersed within the carbon skeletons as isolated atoms and/or few-atom clusters, and NPs started to emerge in PtCo-NC-3 and became prominent in PtCo-NC-4 (at even higher metal loadings, NPs became the dominant species in the samples, Figure 11).

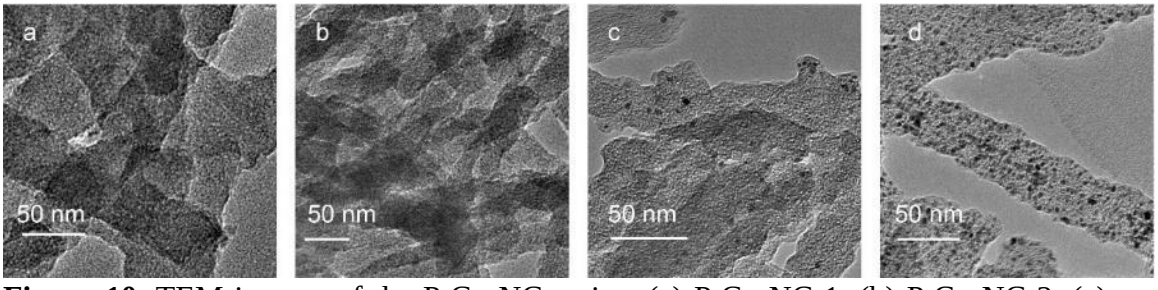

Figure 10. TEM images of the PtCo-NC series**:** (a) PtCo-NC-1, (b) PtCo-NC-2, (c) PtCo-NC-3 and (d) PtCo-NC-4. Scale bars all 50 nm.

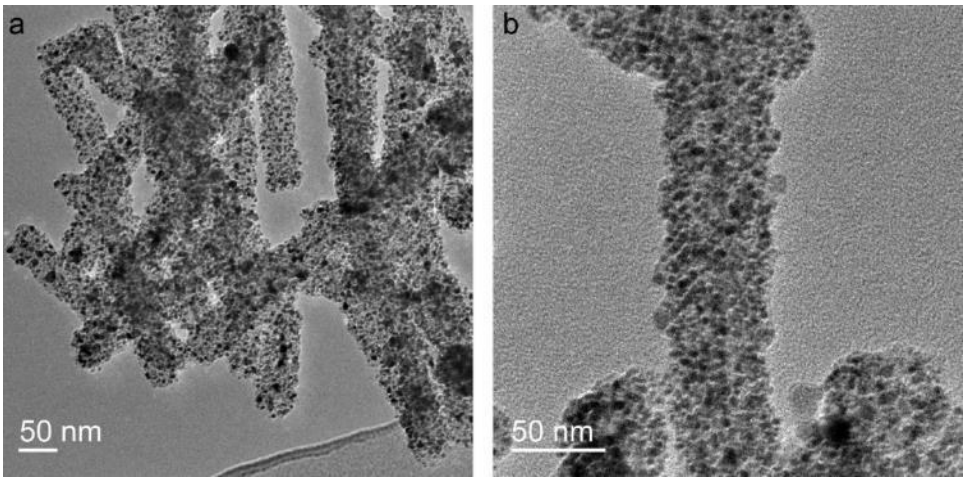

Figure 11. TEM images of (a) Pt and (b) PtCo nanoparticles on carbon nanowires. The samples are prepared with a Pt concentration 5 times than that of Pt-NC-4 (and PtCo-NC-4). Scale bars 50 nm.

The atomic configurations of the metal centers were then examined by XAS measurements. Figure 12a shows the Pt L_3-edge X-ray absorption near-edge structure (XANES) spectra of Pt-NC-1, Pt-NC-3, PtCo-NC-1, PtCo-NC-3 and Pt foil. Pt-NC-1 and PtCo-NC-1 can be seen to show a stronger white line (i.e., the first peak following the absorption edge) than the others, indicating a higher oxidation state of Pt, which is consistent with that of Pt single atoms in a carbon matrix [40-42]. For Pt-NC-3 and PtCo-NC-3 the absorption edge is higher than that of the Pt foil, but lower than those of Pt-NC-1 and PtCo-NC-1. This can be accounted for by the partial clustering of Pt and Co, which led to a reduced Pt oxidation state, as compared to that in Pt-NC-1 and PtCo-NC-1. Notably the white line of Pt-NC-3 is somewhat stronger than that of PtCo-NC-3, likely due to electron transfer from Co to Pt in the latter. The corresponding XANES spectra of the Co K-edge are shown in the Figure 12b. Consistently, PtCo-NC-1 and PtCo-NC-3 exhibit a stronger white line at Co K-edge

than the Co foil, and the pre-edge peak disappears, where the Co oxidation state is consistent with the formation of Co single atoms and few-atom clusters. Furthermore, the fact that PtCo-NC-3 shows a weaker white line and a more intense pre-edge feature at Co K-edge than PtCo-NC-1 suggests that clustering of Pt and Co atoms was more prominent in PtCo-NC-3 than in PtCo-NC-1.

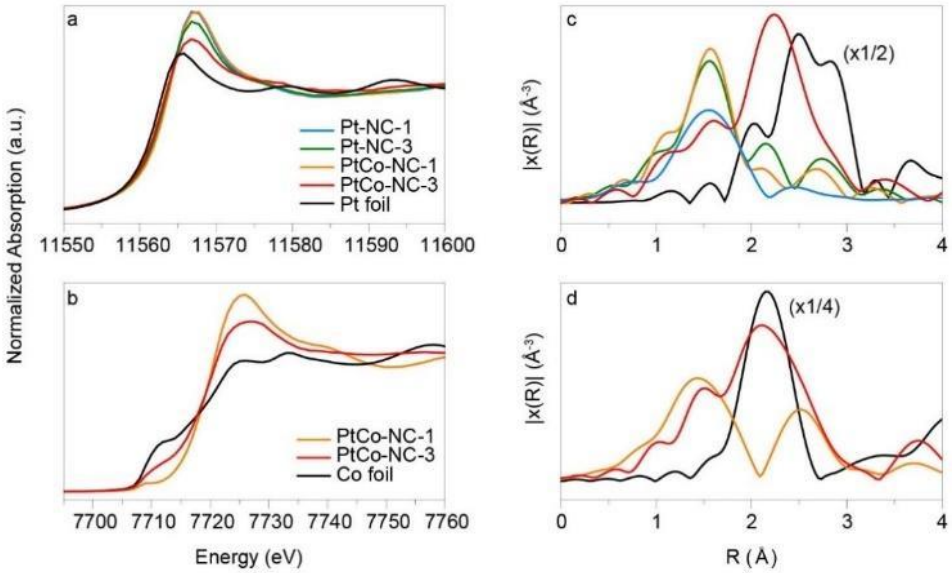

Figure 12. Spectroscopic characterization of the Pt-NC and PtCo-NC samples. (a) Pt XANES spectra of Pt-NC-1, Pt-NC-3, PtCo-NC-1and PtCo-NC-3.(b) Co XANES spectra of PtCo-NC-1 and PtCo-NC-3 (c) Pt FT-EXAFS spectra of Pt-NC-1, Pt-NC-3, PtCo-NC-1 and PtCo-NC-3. (d) Co FT-EXAFS spectra of PtCo-NC-1 and PtCo-NC-3

The relevant Fourier-transform EXAFS spectra of Pt are shown in Figure 12c. Fitting of the EXAFS data (Table 4) yields a Pt-N bond of ca. 2.0 Å for the Pt-NC-1, PtCo-NC-1, Pt-NC-3, and PtCo-NC-3 samples,[43] in agreement with EELS study (Figure

8b). This is consistent with results obtained from DFT calculations, where the Pt-N bond length is found to be 1.95 Å - 2.08 Å in different configurations (Figure 2). Note that no Pt-Pt bond can be identified in the Pt-NC-1 and PtCo-NC-1 samples, consistent with atomic dispersion of Pt within the carbon skeletons. Furthermore, the coordination number (CN) of Pt-N is estimated to be 3.5 for Pt-NC-1 and 3.6 for PtCo-NC-1, suggesting that Pt is mostly embedded with the carbon matrix in the form of $PtN_{3\sim4}$ (Figure 1d).

Table 4. EXAFS fitting results

sample	element	bond	CN	R (Å)	σ^2 (Å) x10^{-3}	E_0 (eV)	R factor
Pt-NC-1	**Pt**	Pt-N	3.5(9)	1.99(2)	7(4)	9(3)	0.0137
Pt-NC-3	**Pt**	Pt-N	2.9(4)	1.99(2)	6(3)	10(1)	0.0105
		Pt-Pt	2(1)	2.71(3)	3(5)	-1(5)	0.0105
PtCo-NC-1	**Pt**	Pt-N	3.6(3)	2.001(9)	7(1)	9.4(8)	0.0108
	Co	Co-N	8(3)	2.03(4)	17(7)	-6(4)	0.0228
		Co-Pt	3(1)	2.81(3)	7(5)	-6(4)	0.0228
PtCo-NC-3	**Pt**	Pt-N	1.7(8)	1.95(5)	7(3)	7(4)	0.0242
		Pt-Co	3(2)	2.65(2)	7(3)	7(4)	0.0242
		Pt-Pt	5(3)	2.68(5)	7(3)	7(4)	0.0242
	Co	Co-N	1.6(3)	1.94(2)	3(2)	-5(3)	0.0242
		Co-Co	1.8(4)	2.50(2)	3(2)	-5(3)	0.0242
		Co-Pt	1.8(4)	2.65(2)	3(2)	-5(3)	0.0242

For Pt-NC-3 and PtCo-NC-3, an additional bond can also be resolved at ca. 2.65 Å, which likely arise from the Pt-Pt/Pt-Co linkages — note that for the Pt foil, the Pt-Pt bond length is 2.76 Å, with a CN of 12 [44, 45]. For Pt-NC-3, the CN of Pt-N is estimated to be 2.9, and that for Pt-Pt is ca. 2.0, consistent with partial clustering in

the sample forming nitrogen-terminated Pt few-atom clusters. For PtCo-NC-3, the CN is 1.7 for Pt-N, 5.0 for Pt-Pt and 3.0 for Pt-Co, suggesting somewhat enhanced clustering in the sample as compared to Pt-NC-3. From the CN values, the average cluster size is calculated to be between 0.65 nm and 1.19 nm by the Calvin equation [46], in good agreement with the formation of $Pt_{2\sim7}$ clusters, as observed in Figure 8c.

The corresponding Co EXAFS spectra are included in the Figure 12d. For PtCo-NC-1, the Co-N bond is resolved at 2.03 Å (CN = 8) [47, 48], and Pt-Co bond at 2.81 Å (CN = 3) [49], suggesting atomic dispersion of Co atoms in the samples in the form of Pt-Co bonding linkages. For the PtCo-NC-3 sample, the Co-N bond can be identified at 1.94 (CN = 1.6), Co-Pt bond at 2.65 Å (CN = 1.8), and Co-Co at 2.50 Å (CN = 1.8). This is consistent with partial clustering of Pt and Co and the dispersion of Co into Pt few-atom clusters.

Taken together, these results suggest a clear structural evolution from metal isolated atoms to few-atom clusters and to nanoparticles with increasing metal loadings in the sample synthesis (Figure 20). For the samples prepared at low metal loadings (Pt-NC-1, PtCo-NC-1, Pt-NC-2 and PtCo-NC-2), isolated Pt atoms and Pt-Co pairs are dispersed within the carbon matrix. At higher metal loadings (Pt-NC-3 and PtCo-NC-3), partial clustering of Pt and Co occurred, with the sparse emergence of metal nanoparticles. At even higher metal loadings (Pt-NC-4 and PtCo-NC-4), nanoparticles become increasingly dominant. Further increase of the metal loadings led to the formation of abundant metal nanoparticles (Figure 11). The fitting of the

EXAFS spectra can be found in Figure 13. Consistent results were obtained in XRD (Figure 14), XPS (Figure 15-18) and Raman (Figure 19) measurements.

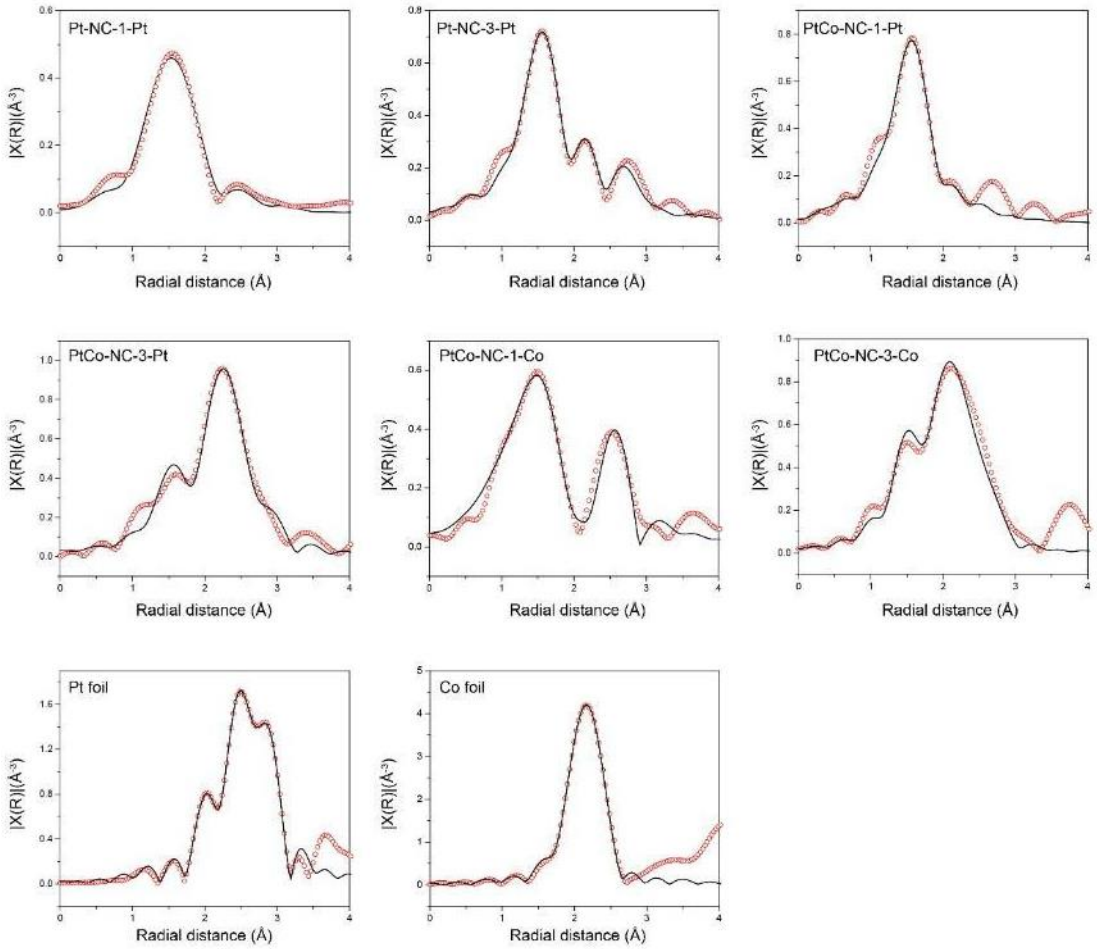

Figure 13. EXAFS spectra of the Pt-NC and PtCo-NC samples. Red circles are experimental data and black curves are best fits. The data for Pt and Co foils are also included as a reference.

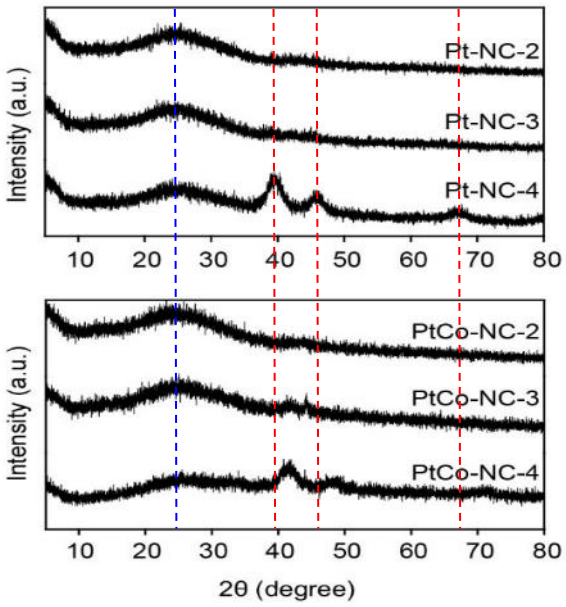

Figure 14. XRD patterns of the Pt-NC and PtCo-NC samples.

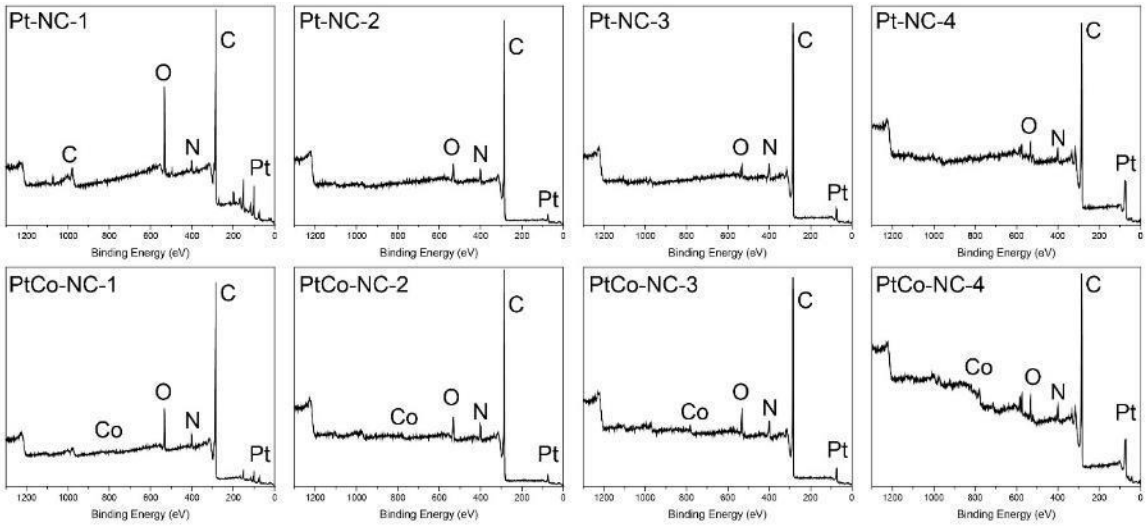

Figure 15. XPS full survey spectra of the Pt-NC and PtCo-NC samples. The elements of C, N, and Pt can be clearly identified with the Pt-NC and PtCo-NC series (with Co for the latter).

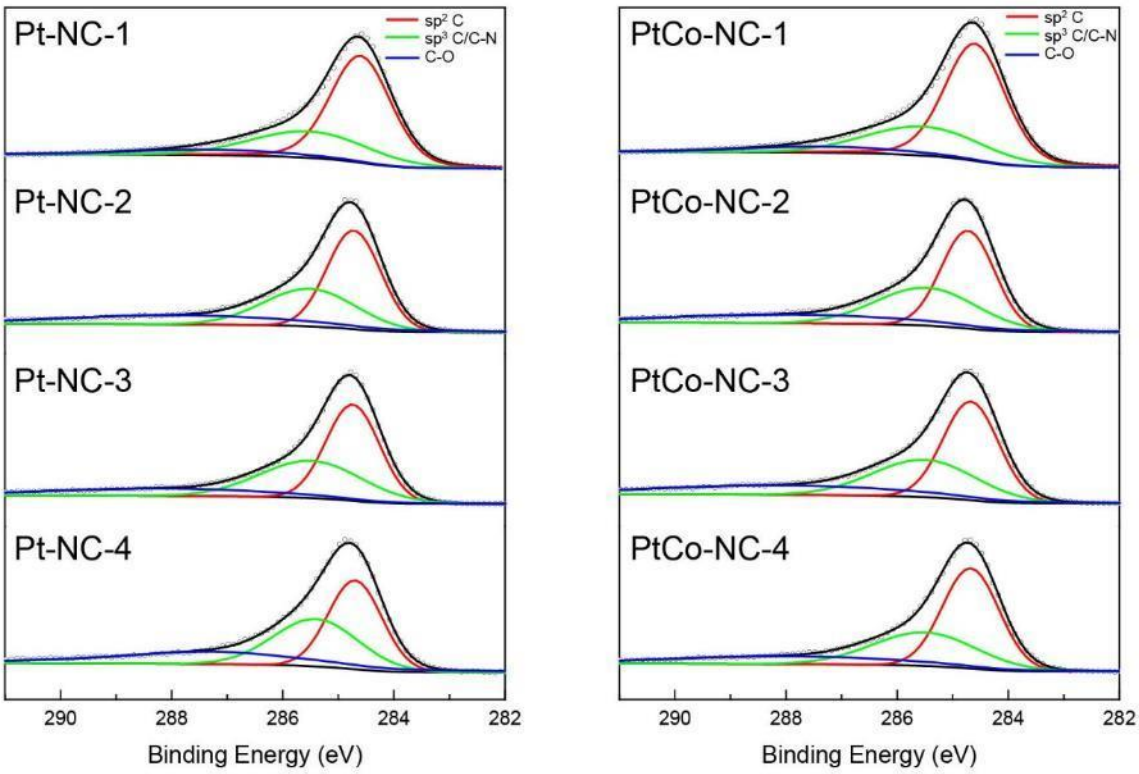

Figure 16. High-resolution XPS scans of the C 1s electrons of the Pt-NC and PtCo-NC samples. Grey circles are experimental data and colored curves are deconvolution fits.

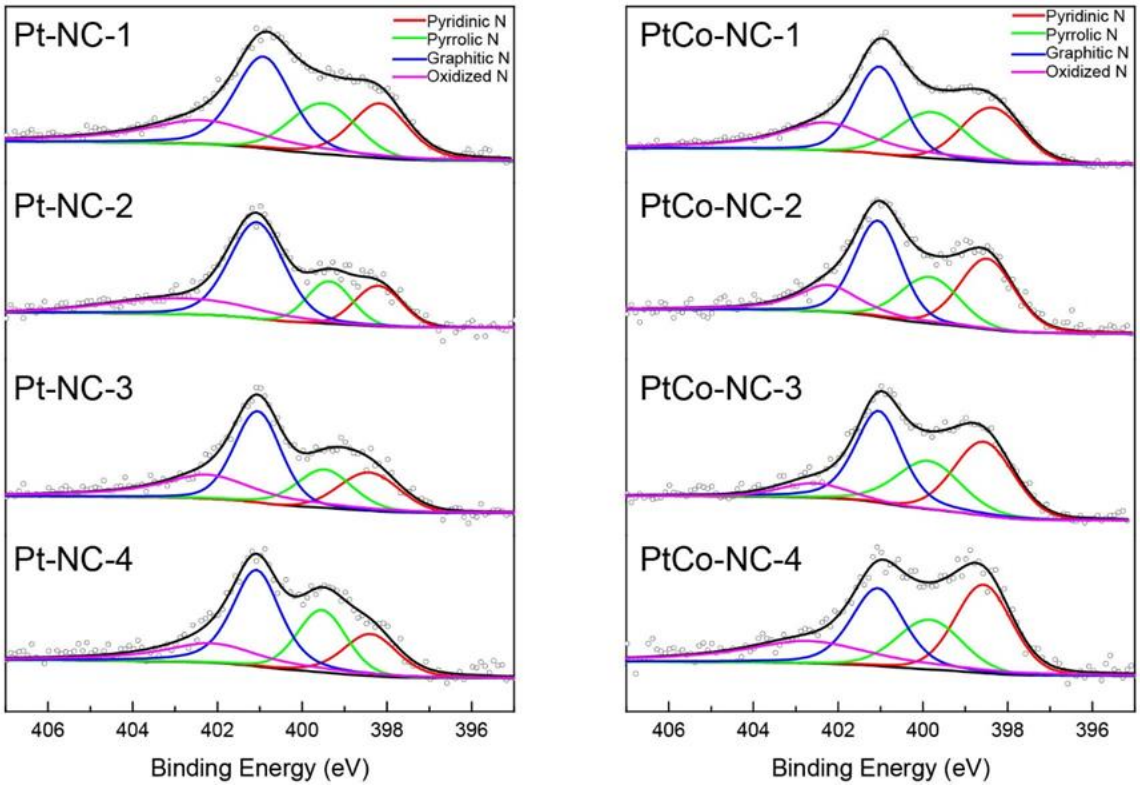

Figure 17. High-resolution XPS scans of the N 1s electrons of the Pt-NC and PtCo-NC samples. Grey circles are experimental data and colored curves are deconvolution fits.

Further structural insights were obtained in spectroscopic measurements. Figure 14 shows the XRD patterns of the two sets of samples. For samples prepared at relatively low metal loadings, only a broad peak centered at ca. 25° can be observed, due to the (002) diffraction of graphitic carbon, confirming successful carbonization of the resin precursors. The fact that no other diffraction peaks can be seen is also consistent with the absence of metal NPs in these samples. For Pt-NC-4, in addition to the carbon (002) diffraction, peaks at 40°, 46° and 67° can also be found, due to the (111), (200) and (220) diffractions of *fcc* Pt (card 00-001-1190).[39] Similar diffraction patterns can

be found with PtCo-NC-4, except that the peak positions appear at slightly higher 2θ angles, indicating lattice shrinkage due to alloying between Pt and Co in the NPs.[50] These observations are in good agreement with results from the TEM studies (Figure 8).

The elemental compositions and valence states were then examined by XPS measurements. Figure 15 depicts the full spectra where the elements of C, N, and Pt can be clearly identified with the Pt-NC and PtCo-NC series (with Co for the latter). Figure 18a depicts the high-resolution scans of the Pt 4f electrons in the Pt-NC samples, where deconvolution yields two doublets. The first pair at ca. 72.5 eV and 75.8 eV can be ascribed to Pt atoms in Pt-N, whereas the other pair at 74.0 eV and 77.3 eV is indicative of Pt atoms in a higher oxidation state, as observed previously with Pt single atoms.[51, 52] For Pt-NC-1, Pt-NC-2, and Pt-NC-3 samples, no other peaks can be resolved, consistent with the absence of large particles. By contrast, the Pt-NC-4 sample displays an additional pair of peaks at 71.4 eV and 74.7 eV, due to metallic Pt in Pt NPs,[53, 54] as observed in TEM measurements (Figure 8). Similar characteristics are observed with the PtCo-NC series (Figure 18b), suggesting good comparability between the Pt-NC and PtCo-NC samples. Yet, it should be noticed that the Pt binding energy in the latter is ca. 0.2 eV lower than that in the former, signifying charge transfer from Co to Pt, in agreement with XANES and DFT results.

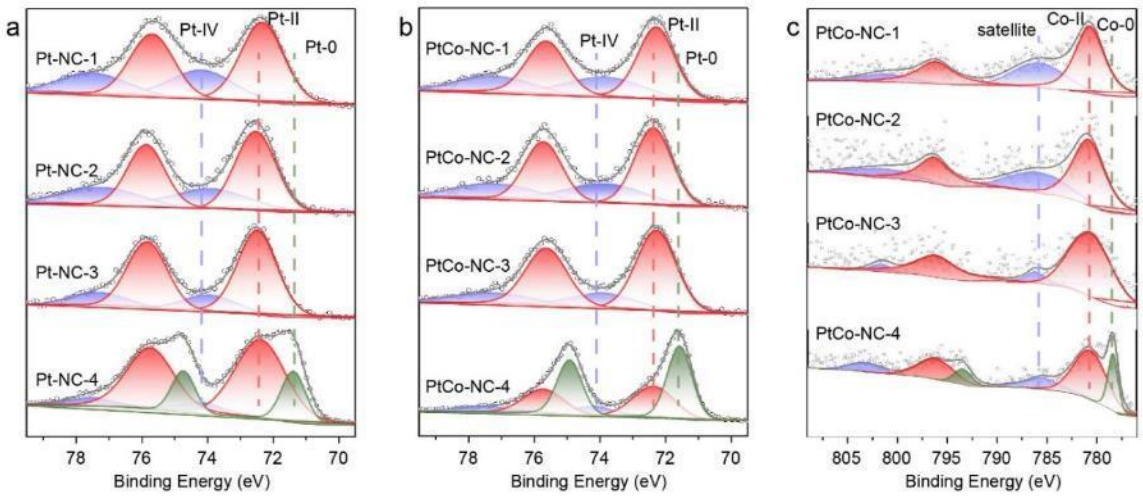

Figure 18. (a) XPS spectra of the Pt 4f electrons in Pt-NC-1, Pt-NC-2, Pt-NC-3 and Pt-NC-4. (b) XPS spectra of the Pt 4f electrons in PtCo-NC-1, PtCo-NC-2, PtCo-NC-3 and PtCo-NC-4. (c) XPS spectra of the Co 2p electrons in PtCo-NC-1, PtCo-NC-2, PtCo-NC-3 and PtCo-NC-4.

Consistent results are obtained in the corresponding Co 2p spectra (Figure 18c), which exhibit a pair of peaks at 780.7 eV and 796.2 eV, due to partial oxidation of the Co atoms. The Co(0) peak can only be found in the PtCo-NC-4 sample at 778.3 eV and 793.4 eV, due to the formation of PtCo alloy NPs. The other elements of C and N do not show any obvious difference among the samples (Figure 16 and 17). The fitting results are summarized in Table 5-9.

Table 5. Fitting results of the Pt 4f XPS data

sample	Pt SA		Pt-O		Pt(0)	
	$4f_{7/2}$	$4f_{5/2}$	$4f_{7/2}$	$4f_{5/2}$	$4f_{7/2}$	$4f_{5/2}$

Pt-NC-1	72.32	75.68	74.18	77.53		
Pt-NC-2	72.52	75.86	73.91	77.26		
Pt-NC-3	72.47	75.82	73.97	77.32		
Pt-NC-4	72.38	75.73	74.2	77.55	71.37	74.73
PtCo-NC-1	72.27	75.63	73.86	77.21		
PtCo-NC-2	72.36	75.71	73.89	77.24		
PtCo-NC-3	72.27	75.62	73.93	77.28		
PtCo-NC-4	72.37	75.72	74.19	77.54	71.57	74.92

Table 6. Fitting results of the Co 2p XPS data

sample	**Co SA**		**satellite**		**Co(0)**	
	$2p_{3/2}$	$2p_{1/2}$	$2p_{3/2}$	$2p_{1/2}$	$2p_{3/2}$	$2p_{1/2}$
PtCo-NC-1	780.68	796.19	785.79	801.29		
PtCo-NC-2	780.79	796.29	785.9	801.40		
PtCo-NC-3	780.66	796.16	786.13	801.63		
PtCo-NC-4	780.64	796.14	785.47	803.23	778.36	793.41

Table 7. Pt to Co atomic ratio by XPS measurements

sample	**Pt:Co mass ratio**	**Pt:Co atomic ration**
PtCo-NC-1	5.07	1.53
PtCo-NC-2	4.33	1.31
PtCo-NC-3	5.65	1.70

PtCo-NC-4	5.58	1.69

Table 8. Fitting results of the C 1s XPS data

sample	C sp^2	C sp^3	C-O
Pt-NC-1	284.60	285.52	287.22
Pt-NC-2	284.72	285.51	287.84
Pt-NC-3	284.74	285.49	288.13
Pt-NC-4	284.76	285.6	287.89
PtCo-NC-1	284.67	285.53	287.74
PtCo-NC-2	284.72	285.47	287.90
PtCo-NC-3	284.67	285.51	288.03
PtCo-NC-4	284.68	285.5	287.94

Table 9. Fitting results of the N 1s XPS data.

sample	Pyridinic (eV)	Pyrrolic (eV)	Graphitic (eV)	Oxidized (eV)
Pt-NC-1	398.17	399.5	400.92	402.36
Pt-NC-2	398.19	399.36	401.07	402.84
Pt-NC-3	398.42	399.47	401.05	402.25
Pt-NC-4	398.39	399.53	401.08	402.14

PtCo-NC-1	398.37	399.79	401.03	402.30
PtCo-NC-2	398.49	399.84	401.06	402.25
PtCo-NC-3	398.56	399.87	401.04	402.57
PtCo-NC-4	398.57	399.85	401.06	402.73

In Raman measurements, similar D and G bands are clearly defined in all samples, further confirming successful carbonization of the resin precursors, and the fact that the D to G band intensity ratio is similar among the samples indicates a rather consistent carbon matrix (Figure 19).

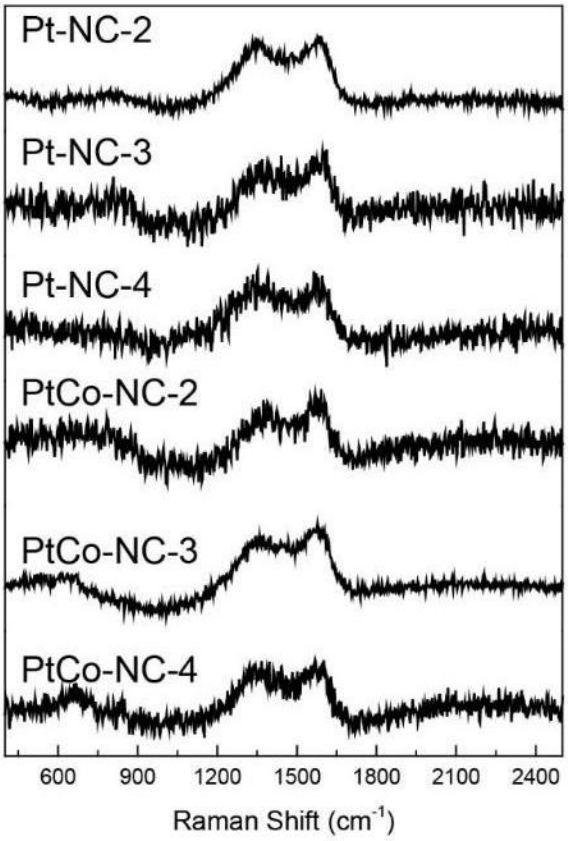

Figure 19. Raman spectra of the Pt-NC and PtCo-NC samples. The D and G bands can be readily identified with a similar band intensity ratio in all samples, suggesting a rather consistent carbon matrix.

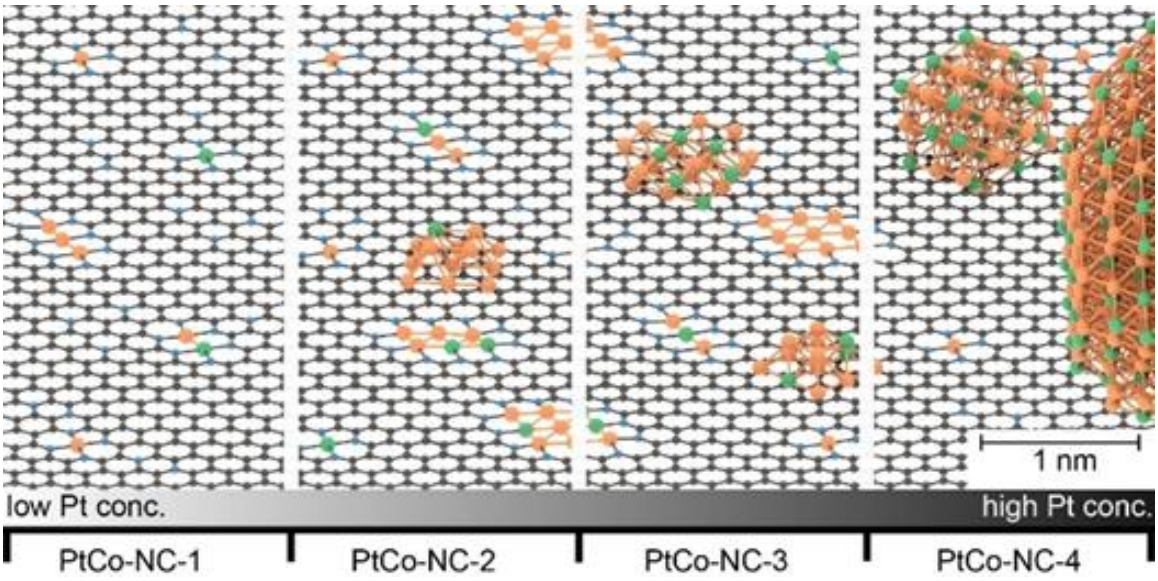

Figure 20. Proposed structures of the PtCo-NC samples based on the experimental characterization. Pt, Co, N and C are denoted by orange, green, blue and black, respectively.

4.3.3 Electrocatalytic activity.

The electrocatalytic activity towards ORR is then assessed and compared. From Figure 23a, one can see that all samples exhibit apparent electrocatalytic activity

towards ORR in 0.1 M $HClO_4$ at the catalyst loading of 0.16 mg cm^{-2}. Yet, the activity of the Pt-NC series increases with samples prepared at increasing $PtCl_4$ feeds, from Pt-NC-1 to Pt-NC-4. Specifically, Pt-NC-1, which consists of only isolated Pt single atoms and shows no voltammetric features for hydrogen adsorption/desorption (Figure 21), exhibits a relatively low activity, with a half-wave potential ($E_{½}$) of +0.72 V vs RHE, in comparison to +0.74 V for Pt-NC-2 and +0.82 V for Pt-NC-3, suggesting a large Pt domain is preferred for ORR. Pt-NC-4 is the best among the series, with $E_{½}$ = +0.87 V and obvious hydrogen adsorption/desorption features (Figure 21). Interestingly, with the incorporation of Co into the samples, the ORR activity is enhanced drastically. For instance, PtCo-NC-1 shows an $E_{½}$ of +0.77 V, ca. 50 mV more positive than that of Pt-NC-1. PtCo-NC-2 and PtCo-NC-3 also show a positive shift of 40 and 50 mV, as compare to Pt-NC-2 and Pt-NC-3, respectively. This enhancement can be ascribed to the Pt-Co coupling (no nanoparticle contribution in these samples). PtCo-NC-4 exhibit an even higher shift of 60 mV to +0.93 V, most likely because the well-known Pt-Co alloying contribution [55-57]. As a reference, the

sample containing only Co shows a very poor activity, indicating minimal contribution from Co SAs or Co NPs (Figure 22).

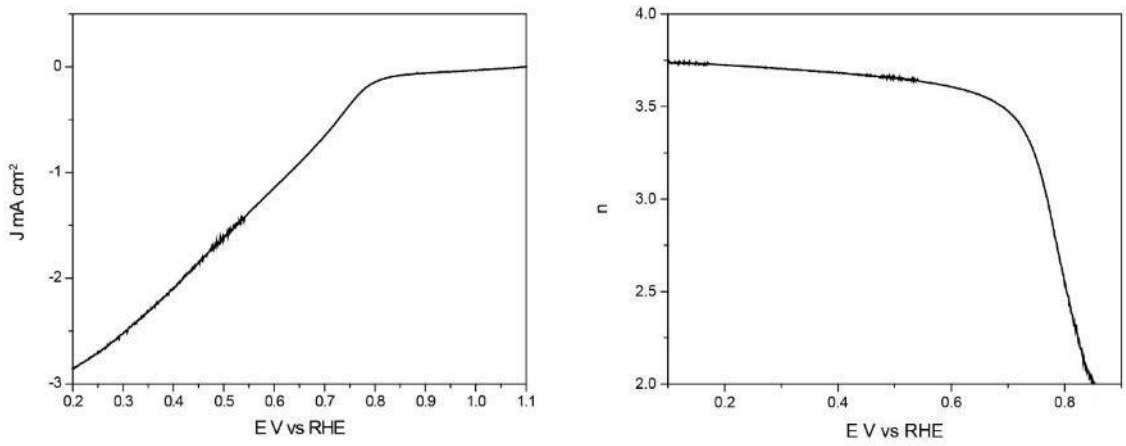

Figure 21. CV curves of the Pt-NC and PtCo-NC samples in 0.1 M $HClO_4$ at the scan rate of 50 mV s^{-1}. Note that only Pt-NC-4 and PtCo-NC-4 show apparent hydrogen adsorption/desorption voltammetric features, whereas the other samples display only featureless responses, consistent with the formation of only Pt isolated atoms/few-atom clusters in the latter, as compared to Pt NPs in Pt-NC-4 and PtCo-NC-4.

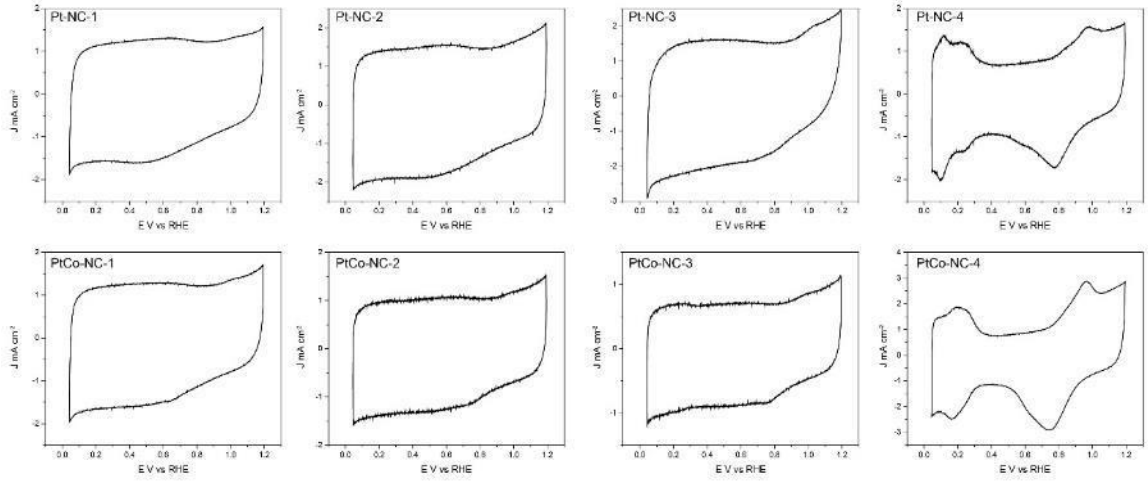

Figure 22. ORR LSV curve and charge transfer number of Co,N-codoped C nanowires. This shows that the ORR activity is poor with Co doping alone, and the ORR activity of the Pt-NC and PtCo-NC series is primarily due to Pt.

Moreover, the electron transfer number (n) involved in ORR of all samples are estimated to be over 3.95 (Figure 23b), suggesting that ORR adopted the 4-electron pathway on these catalysts, $O_2 + 4H^+ + 4e \rightarrow 2H_2O$, and the ORR activity is not limited by the second step (eq. 2), which supports the conclusion that the first step (eq. 1) is most likely the RDS (Figure 1). Remarkably, the PtCo-NC-3, Pt-NC-4 and PtCo-NC-4 samples all outperform commercial 20 wt% Pt/C, despite a significantly lower Pt loading (ca. 1 to 5 wt%). Figure 23c depicts the Tafel plots of the two series of samples. Indeed, the PtCo-NC samples show a smaller Tafel slope than the Pt-NC counterparts, indicating superior electron-transfer kinetics in the former. Among them, PtCo-NC-3 shows a mass activity (at +0.9 V) that even exceeds the DOE 2020 target, with a low Tafel slope of 77.4 mV dec^{-1}. The results are summarized in Table 10.

Table 10. Summary of the ORR activity

sample	E_{onset} (V vs RHE)	$E_{1/2}$ (V vs RHE)	n at +0.7 V	J_k at +0.85V (mA cm^{-2})	J_k at +0.85V (A mg^{-1})	Tafel slope (mV dec^{-1})
Pt-NC-1	0.88	0.72	3.98	0.26	0.65	146.9
Pt-NC-2	0.93	0.74	3.96	0.43	0.63	121.4
Pt-NC-3	0.98	0.82	3.98	2.56	1.13	92.4
Pt-NC-4	1.01	0.87	4.00	5.9	0.76	73.5
PtCo-NC-1	0.94	0.77	3.98	0.61	1.5	106.3
PtCo-NC-2	0.96	0.78	3.98	0.71	0.88	107.4

PtCo-NC-3	1.00	0.87	3.99	6.43	4.16	77.4
PtCo-NC-4	1.03	0.93	3.96	19.75	1.93	53.7
20% Pt/C	0.99	0.86	3.92	2.83	0.09	79.5

From Figure 23d, one can see that the mass activity (at +0.85 V) of both the Pt-NC and PtCo-NC series exhibits a peak-shaped variation with the Pt content. Note that this Pt concentration range corresponds to a structural evolution from Pt isolated atoms to clusters and nanoparticles (Figure 20). The results suggest that a minimum threshold of the Pt domain size needs to be reached for effective ORR electrocatalysis, and the incorporation of Co can significantly enhance the ORR performance by the unique Pt-Co coupling. Among the series, PtCo-NC-3 stands out as the best among the series, with a mass activity of 4.16 $A\,mg_{Pt}^{-1}$ at +0.85 V, 48 times better than that of commercial Pt/C.

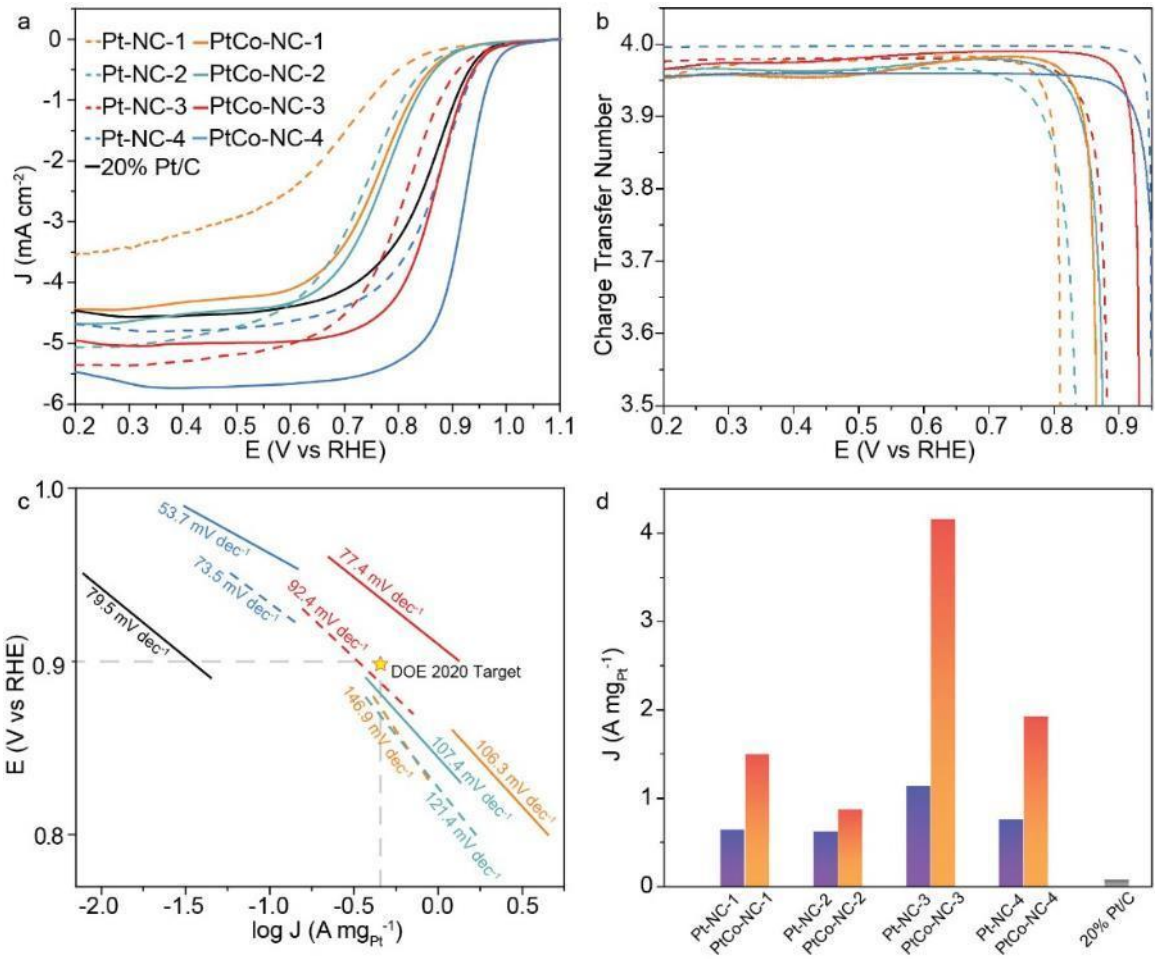

Figure 23. Electrocatalytic performance in oxygen reduction reaction. (a) LSV curves of (dashed curves) Pt-NC and (solid curves) PtCo-NC samples in 0.1 M $HClO_4$, and the corresponding (b) charge transfer number and (c) Tafel plots. In panel (c), the star marks the DOE 2020 target. (d) Mass activity of the samples and 20% Pt/C at +0.85 V vs RHE.

It should be noted that in the above measurements, the overall catalyst loading was kept constant at 0.16 mg cm^{-2} among the Pt-NC and PtCo-NC series, corresponding

to a clear variation of the Pt content in the catalysts, which has been known to impact the catalytic activity [58]. Thus, we carried out further measurements with the series of samples at a consistent Pt loading and compared the ORR performance. Figure 24 show the corresponding electrochemical data with the series of Pt-NC and PtCo-NC samples at the same Pt loading of ca. 3 μg cm^{-2}. Specifically, in comparison to the studies in Figure 23a, the catalyst loadings of Pt-NC-2 and PtCo-NC-2 were increased by 4 times, whereas the loadings of Pt-NC-4 and PtCo-NC-4 were reduced by 60% and that of commercial Pt/C by 90%. One can see that the $E_{½}$ of Pt-NC-2 and PtCo-NC-2 exhibited a positive shift of 20-40 mV, while $E_{½}$ of Pt-NC-4 and PtCo-NC-4 shifted negatively by 40 mV and that of commercial Pt/C by 170 mV. These observations suggest that the ORR activity decreased in the order of PtCo-NC-4 > Pt-NC-4~PtCo-NC-2 > Pt-NC-2 >> Pt/C, consistent with the results obtained from Figure 23a where the catalyst loadings were the same but the Pt contents were different, and further highlight the significant contribution of Pt-Co clustering to the enhancement of the ORR activity.

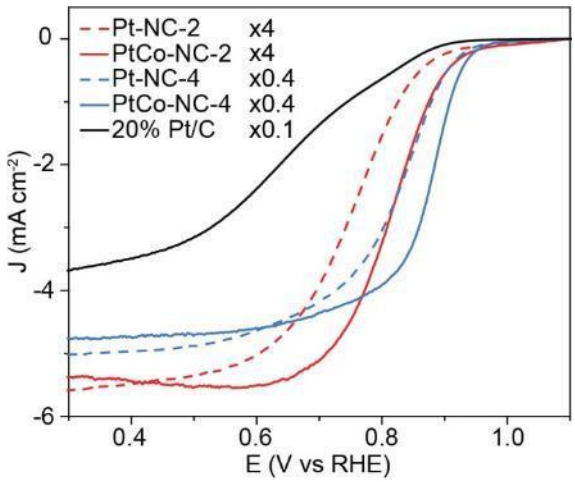

Figure 24. ORR polarization curves of the series of samples at the same Pt loading of ca. 3 μg_{Pt} cm^{-2}. In comparison to the those in Figure 23a, the catalyst loading of Pt-NC-2 and PtCo-NC-2 was increased by a factor of 4 to 0.64 mg cm^{-2}; the loading of Pt-NC-4 and PtCo-NC-4 was reduced by 60% at 0.064 mg cm^{-2}; and the loading of commercial 20% Pt/C was reduced by 90% to 0.016 mg cm^{-2}.

The stability of the samples was then tested. PtCo-NC-2 was found to exhibit a negative shift of only 30 mV after 5000 voltammetric cycles, a performance comparable to that of PtCo-NC-4 (Figure 25). This indicates that the stability of Pt single atoms/few-atom clusters was similar to that of small nanoparticles, and drastically better than that of commercial Pt/C [4, 15]. Yet in poisoning tests (Figure 26), the samples displayed markedly different behaviors. For PtCo-NC-4, which mainly contained PtCo nanoparticles, the ORR activity was drastically reduced upon the addition of SCN^-, whereas minimal impacts were observed after EDTA treatment. By contrast, for PtCo-NC-2 (consisting of few-atom clusters and single atoms), the

ORR electrocatalysis was significantly impeded by both SCN^- and EDTA. Note that SCN^- nondiscriminatorily poisoned single atoms, few-atom clusters and nanoparticles, whereas EDTA attacked predominantly single metal atoms. Therefore, the observed discrepancy of the poisoning effects further confirms the significant contribution of PtCo single atoms/few-atom clusters to the ORR activity in ultralow Pt-loading PtCo-NC.

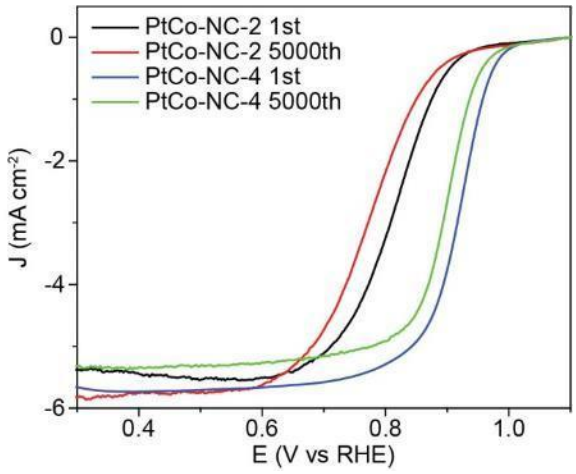

Figure 25. Stability tests of select samples. The catalyst loading of PtCo-NC-2 is 0.64 mg cm^{-2} (or 3 μg_{Pt} cm^{-2}), and that of PtCo-NC-4 is 0.16 mg cm^{-2} (or 10 μg_{Pt} cm^{-2}).

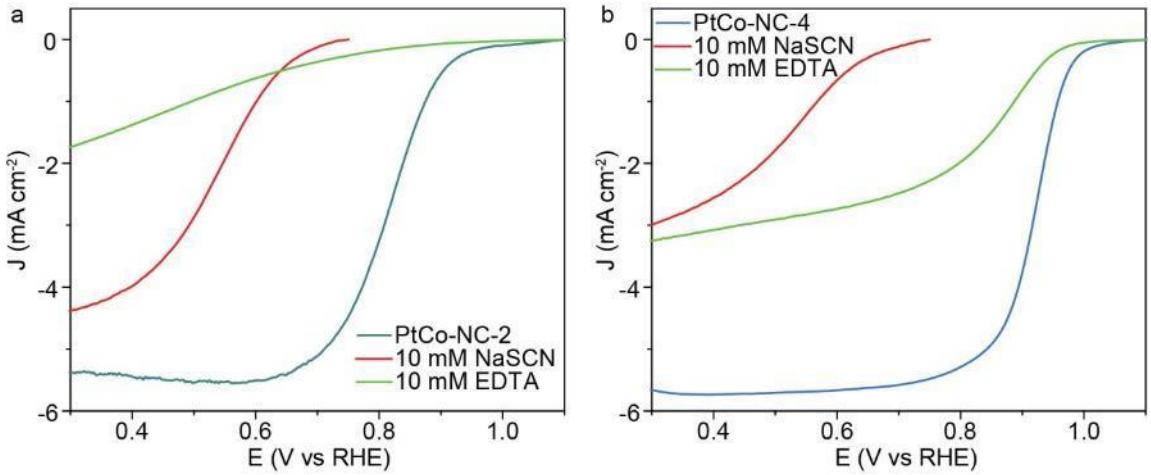

Figure 26. Poisoning test of (a) PtCo-NC-2 and (b) PtCo-NC-4. The NaSCN poisoning tests were carried out in 0.1 M $HClO_4$ with 10 mM NaSCN. The EDTA poisoning tests were measured in 0.1 M $HClO_4$ after the catalysts were treated in a solution of 1 M KOH and 10 mM EDTA at 60 °C overnight. The catalyst loading of PtCo-NC-2 was 0.64 mg cm^{-2} (or 3 μg_{Pt} cm^{-2}), and that of PtCo-NC-4 0.16 mg cm^{-2} (or 10 μg_{Pt} cm^{-2}).

4.4 Experimental section

Synthesis of tellurium nanowires. Tellurium nanowires (Te NWs) were prepared by following a procedure described previously [59]. For a typical experiment, 0.1844 g of Na_2TeO_3 and 2g of polyvinylpyrrolidone (PVP) were dissolved in 65 mL of nanopure water under vigorous stirring, into which were then injected 3.3 mL of N_2H_4 and 6.7 mL of ammonia. The solution was transferred to a 100 mL Teflon lined autoclave

container and heated at 180 °C for 3 h. The autoclave was cooled down naturally and stored in a 4 °C refrigerator for further use.

Synthesis of Te nanowires coated with melamine-formaldehyde resin. The preparation of core-shell nanofibers (Te-MF) consisting of Te nanowires coated with a melamine-formaldehyde (MF) resin shell has been detailed previously [32, 38]. In brief, 10 mL of Te NWs was centrifuged at 3000 rpm for 2 min with the addition of acetone as a precipitation agent. After washing with water and ethanol for 3 times, Te NWs were dispersed in 10 mL of water. Separately, 0.126 g of melamine in 10 mL of water was added into a 50 mL round-bottom flask, and the solution was heated at 90 °C under magnetic stirring, into which were then injected the Te NWs solution, 20 μL of 0.2 M NaOH, and 0.53 mL of formaldehyde. The solution was heated at 90 °C for 7 h before being cooled down naturally. The product was collected by centrifugation at 5000 rpm for 5 min, washed with water and ethanol, and dried in a freeze dryer for 24 h.

Synthesis of Pt and PtCo doped carbon nanowire. In a typical experiment, 100 mg of the Te-MF nanofibers obtained above was dispersed into 30 mL of nanopure water under magnetic stirring at 350 rpm and heated at 50 °C, into which was then added a varied amount of $PtCl_4$ (0.5, 1, 2, and 6 mg). The reaction was run 24 h, and the color of the solution was found to change from blue to pale white. The solids were then collected by centrifugation, and rinsed with water for several times. The obtained

product was equally divided into two parts. One part was directly dried with a freeze drier, while the other was mixed with a certain amount of $CoCl_2 \cdot 6H_2O$ (0.25, 0.5, 1, and 3 mg), and dried with a freeze drier. The mixtures were placed in a tube furnace and heated at a 900 °C for 3 h under a nitrogen flow of 200 cc min^{-1}. The resulting samples were denoted as Pt-NC-*y* or PtCo-NC-*y* with *y* = 1, 2, 3 and 4.

Characterization. Transmission electron microscopic (TEM) images and electron energy loss spectroscopic (EELS) data were acquired with a Nion U-HERMS200 microscope operated at 60 kV. High-angle annular dark field-scanning transmission electron microscopic (HAADF-STEM) studies were carried out with a probe semi-angle of 35 mrad at a spatial resolution of 0.11 nm. For EELS measurements, half convergence angle was set at 20 mrad, and a current was set at 150 pA with a dispersion of 0.268 eV $channel^{-1}$. The integral time for spectral collection of the Pt signals was 2 s, and that of C, N signal was 12 s. High-resolution TEM (HRTEM) studies and elemental mapping based on energy-dispersive X-ray spectroscopy (EDS) were acquired with a FEI Tecnai G2 TF20 transmission electron microscope operated at 200 kV. Inductively coupled plasma-optical emission spectrometry (ICP-OES) measurements were carried out with a SPECTRO BLUE SOP instrument. X-ray diffraction (XRD) studies were performed with a SmartLab 9 KW XRD system. Raman spectra were collected with a Laser Microscopic Confocal Raman Spectrometer. X-ray photoelectron spectroscopic (XPS) data were acquired with a PHI-5702 XPS instrument.

X-ray absorption spectroscopy (XAS). Co K-edge and Pt L_3-edge XAS data were collected at the CLS@APS (Sector 20-BM) beamline at the Advanced Photon Source (operating at 7.0 GeV) in Argonne National Laboratory, Chicago, IL, USA. Solid powder samples were loaded onto a Kapton tape and folded to ensure adequate signals. Samples were measured in the fluorescence mode simultaneously with each element foil reference. All measurements were conducted at room temperature and ambient pressure. Extended X-ray absorption fine structure (EXAFS) data was transformed and normalized into k- and R-space using the Athena program following conventional procedures. A k weighting of 2 was used to obtain all FT-EXAFS spectra. The k-range used for each sample is as follows: 3.9–8.7 $Å^{-1}$ for Pt-NC-1, 2.5–10.0 $Å^{-1}$ for Pt-NC-3, 3.0–10.7 $Å^{-1}$ for PtCo-NC-1-Co, 2.6–11.0 $Å^{-1}$ for PtCo-NC-1-Pt, 3.3–11.8 $Å^{-1}$ for PtCo-NC-3-Co, 3.4–10.3 $Å^{-1}$ for PtCo-NC-3-Pt. The R-range used for each element is as follows: 1.0-3.0 Å for Pt-NC-1, 1.0–3.4 Å for Pt-NC-3, 1.0–3.0 Å for PtCo-NC-1-Co, 1.0-2.4 Å for PtCo-NC-1-Pt, 1.0–3.4 Å for PtCo-NC-3-Co, 1.0–3.6 Å for PtCo-NC-3-Pt. Self-consistent multiple-scattering calculations were performed using the FEFF6 program to obtain the scattering amplitudes and phase-shift functions used to fit various scattering paths with the Artemis program. In the fitting of PtCo-NC-1 Co K-edge, the E_0 values were correlated together to minimize the number of independent values, allowing reliable fitting results to be obtained. For the PtCo-NC-3 sample the Co K-edge and Pt L_3-

edge were fitted simultaneously. The Pt-Co and Co-Pt bond distances were correlated, as well as the E_0 and σ^2 values for each individual element.

Electrochemistry. Electrochemical measurements were carried out with a CHI 710 electrochemical workstation in a conventional three-electrode configuration. A Ag/AgCl electrode in 0.1 M KCl was used as the reference electrode and a graphite rod as the counter electrode. The Ag/AgCl reference was calibrated against a reversible hydrogen electrode (RHE) and all potentials in the present study were referenced to this RHE. To prepare catalyst inks, 4 mg of the catalysts obtained above were added into 1 mL of ethanol and 10 μL of nafion solution under sonication to form a homogeneous dispersion. Ten μL of the ink was then dropcast onto a clean glassy carbon disk electrode (surface area 0.246 cm^2) at the catalyst loading of 0.16 mg cm^{-2}. iR compensation was set at 90% of solution resistance in all measurements. The number of electron transfer is calculated by $n = \frac{4i_d}{i_d + \frac{i_r}{N}}$, where i_d and i_r are the disk and ring currents, respectively and N is the collection efficiency of the ring electrode (0.37). The ORR performance was also tested with the series of samples at the same Pt loading of ca. 3 μg cm^{-2}. NaSCN poisoning test was carried out in a solution of 0.1 M $HClO_4$ and 10 mM NaSCN. EDTA poisoning test was carried out after treating the catalyst samples with 10 mM EDTA and 1 M KOH at 60 °C overnight.

Computational method. Computation studies were carried out with open-source plane wave code Quantum ESPRESSO [60]. A two-dimensional 8 x 8 supercell was built with a vacuum thickness set at 14 Å to avoid interaction between periodic images. The ultrasoft pseudopotential [61] was adopted with kinetic and charge density cutoff energy at 40 Ry and 240 Ry, respectively. A 2 x 2 x 1 Monkhorst-Pack K-point grid was sampled to converge the total energy to 10^{-3} eV. Marzari-Vanderbilt smearing [62] was adopted with 0.01 Ry. For the geomatic relaxation, the electronic energy was converged to 10^{-6} Ry and force converge to 10^{-4} a.u., respectively. Density functional perturbation theory (DFPT) [63] was employed to compute the vibration frequencies of surface species for zero-point energy (ZPE) and entropy contribution, similar as previous work [32, 38]. Atomic charge was analyzed based on Bader charge partitioning scheme [64].

4.5 Conclusion

In summary, two significant findings were obtained in this study. First, Pt~9 clusters were found to represent the threshold domain size of platinum towards ORR electrocatalysis in acid, whereas smaller clusters exhibited only limited ORR activity, as compared to conventional nanoparticles and bulk forms. Second, the electrocatalytic activity of few-atom Pt clusters can be markedly enhanced by clustering with Co atomic species, as clearly manifested in both theoretical calculations and experimental measurements, and Pt2~7 clusters doped with Co

atoms were found to be the optimal sample, with a mass activity that was almost 50 times that of commercial Pt/C. This was accounted for by the formation of Pt-Co bonding interactions that facilitated the adsorption of important oxygen intermediates. Results from this study highlight the fundamental significance of atomic alloying in diminishing the threshold size of precious metal catalysts to the few-atom cluster level. The minimization of catalyst cost and remarkable enhancement of electrocatalytic performance is anticipated to play a critical role in the eventual practical implementation of electrochemical energy technologies.

4.6 Reference

1. Pegis, M. L.; Wise, C. F.; Martin, D. J.; Mayer, J. M., Oxygen Reduction by Homogeneous Molecular Catalysts and Electrocatalysts. *Chem Rev* **2018,** *118* (5), 2340-2391.

2. Kulkarni, A.; Siahrostami, S.; Patel, A.; Norskov, J. K., Understanding Catalytic Activity Trends in the Oxygen Reduction Reaction. *Chem Rev* **2018,** *118* (5), 2302-2312.

3. Cheng, F. Y.; Chen, J., Metal-air batteries: from oxygen reduction electrochemistry to cathode catalysts. *Chem Soc Rev* **2012,** *41* (6), 2172-2192.

4. Zhou, Z.-Y.; Kang, X.; Song, Y.; Chen, S., Enhancement of the electrocatalytic activity of Pt nanoparticles in oxygen reduction by chlorophenyl functionalization. *Chem. Commun.* **2012,** *48* (28), 3391-3393.

5. Nie, Y.; Li, L.; Wei, Z. D., Recent advancements in Pt and Pt-free catalysts for oxygen reduction reaction. *Chem Soc Rev* **2015,** *44* (8), 2168-2201.

6. Xiong, Y.; Yang, Y.; DiSalvo, F. J.; Abruna, H. D., Metal-Organic-Framework-Derived Co-Fe Bimetallic Oxygen Reduction Electrocatalysts for Alkaline Fuel Cells. *J. Am. Chem. Soc.* **2019,** *141* (27), 10744-10750.

7. Shen, H. J.; Gracia-Espino, E.; Ma, J. Y.; Zang, K. T.; Luo, J.; Wang, L.; Gao, S. S.; Mamat, X.; Hu, G. Z.; Wagberg, T.; Guo, S. J., Synergistic Effects between Atomically Dispersed Fe-N-C and C-S-C for the Oxygen Reduction Reaction in Acidic Media. *Angew. Chem. Int. Ed.* **2017,** *56* (44), 13800-13804.

8. Chen, P.; Zhou, T.; Xing, L.; Xu, K.; Tong, Y.; Xie, H.; Zhang, L.; Yan, W.; Chu, W.; Wu, C.; Xie, Y., Atomically Dispersed Iron–Nitrogen Species as Electrocatalysts for Bifunctional Oxygen Evolution and Reduction Reactions. *Angew. Chem. Int. Ed.* **2017,** *56* (2), 610-614.

9. Frank, B.; Kahl, P.; Podbiel, D.; Spektor, G.; Orenstein, M.; Fu, L. W.; Weiss, T.; Horn-von Hoegen, M.; Davis, T. J.; zu Heringdorf, F. J. M.; Giessen, H., Short-range surface plasmonics: Localized electron emission dynamics from a 60-nm spot on an atomically flat single-crystalline gold surface. *Sci. Adv.* **2017,** *3* (7), e1700721.

10. Wang, Z. X.; Yao, X. Z.; Kang, Y. Q.; Miao, L. Q.; Xia, D. S.; Gan, L., Structurally Ordered Low-Pt Intermetallic Electrocatalysts toward Durably High Oxygen Reduction Reaction Activity. *Adv. Funct. Mater.* **2019,** *29* (35), 1902987.

11. Wang, R. H.; Wang, L.; Zhou, W.; Chen, Y. J.; Yan, H. J.; Ren, Z. Y.; Tian, C. G.; Shi, K. Y.; Fu, H. G., Ni2P Entwined by Graphite Layers as a Low-Pt Electrocatalyst in Acidic Media for Oxygen Reduction. *ACS Appl. Mater. Interfaces* **2018,** *10* (12), 9999-10010.

12. Saha, S.; Rodas, J. A. C.; Tan, S.; Li, D. M., Performance evaluation of platinum-molybdenum carbide nanocatalysts with ultralow platinum loading on anode and cathode catalyst layers of proton exchange membrane fuel cells. *J. Power Sources* **2018,** *378*, 742-749.

13. Liu, Y.; Kelly, T. G.; Chen, J. G.; Mustain, W. E., Metal Carbides as Alternative Electrocatalyst Supports. *ACS Catal.* **2013,** *3* (6), 1184-1194.

14. Yamamoto, K.; Imaoka, T.; Chun, W.-J.; Enoki, O.; Katoh, H.; Takenaga, M.; Sonoi, A., Size-specific catalytic activity of platinum clusters enhances oxygen reduction reactions. *Nat. Chem.* **2009,** *1* (5), 397-402.

15. Peng, Y.; Lu, B.; Chen, S., Carbon-Supported Single Atom Catalysts for Electrochemical Energy Conversion and Storage. *Adv Mater* **2018,** *30* (48), 1801995.

16. Song, X.; Li, N.; Zhang, H.; Wang, H.; Wang, L.; Bian, Z., Promotion of hydrogen peroxide production on graphene-supported atomically dispersed platinum: Effects of size on oxygen reduction reaction pathway. *Journal of Power Sources* **2019,** *435*, 226771.

17. Choi, C. H.; Kim, M.; Kwon, H. C.; Cho, S. J.; Yun, S.; Kim, H.-T.; Mayrhofer, K. J. J.; Kim, H.; Choi, M., Tuning selectivity of electrochemical

reactions by atomically dispersed platinum catalyst. *Nat. Commun.* **2016,** *7* (1), 10922.

18. Yang, S.; Tak, Y. J.; Kim, J.; Soon, A.; Lee, H., Support Effects in Single-Atom Platinum Catalysts for Electrochemical Oxygen Reduction. *ACS Catal.* **2017,** *7* (2), 1301-1307.

19. Yang, S.; Kim, J.; Tak, Y. J.; Soon, A.; Lee, H., Single-Atom Catalyst of Platinum Supported on Titanium Nitride for Selective Electrochemical Reactions. *Angew. Chem. Int. Ed.* **2016,** *55* (6), 2058-2062.

20. Li, T.; Liu, J.; Song, Y.; Wang, F., Photochemical Solid-Phase Synthesis of Platinum Single Atoms on Nitrogen-Doped Carbon with High Loading as Bifunctional Catalysts for Hydrogen Evolution and Oxygen Reduction Reactions. *Acs Catal* **2018,** *8* (9), 8450-8458.

21. Dong, J.-C.; Zhang, X.-G.; Briega-Martos, V.; Jin, X.; Yang, J.; Chen, S.; Yang, Z.-L.; Wu, D.-Y.; Feliu, J. M.; Williams, C. T.; Tian, Z.-Q.; Li, J.-F., In situ Raman spectroscopic evidence for oxygen reduction reaction intermediates at platinum single-crystal surfaces. *Nat. Energy* **2019,** *4* (1), 60-67.

22. Mayrhofer, K. J. J.; Blizanac, B. B.; Arenz, M.; Stamenkovic, V. R.; Ross, P. N.; Markovic, N. M., The impact of geometric and surface electronic properties of Pt-catalysts on the particle size effect in electocatalysis. *J. Phys. Chem. B* **2005,** *109* (30), 14433-14440.

23. Stamenkovic, V. R.; Fowler, B.; Mun, B. S.; Wang, G.; Ross, P. N.; Lucas, C. A.; Marković, N. M., Improved Oxygen Reduction Activity on

Pt₃Ni(111) via Increased Surface Site Availability. *Science* **2007,** *315* (5811), 493-497.

24. Stamenkovic, V.; Mun, B. S.; Mayrhofer, K. J. J.; Ross, P. N.; Markovic, N. M.; Rossmeisl, J.; Greeley, J.; Nørskov, J. K., Changing the Activity of Electrocatalysts for Oxygen Reduction by Tuning the Surface Electronic Structure. *Angew. Chem. Int. Ed.* **2006,** *45* (18), 2897-2901.

25. Strasser, P.; Koh, S.; Anniyev, T.; Greeley, J.; More, K.; Yu, C.; Liu, Z.; Kaya, S.; Nordlund, D.; Ogasawara, H.; Toney, M. F.; Nilsson, A., Lattice-strain control of the activity in dealloyed core–shell fuel cell catalysts. *Nat. Chem.* **2010,** *2* (6), 454-460.

26. Liu, H.-l.; Nosheen, F.; Wang, X., Noble metal alloy complex nanostructures: controllable synthesis and their electrochemical property. *Chem. Soc. Rev.* **2015,** *44* (10), 3056-3078.

27. Oezaslan, M.; Strasser, P., Activity of dealloyed PtCo3 and PtCu3 nanoparticle electrocatalyst for oxygen reduction reaction in polymer electrolyte membrane fuel cell. *J. Power Sources* **2011,** *196* (12), 5240-5249.

28. Chong, L.; Wen, J. G.; Kubal, J.; Sen, F. G.; Zou, J. X.; Greeley, J.; Chan, M.; Barkholtz, H.; Ding, W. J.; Liu, D. J., Ultralow-loading platinum-cobalt fuel cell catalysts derived from imidazolate frameworks. *Science* **2018,** *362* (6420), 1276-+.

29. Chai, G. L.; Hou, Z.; Shu, D. J.; Ikeda, T.; Terakura, K., Active sites and mechanisms for oxygen reduction reaction on nitrogen-doped carbon alloy catalysts:

Stone-Wales defect and curvature effect. *J. Am. Chem. Soc.* **2014,** *136* (39), 13629-40.

30. Viswanathan, V.; Hansen, H. A.; Rossmeisl, J.; Norskov, J. K., Universality in Oxygen Reduction Electrocatalysis on Metal Surfaces. *ACS Catal.* **2012,** *2* (8), 1654-1660.

31. Peng, Y.; Lu, B.; Wang, N.; Li, L.; Chen, S., Impacts of interfacial charge transfer on nanoparticle electrocatalytic activity towards oxygen reduction. *Phys. Chem. Chem. Phys.* **2017,** *19* (14), 9336-9348.

32. Lu, B. Z.; Smart, T. J.; Qin, D. D.; Lu, J. E.; Wang, N.; Chen, L. M.; Peng, Y.; Ping, Y.; Chen, S. W., Nitrogen and Iron-Codoped Carbon Hollow Nanotubules as High-Performance Catalysts toward Oxygen Reduction Reaction: A Combined Experimental and Theoretical Study. *Chem. Mater.* **2017,** *29* (13), 5617-5628.

33. Li, M. T.; Zhang, L. P.; Xu, Q.; Niu, J. B.; Xia, Z. H., N-doped graphene as catalysts for oxygen reduction and oxygen evolution reactions: Theoretical considerations. *J. Catal.* **2014,** *314*, 66-72.

34. Darby, M. T.; Stamatakis, M.; Michaelides, A.; Sykes, E. C. H., Lonely Atoms with Special Gifts: Breaking Linear Scaling Relationships in Heterogeneous Catalysis with Single-Atom Alloys. *J. Phys. Chem. Lett.* **2018,** *9* (18), 5636-5646.

35. He, Z.; Yang, Y.; Liu, J.-W.; Yu, S.-H., Emerging tellurium nanostructures: controllable synthesis and their applications. *Chem. Soc. Rev.* **2017,** *46* (10), 2732-2753.

36. Yang, Y.; Liu, J.-W.; Yu, S.-H., Coiling ultrathin tellurium nanowires into nanorings by Pickering emulsion. *Chem. Commun.* **2016,** *52* (52), 8091-8094.

37. Zhang, W.; Wu, Z. Y.; Jiang, H. L.; Yu, S. H., Nanowire-Directed Templating Synthesis of Metal-Organic Framework Nanofibers and Their Derived Porous Doped Carbon Nanofibers for Enhanced Electrocatalysis. *J. Am. Chem. Soc.* **2014,** *136* (41), 14385-14388.

38. Lu, B. Z.; Guo, L.; Wu, F.; Peng, Y.; Lu, J. E.; Smart, T. J.; Wang, N.; Finfrock, Y. Z.; Morris, D.; Zhang, P.; Li, N.; Gao, P.; Ping, Y.; Chen, S. W., Ruthenium atomically dispersed in carbon outperforms platinum toward hydrogen evolution in alkaline media. *Nat. Commun.* **2019,** *10*, 631.

39. Jamil, R.; Sohail, M.; Baig, N.; Ansari, M. S.; Ahmed, R., Synthesis of Hollow Pt-Ni Nanoboxes for Highly Efficient Methanol Oxidation. *Sci. Rep.* **2019,** *9*, 15273

40. Qiao, B. T.; Wang, A. Q.; Yang, X. F.; Allard, L. F.; Jiang, Z.; Cui, Y. T.; Liu, J. Y.; Li, J.; Zhang, T., Single-atom catalysis of CO oxidation using Pt-1/FeOx. *Nat. Chem.* **2011,** *3* (8), 634-641.

41. Wei, H. S.; Liu, X. Y.; Wang, A. Q.; Zhang, L. L.; Qiao, B. T.; Yang, X. F.; Huang, Y. Q.; Miao, S.; Liu, J. Y.; Zhang, T., FeOx-supported platinum single-atom and pseudo-single-atom catalysts for chemoselective hydrogenation of functionalized nitroarenes. *Nat. Commun.* **2014,** *5*, 5634.

42. Itoi, H.; Nishihara, H.; Kobayashi, S.; Ittisanronnachai, S.; Ishii, T.; Berenguer, R.; Ito, M.; Matsumura, D.; Kyotani, T., Fine Dispersion of Pt4-5

Subnanoclusters and Pt Single Atoms over Porous Carbon Supports and Their Structural Analyses with X-ray Absorption Spectroscopy. *J. Phys. Chem. C* **2017,** *121* (14), 7892-7902.

43. Sun, M. H.; Ji, J. P.; Hu, M. Y.; Weng, M. Y.; Zhang, Y. P.; Yu, H. S.; Tang, J. J.; Zheng, J. C.; Jiang, Z.; Pan, F.; Liang, C. D.; Lin, Z., Overwhelming the Performance of Single Atoms with Atomic Clusters for Platinum-Catalyzed Hydrogen Evolution. *ACS Catal.* **2019,** *9* (9), 8213-8223.

44. Liu, C. G.; Zhang, L. L.; Chen, X. M., CO oxidation over the polyoxometalate-supported single-atom catalysts M-1/POM (Fe, Co, Mn, Ru, Rh, Os, Ir, and Pt; POM = [PW12O40](3-)): a computational study on the activation of surface oxygen species. *Dalton Trans.* **2019,** *48* (18), 6228-6235.

45. Kaito, T.; Tanaka, H.; Mitsumoto, H.; Sugawara, S.; Shinohara, K.; Ariga, H.; Uehara, H.; Takakusagi, S.; Asakura, K., In Situ X-ray Absorption Fine Structure Analysis of PtCo, PtCu, and PtNi Alloy Electrocatalysts: The Correlation of Enhanced Oxygen Reduction Reaction Activity and Structure. *J. Phys. Chem. C* **2016,** *120* (21), 11519-11527.

46. Frenkel, A. I.; Yevick, A.; Cooper, C.; Vasic, R., Modeling the Structure and Composition of Nanoparticles by Extended X-Ray Absorption Fine-Structure Spectroscopy. *Annu. Rev. Anal. Chem.* **2011,** *4* (1), 23-39.

47. Wang, J.; Huang, Z.; Liu, W.; Chang, C.; Tang, H.; Li, Z.; Chen, W.; Jia, C.; Yao, T.; Wei, S.; Wu, Y.; Li, Y., Design of N-Coordinated Dual-Metal Sites: A

Stable and Active Pt-Free Catalyst for Acidic Oxygen Reduction Reaction. *J. Am. Chem. Soc.* **2017,** *139* (48), 17281-17284.

48. Han, Y.; Wang, Y.-G.; Chen, W.; Xu, R.; Zheng, L.; Zhang, J.; Luo, J.; Shen, R.-A.; Zhu, Y.; Cheong, W.-C.; Chen, C.; Peng, Q.; Wang, D.; Li, Y., Hollow N-Doped Carbon Spheres with Isolated Cobalt Single Atomic Sites: Superior Electrocatalysts for Oxygen Reduction. *J. Am. Chem. Soc.* **2017,** *139* (48), 17269-17272.

49. Kanan, M. W.; Yano, J.; Surendranath, Y.; Dincă, M.; Yachandra, V. K.; Nocera, D. G., Structure and Valency of a Cobalt−Phosphate Water Oxidation Catalyst Determined by in Situ X-ray Spectroscopy. *J. Am. Chem. Soc.* **2010,** *132* (39), 13692-13701.

50. Jiang, K.; Zhao, D.; Guo, S.; Zhang, X.; Zhu, X.; Guo, J.; Lu, G.; Huang, X., Efficient oxygen reduction catalysis by subnanometer Pt alloy nanowires. *Sci. Adv.* **2017,** *3* (2), e1601705.

51. Liu, J.; Jiao, M.; Lu, L.; Barkholtz, H. M.; Li, Y.; Wang, Y.; Jiang, L.; Wu, Z.; Liu, D.-j.; Zhuang, L.; Ma, C.; Zeng, J.; Zhang, B.; Su, D.; Song, P.; Xing, W.; Xu, W.; Wang, Y.; Jiang, Z.; Sun, G., High performance platinum single atom electrocatalyst for oxygen reduction reaction. *Nat Commun* **2017,** *8* (1), 15938.

52. Li, J.; Zhang, B.; Chen, Y.; Zhang, J.; Yang, H.; Zhang, J.; Lu, X.; Li, G.; Qin, Y., Styrene hydrogenation performance of Pt nanoparticles with controlled size prepared by atomic layer deposition. *Catal. Sci. Technol.* **2015,** *5* (8), 4218-4223.

53. Vovk, E. I.; Kalinkin, A. V.; Smirnov, M. Y.; Klembovskii, I. O.; Bukhtiyarov, V. I., XPS Study of Stability and Reactivity of Oxidized Pt Nanoparticles Supported on TiO2. *J. Phys. Chem. C* **2017,** *121* (32), 17297-17304.

54. Shi, Q. R.; Zhu, C. Z.; Engelhard, M. H.; Du, D.; Lin, Y. H., Highly uniform distribution of Pt nanoparticles on N-doped hollow carbon spheres with enhanced durability for oxygen reduction reaction. *Rsc. Adv.* **2017,** *7* (11), 6303-6308.

55. Wang, D.; Xin, H. L.; Hovden, R.; Wang, H.; Yu, Y.; Muller, D. A.; DiSalvo, F. J.; Abruña, H. D., Structurally ordered intermetallic platinum–cobalt core–shell nanoparticles with enhanced activity and stability as oxygen reduction electrocatalysts. *Nature Materials* **2013,** *12* (1), 81-87.

56. Guo, S. J.; Li, D. G.; Zhu, H. Y.; Zhang, S.; Markovic, N. M.; Stamenkovic, V. R.; Sun, S. H., FePt and CoPt Nanowires as Efficient Catalysts for the Oxygen Reduction Reaction. *Angew. Chem. Int. Ed.* **2013,** *52* (12), 3465-3468.

57. Wang, C.; van der Vliet, D.; Chang, K.-C.; You, H.; Strmcnik, D.; Schlueter, J. A.; Markovic, N. M.; Stamenkovic, V. R., Monodisperse Pt3Co Nanoparticles as a Catalyst for the Oxygen Reduction Reaction: Size-Dependent Activity. *J. Phys. Chem. C* **2009,** *113* (45), 19365-19368.

58. Mayrhofer, K. J. J.; Strmcnik, D.; Blizanac, B. B.; Stamenkovic, V.; Arenz, M.; Markovic, N. M., Measurement of oxygen reduction activities via the rotating disc electrode method: From Pt model surfaces to carbon-supported high surface area catalysts. *Electrochim. Acta* **2008,** *53* (7), 3181-3188.

59. Liu, J.-W.; Zhu, J.-H.; Zhang, C.-L.; Liang, H.-W.; Yu, S.-H., Mesostructured Assemblies of Ultrathin Superlong Tellurium Nanowires and Their Photoconductivity. *J. Am. Chem. Soc.* **2010,** *132* (26), 8945-8952.

60. Giannozzi, P.; Baroni, S.; Bonini, N.; Calandra, M.; Car, R.; Cavazzoni, C.; Ceresoli, D.; Chiarotti, G. L.; Cococcioni, M.; Dabo, I.; Dal Corso, A.; de Gironcoli, S.; Fabris, S.; Fratesi, G.; Gebauer, R.; Gerstmann, U.; Gougoussis, C.; Kokalj, A.; Lazzeri, M.; Martin-Samos, L.; Marzari, N.; Mauri, F.; Mazzarello, R.; Paolini, S.; Pasquarello, A.; Paulatto, L.; Sbraccia, C.; Scandolo, S.; Sclauzero, G.; Seitsonen, A. P.; Smogunov, A.; Umari, P.; Wentzcovitch, R. M., QUANTUM ESPRESSO: a modular and open-source software project for quantum simulations of materials. *J. Phys. Condens. Matter* **2009,** *21* (39).

61. Garrity, K. F.; Bennett, J. W.; Rabe, K. M.; Vanderbilt, D., Pseudopotentials for high-throughput DFT calculations. *Comp. Mater. Sci.* **2014,** *81*, 446-452.

62. Marzari, N.; Vanderbilt, D.; De Vita, A.; Payne, M. C., Thermal contraction and disordering of the Al(110) surface. *Phys. Rev. Lett.* **1999,** *82* (16), 3296-3299.

63. Baroni, S.; de Gironcoli, S.; Dal Corso, A.; Giannozzi, P., Phonons and related crystal properties from density-functional perturbation theory. *Rev. Mod. Phys.* **2001,** *73* (2), 515-562.

64. Yu, M.; Trinkle, D. R., Accurate and efficient algorithm for Bader charge integration. *J. Chem. Phys.* **2011,** *134* (6), 064111.

Chapter 5 Charge transfer induced activity enhancement

-Examples of oxygen vacancy doped TiO2 enhance the activity of ethanol oxidation catalyzed by Pd nanoparticles, and black phosphorus donate electrons to loaded Pt, Ag and Au nanoparticles for ORR activity change

5.1 Abstract

Nanocomposites based on Pd nanoparticles deposited onto TiO_2 nanobelts were successfully prepared by chemical reduction of Pd(II) precursors and the catalytic activity towards ethanol oxidation reaction (EOR) was examined and compared within the context of TiO_2 oxygen vacancies formed by thermal annealing at controlled temperatures (400, 500, or 600 C) in a hydrogen atmosphere. Transmission electron microscopic measurements showed that the Pd nanoparticles (about 5 nm in diameter) were clustered somewhat on the surfaces of hydrogen-treated TiO_2 nanobelts (Pd/hTiO_2), but distributed rather evenly on the untreated ones (Pd/TiO_2). X-ray photoelectron spectroscopic studies suggested electron transfer from Ti to Pd in the Pd/hTiO_2 samples, as compared to Pd/TiO_2. This was accounted for by the formation of oxygen vacancies in TiO_2 nanobelts, the concentration of which increased with increasing thermal annealing temperature, as evidenced in electron paramagnetic resonance measurements. Significantly, voltammetric and electrochemical impedance measurements showed markedly enhanced electrocatalytic activity of Pd/TiO_2 and Pd/hTiO_2 hybrids towards EOR in alkaline

media, as compared to commercial 20 wt.% Pd/C, and the activity increased drastically with the concentration of oxygen vacancies, within the context of onset and peak potentials, anodic peak current density, electron-transfer kinetics and stability. This was most likely because oxygen vacancies facilitated the formation of hydroxyl species on the oxide surface that played a critical role in the oxidation of ethanol to acetate.

5.2 Introduction

Direct ethanol fuel cells (DEFCs) represent a unique fuel cell technology that has been attracting extensive interest, largely because of the remarkable energy density of ethanol (8.01 KWh/Kg), ready availability of ethanol by fermentation, low toxicity, and ease of storage and transportation, as compared to other fuels such as hydrogen, methanol and formic acid.[1] In addition, ethanol has a large molecule weight that can minimize the "crossover" effect.[2-4] While both acid and alkaline electrolytes have been used in DEFCs, the electron-transfer kinetics of both ethanol oxidation at the anode and oxygen reduction at the cathode has been found to be faster in alkaline media than in acidic media.[5] In general, there are two major pathways of ethanol oxidation in alkaline media. One involves 12-electron, complete oxidation of ethanol to CO_3^{2-}, and the other is a 4-electron process, where ethanol is oxidized into acetaldehyde and acetate only.[6] Certainly, to maximize fuel cell efficiency, the former pathway is desired; however, it is challenging to break the C-C bonds. Thus, developing catalysts for effective oxidation of ethanol has remained an important

research topic of alkaline DEFCs. Currently, platinum-based nanoparticles have been the catalysts of choice for DEFC reactions.[7] Yet, because of high costs and limited reserves, the practical applications of Pt-based catalysts have been markedly hampered; in addition, platinum-based catalysts are known to be prone to CO poisoning.[8]

Within such a context, palladium-based nanoparticles have been used as an effective alternative for the electrocatalytic oxidation of ethanol, largely because of its apparent EOR activity and tolerance against CO poisoning.[9, 10] Two strategies are generally employed to improve the use of the catalysts (and thus to reduce the costs) and to enhance the activity. One is to prepare binary or trinary alloys, where the activities may be enhanced by the electronic effects and/or geometrical strains. For example, Jeon et al. prepared a series of graphene-supported Pd_xNi_{100-x} alloy nanoparticles and found that the $Pd_{50}Ni_{50}$ sample exhibited the best activity among the series toward ethanol oxidation, with acetic acid being the primary product.[11] Jiang et al. used P dopants to successfully increase EOR performance of PdNi alloys and observed that acetate was the final product.[12] In another study,[13] Li and coworkers grew PdCo nanotubes on carbon fiber cloth, and the resulting nanocomposites exhibited enhanced EOR activity and resistance against CO poisoning, as compared to the monometallic Pd counterparts. The other strategy involves the use of appropriate materials as the catalyst supports, which may exert synergistic effects on the electronic structure of the metal catalysts as well as enhance the durability of the catalysts. These include, for instance, N-doped carbon,[14] molybdenum carbide,[15]

tungsten carbide,[16] titanium nitride,[17] etc. In addition, transition-metal oxides have also been used as catalyst supports,[18-23] primarily because of their low costs, high natural abundance, low toxicity and high durability in alkaline media.[24] Among these, in contrast to other metal oxides such as Al_2O_3 and SiO_2, TiO_2 is a reducible oxide and can generate oxygen vacancies upon controlled chemical reduction, which may be exploited as a unique variable in the manipulation of the electrocatalytic activity of the metal nanoparticles towards ethanol oxidation.[25-29] Note that for ethanol oxidation on palladium catalysts, it is generally accepted that the dissociative adsorption of ethanol onto the catalyst surface is a rapid process, and the rate-determining step is the desorption of the ethoxi moieties (CH_3CO_{ads}) by adsorbed hydroxyl groups (OH_{ads}) on the Pd surface, forming acetate as the final product.[12, 30] This may be facilitated by using oxygen-deficient TiO_2 as the supporting substrate, where oxygen vacancies are known to be advantageous for the formation of OH_{ads} species.[31, 32] Additional benefits may arise from the strong metal-support interactions that manipulate the bonding interactions between palladium and carboneous intermediates.[25] This is the primary motivation of the present study.

Herein, a facile wet chemistry method was employed to deposit palladium nanoparticles on TiO_2 nanobelts. Oxygen vacancies in TiO_2 were produced by thermal treatment at elevated temperatures in a hydrogen atmosphere, and evaluated by electron paramagnetic resonance measurements. Electrochemical measurements showed that the resulting nanocomposites exhibited apparent electrocatalytic activity

towards ethanol oxidation, which was markedly enhanced with oxygen vacancies, in comparison to commercial Pd/C catalysts.

5.3 Result and Discussion

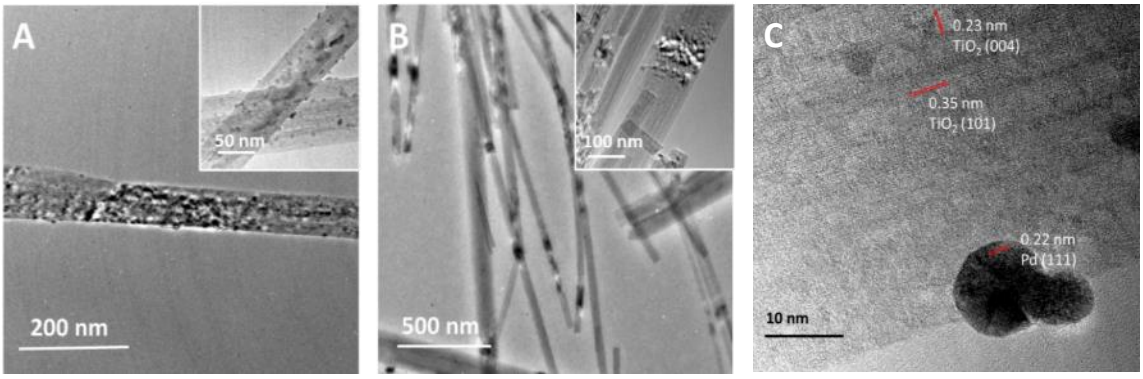

Figure 1. Representative TEM images of (A) Pd/TiO_2 and (B) Pd/hTiO_2-600. Insets show the corresponding TEM images at higher magnification. Panel (C) is a high-resolution TEM image of Pd/TiO_2 hybrids that depicts the lattice fringes.

Figure 1 depicts the representative TEM images of the (A) Pd/TiO_2 and (B) Pd/hTiO_2-600 nanobelt hybrids, respectively. One can see that the TiO_2 nanobelts exhibited a width of *ca*. 70 nm and length ranging from a few hundred nm up to microns, along with well-defined lattice fringes (Figure 1C) where the interplanar distances of 0.23 nm and 0.35 nm were consistent with the d-spacings of the (004) and (101) crystalline planes of anatase TiO_2, respectively.[33] From Figure 1A, one can see that in Pd/TiO_2, a number of palladium nanoparticles of about 5 nm in diameter were rather uniformly distributed on the TiO_2 nanobelt surfaces, with no apparent

agglomeration. In contrast, for the Pd/hTiO_2-600 sample in Figure 1B, the Pd nanoparticles could be identified only on a certain section of the TiO_2 nanobelts, forming a bamboo-like structure of the resulting hybrids. This is likely because after hydrogen treatment, the TiO_2 nanobelt surface was (partially) reduced, and the sections with enhanced electron density served as the preferred binding sites for Pd deposition. Furthermore, one can see that the palladium nanoparticles also exhibited well-defined lattice fringes where the interplanar spacing of 0.22 nm is in good agreement with the separation of the (111) crystalline planes of *fcc* Pd (Figure 1C).[23] Consistent behaviors were observed with Pd/hTiO_2-400 and Pd/hTiO_2-500.

The formation of Pd/TiO_2 and Pd/hTiO_2 nanocomposites was also evidenced in XPS measurements. From the survey spectra in Figure 2A, the Pd 3d electrons can be readily identified at ca. 335 eV, Pd 3p electrons at 562 eV, Ti 2p electrons at 458 eV and O 1s electrons at 531 eV (along with C 1s electrons of residual carbon at around 285 eV) for both Pd/TiO_2 and Pd/hTiO_2 hybrids. In high-resolution scans, one can see from panel (B) that the Pd 3d electrons exhibited a doublet at 340.6 and 335.3 eV for Pd/TiO_2, corresponding to a spin-orbit coupling of 5.3 eV, consistent with those of metallic Pd;[34] and the binding energies are about 0.4 eV lower for Pd/hTiO_2 at 340.2 and 334.9 eV. From panel (C), the doublet for Ti $2p_{3/2}$ and $2p_{1/2}$ electrons can be found at 458.8 and 464.5 eV for Pd/TiO_2, with a spin-orbit coupling of 5.7 eV, in good agreement with Ti(IV) in TiO_2;[35, 36] yet in Pd/hTiO_2 the binding energies are somewhat higher at 459.0 and 464.8 eV. This suggests charge transfer from Ti to Pd, likely due to the formation of oxygen vacancies by hydrogen treatment of the TiO_2

nanobelts. For O 1s electrons in panel (D), Pd/TiO_2 exhibited two peaks at the binding energies of 530.1 and 532.6 eV, which may be ascribed to oxygen in TiO_2 and hydroxyl groups adsorbed on the TiO_2 surfaces, respectively.[37] For Pd/hTiO_2, whereas the binding energy of surface hydroxyl groups remained invariant at 532.6 eV, the TiO_2 oxygen binding energy is somewhat higher at 530.3 eV, suggesting that the TiO_2 nanobelts indeed became oxygen-deficient after hydrogen treatment.[38] In addition, based on the integrated peak areas, the Pd mass contents in the nanocomposites were found to be rather consistent at 13.3 wt.% for Pd/TiO_2 and 15.1 wt.% for Pd/hTiO_2.

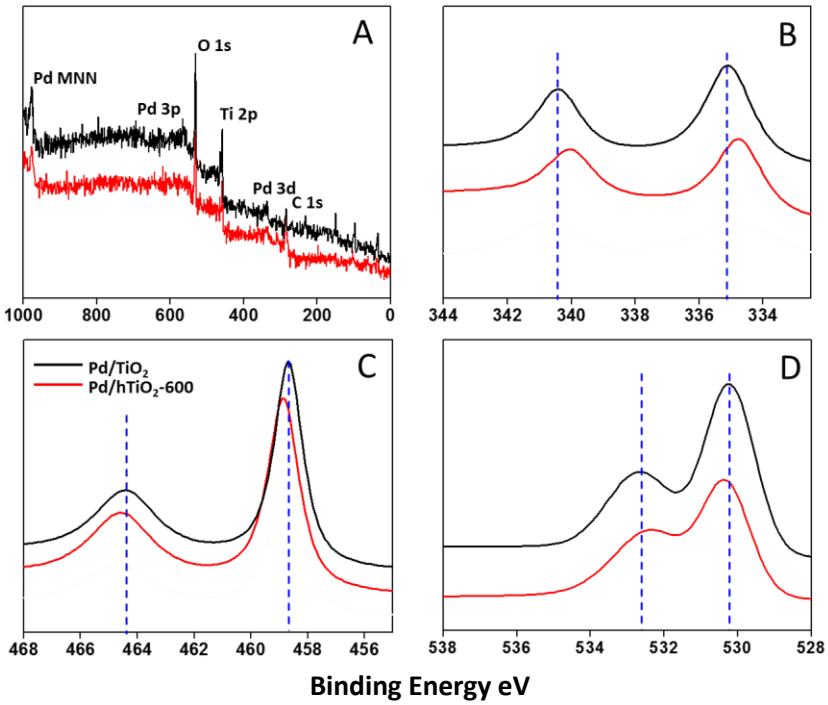

Figure 2. (A) XPS survey spectra and high resolution scans of (B) Pd 3d, (C) Ti 2p and (D) O 1s electrons of Pd/TiO_2 and Pd/hTiO_2-600 nanocomposites..

EPR studies further supported the notion that oxygen vacancies were formed in the nanocomposites that had been subjected to hydrogen treatment. As shown in Figure 3, one can see that the as-produced TiO_2 nanobelts (black curve) exhibited only a featureless profile within the magnetic field strength of 3360 to 3385 G, and a similar response was observed after Pd deposition (red curve), suggesting that $NaBH_4$ reduction (for the synthesis of Pd nanoparticle) did not cause marked changes of the TiO_2 structures. Yet, a well-defined resonance emerged at *ca*. 3370 G after hydrogen treatment (green curve), and the resonance became increasingly intensified with increasing thermal treatment temperature from 400 to 600 C (aqua blue, magenta, and blue curves), with the corresponding g value estimated to be 2.001.[39] This suggests the formation of unpaired electrons being trapped in TiO_2, as a result of partial reduction of TiO_2 by hydrogen treatment,[40-44] and the concentration of oxygen vacancies increased with increasing thermal annealing temperature, consistent with the results in XPS measurements (Figure 2).

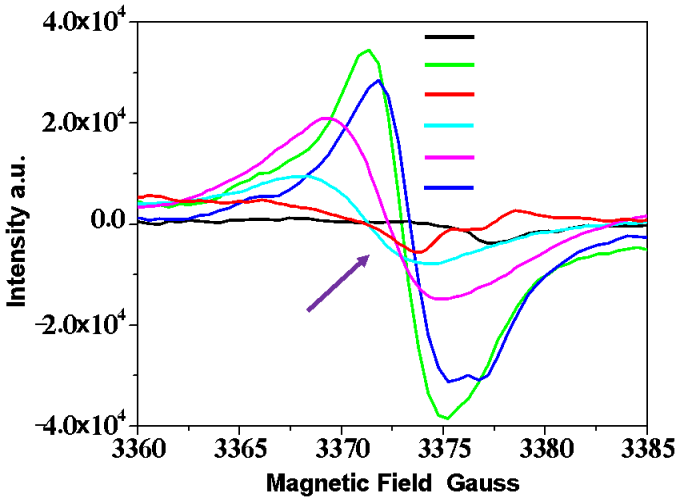

Figure 3. EPR spectra of TiO_2 nanobelts, Pd/TiO_2, and Pd/TiO_2-T nanocomposites

Significantly, the nanocomposites prepared above exhibited apparent electrocatalytic activity towards ethanol oxidation. Figure 4 shows the cyclic voltammograms of the nanocomposites in 1 M KOH with and without 0.1 M ethanol at the potential sweep rate of 50 mV/s, using commercial 20 wt.% Pd/C as the reference. It can be seen that in 1 M KOH alone, all samples exhibited a cathodic peak at +0.634 V, arising from the reduction of palladium oxide formed during the anodic scan. From the integrated peak area,[45] the effective electrochemical surface area (ECSA, Table 1) of the nanocomposite catalysts was estimated to be 5.29 m^2/g_{Pd} for Pd/TiO_2, 14.2 m^2/g_{Pd} for Pd/hTiO_2-400, 6.15 m^2/g_{Pd} for Pd/hTiO_2-500, and 11.00 m^2/g_{Pd} for Pd/hTiO_2-600, in comparison with 18.35 m^2/g_{Pd} for Pd/C, likely due to the smaller size of the Pd nanoparticles in Pd/C than those in the nanocomposites (Figure 1).

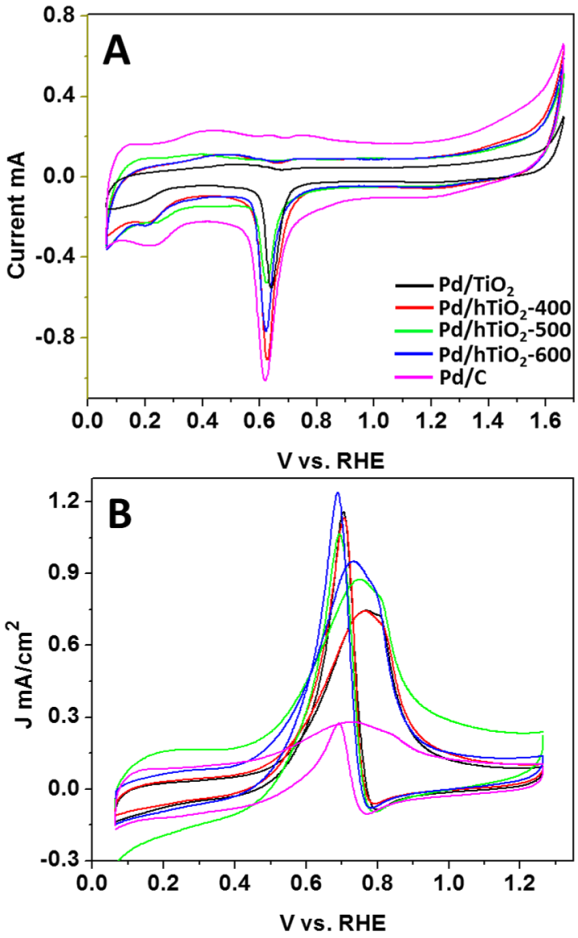

Figure 4. Cyclic voltammograms of a glassy carbon electrode (0.196 cm^2) modified with a calculated amount of Pd/TiO_2, $Pd/hTiO_2$ and Pd/C. The data in panel (A) were acquired in 1 M KOH only, and those in panel (B) were in a solution containing 1 M KOH along with 0.1 M ethanol. The potential scan rate is 50 mV/s. The catalyst loading is 100 μg for Pd/TiO_2 and $Pd/hTiO_2$ nanocomposites, and 50 μg for Pd/C.

Table 1. Summary of the EOR performance of Pd/TiO_2, $Pd/hTiO_2$-600 and Pd/C

Sample	*Pd/TiO$_2$*	*Pd/hTiO$_2$-600*	*Pd/C*
Loading wt% by XPS	13.3	15.1	20
Onset (V vs. RHE)	0.456	0.377	0.469
E_a (V vs. RHE)	0.769	0.728	0.730
J_a (mA/cm^2)	0.68	0.88	0.17
E_c (V vs. RHE)	0.703	0.687	0.692
J_c (mA/cm^2)	1.25	1.31	0.37
J_a/J_c	0.50	0.44	0.40
ECSA (m^2/g_{Pd})	5.29	11.00	18.35
R_{ct} (W, at +0.7 V)	1557	468	1328

With the addition of 0.1 M ethanol in the electrolyte solution, drastic differences were observed. From Figure 4B, one can see that all samples exhibited a clearly defined oxidation peak in both the anodic and cathodic scans at approximately the same electrode potentials, suggesting apparent electrocatalytic activity towards ethanol oxidation. Yet, a close analysis showed that the performance actually varied among

the series of the nanocomposites. For instance, for the Pd/TiO_2 nanocomposites, in the anodic scan, nonzero oxidation currents started to emerge at *ca*. +0.456 V, and reached a maximum at +0.769 V with a peak current density of 0.68 mA/cm^2; in the reverse potential scan, the oxidation peak appeared at +0.703 V with a current density of 1.25 mA/cm^2. Yet when TiO_2 nanobelts were subjected to hydrogen treatment prior to Pd nanoparticle deposition, the resulting nanocomposites exhibited markedly enhanced EOR activity. For instance, the onset potential, anodic peak potential, and anodic peak current density are +0.396 V, +0.767 V, and 0.65 mA/cm^2 for $Pd/hTiO_2$-400, +0.408 V, +0.748 V, and 0.70 mA/cm^2 for $Pd/hTiO_2$-500, and +0.377 V, +0.728 V and +0.88 mA/cm^2 for $Pd/hTiO_2$-600. Apparently, $Pd/hTiO_2$-600 stood out as the best among the series (Table 1). Remarkably, these nanocomposites all exhibited a drastically better performance than commercial 20 wt.% Pd/C, where the onset potential was identified at +0.464 V, anodic peak at +0.734 V (peak current density 0.17 mA/cm^2), and cathodic peak at +0.694 V (peak current density 0.37 mA/cm^2). These results are summarized in Table 1, from which one can see that the EOR performance increased in the order of Pd/C < Pd/TiO_2 < $Pd/hTiO_2$-400 < $Pd/hTiO_2$-500 < $Pd/hTiO_2$-600. A similar trend was observed with the mass activity, where the anodic mass activity of $Pd/hTiO_2$-600 (59.75 mA/mg_{Pd}) was about twice that of Pd/TiO_2 (33.06 mA/mg_{Pd}) and Pd/C (25.42 mA/mg_{Pd}), as showed in Figure 5.

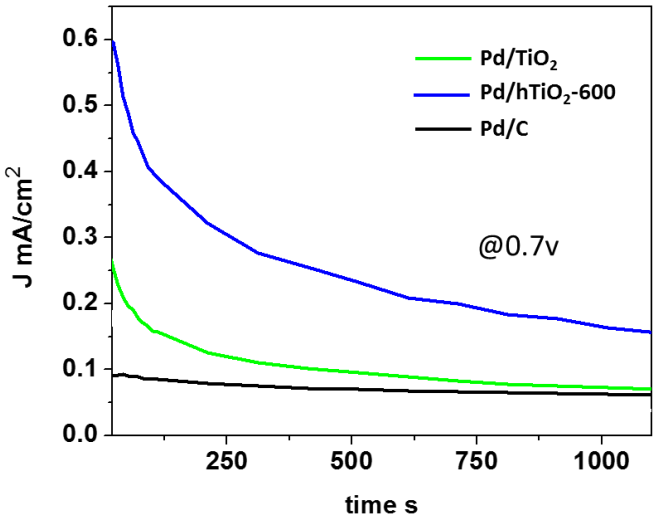

Figure 5. Mass-normalized voltammograms of Pd/TiO_2, $Pd/hTiO_2$-600 and Pd/C in 1 M KOH + 0.1 M EtOH. Potential scan rate 50 mV/s.

Mechanistically, the electrochemical oxidation of ethanol is generally believed to involve the following steps,[12, 30]

$$Pd + CH_3CH_2OH \rightarrow Pd\text{-}(CH_3CH_2OH)_{ads} \quad (1)$$

$$Pd\text{-}(CH_3CH_2OH)_{ads} + 3OH \rightarrow Pd\text{-}(CH_3CO)_{ads} + 3H_2O + 3e \quad (2)$$

$$Pd\text{-}(CH_3CO)_{ads} + Pd\text{-}(OH)_{ads} \rightarrow (Pd\text{-}CH_3COOH)_{ads} + Pd \quad (3)$$

$$(Pd\text{-}CH_3COOH)_{ads} + OH^- \rightarrow Pd + CH_3COO^- + H_2O \quad (4)$$

where adsorption of ethanol molecules on the Pd surfaces is a critical first step (1); the adsorbed ethanol then undergoes three-electron oxidation into ethoxi (2), which reacts further with surface hydroxyl groups to produce acetate (3); and the acetate then desorbs from the electrode surface as the final product (4). In the anodic scan,

the reaction kinetics was initially enhanced at increasingly positive electrode potentials, reached a maximum and then decreased with a further increase of the electrode potential because of the formation of palladium oxide, which passivated the catalyst surface. In the reverse (cathodic) scan, the palladium oxide was electrochemically reduced, leading to the formation of a "clean" catalyst surface that exhibited obvious electrocatalytic activity towards ethanol oxidation. Thus, a higher ratio of the anodic to cathodic peak currents (J_a/J_c) suggests the generation of less poisoning intermediates on the Pd surface.[11] From Figure 4B, the ratio was estimated to be 0.50 for Pd/TiO_2 and 0.44 for Pd/hTiO_2-600, both higher than that (0.40) of Pd/C (Table 1), again, suggesting that the efficiency in the electrocatalytic oxidation of ethanol increased in the order of Pd/C < Pd/TiO_2 < Pd/TiO_2.

In the present study, the fact that the electrocatalytic activity of Pd/TiO_2 and Pd/hTiO_2 nanocomposites was markedly better than that of Pd/C suggests a synergistic interaction between TiO_2 and Pd nanoparticles in ethanol oxidation reaction process. This can be accounted for by the strong interactions between TiO_2 and Pd, as TiO_2 favored the formation of $(OH)_{ads}$ which helped strip absorbed ethoxi intermediates from the Pd surface, and the impacts were enhanced with oxygen-deficient TiO_2, leading to improved activity in ethanol oxidation.[31, 32, 46] In the present study, Pd/TiO_2-600 outperformed others in the series because of its highest concentration of oxygen vacancies (Figure 3).

Table 2. Summary of EOR performance of relevant Pd-based catalysts in recent literature

sample	Onset potential V vs. RHE	Peak potential V vs. RHE	Peak current	Particle size
Pd/Au[47]	0.44	0.85	2.28 A/mg_{Pd+Au} (1 M KOH, 1 M EtOH)	10 nm
Pd/CNT[48]	0.50	0.90	0.58 A/mg_{Pd} (0.5 M KOH, 0.5 M EtOH)	2 nm
Pd/polyhedron[49]	0.387	0.747	2 A/mg_{Pd} (1 M KOH, 0.5 M EtOH)	2 nm
Pd/$NiCoO_x$[50]	0.443	0.903	0.43 A/mg_{Pd} (0.1 M KOH, 0.5 M EtOH)	5 nm
Pd/PEDOT[51]	0.470	0.770	3.4 mA/cm^2(1 M KOH, 1 M EtOH)	3.6 nm
Pd/MgO[52]	0.407	0.777	85 mA/cm^2(1 M KOH, 1 M EtOH)	10 nm
Pd/hTiO_2-600	0.377	0.728	0.88 mA/cm^2(1 M KOH, 0.1 M EtOH)	5 nm

Significantly, the EOR performance of Pd/hTiO_2-600 was highly comparable to, and in some cases even better than, results reported in recent studies with relevant Pd-based nanocomposites (Table 2). For instance, Cai et al. deposited a Pd monolayer on the surface of *ca*. 10 nm Au nanoparticles, and the catalysts showed an onset and peak potential at +0.44 V and +0.85 V, respectively, in a solution of 1 M KOH and 1 M EtOH, where the peak current was estimated to be 2.28 A/mg_{Pd+Au}, greater than that of commercial palladium black.[47] Lin et al. deposited 2 nm Pd nanoparticles on carbon nanotubes and observed a peak current of 0.58 A/mg_{Pd} in 0.5 M KOH and 0.5 M EtOH.[48] Gao et al. deposited 2 nm Pd nanoparticles on polyhedrin and the resulting nanocomposites showed the onset and peak potentials at +0.387 V and +0.747 V,

respectively.[49] Lei et al. prepared a nanocomposite by depositing 5 nm Pd and $NiCoO_x$ nanoparticles on carbon substrates, and the onset and peak potentials were identified at +0.443 V and +0.903 V, along with a peak current of 0.43 A/mg in the solution of 0.1 M KOH and 0.5 M EtOH.[50] Xu et al. loaded 3.6 nm Pd nanoparticles on 50 nm poly(3,4-ethyl-enedioxythiophene) particles, and the nanocomposite exhibited onset and peak potentials at +0.407 and +0.777 V.[51] Shen et al. used MgO as a support to load 10 nm Pd nanoparticles and found that the current density (85 mA/cm^2) was 3.4 times greater than that of Pd/C in 1 M KOH and 1 M EtOH. The onset and peak potentials were identified at +0.407 and +0.777 V, respectively.[52]

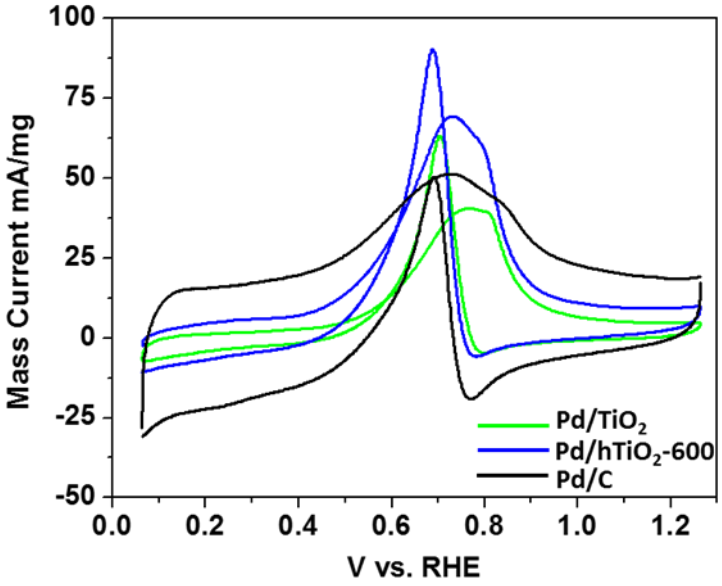

Figure 6. Chronoamperometric curves at +0.7 V with the same electrodes in Figure 4 in 1 M KOH and 0.1 M EtOH.

Durability is another important parameter in the evaluation of catalyst performance. Figure 6 depicts the chronoamperometric profiles of the various catalysts when the electrode potential was stepped from +0.1 V to +0.7 V (vs. RHE). It can be seen that the current density of the Pd/hTiO$_2$-600 sample remained the highest at all times (up to 1200 s). For instance, even after 1000 s of continuous operation, the Pd/hTiO$_2$-600 still showed a current density of 0.16 mA/cm^2, which was more than twice those of Pd/C (0.06 mA/cm^2) and Pd/TiO$_2$ (0.07 mA/cm^2).

The electron-transfer kinetics of ethanol oxidation at these nanocomposites was then examined by electrochemical impedance measurements. Figure 8 shows the Nyquist plots of ethanol oxidation catalyzed by the series of nanocomposites at +0.7 V. It can be seen that all samples show a semicircle, which was fitted well by the equivalent circuit depicted in the figure inset. From the fittings, the charge-transfer resistance (R_{ct}) was estimated to be 1557 W for Pd/TiO$_2$ and 1328 W for Pd/C, and markedly lower for the Pd/hTiO$_2$ series: 1081 W for Pd/hTiO$_2$-400, 813 W for Pd/hTiO$_2$-500, and 468 W for Pd/hTiO$_2$-600. Similar trends were observed at other electrode potentials (Figure 7). This is consistent with results in the voltammetric measurements (Figure 4) where the EOR activity increased with increasing thermal annealing temperature, due to the enhanced generation of oxygen vacancies that facilitated the formation of hydroxyl species needed for the oxidation of ethanol to acetate.

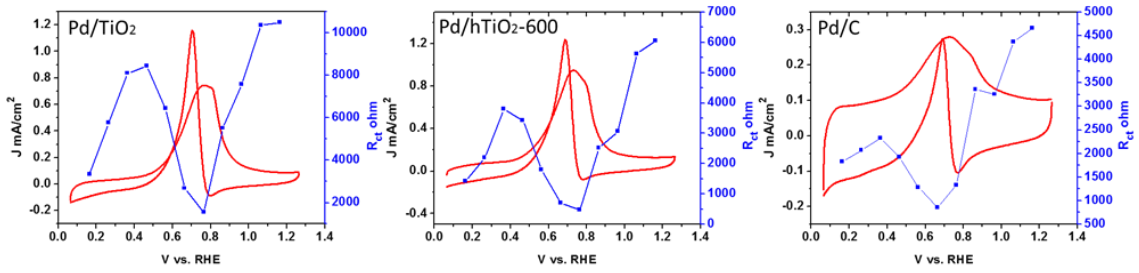

Figure 7. Cyclic voltammograms (red curves) and charge transfer resistance (R_{ct}, blue curves) of Pd/TiO_2, $Pd/hTiO_2$, and Pd/C catalysts in 1 M KOH and 0.1 M EtOH. CV scan rate 50 mV/s.

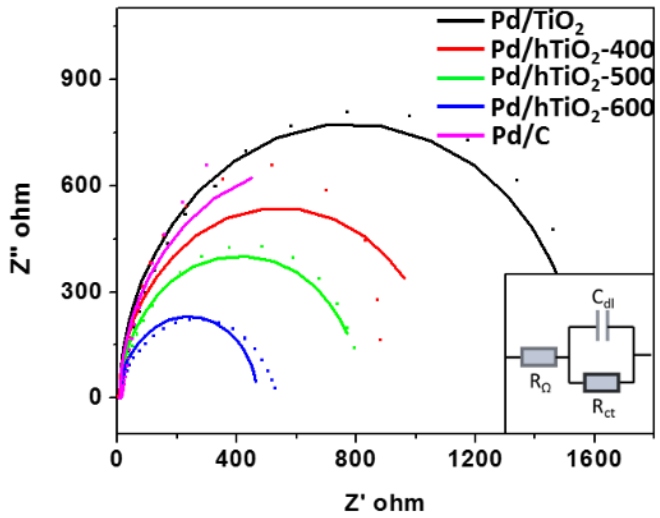

Figure 8. Nyquist plots of Pd/TiO_2, $Pd/hTiO_2$–T, and Pd/C electrodes at +0.7 V (vs. RHE). Symbols are experimental data and curves are fits by the equivalent circuit depicted in the inset, where R_W is the solution (uncompensated) resistance, R_{ct} is the charge-transfer resistance, and C_{dl} is the electrode double-layer capacitance.

5.4 Experiment

Materials

P25 titanium dioxide (TiO_2, Alfa Aesar), sodium hydroxide (NaOH, Fisher Scientific), hydrochloric acid (HCl, 37% v/v, Fisher Chemical), hydrogen gas (ultrahigh purity, Praxair), palladium(II) chloride ($PdCl_2$, Acros), trisodium citrate dehydrate (Fisher Scientific), sodium borohydride ($NaBH_4$, >98%, Acros), ethanol (EtOH, HPLC grade, Fisher Chemicals), and Pd/C (20 wt.%, *ca*. 4.6 nm in diameter,[53] Alfa Aesar) were used as received. Water was supplied from a Barnstead Nanopure water system (18.3 MW cm).

Synthesis of TiO_2 nanobelts

TiO_2 nanobelts were synthesized by adopting a hydrothermal process reported previously.[54] Briefly, 0.1 g of commercial P25 was mixed with 20 mL of a 10 M NaOH aqueous solution, followed by hydrothermal treatment at 200 C in Teflon-lined autoclave for 2 d. The obtained product was washed with Nanopure water for several times, affording sodium titanate nanobelts. These were then dipped in a 0.1 M HCl aqueous solution for 24 h and washed thoroughly with deionized water to produce hydrogen titanate nanobelts. Anatase TiO_2 nanobelts were obtained by annealing the hydrogen titanate at 600 C for 1 h in ambient. Further annealing of the obtained anatase TiO_2 nanobelts was carried out in a hydrogen atmosphere at varied temperatures (400, 500 or 600 C) for 1 h, affording hydrogen-treated TiO_2 nanobelts which were denoted as hTiO_2-T with T being the annealing temperature.[38]

Synthesis of Pd/TiO_2 and Pd/hTiO_2 nanocomposites

In a typical synthesis of the Pd/TiO_2 nanocomposites, 5 mg of the TiO_2 nanobelts obtained above was dispersed in 10 mL of Nanopure water under sonication for 30 min to form a homogeneous suspension. Then, 525 μL of 10 mM H_2PdCl_4 and 10 mL of 0.525 mM trisodium citrate were added under magnetic stirring for 2 h. After that, 5 mL of 30 mM $NaBH_4$ was added in a dropwise fashion at the controlled temperature of 10 C under vigorous stirring, and the solution was found to exhibit an apparent color change from orange to dark brown, signifying the formation of Pd nanoparticles. The solution was stirred for another 2 h and centrifuged at 3000 rpm for 5 min. The product was collected and washed by water and ethanol for several times and dried in a vacuum oven at room temperature overnight, affording Pd/TiO_2 nanocomposites. Palladium nanoparticles were also deposited on $hTiO_2$-T nanobelts in a similar fashion. The resulting nanocomposites were referred to as $Pd/hTiO_2$-T.

Characterization

The morphologies of the nanocomposites were characterized by transmission electron microscopy (TEM), with a Philips CM300 scope operated at 300 kV. Elemental composition and electronic structures were characterized by X-ray photoelectron spectroscopy (XPS) measurements with a PHI 5400/XPS instrument equipped with an Al K_α source operated at 350 W and 10^{-9} Torr. Electron paramagnetic resonance (EPR) measurements were carried out with a Bruker EMX EPR spectrometer at the X-band frequency (~ 9.4 GHz) using an ER 4122SHQE resonator. All spectra were recorded using a power of 1 mW, a modulation amplitude of 1 G, and a modulation frequency of 100 KHz.

Electrochemistry

Electrochemical tests were carried out with a CHI 440 electrochemical workstation in a conventional three-electrode configuration, with a glassy carbon working electrode, a Ag/AgCl reference and a Pt wire counter electrode. The Ag/AgCl reference was calibrated against a reversible hydrogen electrode (RHE) and the potentials in the present study were all reported with respect to the RHE. The glassy carbon electrode was first polished with 0.05 mm Al_2O_3 slurries to a mirror finish, and cleaned in dilute HNO_3 to remove residual Al_2O_3, followed by extensive rinsing with Nanopure water. To prepare catalyst inks, a calculated amount of the nanocomposites obtained above was suspended in ethanol at a concentration of 10 mg/mL. Then, into 1 mL of this suspension was added 4 mg of carbon black and 10 L of Nafion under sonication for 30 min. 10 L of the suspension was dropcast onto the polished glassy carbon electrode surface, onto which was then added 5 L of 20% Nafion. The electrode was dried in ambient before being immersed into electrolyte solutions for data acquisition. Electrochemical impedance measurements were performed with a Gamry Reference 600 electrochemical workstation within the frequency range of 100 mHz to 100 kHz and the AC amplitude of 5 mV.

5.5 Conclusion

In this study, a series of nanocomposites were prepared by depositing Pd nanoparticles onto TiO_2 nanobelts. Whereas Pd nanoparticles were rather homogeneously distributed on the as-prepared TiO_2 nanobelts, clustering of the

nanoparticles was observed when the nanobelts were subjected to thermal annealing in a hydrogen atmosphere, due to partial reduction of Ti(IV) to Ti(III) and the generation of oxygen vacancies, as confirmed by XPS and EPR measurements. This was found to facilitate electrocatalytic oxidation of ethanol in an alkaline solution. In fact, the electrocatalytic activity was found to increase with increasing concentration of oxygen vacancies in the nanocomposites, which might be ascribed to the ready generation of surface-adsorbed hydroxyl groups that were needed for the oxidation of ethanol to acetate. Within the context of onset potential, anodic and cathodic peak potentials, peak current density and electron-transfer kinetics, the sample prepared with TiO_2 thermally treated at 600 C stood out as the best catalyst among the series, with a performance markedly better than that of commercial Pd/C as well as leading results in recent literature on relevant catalysts. The results highlight the significance of structural defects of supporting substrates in the manipulation and engineering of nanoparticle electrocatalytic activity in ethanol oxidation.

5.6 Discussion about black phosphorus donate electrons to metal nanoparticles and ORR activity change

Similarly, the black phosphorus can donate electrons to the metal loaded on it and influence their catalytic activity.

Based on the structural models displayed in Figure 10, one can see from Figure 9 that interfacial charge transfer did occur from BP to metals, with 0.23, 0.12, and 0.02

electron gained per metal atom of Pt, Au and Ag, respectively. Note that this trend is consistent with the change of metal binding energy in XPS measurements, which is 0.53, 0.21 and 0.15 eV for Pt, Au and Ag, respectively, as compared to the carbon-supported counterparts.

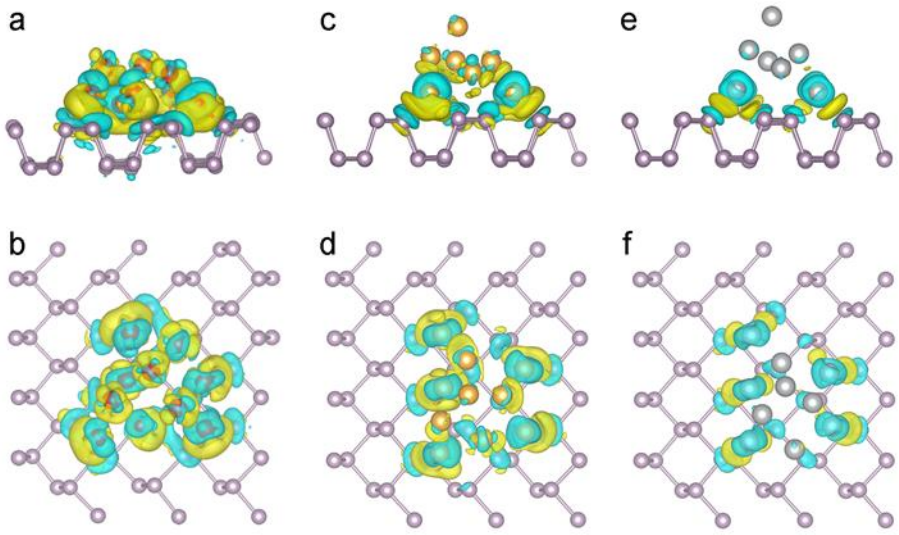

Figure 9. DFT calculations of charge transfer from BP to supported metal nanoparticles: (top) front view, and (bottom) top view. (a-b) Pt-BP; (c-d) Au-BP; (e-f) Ag-BP. The cyan area indicates electron loss and the yellow area indicates electron gain. The isosurface value is 0.003 e/au^3.

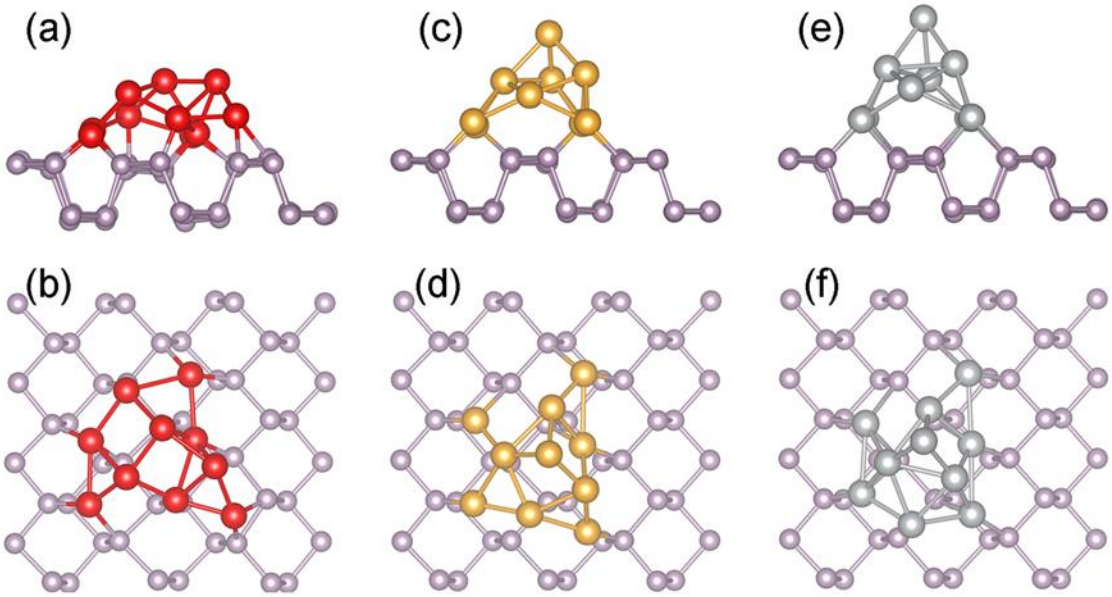

Figure 10. Structural models of M-BP for DFT calculations: (top) front view, and (bottom) top view. (a-b), Pt-BP; (c-d), Au-BP; (e-f), Ag-BP.

From Figure 11a, one can see that in comparison to M-CB, the mass activity at the potential of +0.8 V can be seen to increase by 99% for Ag-TLBP and 164% for Au-TLBP, but decreased by 50% for Pt-TLBP. Similarly, the $E_{1/2}$ of Ag-TLBP and Au-TLBP shifted positively by 46 mV and 90 mV, respectively, while Pt-TLBP shifted negatively by 47 mV, compared to the respective M-CB counterpart (Figure 11b). These can all be ascribed to interfacial charge transfer from TLBP to the supported metal nanoparticles that has been quantified by XPS measurements and DFT calculations (Figure 11c,d). Such a correlation between the ORR performance and electronic property can be understood within the "volcano plot" framework. As shown in Figure 11e, an increased electron density of Pt pushes the ORR activity further downhill, as the binding to oxygen species became too strong; whereas for Au

and Ag, increasing electron density pushes the ORR activity uphill due to enhanced binding to the oxygen intermediates.[55-58]

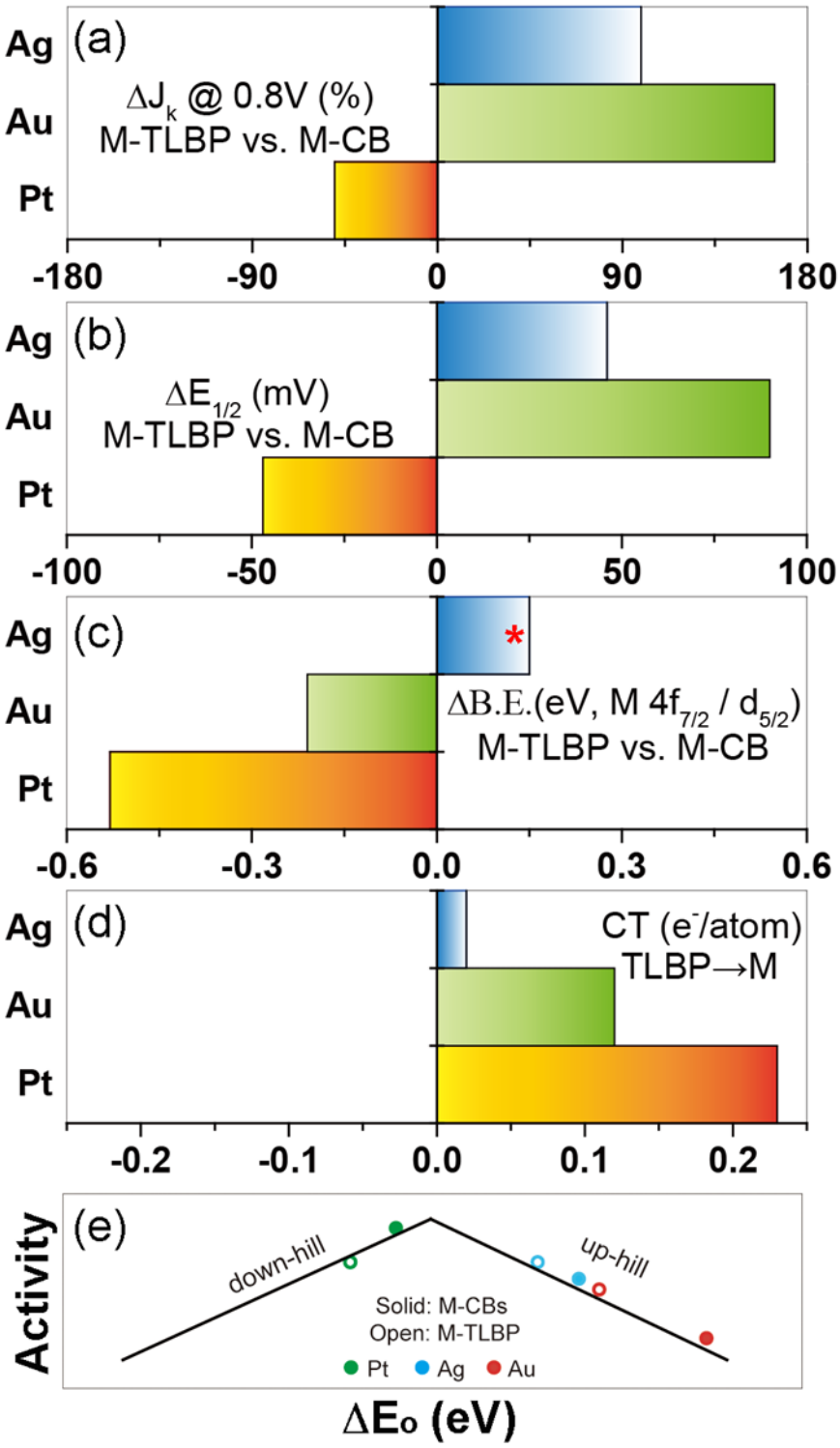
(a)
Ag
Au
Pt
ΔJk @ 0.8V (%)
M-TLBP vs. M-CB
-180
-90
0
90
180
(b)
ΔE1/2 (mV)
M-TLBP vs. M-CB
-100
-50
50
100
(c)
*
ΔB.E.(eV, M 4f7/2 / d5/2)
M-TLBP vs. M-CB
-0.6
-0.3
0.0
0.3
0.6
(d)
CT (e-/atom)
TLBP→M
-0.2
-0.1
0.1
0.2
(e)
Activity
down-hill
up-hill
Solid: M-CBs
Open: M-TLBP
Pt
Ag
Au
ΔEo (eV)

Figure 11. Comparative summary of ORR performance between M-TLBP and M-CB (or TLMP). Changes of (a) kinetic current density (J_k) at +0.8 V, (b) half-wave potential ($E_{1/2}$), and (c) binding energy (DBE) of the Pt $4f_{7/2}$, Au $4f_{7/2}$ and Ag $3d_{5/2}$ electrons between M-TLBP and M-CB, and P $2p_{3/2}$ electrons between M-TLBP and TLBP. (d) Schematic illustration of the effects of BP on the metal ORR performance within the "volcano plot" framework (note the axes are not in scale).

5.7 Reference

1. Bai, Y. X.; Wu, J. J.; Xi, J. Y.; Wang, J. S.; Zhu, W. T.; Chen, L. Q.; Qiu, X. P., Electrochemical oxidation of ethanol on Pt-ZrO2/C catalyst. *Electrochem Commun* **2005,** *7* (11), 1087-1090.

2. Pethaiah, S. S.; Arunkumar, J.; Ramos, M.; Al-Jumaily, A.; Manivannan, N., The impact of anode design on fuel crossover of direct ethanol fuel cell. *Bulletin of Materials Science* **2016,** *39* (1), 273-278.

3. Almheiri, S.; Liu, H. T., Direct measurement of methanol crossover fluxes underland and channel in direct methanol fuel cells. *Int J Hydrogen Energ* **2015,** *40* (34), 10969-10978.

4. Yamaguchi, T.; Zhou, H.; Nakazawa, S.; Hara, N., An extremely low methanol crossover and highly durable aromatic pore-filling electrolyte membrane for direct methanol fuel cells. *Adv Mater* **2007,** *19* (4), 592-+.

5. Huang, C. Y.; Lin, J. S.; Pan, W. H.; Shih, C. M.; Liu, Y. L.; Lue, S. J., Alkaline direct ethanol fuel cell performance using alkali-impregnated polyvinyl alcohol/functionalized carbon nano-tube solid electrolytes. *J Power Sources* **2016,** *303*, 267-277.

6. Wang, Y.; Zou, S. Z.; Cai, W. B., Recent Advances on Electro-Oxidation of Ethanol on Pt- and Pd-Based Catalysts: From Reaction Mechanisms to Catalytic Materials. *Catalysts* **2015,** *5* (3), 1507-1534.

7. Yu, W. T.; Porosoff, M. D.; Chen, J. G. G., Review of Pt-Based Bimetallic Catalysis: From Model Surfaces to Supported Catalysts. *Chem Rev* **2012,** *112* (11), 5780-5817.

8. Ahmed, M. S.; Park, D.; Jeon, S., Ultrasmall PdmMn1-mOx binary alloyed nanoparticles on graphene catalysts for ethanol oxidation in alkaline media. *J Power Sources* **2016,** *308*, 180-188.

9. Idriss, H., Ethanol Reactions over the Surfaces of Noble Metal/Cerium Oxide Catalysts. *Platinum Metals Review* **2004,** *48* (3), 105-115.

10. He, Q. G.; Chen, W.; Mukerjee, S.; Chen, S. W.; Laufek, F., Carbon-supported PdM (M = Au and Sn) nanocatalysts for the electrooxidation of ethanol in high pH media. *Journal of Power Sources* **2009,** *187* (2), 298-304.

11. Ahmed, M. S.; Jeon, S., Highly Active Graphene-Supported NixPd100-x Binary Alloyed Catalysts for Electro-Oxidation of Ethanol in an Alkaline Media. *Acs Catal* **2014,** *4* (6), 1830-1837.

12. Jiang, R. Z.; Tran, D. T.; McClure, J. P.; Chu, D., A Class of (Pd-Ni-P) Electrocatalysts for the Ethanol Oxidation Reaction in Alkaline Media. *Acs Catal* **2014,** *4* (8), 2577-2586.

13. Wang, A. L.; He, X. J.; Lu, X. F.; Xu, H.; Tong, Y. X.; Li, G. R., Palladium-Cobalt Nanotube Arrays Supported on Carbon Fiber Cloth as High-Performance Flexible Electrocatalysts for Ethanol Oxidation. *Angewandte Chemie-International Edition* **2015,** *54* (12), 3669-3673.

14. Jin, H. Y.; Xiong, T. Y.; Li, Y.; Xu, X.; Li, M. M.; Wang, Y., Improved electrocatalytic activity for ethanol oxidation by Pd@N-doped carbon from biomass. *Chem Commun* **2014,** *50* (84), 12637-12640.

15. Yan, Z. X.; Xie, J. M.; Shen, P. K.; Zhang, M. M.; Zhang, Y.; Chen, M., Pd supported on 2-4 nm MoC particles with reduced particle size, synergistic effect and high stability for ethanol oxidation. *Electrochim Acta* **2013,** *108*, 644-650.

16. Hu, F. P.; Cui, G. F.; Wei, Z. D.; Shen, P. K., Improved kinetics of ethanol oxidation on Pd catalysts supported on tungsten carbides/carbon nanotubes. *Electrochem Commun* **2008,** *10* (9), 1303-1306.

17. Thotiyl, M. M. O.; Kumar, T. R.; Sampath, S., Pd Supported on Titanium Nitride for Efficient Ethanol Oxidation. *J Phys Chem C* **2010,** *114* (41), 17934-17941.

18. Ito, Y.; Takeuchi, T.; Tsujiguchi, T.; Abdelkareem, M. A.; Nakagawa, N., Ultrahigh methanol electro-oxidation activity of PtRu nanoparticles prepared on TiO2-embedded carbon nanofiber support. *J Power Sources* **2013,** *242*, 280-288.

19. Ju, J. F.; Shi, Y. J.; Wu, D. H., TiO2 nanotube supported PdNi catalyst for methanol electro-oxidation. *Powder Technol* **2012,** *230*, 252-256.

20. Kang, S. H.; Sung, Y. E.; Smyrl, W. H., The effectiveness of sputtered PtCo catalysts on TiO2 nanotube arrays for the oxygen reduction reaction. *J Electrochem Soc* **2008,** *155* (11), B1128-B1135.

21. Liu, K.; Song, Y.; Chen, S. W., Defective TiO2-supported Cu nanoparticles as efficient and stable electrocatalysts for oxygen reduction in alkaline media. *Nanoscale* **2015,** *7* (3), 1224-1232.

22. Maheswari, S.; Sridhar, P.; Pitchumani, S., Pd-TiO2/C as a methanol tolerant catalyst for oxygen reduction reaction in alkaline medium. *Electrochemistry Communications* **2013,** *26*, 97-100.

23. Qin, Y. H.; Li, Y. F.; Lam, T.; Xing, Y. C., Nitrogen-doped carbon-TiO2 composite as support of Pd electrocatalyst for formic acid oxidation. *J Power Sources* **2015,** *284*, 186-193.

24. Li, W.; Bai, Y.; Li, F. J.; Liu, C.; Chan, K. Y.; Feng, X.; Lu, X. H., Core-shell TiO2/C nanofibers as supports for electrocatalytic and synergistic photoelectrocatalytic oxidation of methanol. *J Mater Chem* **2012,** *22* (9), 4025-4031.

25. Jang, M. H.; Agarwal, R.; Nukala, P.; Choi, D.; Johnson, A. T. C.; Chen, I. W.; Agarwal, R., Observing Oxygen Vacancy Driven Electroforming in Pt-TiO2-Pt Device via Strong Metal Support Interaction. *Nano Lett* **2016,** *16* (4), 2139-2144.

26. Santara, B.; Giri, P. K.; Dhara, S.; Imakita, K.; Fujii, M., Oxygen vacancy-mediated enhanced ferromagnetism in undoped and Fe-doped TiO2 nanoribbons. *J Phys D Appl Phys* **2014,** *47* (23).

27. Khan, M.; Li, J.; Cao, W. B.; Mansoor, B.; Rehman, F., Effect of oxygen vacancy on the improved photocatalytic activity of Cr-doped TiO2. *Int J Mod Phys B* **2014,** *28* (25).

28. Liu, L. J.; Gao, F.; Zhao, H. L.; Li, Y., Tailoring Cu valence and oxygen vacancy in Cu/TiO2 catalysts for enhanced CO2 photoreduction efficiency. *Applied Catalysis B-Environmental* **2013,** *134*, 349-358.

29. Liu, P.; Zhao, Y.; Qin, R.; Mo, S.; Chen, G.; Gu, L.; Chevrier, D. M.; Zhang, P.; Guo, Q.; Zang, D.; Wu, B.; Fu, G.; Zheng, N., Photochemical route for synthesizing atomically dispersed palladium catalysts. *Science* **2016,** *352* (6287), 797-800.

30. Liang, Z.; Zhao, T.; Xu, J.; Zhu, L., Mechanism study of the ethanol oxidation reaction on palladium in alkaline media. *Electrochim Acta* **2009,** *54* (8), 2203-2208.

31. Bagheri, S.; Muhd Julkapli, N.; Bee Abd Hamid, S., Titanium dioxide as a catalyst support in heterogeneous catalysis. *The Scientific World Journal* **2014,** *2014*.

32. Song, Y. Y.; Wei, C. H.; Zhang, X. L.; Wei, X.; Song, X. P.; Sun, Z. B., Nanoporous Pd/TiO2 composites prepared by one-step dealloying and their electrocatalytic performance for methanol/ethanol oxidation. *Materials Chemistry and Physics* **2015,** *161*, 153-161.

33. Wu, H. B.; Hng, H. H.; Lou, X. W. D., Direct synthesis of anatase TiO2 nanowires with enhanced photocatalytic activity. *Adv Mater* **2012,** *24* (19), 2567-2571.

34. Brun, M.; Berthet, A.; Bertolini, J., XPS, AES and Auger parameter of Pd and PdO. *Journal of electron spectroscopy and related phenomena* **1999,** *104* (1), 55-60.

35. Qin, X. Q.; He, F.; Chen, L. X.; Meng, Y. H.; Liu, J.; Zhao, N. Q.; Huang, Y., Oxygen-vacancy modified TiO2 nanoparticles as enhanced visible-light driven photocatalysts by wrapping and chemically bonding with graphite-like carbon. *Rsc Adv* **2016,** *6* (13), 10887-10894.

36. Palanisamy, B.; Babu, C. M.; Sundaravel, B.; Anandan, S.; Murugesan, V., Sol-gel synthesis of mesoporous mixed Fe2O3/TiO2 photocatalyst: application for degradation of 4-chlorophenol. *J Hazard Mater* **2013,** *252-253*, 233-42.

37. Zoulalian, V.; Zurcher, S.; Tosatti, S.; Textor, M.; Monge, S.; Robin, J. J., Self-assembly of poly(ethylene glycol)-poly(alkyl phosphonate) terpolymers on titanium oxide surfaces: synthesis, interface characterization, investigation of nonfouling properties, and long-term stability. *Langmuir* **2010,** *26* (1), 74-82.

38. Wang, G.; Wang, H.; Ling, Y.; Tang, Y.; Yang, X.; Fitzmorris, R. C.; Wang, C.; Zhang, J. Z.; Li, Y., Hydrogen-treated TiO2 nanowire arrays for photoelectrochemical water splitting. *Nano Lett* **2011,** *11* (7), 3026-3033.

39. Sweeney, S. W.; Roseman, G.; Deming, C. P.; Wang, N.; Nguyen, T. A.; Millhauser, G. L.; Chen, S. W., Impacts of oxygen vacancies on the electrocatalytic

activity of AuTiO2 nanocomposites towards oxygen reduction. *International Journal of Hydrogen Energy* **2016,** *41* (40), 18005-18014.

40. Su, T.; Yang, Y. L.; Na, Y.; Fan, R. Q.; Li, L.; Wei, L. G.; Yang, B.; Cao, W. W., An Insight into the Role of Oxygen Vacancy in Hydrogenated TiO2 Nanocrystals in the Performance of Dye-Sensitized Solar Cells. *Acs Appl Mater Inter* **2015,** *7* (6), 3754-3763.

41. Pan, X.; Yang, M. Q.; Fu, X.; Zhang, N.; Xu, Y. J., Defective TiO2 with oxygen vacancies: synthesis, properties and photocatalytic applications. *Nanoscale* **2013,** *5* (9), 3601-14.

42. Wajid Shah, M.; Zhu, Y.; Fan, X.; Zhao, J.; Li, Y.; Asim, S.; Wang, C., Facile Synthesis of Defective TiO2-x Nanocrystals with High Surface Area and Tailoring Bandgap for Visible-light Photocatalysis. *Scientific reports* **2015,** *5*, 15804.

43. Pan, X.; Xu, Y.-J., Defect-Mediated Growth of Noble-Metal (Ag, Pt, and Pd) Nanoparticles on TiO2with Oxygen Vacancies for Photocatalytic Redox Reactions under Visible Light. *The Journal of Physical Chemistry C* **2013,** *117* (35), 17996-18005.

44. Pan, X. Y.; Xu, Y. J., Fast and spontaneous reduction of gold ions over oxygen-vacancy-rich TiO2: A novel strategy to design defect-based composite photocatalyst. *Applied Catalysis a-General* **2013,** *459*, 34-40.

45. Sarkar, S.; Jana, R.; Suchitra; Waghmare, U. V.; Kuppan, B.; Sampath, S.; Peter, S. C., Ordered Pd2Ge Intermetallic Nanoparticles as Highly Efficient and Robust Catalyst for Ethanol Oxidation. *Chem Mater* **2015,** *27* (21), 7459-7467.

46. Zhang, J.; Zhang, M.; Jin, Z.; Wang, J.; Zhang, Z., Study of high-temperature hydrogen reduced Pt 0/TiO 2 by X-ray photoelectron spectroscopy combined with argon ion sputtering—Diffusion-encapsulation effect in relation to strong metal–support interaction. *Applied Surface Science* **2012,** *258* (8), 3991-3999.

47. Wang, H.; Jiang, K.; Chen, Q. L.; Xie, Z. X.; Cai, W. B., Carbon monoxide mediated chemical deposition of Pt or Pd quasi-monolayer on Au surfaces with superior electrocatalysis for ethanol oxidation in alkaline media. *Chem Commun* **2016,** *52* (2), 374-377.

48. Yang, G. H.; Zhou, Y. Z.; Pan, H. B.; Zhu, C. Z.; Fu, S. F.; Wai, C. M.; Du, D.; Zhu, J. J.; Lin, Y. H., Ultrasonic-assisted synthesis of Pd-Pt/carbon nanotubes nanocomposites for enhanced electro-oxidation of ethanol and methanol in alkaline medium. *Ultrason Sonochem* **2016,** *28*, 192-198.

49. Pang, G. G.; Sun, M. X.; Liu, P.; Hou, L.; Gao, F. M., Facile synthesis of Pd nanostructures with enhanced electrocatalytic performance for ethanol oxidation by a bio-based method. *Rsc Adv* **2016,** *6* (24), 19734-19741.

50. Wang, W.; Yang, Y.; Liu, Y. Q.; Zhang, Z.; Dong, W. K.; Lei, Z. Q., Hybrid NiCoOx adjacent to Pd nanoparticles as a synergistic electrocatalyst for ethanol oxidation. *J Power Sources* **2015,** *273*, 631-637.

51. Yue, R. R.; Wang, H. W.; Bin, D.; Xu, J. K.; Du, Y. K.; Lu, W. S.; Guo, J., Facile one-pot synthesis of Pd-PEDOT/graphene nanocomposites with hierarchical structure and high electrocatalytic performance for ethanol oxidation. *J Mater Chem A* **2015,** *3* (3), 1077-1088.

52. Li, N.; Zeng, Y. X.; Chen, S.; Xu, C. W.; Shen, P. K., Ethanol oxidation on Pd/C enhanced by MgO in alkaline medium. *Int J Hydrogen Energ* **2014,** *39* (28), 16015-16019.

53. Hu, C. Y.; Wang, X., Highly dispersed palladium nanoparticles on commercial carbon black with significantly high electro-catalytic activity for methanol and ethanol oxidation. *Int J Hydrogen Energ* **2015,** *40* (36), 12382-12391.

54. Hu, P. Q.; Du, G. J.; Zhou, W. J.; Cui, J. J.; Lin, J. J.; Liu, H.; Liu, D.; Wang, J. Y.; Chen, S. W., Enhancement of Ethanol Vapor Sensing of TiO2 Nanobelts by Surface Engineering. *Acs Applied Materials & Interfaces* **2010,** *2* (11), 3263-3269.

55. Wang, L. K.; Tang, Z. H.; Yan, W.; Yang, H. Y.; Wang, Q. N.; Chen, S. W., Porous Carbon-Supported Gold Nanoparticles for Oxygen Reduction Reaction: Effects of Nanoparticle Size. *Acs Appl Mater Inter* **2016,** *8* (32), 20635-20641.

56. Stamenkovic, V. R.; Fowler, B.; Mun, B. S.; Wang, G. F.; Ross, P. N.; Lucas, C. A.; Markovic, N. M., Improved oxygen reduction activity on Pt3Ni(111) via increased surface site availability. *Science* **2007,** *315* (5811), 493-497.

57. Chang, J. F.; Feng, L. G.; Liu, C. P.; Xing, W.; Hu, X. L., Ni2P enhances the activity and durability of the Pt anode catalyst in direct methanol fuel cells. *Energ Environ Sci* **2014,** *7* (5), 1628-1632.

58. Xu, B.; Zhou, G.; Wang, X., Rational synthesis and the structure-property relationships of nanoheterostructures: a combinative study of experiments and theory. *Npg Asia Mater* **2015,** *7*, e164.

Chapter 6. TiO2 functionalized with alkyne ligand for efficient charge transfer: a powerful tool for injecting electrons from ligand to metal oxide

6.1 Abstract

Photo-induced charge transfer at the molecule/semiconductor interfaces are essential for their diverse applications in photocatalysis and optoelectronics. Currently most efforts have been concentrated on chromophore molecular engineering which bound to metal oxide by hydroxylic or carboxylic anchors, while generally, the limited interfacial electronic coupling between these anchoring groups and cores represents a major bottleneck that limits the performance. However, exploring new anchoring groups has long been ignored. Herein, acetylene derivatives are demonstrated as new, effective capping ligands for the surface functionalization of metal oxide nanoparticles, as exemplified with TiO_2, RuO_2, and ZnO. Experimental studies and first-principles calculations suggest the formation of M-O-C≡C- core-ligand linkages that lead to effective interfacial charge delocalization, in contrast to hopping/tunneling by the conventional M-O-CO- interfacial bonds in the carboxyl-capped counterparts. This results in the formation of an interfacial state within the oxide bandgap and much enhanced sensitization of the nanoparticle photoluminescence emissions as well as photocatalytic activity, as manifested in the comparative studies with TiO_2 nanoparticles functionalized with ethynylpyrene and pyrenecarboxylic acid. These results highlight the significance of the unique

interfacial bonding chemistry by acetylene anchoring group in facilitating efficient charge transfer across the oxide-ligand interface and the fundamental implication in their practical applications.

6.2 Introduction

In recent decades, metal oxide nanoparticles have been attracting extensive interest primarily because of their unique optical and electronic properties that can be exploited for diverse applications, such as catalysis, optoelectronics, bioimaging, and biodiagnosis.[1-5] The materials properties can be readily manipulated by deliberate functionalization with select molecules/ions involving a variety of oxide-ligand interfacial linkages.[6-11] It should be noted that in these earlier studies, the metal oxide nanoparticle-anchor interactions entail mostly non-conjugated linkages, which limit the electronic coupling between the nanoparticle core and functional moieties of the capping ligands, resulting in inefficient interfacial charge transfer by hopping/tunneling.[12] For instance, carboxylic acids represent the most widely used surface capping ligands for metal oxide nanoparticles,[13-20] and several structural models have been proposed to account for the interfacial bonding interactions between COOH and metal oxide surface, with the exact structural configuration under active debates.[21] Phenolic hydroxide derivatives have also been used for metal oxide surface functionalization through ether-like M-O-R interfacial bonds.[22-29] However, due to their non-conjugated nature of the chemical bond, interfacial charge transfer remains limited. More recently, pyridine and tetrazole moieties have been used as

anchors onto metal oxide nanoparticle surfaces by strong coordination between the N lone pair electrons and Lewis acid sites of the metal oxides; yet the electrons are found to be mostly localized on the heterocycle anchor, rather than delocalized to the metal oxides, leading to inefficient interfacial charge transfer.[30, 31]

An immediate question arises. Can the interfacial electron transfer be enhanced by the formation of conjugated covalent linkages? Note that for metal nanoparticles, extensive research has indeed demonstrated that effective intraparticle charge transfer occurs between the particle-bound functional moieties via conjugated metal-ligand interfacial bonds.[32-36] For instance, acetylene derivatives can self-assemble onto transition-metal nanoparticle surfaces, forming metal-vinylidene (M=C=CH-) π bonds,[37] where the electronic coupling (H_{ab}) between the electron donor and acceptor states has been found to significantly increase, as compared to that with saturated interfacial linkages.[38] In a more recent study,[39] photo-gated intraparticle charge delocalization was observed with acetylene-functionalized TiO_2 nanoparticles, suggesting that the oxide-acetylene interfacial bonds behaved analogously to metal-vinylidene conjugated linkages. Yet, thus far, the exact chemical nature of the metal oxide-acetylene bonds has remained largely elusive; and more significantly, it remains unclear whether this is a generic phenomenon among a wide range of transition metal oxides. The issues are further compounded by two possible anchoring sites of the metal oxides (i.e., the metal and oxygen sites). Resolving the nature of these bonds and their effect on interfacial charge transfer are the primary motivation of the present study.

Herein, stable TiO_2 nanoparticles were prepared by the functionalization of acetylene derivatives, and used as the initial illustrating example to unravel the chemical structure of the interfacial bonding interactions and the impacts on the nanoparticle optical and electronic properties. Results from FTIR and ^1H NMR measurements, in conjunction with density functional theory (DFT) calculations, suggested the formation of Ti-O-C≡C- interfacial bonds. Steady-state photoluminescence (SSPL) measurements exhibited an additional emission band beyond the band edge emission, suggesting the formation of an interfacial state (IS) between the TiO_2 conduction band (CB) and valence band (VB). This was confirmed in DFT calculations where the formation of IS was due to charge transfer from the acetylene moiety (C≡C) of the alkyne ligands to TiO_2 based on Bader charge analysis and charge density redistribution. By contrast, no such IS was formed with the conventional anchors of carboxylic ligands where interfacial charge transfer was blocked. To further illustrate the efficient charge transfer via the Ti-O-C≡C- interfacial bonds, ethynylpyrene was employed to functionalize TiO_2 nanoparticles (TiO_2-EPy). Results showed that the IS emission was readily sensitized by the pyrene groups, as manifested in both steady-state and time-resolved photoluminescence measurements, in sharp contrast with the pyrenecarboxylic acid-functionalized (TiO_2-PyCA) counterpart, leading to much better photocatalytic performance towards methylene blue degradation with TiO_2-EPy than with TiO_2-PyCA. Similar conjugated interfacial bonding interactions, and hence interfacial charge transfer, were observed with other transition metal oxides, such as RuO_2 and ZnO. Taken together, these results suggest that the unique oxide-acetylene

interfacial bonding interaction can be exploited as a new, powerful variable in the manipulation of the optical and electronic properties of metal oxide nanoparticle, a critical step towards their diverse practical applications.

6.3 Result and Discussion

TiO_2 nanoparticles were used as the initial illustrating examples. Four samples were prepared by a two-phase hydrothermal method using titanium(IV) n-propoxide as the precursor along with select organic capping ligands:[39] two functionalized with acetylene derivatives such as n-octyne (TiO_2-HC8) and ethynylpyrene (TiO_2-EPy),

and the other two capped with carboxylic derivatives such as oleic acid (TiO_2-OA) and pyrenecarboxylic acid (TiO_2-PyCA), as schematically illustrated in Figure 1A. The morphology of the TiO_2 nanoparticles was first examined by TEM measurements. Figure 1B depicts a representative TEM image of the TiO_2-HC8

nanoparticles, where individual nanoparticles can be readily resolved. In high-resolution TEM measurements (Figure 1C), the nanoparticles can be seen to exhibit well-defined lattice fringes, where the interplanar spacing of 0.35 nm is consistent with that of anatase TiO_2 (101) (JCPDS75-1537).[40] Furthermore, statistical analysis

based on more than 100 nanoparticles showed that the nanoparticles mostly fell within the narrow size range of 3.5 to 4.5 nm in diameter, with an average of 4.0 ± 0.4 nm, as manifested in the core size histogram in Figure 1D.

Figure 1. (A) Schematic illustration of four organically functionalized TiO_2

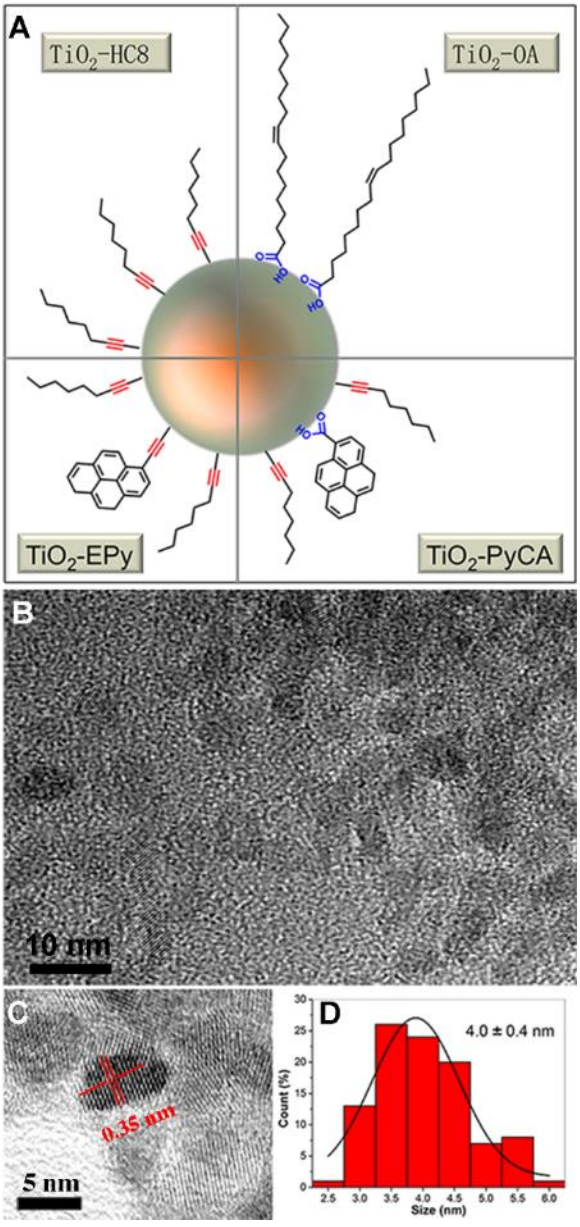

nanoparticles: TiO_2-HC8, TiO_2-OA, TiO_2-EPy, and TiO_2-PyCA. (B-C) Representative TEM images of TiO_2-HC8 nanoparticles, and (D) the corresponding core size histogram.

The structures of the organic capping layers were then investigated by FTIR and ^{1}H NMR measurements. Figure 3A depicts the FTIR spectra of TiO_2-HC8 and TiO_2-EPy nanoparticles, along with those of octyne and EPy free monomers. Both nanoparticle samples can be seen to exhibit well-defined vibrational bands at 2958, 2924, 2872 and 2850 cm^{-1}, characteristic of the C-H stretches of CH_2 and CH_3 and consistent with those of monomeric octyne, suggesting that the octyne ligands were indeed successfully bounded onto the TiO_2 nanoparticle surface. The TiO_2–EPy sample also exhibited a vibrational band at 3040 cm^{-1}, due to the H-C= vibration of the pyrene rings,[41] confirming the incorporation of EPy ligands on the TiO_2 nanoparticle surface. Additionally, one can see that octyne and EPy monomers exhibited a prominent vibrational band at 3313 and 3297 cm^{-1}, respectively, due to the terminal ≡C-H stretch.[42, 43] This vibration vanished altogether for TiO_2-HC8 and TiO_2-EPy, suggesting ready cleavage of the ≡C−H bond when the acetylene derivatives were bound onto the TiO_2 surface. This also indicates that the nanoparticle samples were spectroscopically clean, and free of excess ligands. Consistent results were obtained in ^{1}H NMR measurements. Figure 3B shows the ^{1}H NMR spectra of the TiO_2-HC8 and TiO_2-EPy nanoparticles in CD_2Cl_2, where the broad peak at 0.89 ppm is due to terminal methyl protons of the octyne ligands, whereas the peaks at 1.28 and 1.54 ppm to the methylene protons. For the TiO_2-EPy sample, an additional broad peak

can be identified at 7.35-8.65 ppm for the pyrene ring protons.[41] In addition, based on the integrated peak areas, the mole ratio between the octyne and EPy ligands on the TiO_2 surface was estimated to be 1:0.66. Also, the fact that only broad peaks were observed and the terminal ≡C-H protons cannot be seen in the nanoparticle samples (3.43 ppm for EPy and 2.87 ppm for octyne)[41, 44] further confirms the absence of free ligands in the nanoparticle samples, in good agreement with results from FTIR measurements in Figure 3A. Besides these broad peaks, these are several sharp peaks at 2.34 ppm (methyl protons), 7.15 and 7.24 ppm (phenol protons) are from residual toluene [45].

To understand the interfacial structure of acetylene-capped TiO_2, we carried out DFT calculations with a fully relaxed five-layer symmetric TiO_2 slab model. The TiO_2 slab is in anatase phase with the (101) lattice surface exposed, according to the experimental results in Figure 1C. To simplify the calculation, the simplest ligand -C≡C-CH_3 was used, and the optimized structure of the supercell and slab surface is shown in Figure 3C and its inset. In the stable configuration, the carbon atom was found to bind to the oxygen atom, instead of the titanium atom, on the TiO_2 surface, forming a Ti-O-C≡C- interfacial linkage. Note that when we placed the ligand onto the titanium site as the initial configuration, it eventually migrated to the oxygen site after geometric relaxation (Figure 2), suggesting that a Ti-C≡C- interfacial bond is energetically unfavorable. Moreover, one can see that in Ti-O-C≡C-, the C-O bond length is 1.289 Å, which is intermediate between a carbon-oxygen single bond (1.43 Å) and double bond (1.23 Å); concurrently, the C≡C bond length became somewhat

elongated to 1.217 Å, as compared to that of a free monomer (1.20 Å), whereas the C-C bond shrank slightly to 1.452 Å from 1.47 Å for a Csp^3-Csp single bond.[46] Taken together, these results suggest that the formation of Ti-O-C≡C- interfacial linkage was likely facilitated by partial charge transfer of the π-electrons in C≡C to TiO_2, leading to shortened and strengthened C-O and C-C bonds at the core-ligand interface.

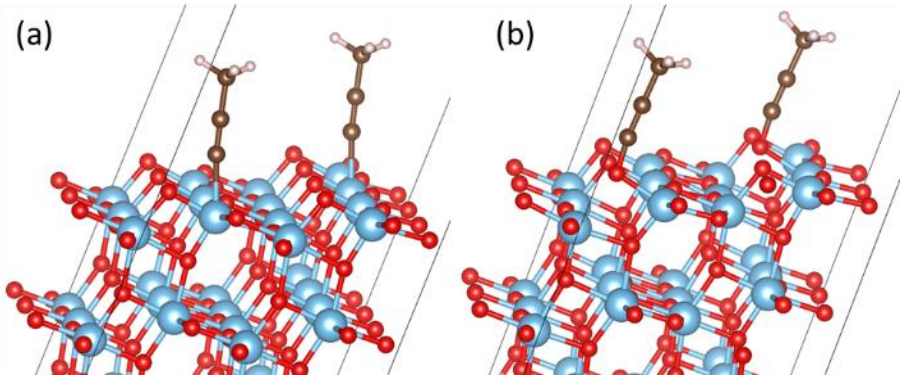

Figure 2. Interfacial structures of alkyne-modified TiO_2: (a) when the ligands are placed on Ti atoms initially, and (b) the corresponding structure after relax calculation where the ligands moved to the O atoms spontaneously. This suggests that the O atom, rather than the Ti atom, in TiO_2 is the anchoring site, forming a Ti-O-C≡C-, instead of Ti-C≡C-, interfacial bond.

Figure 3. (A) FTIR spectra of octyne, EPy, TiO_2-HC8, and TiO_2-EPy. (B) ^1H NMR spectra of TiO_2-HC_8 and TiO_2-EPy nanoparticles in CD_2Cl_2. (C) Configuration of the TiO_2-alkyne interface, with the atoms in blue, red, brown and white for Ti, O, C, and

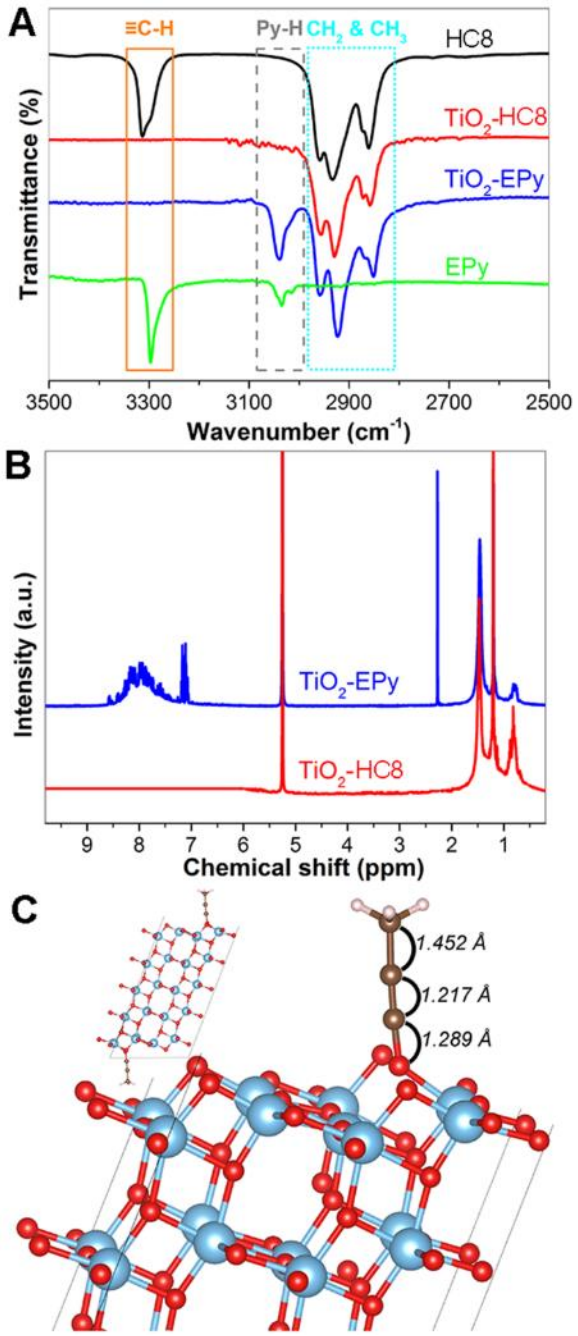

H, respectively. Inset is the overall configuration of a five-layer TiO_2 model with symmetric ligands on the surface.

The apparent electronic coupling between the acetylene moiety and TiO_2 nanoparticles leads to new optical properties of the nanoparticle, as manifested in

UV-vis and photoluminescence measurements. Figure 5A depicts the UV-vis absorption spectrum of the TiO_2-HC8 nanoparticles, where the bandgap was estimated to be about 3.51 eV from the Tauc plot (Figure 5A inset).[47] Note that this was somewhat larger than that of bulk anatase TiO_2 (3.2 eV), likely due to quantum confinement effect, as the average size of the TiO_2 nanoparticles was smaller than the Bohr exciton radius (2.35 nm).[48] Figure 5B shows the corresponding SSPL profiles. One can see that at the excitation (λ_{ex}) of 254 nm, the emission (λ_{em}) peaked at 355 nm (red-shaded). At increasing λ_{ex} (e.g., 294 and 304 nm), an additional emission peak emerged at around 420 nm (2.95 eV, aqua-shaded), and the intensities of these two emission peaks reached the maxima at λ_{ex1} = 295 nm and λ_{ex2} = 355 nm, respectively. Interestingly, for TiO_2-OA nanoparticles that exhibited a very similar band gap energy (ca. 3.2 eV), only a single emission peak was observed at λ_{em} = 375 nm within a similar range of λ_{ex}. Therefore, for the TiO_2-HC8 nanoparticles, the emission at λ_{em1} = 355 nm was likely due to the band-edge emission of TiO_2, where the energy (3.49 eV) is very close to the band-gap estimated by UV-vis measurements (3.51 eV); while the second emission at λ_{em2} = 420 nm suggests the formation of an interfacial state (IS), due to electronic interactions between the acetylene moiety and TiO_2, as schematically illustrated in Figure 5C.

This is, in fact, confirmed by results from DFT calculations. Figure 5D depicts the plot of density of states (DOS) for a TiO_2 slab. One can see that the band gap (2.2 eV) between the valence band (VB, zone I) and conduction band (CB, zone IV) was somewhat underestimated, as compared to the experimental results from Figure 5A

(this is due to the well-known self-interaction errors at the standard PBE level; consistent results were obtained by employing a higher level of theory such as DFT with hybrid functionals HSE06, as shown in Figure 4).[49-51] Yet, upon the adsorption of acetylene derivatives onto the TiO_2 surface, new states are generated within the band gap (zones II and III), consistent with the experimental SSPL results, where a new emission band emerged at 420 nm (Figure 5B) (from Figure 4 one can see that the experimental band gap of bulk TiO_2 was well-reproduced by using more accurate HSE06 hybrid functional to calculate the electronic structure of functionalized TiO_2 slabs). Furthermore, from the PDOS (projected density of states) plots of the 2p orbitals of C2 (red), C1 (green), and O (blue) atoms and the 3d orbitals of Ti (pink) atom in Figure 5D, one can see that the IS is mainly composed of the 2p orbitals of sp-hybridized carbon (C≡C) and O atoms, with minor contributions from the 3d orbitals of the adjacent Ti atom. Consistent results can be obtained from the plots of charge density distribution within different energy windows, zone I (Figure 5E), zone II (Figure 5F), zone III (Figure 5G), and zone IV (Figure 5H). From Figure 5E, it is clear that the major contribution to the valence band (zone I) is from the O atom, whereas contributions to the conduction band (zone IV) are primarily from the Ti atom, which is also manifested by the pink curve (Ti-3d) in Figure 5D. Consistent with PDOS plots in Figure 5D, the IS can be seen from Figure 5F-H to be mainly due to the sp-hybridized carbon, with additional contributions from adjacent oxygen and titanium atoms.

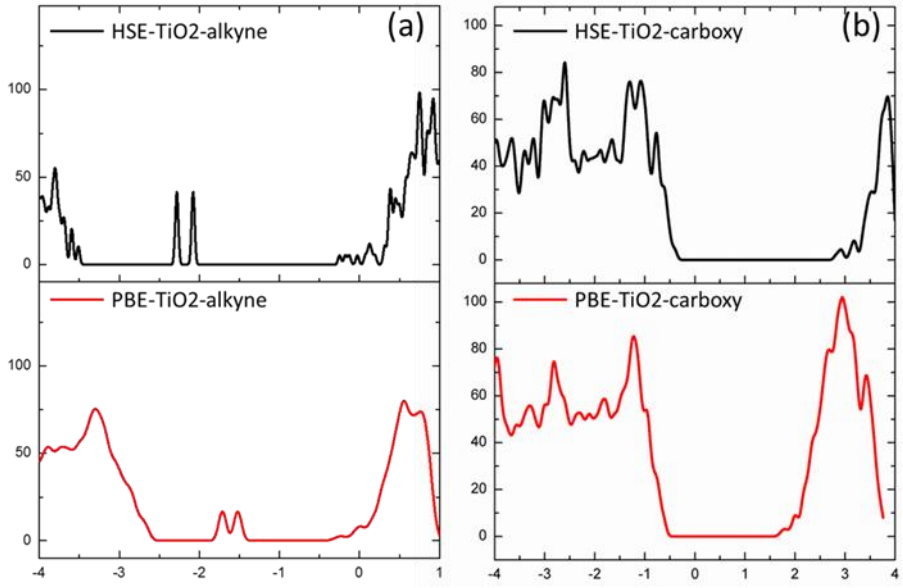

Figure 4. Total density of states (TDOS) calculated by HSE and PBE of (a) TiO_2-alkyne (b) TiO_2-carboxy structures.

Figure 5. (A) UV-vis spectra of TiO_2-HC8. Inset is the corresponding Tauc plot, where α is the absorbance and hν is the photon energy. (B) SSPL spectra of TiO_2-HC8 at various excitation wavelengths. The shadowed ones represent maximal emissions at select excitation wavelengths. (C) Schematic illustration of the band structure of TiO_2-HC8 based on the SSPL results. (D) Total density of states (TDOS) plot of TiO_2-C≡C-CH_3 (black curve) and projected density of states (PDOS) plot of the 2p orbitals of C2 (red), C1 (green), and O (blue) atom, and the 3d orbital of the Ti (pink) atom. The corresponding energy-resolved charge density distributions are included in panel (E) for zone I, panel (F) for zone II, panel (G) for zone III, and

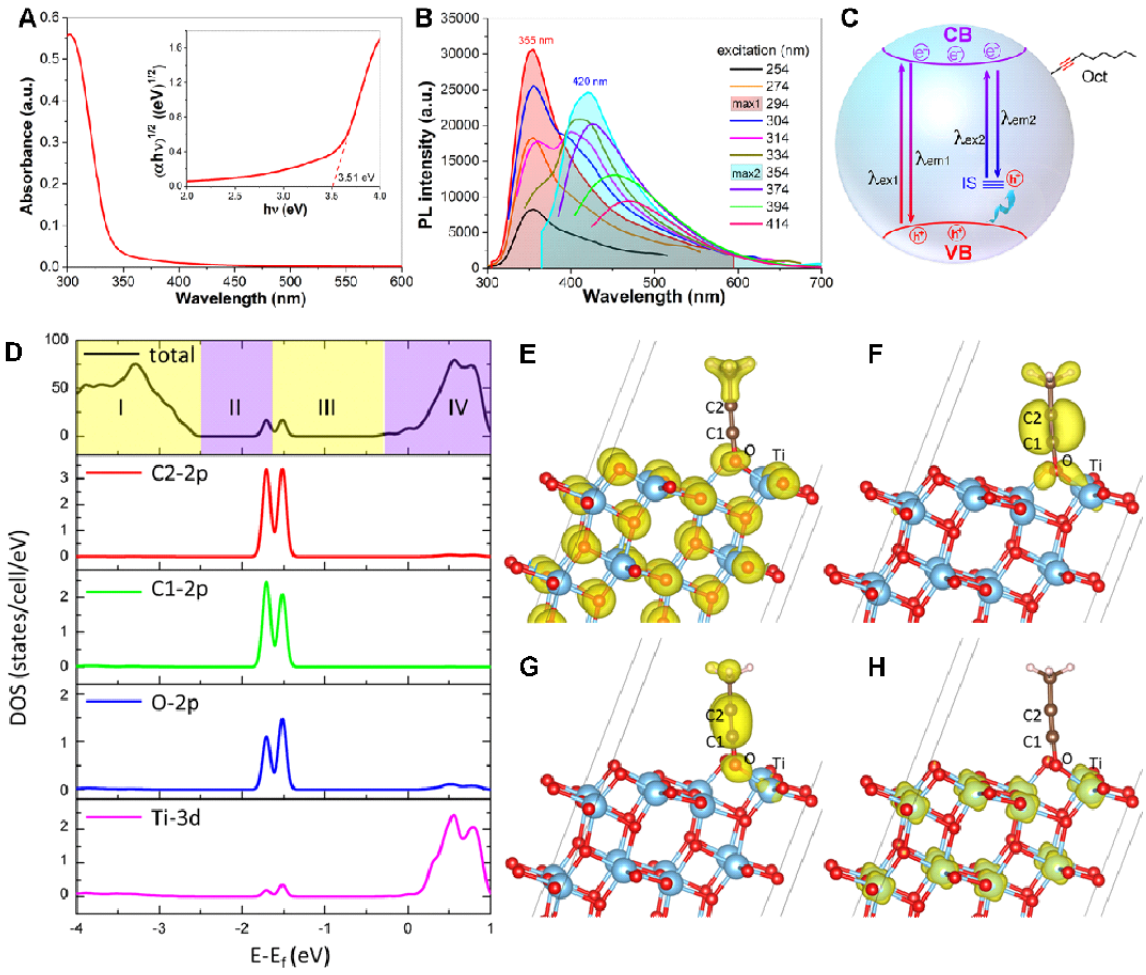

panel (H) for zone IV. The isovalue is 0.1 e/au^3 for panels (E) and (H), and 0.005 e/au^3 for panels (F) and (G).

The emergence of IS due to the formation of Ti-O-C≡C- interfacial bond was further evidenced by comparing the DOS profiles of pristine and organically modified TiO_2 slabs. From Figure 8, one can see that (i) the bandgap of the TiO_2 slab remained almost unchanged regardless of surface modification, and (ii) the alkyne-functionalized TiO_2 slab exhibited apparent states within the bandgap (green curve), a behavior unseen in pristine TiO_2 (black curve) or TiO_2 slabs modified with carboxyl (red curve) or alkane (blue curve). Note that the results for carboxy-modified TiO_2 are

consistent with those of TiO_2-OA, suggesting the formation of Ti-O-C(OH)- linkage in TiO_2-OA,[52] a leading structural model postulated in the literature,[53-55] while alkane-functionalized TiO_2 cannot be verified by experiments due to the lack of effective synthesis methods. Nevertheless, these results clearly suggest that the formation of IS within the TiO_2 bandgap is due to the unique Ti-O-C≡C- interfacial bonding interactions.

Further insights into the interfacial bonding chemistry can be obtained from analysis of charge distributions within the nanoparticles. From Figure 10A, one can see that there is a large cyan area around the C≡C carbon atoms and adjacent oxygen atom, indicating a significant electron loss from this region; whereas several yellow areas can be identified all over the TiO_2 slab, suggesting electron gain of the Ti and O atoms (of TiO_2). This signifies strong spontaneous charge delocalization from the acetylene moiety to TiO_2. By contrast, no obvious charge delocalization was observed with carboxy-functionalized TiO_2. From Figure 10B, it can be seen that almost all the yellow and blue areas are confined to the ligand, indicating that charge delocalization from the ligand to TiO_2 was impeded. This result is in coincidence with the Bader charge analysis (Table 1), where the Bader charge of TiO_2-alkyne is ca. 1.2 electron per ligand from alkyne to TiO_2, while charge transfer is negligible with only ca. 0.01 electron per ligand from TiO_2 to carboxy for the TiO_2-carboxy counterpart. This reflects virtually barrierless charge transfer at the TiO_2-alkyne interface, whereas at the TiO_2-carboxy interface, an appreciable driving force is needed to facilitate hopping/tunneling charge transfer across the TiO_2-ligand interface. Note that the level

of theory and the slab models used in the above calculations were validated by comparing results using slab models of various layers of TiO_2 with HSE06 exchange correlation functional (Figure 7 and Table 1), which showed excellent agreement with the experimental band gap of TiO_2. In addition, constrained DFT calculations[56] of TiO_2-alkyne and TiO_2-carboxy clusters (Figure 6) show that the electronic coupling (H_{ab}) between TiO_2 and the end ligand of the former is ca. 5 times that of the latter, indicating that indeed the Ti-O-C≡C- bonding linkage significantly facilitated interfacial charge transfer.

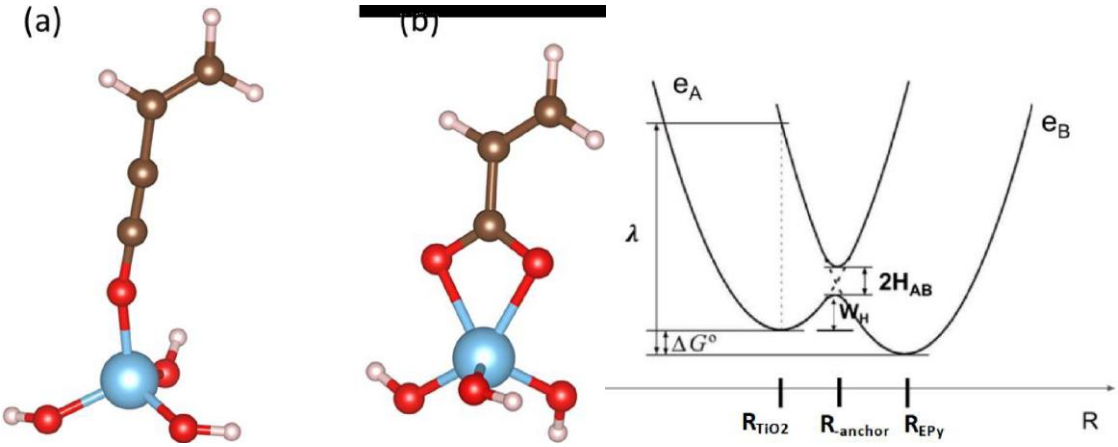

Figure 6. Optimized geometrical structures by CDFT calculation of (A) Ti(OH)3-O-C≡C-CH=CH2, and (B) Ti(OH)3-OOC-CH=CH2. The extra electron is placed and localized on -CH=CH2 and -Ti(OH)3, respectively, for the calculations of electronic coupling (Hab) between the two sites. Within CDFT, an external potential is added to the self-consistent potential entering the Kohn-Sham equations, and its strength is varied self-consistently in order to localize a desired integer number of charges N0 on a specified site. Inset shows the potential energy surface of charge transfer from TiO2

to ligand (e.g., EPy) through an anchor group (i.e., -COO-or -C≡C-). Hab is the electronic coupling between TiO2 and ligand EPy, which is larger with -C≡C-than with -COO-and results in a lower barrier WH for excited electron or hole transfer from TiO2 to Epy.

Note that PL and photocatalysis involve excited states. In the present study, since we are mainly interested in charge (electron or hole) transfer between TiO2 and ligands (e.g., EPy) bridged by different anchor groups (instead of an electron-hole recombination process), we can still use a Marcus' theory type of picture for simplicity, as shown in Figure 6 inset (the exact shape and relative position of potential energy surfaces can be different but does not affect the conclusion here).

The physical justification for this picture is the following: after an electron is excited from the valence to conduction bands leaving a hole in the valence band, electron transfer occurs in the conduction band and hole transfer in the valence band. In principle, the system is still neutral. If we consider that electron and hole transfers are relatively uncorrelated (i.e., neglect electron hole interaction), we can add an electron to the system which will occupy the lowest conduction band/unoccupied state and compute the charge transfer rate between TiO2 and ligand; or we can add a hole to the system which will stay at the valence band for hole conduction. The charge transfer direction is determined by the relative band alignment between TiO2 and the specific ligand (e.g., EPy). In our CDFT calculation (Figure 6), we added an excess electron to the system to simulate the process of excited electron transfer between TiO2 and ligand bridged by anchor groups.

When we change the anchor group from -COO-to -C≡C-(Ranchor in Figure 6 inset), the electrons become delocalized due to the formation of conjugated interfacial bonds that causes a large electronic coupling (HAB in Figure 6 inset) between TiO2 and EPy. If the overall potential energy surfaces of TiO2 and Epy are not strongly modified by the anchor group (i.e., λ and ΔG_0 are unchanged when we change the anchor groups, which is a reasonable assumption considering the relatively small size of the anchor group compared to TiO2 and ligands), the charge transfer barrier (W_H) will diminish, because

$W_H=(\lambda+\Delta G_0)^2/4\lambda-(|H_{AB}|+(\lambda+\Delta G_0)/2-\sqrt{(\lambda+\Delta G_0)^2/4+|H_{AB}|^2})$ Eq.1

which is based on a generalized Landau-Zener theory that correctly provides both the small coupling HAB limit (nonadiabatic charge transfer in the Marcus' theory) and the large coupling limit (adiabatic charge transfer in the transition state theory).

In the CDFT calculation (Figure 6), we found the electronic coupling between TiO2 and Epy (H_{AB}, which is computed with one extra electron to represent the excited electron transfer process) is five times larger with the -C≡C-anchor group than with -COO-. Based on the Eq. 1, WH will be much smaller, and the charge transfer rate (k) will be much larger due to the exponential dependence of k on W_H Eq. 2

$k=\kappa_{el}\nu_n\exp(-W_H/k_BT)$ Eq.2

In other words, the results that we obtained in ground state charge transfer demonstrate that conjugated interfacial bonding interactions indeed improve charge delocalization across the oxide-ligand interface, which is essentially related to the

enhanced electronic coupling between TiO2 and EPy bridged by -C≡C-, in comparison to -COO-.

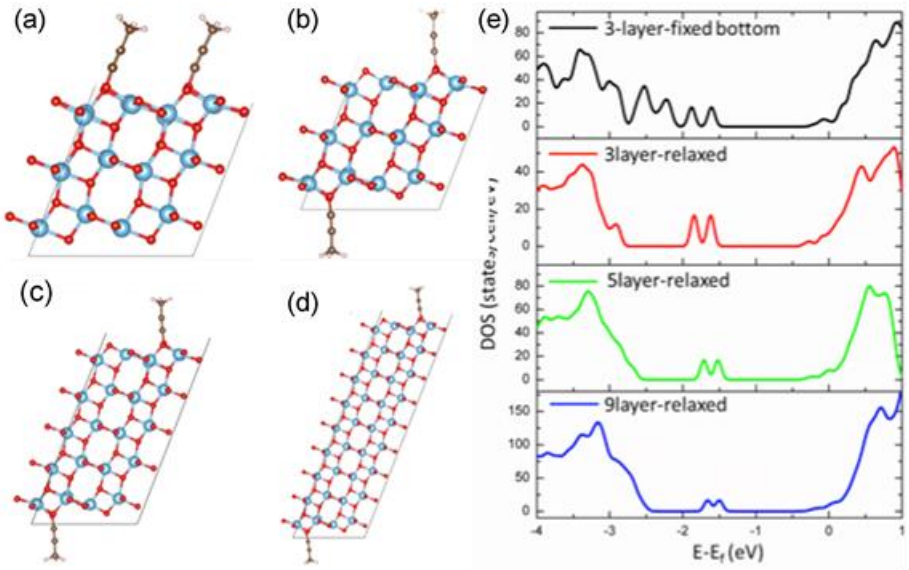

Figure 7. (a) Three-layer fixed bottom model with two ligands on the surface, and (b) 3, (c) 5, (d) 9-layer relaxed surface model with alkyne ligands on the surface. (e) The corresponding total density of states (TDOS) profiles of the various models.

Table 1. Bader charge of TiO_2-alkyne and TiO_2-carboxy by PBE and HSE06

Exchange collection functional	Charge of alkyne (e)			Charge of carboxylic acid (e)		
	on TiO_2	isolated	difference	on TiO_2	isolated	difference
PBE	13.60	14.80	-1.20	29.77	29.75	+0.02
HSE06	13.67	14.81	-1.14	29.77	29.76	+0.01

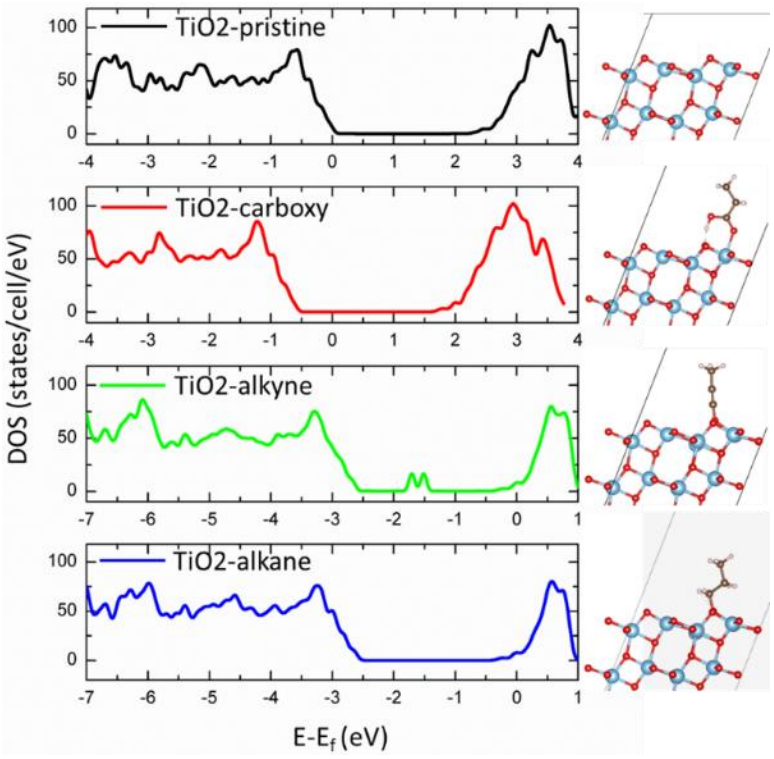

Figure 8. Total density of states (TDOS) and interfacial configurations of a pristine TiO_2 slab, and a slab functionalized with carboxy (-COOH), alkyne (-C≡C-), and alkane (-CH_2-CH_2-) ligands.

This is actually a general phenomenon for a wide range of transition-metal oxides, as manifested in further studies with RuO_2 and ZnO. These two oxides were chosen because of the unique electronic structures of the metal centers, zinc(II) with a full d-electron subshell and ruthenium(IV) with a half-full d-electron subshell, in comparison with Ti(IV) in TiO_2 that has an empty d-electron subshell. From DFT calculations, it can be seen that (i) both oxide nanoparticles also showed a stable structure with the alkyne ligands bonded to the oxygen atoms, instead of the metal atoms (ZnO-alkyne in Figure 9A, and RuO_2-alkyne in Figure 9B), consistent with results for TiO_2-alkyne (Figure 10A); and (ii) there is an apparent charge transfer of 1.10 and 1.43 electrons from the alkyne ligand to ZnO and RuO_2 (cyan area), respectively, also comparable to that (1.2 electrons) for TiO_2-alkyne. By contrast, charge transfer from carboxylic ligands to ZnO and RuO_2 was negligible at only 0.06, and 0.64 electron (Figure 9C-D), respectively, very similar to that (0.01 electron) for TiO_2-carboxy (Figure 10B). Taken together, these results suggest that (i) acetylene derivatives can indeed serve as effective capping ligands for the surface functionalization of a wide range of metal oxide nanoparticles, and (ii) apparent charge transfer occurs between the acetylene moiety and metal oxide, due to the formation of conjugated M-O-C≡C- interfacial bonds, in contrast to conventional capping ligands (e.g., carboxylic derivatives) where charge transfer across the core-ligand interface is negligible. This may have significant implication in practical applications of these oxide nanomaterials, as demonstrated below.

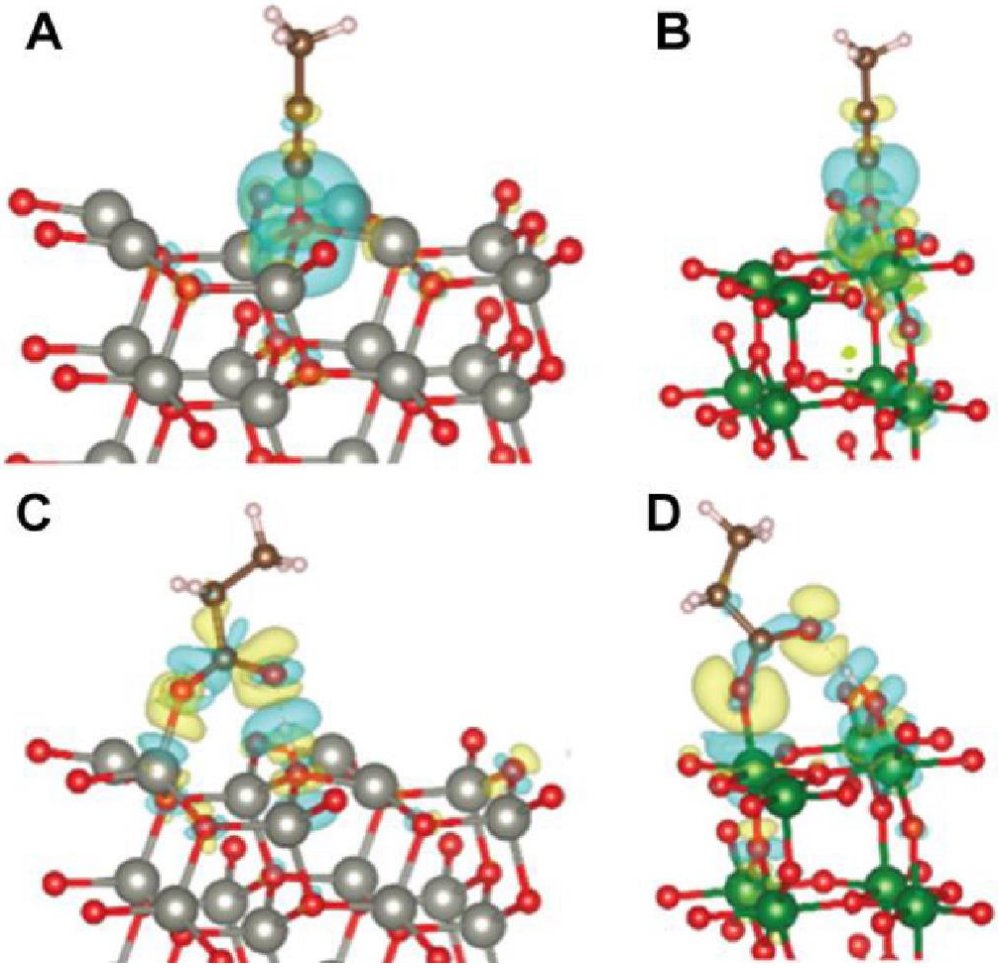

Figure 9. Charge transfer between ligands and metal oxide slabs: (A) ZnO-alkyne, (B) RuO2-alkyne, (C) ZnO-carboxy, and (D) RuO2-carboxy. The cyan area indicates electron loss, and yellow area indicates electron gain. The isosurface value is 0.003 e/au3.

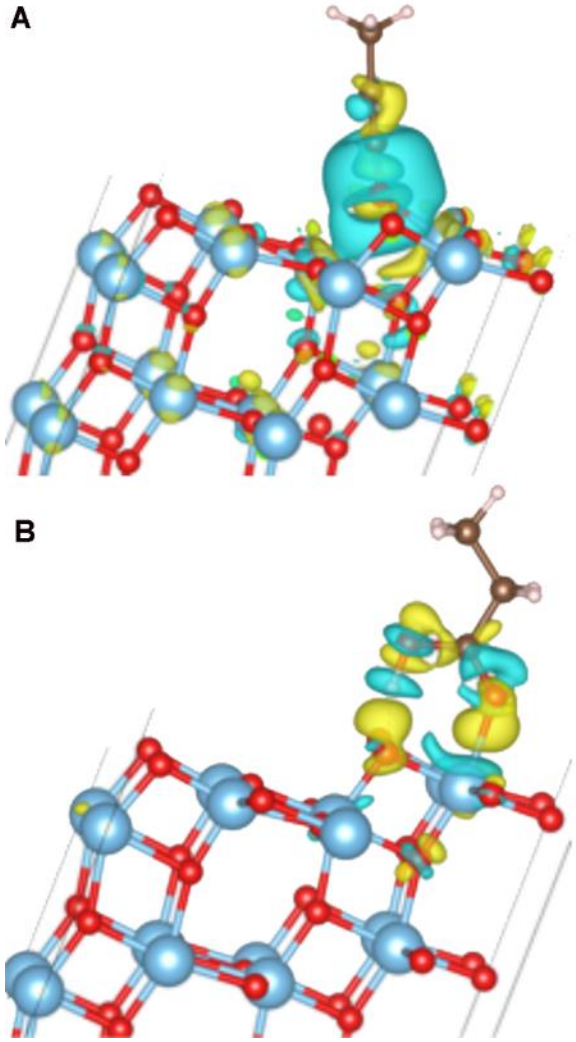

Figure 10. Charge transfer between ligand and TiO_2 slab: (A) TiO_2-alkyne (B) TiO_2-carboxy. The cyan area indicates electron loss and yellow area indicates electron gain. The isosurface value is 0.003 e/au^3.

One can envisage that if a suitable electron donor is bound onto a metal oxide nanoparticle via the M-O-C≡C- linkage, effective charge transfer occurs from the electron-donating moiety to the metal oxide, leading to the emergence of new optical and electronic properties. By contrast, such interfacial charge transfer will be

impeded with a carboxy anchor. In the present study, pyrene is used as a molecular probe to highlight the significance of such interfacial bonding contacts in the manipulation of nanoparticle interfacial charge transfer and optical and electronic properties. Two samples, TiO_2-EPy and TiO_2-PyCA were prepared and compared (Figure 1A). Figure 11A depicts the UV-vis absorption spectra of EPy and TiO_2-EPy. It can be seen that EPy monomers exhibited four prominent peaks at 314, 328, 343 and 360 nm, due to the $S_o \rightarrow S_n$ transitions of the pyrene π electrons;[57] consistent absorption features can also be observed with TiO_2-EPy, though with a slight red-shift of 4 to 7 nm, likely due to enhanced interactions between the pyrene moieties, as they were in close proximity on the nanoparticle surface, akin to the situation of pyrene-containing polymers.[58] Furthermore, in comparison to TiO_2-HC8, one can see that TiO_2-EPy showed a diminishment of the effective bandgap to 2.94 eV (Figure 11A inset), suggestive of enhanced absorption in the visible range, as compared to pristine TiO_2. This is likely because electronic transition involving the IS became dominant as a result of the formation of Ti-O-C≡C- interfacial bonds.

Figure 11. (A) UV-vis spectra of monomeric EPy, TiO_2-HC8, and TiO_2-EPy. Inset shows the corresponding Tauc plots. (B) Normalized steady-state excitation and emission spectra of monomeric EPy, TiO_2-HC8, and TiO_2-EPy. (C) Schematic illustration of the charge transfer process at the Ti-O-C≡C-Py interface. (D) TRPL decay profiles of monomeric EPy, TiO_2-HC8 and TiO_2-EPy. The grey curve is the background of the instrument response function (IRF). Symbols are experimental data and solid curves are exponential fits. The fitting results are summarized in the inset table. (E) UV-vis spectra of a MB solution before and after UV photoirradiation for 15 min using TiO_2-EPy or TiO_2-PyCA as catalysts. The inset shows the photographs

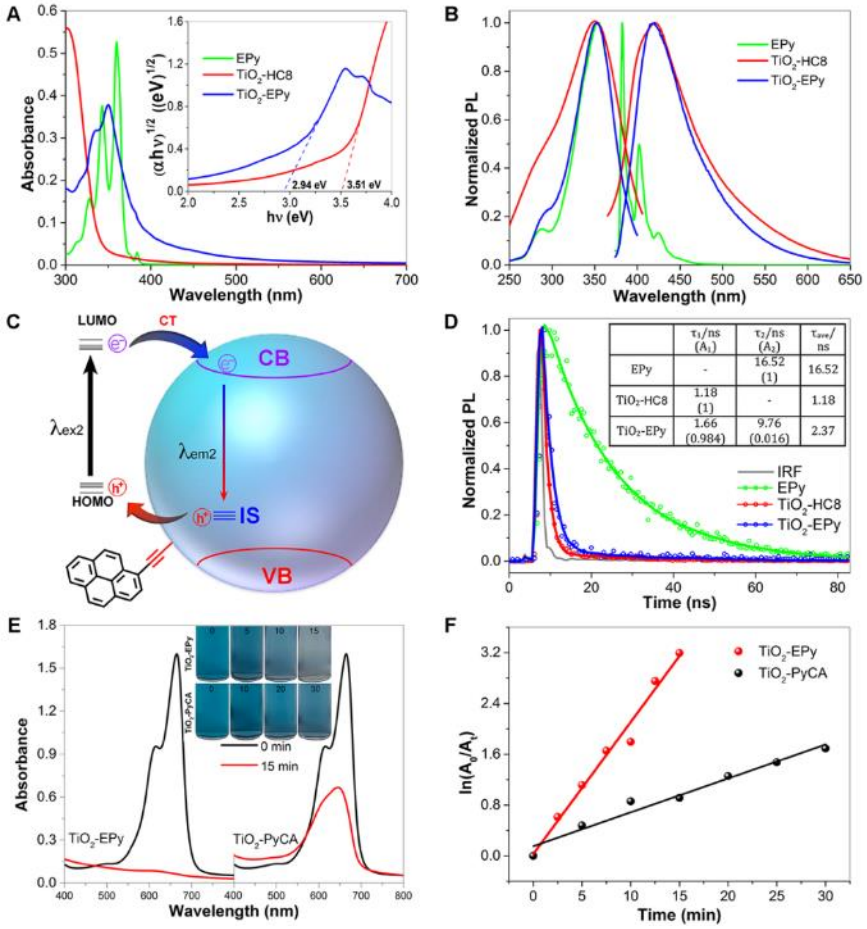

	τ_1/ns (A_1)	τ_2/ns (A_2)	τ_{ave}/ns
EPy	-	16.52 (1)	16.52
TiO_2-HC8	1.18 (1)	-	1.18
TiO_2-EPy	1.66 (0.984)	9.76 (0.016)	2.37

of the solution at different times (in min). (F) Variation of MB peak absorbance with photoirradiation time. Symbols are experimental data and lines are linear regressions.

This distinction is also manifested in SSPL measurements. Form Figure 11B, it can be seen that monomeric EPy exhibited three characteristic emissions at 382, 402, and 425 nm,[57] and rapidly decayed in intensity with an increase of the excitation wavelength. By contrast, TiO_2-EPy displayed only a single, broad emission centered at λ_{em} = 420 nm, independent of the excitation wavelength. Note that this emission peak position is the same as λ_{em2} of TiO_2-HC8 (Figure 5B), suggesting that it arose from the radiative recombination of CB electrons and IS holes of TiO_2 (Figure 5C). In addition, the photoluminescence quantum yield (φ) of TiO_2-EPy was estimated to be

36.6%, using quinine sulfate in 0.1 M H_2SO_4 as the standard (φ = 54%),[59] which is markedly higher than that of TiO_2-HC8 (6.9%). This can be accounted for by charge donation from the pyrene group to TiO_2 CB and the subsequent radiative decay to the IS holes, leading to marked sensitization of the TiO_2 IS emission, consistent with results from UV-vis (Figure 11A) and DFT calculations (Figure 5D). Based on the above data, the electronic structure of TiO_2-EPy is schematically illustrated in Figure 11C. For comparison, TiO_2-PyCA nanoparticles, where the pyrene moiety was anchored onto the TiO_2 surface by the COOH moiety (Figure 1A), no apparent variation was observed of the SSPL profile.

The electron transfer dynamics from pyrene to the TiO_2-alkyne interface (Ti-O-C≡C-) were also investigated by time-resolved photoluminescence (TRPL) measurements. Figure 11D shows the normalized decay profiles after pulsed laser excitation at 337 nm for the series of samples (the grey curve is the background of the instrument response function, IRF). Note that at this excitation, the emission of TiO_2-HC8 and TiO_2-EPy is dominated by λ_{em2} (Figure 5B). The data may be fitted by either single- or double-exponential decay kinetics,[60] $I(t) = A_1 e^{-\frac{t}{\tau_1}} + A_2 e^{-\frac{t}{\tau_2}}$, $I(t) = A_1 e^{-\frac{t}{-1}} + A_2 e^{-\frac{t}{-2}}$, where $A_1 + A_2 = 1$, and the fitting parameters were listed in the inset to Figure 11D. For monomeric EPy, the data were fitted by a single exponential function, and the decay lifetime (τ) was estimated to be ca. 16.52 ns, consistent with results observed earlier with pyrene derivative,[57] due to the recombination of S_n excited electrons to S_0 holes of pyrene. TiO_2-HC8 nanoparticles also showed a single decay lifetime, which was markedly shorter at 1.18 ns for the recombination of

excited electrons at CB to IS holes. The fact that both EPy and TiO_2-HC8 showed only a single photoluminescence pathway is consistent with results from the SSPL measurements (Figure 11B). For TiO_2-EPy nanoparticles where the TiO_2 cores were functionalized with a mixed monolayer of octyne and EPy ligands, the data were fitted by a double-exponential equation, and two lifetimes were identified at τ_1 = 1.66 ns and τ_2 = 9.76 ns. The long component is consistent with the slow decay of pyrene, while the short lifetime was close to that of TiO_2-HC8 and might be attributed to the fast decay of IS. Moreover, the contributions of the fast and slow decay components were estimated to be 98.4% and 1.6%, respectively, suggesting that the dominant pathway for electron transfer entailed excited electrons on TiO_2 CB to IS. Again, this is in agreement with the SSPL results, where the quenching of pyrene emission and the enhancement of IS emission was accounted for by the efficient electron transfer from pyrene to TiO_2 CB. Additionally, the average lifetime $\langle\tau\rangle$ can be calculated by $\langle\tau\rangle = \frac{A_1\tau_1^2+A_2\tau_2^2}{A_1\tau_1+A_2\tau_2}\langle\tau\rangle = \frac{A_1\tau_1^2+A_2\tau_2^2}{A_1\tau_1+A_2\tau_2}$, and was found to be 2.37 ns for TiO_2-EPy, which is somewhat higher than that of TiO_2-HC8. Furthermore, the electron transfer rate constant (k_{et}), which can be estimated by $k_{et} = \frac{1}{\langle\tau\rangle_{TiO2-EPy}} - \frac{1}{\langle\tau\rangle_{EPy}}$, was 3.61×10^8 s^{-1}, indicating fast charge-transfer kinetics from pyrene to TiO_2 CB. For comparison, TiO_2-PyCA, where the pyrene moiety was anchored onto the TiO_2 surface by a carboxyl linker instead (Figure 1A), the lifetime remained almost invariant, as compared to that of monomeric PyCA (τ= 6.13 ns), because of impeded charge transfer at the core-ligand interface.

In theoretical simulation, we applied phenylacetylene as a simplified representation of EPy in TiO_2-EPy to bind onto the surface of a TiO_2 slab (Figure 12A). The DOS plot (Figure 12B) suggests that IS remained visible, and an additional gap state emerged due to the conjugation between the phenyl ring (representing EPy) and the CαC moiety. By contrast, no obvious IS was formed with aromatic derivatives that featured a COOH anchor.[52] These results are in complete agreement with the experimental data presented above.

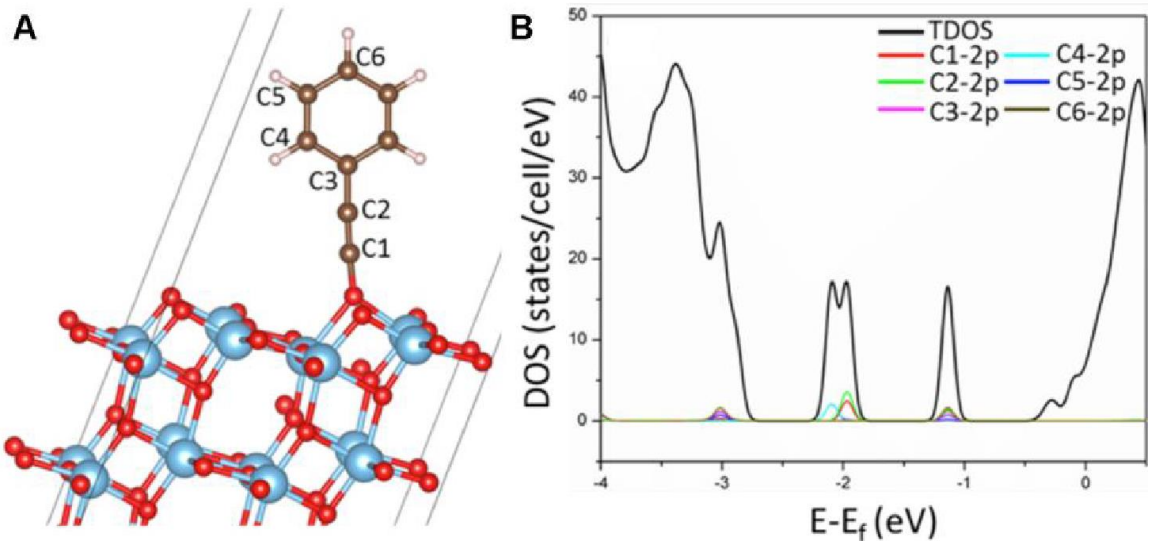

Figure 12. (A) Interfacial configuration and (B) DOS of a phenylacetylene-modified TiO2 slab.

Such unique interfacial bonding interactions markedly impact the nanoparticle photocatalytic activity, as manifested in the photocatalytic degradation of methylene blue (MB) by TiO_2-EPy and TiO_2-PyCA. Figure 11E depicts the UV-vis spectra of a MB solution (10 mg/L) containing 0.4 mg/L of the catalysts before and after 15 min's

UV photoirradiation (365 nm, 16 W/cm^2). It can be seen that MB was almost completely degraded in 15 min by TiO_2-EPy, while only 55% by TiO_2-PyCA (Figure 11E inset). In fact, from Figure 11F, one can see that the degradation rate constant for TiO_2-EPy (0.208 min^{-1}) is ~ 4 times that for TiO_2-PyCA (0.054 min^{-1}) and ~ 15 times that for TiO_2-HC8 (0.014 min^{-1}). This indicated that the enhanced photocatalytic performance of TiO_2-EPy is sensitized by pyrene groups though the acetylene linkage.

6.4 Experiment and Calculation

Chemicals. *n*-Octyne (HC8, 98%, Alfa Aesar), ethynylpyrene (EPy, 96%, Alfa Aesar), oleic acid (OA, Spectrum), pyrenecarboxylic acid (PyCA, 97%, TCI America), titanium(IV) *n*-propoxide (99%, ACROS), *tert*-butylamine (99%, ACROS), quinine sulfate (Sigma-Aldrich), and methylene blue (MB, 95%, Acros) were used as received without any further purification. Solvents were purchased at the highest purity available from typical commercial sources and also used as received. Water was deionized with a Barnstead Nanopure Water System (18.3 MΩ•cm).

Synthesis of alkyne-functionalized TiO_2 nanoparticles. Alkyne functionalized TiO_2 nanoparticles were synthesized via a two-phase hydrothermal approach.[39] Briefly, 50 L of *tert*-butylamine was dissolved in 5 mL of water and the solution was transferred into a 20 mL Teflon-lined stainless-steel autoclave. Separately, a mixture of octyne (0.5 mL), titanium(IV) *n*-propoxide (75 mg) and toluene (5.0 mL) was

transferred to the autoclave slowly to form a two-phase reaction system. The autoclave was sealed and heated at 180 °C for 12 h. After it was cooled down to room temperature, the toluene layer was collected and dried by rotatory evaporation. The products were rinsed by methanol for 6 times to remove excess free ligands, and the obtained purified products were denoted as TiO_2-HC8, which were readily soluble in nonpolar solvents, such as CH_2Cl_2, $CHCl_3$, toluene, THF, etc.

Pyrene-functionalize TiO_2 nanoparticles were prepared in the same manner, except that 12 mg of EPy was added into toluene layer along with octyne, such that the resulting TiO_2 nanoparticles were capped by a mixed monolayer of octyne and EPy (and denoted as TiO_2-EPy).

Two control samples were also prepared by adopting the same procedure. In the first one, 0.5 mL of oleic acid was used in place of octyne to synthesize oleic acid-protected TiO_2 (TiO_2-OA) nanoparticles. The other entailed the addition of 0.5 mL of oleic acid and 12 mg of PyCA to synthesize PyCA and oleic acid co-protected TiO_2 (TiO_2-PyCA) nanoparticles.

Characterizations. TEM measurements were carried out with a Philips CM300 microscope operated at 300 kV. FTIR spectra were collected with a PerkinElmer FTIR spectrometer (spectral resolution 4 cm^{-1}), where the samples were prepared by casting the nanoparticle solutions onto a ZnSe disk. ^1H NMR measurements were carried out by using concentrated nanoparticle solutions in CD_2Cl_2 with a Varian Unity 500 MHz NMR spectrometer. UV-vis and SSPL spectra were acquired with a PerkinElmer Lambda 35 UV-vis absorption spectrometer and PTI fluorospectrometer,

respectively. TRPL decay spectra were collected on a Horiba QM-3304 instrument at the pulsed laser excitation of 337 nm in the time-correlated single-photon counting (TCSPC) mode.

Photocatalysis. In the photocatalytic degradation of MB by TiO_2-EPy and TiO_2-PyCA, 20 mg of the catalysts prepared above was added into 50 mL of an aqueous solution (10 mg/mL) of MB, corresponding to a catalyst loading of 0.4 mg/mL. The solution was under magnetic stirring in the dark for 30 min to reach an adsorption equilibrium, prior to photoirradiation with a UV lamp (365 nm, 16 W/cm^2). An aliquot of the solution was taken out in the time interval of 2.5 min and a UV-vis spectrum was recorded until there was no change of the UV profile.

Computational Methods. DFT calculations were performed with the open source planewave code, Quantum ESPRESSO.[61] 1 × 3 supercells were built for TiO_2 (101) of five layers in thickness. The vacuum thickness was set at 12 Å to avoid interactions between periodic images. The slab models included ligands with inversion symmetry to avoid net dipoles in the cell. The ultrasoft pseudopotential[62] was adopted with a kinetic cutoff energy of 40 Ry and charge density cutoff of 240 Ry for the Perdew-Burke-Eernzerhof (PBE) calculations. The optimized norm-conserving Vanderbilt (ONCV) pseudopotential[63] was adopted with a kinetic cutoff energy of 90 Ry and charge density cutoff of 360 Ry for the Heyd-Scuseria-Ernzerhof (HSE06) hybrid functional calculations.[64] The proportion of Hartree-Fock (HF) exchange is set to 22%. The 4 × 2 × 1 and 2 × 2 × 1 Monkhorst-Pack K-point is used for PBE and hybrid functional calculations, respectively. The Marzari-Vanderbilt smearing[65] was

adopted at the smearing of 0.001 Ry for all calculations except for pristine TiO_2. The electronic energy was converged to 10^{-8} Ry and force was converged to 10^{-4} a.u. Energy resolved charge density distribution was analyzed by open source code JDFTx.[66]

6.5 Conclusion

Results presented herein clearly demonstrate that acetylene derivatives can serve as effective capping ligands for metal oxide nanoparticles, and the resulting M-O-C≡C- interfacial linkages lead to markedly enhanced electronic coupling between the ligand electrons and metal-oxide cores, whereas interfacial charge transfer is significantly impeded with conventional anchor groups such as the carboxy moiety. This suggests that with a deliberate manipulation of the nanoparticle interfacial point of anchor, the optical and electronic properties of the metal-oxide nanoparticles can be controlled at an unprecedented level of sophistication, a variable that has remained largely unexplored thus far. This will have significant implication in their diverse practical applications, such as photocatalysis, photovoltaics, and photodynamic therapeutics.

6.6 Reference

1. Long, M. C.; Brame, J.; Qin, F.; Bao, J. M.; Li, Q. L.; Alvarez, P. J. J., Phosphate Changes Effect of Humic Acids on TiO2 Photocatalysis: From Inhibition to Mitigation of Electron-Hole Recombination. *Environ Sci Technol* **2017,** *51* (1), 514-521.

2. Youngblood, W. J.; Lee, S. H. A.; Kobayashi, Y.; Hernandez-Pagan, E. A.; Hoertz, P. G.; Moore, T. A.; Moore, A. L.; Gust, D.; Mallouk, T. E., Photoassisted Overall Water Splitting in a Visible Light-Absorbing Dye-Sensitized Photoelectrochemical Cell. *J Am Chem Soc* **2009,** *131* (3), 926-927.

3. Yella, A.; Lee, H. W.; Tsao, H. N.; Yi, C. Y.; Chandiran, A. K.; Nazeeruddin, M. K.; Diau, E. W. G.; Yeh, C. Y.; Zakeeruddin, S. M.; Gratzel, M., Porphyrin-Sensitized Solar Cells with Cobalt (II/III)-Based Redox Electrolyte Exceed 12 Percent Efficiency. *Science* **2011,** *334* (6056), 629-634.

4. Yang, J. B.; Ganesan, P.; Teuscher, J.; Moehl, T.; Kim, Y. J.; Yi, C. Y.; Comte, P.; Pei, K.; Holcombe, T. W.; Nazeeruddin, M. K.; Hua, J. L.; Zakeeruddin, S. M.; Tian, H.; Gratzel, M., Influence of the Donor Size in D-pi-A Organic Dyes for Dye-Sensitized Solar Cells. *J Am Chem Soc* **2014,** *136* (15), 5722-5730.

5. Kairdolf, B. A.; Smith, A. M.; Stokes, T. H.; Wang, M. D.; Young, A. N.; Nie, S. M., Semiconductor Quantum Dots for Bioimaging and Biodiagnostic Applications. *Annu Rev Anal Chem* **2013,** *6*, 143-162.

6. Ardo, S.; Meyer, G. J., Photodriven heterogeneous charge transfer with transition-metal compounds anchored to TiO2 semiconductor surfaces. *Chem Soc Rev* **2009,** *38* (1), 115-164.

7. Silvi, S.; Credi, A., Luminescent sensors based on quantum dot-molecule conjugates. *Chem Soc Rev* **2015,** *44* (13), 4275-4289.

8. Gao, X. H.; Cui, Y. Y.; Levenson, R. M.; Chung, L. W. K.; Nie, S. M., In vivo cancer targeting and imaging with semiconductor quantum dots. *Nat Biotechnol* **2004,** *22* (8), 969-976.

9. Greenham, N. C.; Peng, X. G.; Alivisatos, A. P., Charge separation and transport in conjugated-polymer/semiconductor-nanocrystal composites studied by photoluminescence quenching and photoconductivity. *Phys Rev B* **1996,** *54* (24), 17628-17637.

10. Heinz, H.; Pramanik, C.; Heinz, O.; Ding, Y. F.; Mishra, R. K.; Marchon, D.; Flatt, R. J.; Estrela-Lopis, I.; Llop, J.; Moya, S.; Ziolo, R. F., Nanoparticle decoration with surfactants: Molecular intercations, assmbly, and applications. *Surf Sci Rep* **2017,** *72* (1), 1-58.

11. Duncan, W. R.; Prezhdo, O. V., Theoretical studies of photoinduced electron transfer in dye-sensitized TiO(2). *Annu Rev Phys Chem* **2007,** *58*, 143-184.

12. Vura-Weis, J.; Abdelwahed, S. H.; Shukla, R.; Rathore, R.; Ratner, M. A.; Wasielewski, M. R., Crossover from Single-Step Tunneling to Multistep Hopping for Molecular Triplet Energy Transfer. *Science* **2010,** *328*, 1547-1500.

13. Asghar, M. I.; Miettunen, K.; Halme, J.; Vahermaa, P.; Toivola, M.; Aitola, K.; Lund, P., Review of stability for advanced dye solar cells. *Energ Environ Sci* **2010,** *3* (4), 418-426.

14. Hagfeldt, A.; Boschloo, G.; Sun, L. C.; Kloo, L.; Pettersson, H., Dye-Sensitized Solar Cells. *Chem Rev* **2010,** *110* (11), 6595-6663.

15. Sodeyama, K.; Sumita, M.; O'Rourke, C.; Terranova, U.; Islam, A.; Han, L.; Bowler, D. R.; Tateyama, Y., Protonated Carboxyl Anchor for Stable Adsorption of Ru N749 Dye (Black Dye) on a TiO2 Anatase (101) Surface. *J Phys Chem Lett* **2012,** *3* (4), 472-7.

16. Ashford, D. L.; Song, W.; Concepcion, J. J.; Glasson, C. R.; Brennaman, M. K.; Norris, M. R.; Fang, Z.; Templeton, J. L.; Meyer, T. J., Photoinduced electron transfer in a chromophore-catalyst assembly anchored to TiO2. *J Am Chem Soc* **2012,** *134* (46), 19189-98.

17. Hu, K.; Robson, K. C. D.; Johansson, P. G.; Berlinguette, C. P.; Meyer, G. J., Intramolecular Hole Transfer at Sensitized TiO2 Interfaces. *J Am Chem Soc* **2012,** *134* (20), 8352-8355.

18. Chen, H. Y.; Ardo, S., Direct observation of sequential oxidations of a titania-bound molecular proxy catalyst generated through illumination of molecular sensitizers. *Nat Chem* **2018,** *10* (1), 17-23.

19. Ye, S.; Kathiravan, A.; Hayashi, H.; Tong, Y. J.; Infahsaeng, Y.; Chabera, P.; Pascher, T.; Yartsev, A. P.; Isoda, S.; Imahori, H.; Sundstrom, V., Role of Adsorption Structures of Zn-Porphyrin on TiO2 in Dye-Sensitized Solar Cells Studied by Sum Frequency Generation Vibrational Spectroscopy and Ultrafast Spectroscopy. *J Phys Chem C* **2013,** *117* (12), 6066-6080.

20. Long, R.; Casanova, D.; Fang, W. H.; Prezhdo, O. V., Donor−Acceptor Interaction Determines the Mechanism of Photoinduced Electron Injection from

Graphene Quantum Dots into TiO2: π-Stacking Supersedes Covalent Bonding. *J Am Soc Chem* **2017,** *139* (7), 2619-2629.

21. Galoppini, E., Linkers for anchoring sensitizers to semiconductor nanoparticles. *Coordin Chem Rev* **2004,** *248* (13-14), 1283-1297.

22. Kamegawa, T.; Matsuura, S.; Seto, H.; Yamashita, H., A Visible-Light-Harvesting Assembly with a Sulfocalixarene Linker between Dyes and a Pt-TiO2 Photocatalyst. *Angew Chem Int Edit* **2013,** *52* (3), 916-919.

23. Amstad, E.; Gillich, T.; Bilecka, I.; Textor, M.; Reimhult, E., Ultrastable Iron Oxide Nanoparticle Colloidal Suspensions Using Dispersants with Catechol-Derived Anchor Groups. *Nano Lett* **2009,** *9* (12), 4042-4048.

24. Rajh, T.; Chen, L. X.; Lukas, K.; Liu, T.; Thurnauer, M. C.; Tiede, D. M., Surface restructuring of nanoparticles: An efficient route for ligand-metal oxide crosstalk. *J Phys Chem B* **2002,** *106* (41), 10543-10552.

25. Lana-Villarreal, T.; Rodes, A.; Perez, J. M.; Gomez, R., A spectroscopic and electrochemical approach to the study of the interactions and photoinduced electron transfer between catechol and anatase nanoparticles in aqueous solution. *J Am Chem Soc* **2005,** *127* (36), 12601-12611.

26. Notestein, J. M.; Iglesia, E.; Katz, A., Photoluminescence and charge-transfer complexes of calixarenes grafted on TiO2 nanoparticles. *Chem Mater* **2007,** *19* (20), 4998-5005.

27. Park, Y.; Singh, N. J.; Kim, K. S.; Tachikawa, T.; Majima, T.; Choi, W., Fullerol-Titania Charge-Transfer-Mediated Photocatalysis Working under Visible Light. *Chem-Eur J* **2009,** *15* (41), 10843-10850.

28. Xu, C. J.; Xu, K. M.; Gu, H. W.; Zheng, R. K.; Liu, H.; Zhang, X. X.; Guo, Z. H.; Xu, B., Dopamine as a robust anchor to immobilize functional molecules on the iron oxide shell of magnetic nanoparticles. *J Am Chem Soc* **2004,** *126* (32), 9938-9939.

29. Marczak, R.; Werner, F.; Gnichwitz, J. F.; Hirsch, A.; Guldi, D. M.; Peukert, W., Communication via Electron and Energy Transfer between Zinc Oxide Nanoparticles and Organic Adsorbates. *J Phys Chem C* **2009,** *113* (11), 4669-4678.

30. Ooyama, Y.; Inoue, S.; Nagano, T.; Kushimoto, K.; Ohshita, J.; Imae, I.; Komaguchi, K.; Harima, Y., Dye-Sensitized Solar Cells Based On Donor-Acceptor pi-Conjugated Fluorescent Dyes with a Pyridine Ring as an Electron-Withdrawing Anchoring Group. *Angew Chem Int Edit* **2011,** *50* (32), 7429-7433.

31. Massin, J.; Ducasse, L.; Toupance, T.; Olivier, C., Tetrazole as a New Anchoring Group for the Functionalization of TiO2 Nanoparticles: A Joint Experimental and Theoretical Study. *J Phys Chem C* **2014,** *118* (20), 10677-10685.

32. Ciampi, S.; Harper, J. B.; Gooding, J. J., Wet chemical routes to the assembly of organic monolayers on silicon surfaces via the formation of Si-C bonds: surface preparation, passivation and functionalization. *Chem Soc Rev* **2010,** *39* (6), 2158-2183.

33. Hu, P. G.; Chen, L. M.; Kang, X. W.; Chen, S. W., Surface Functionalization of Metal Nanoparticles by Conjugated Metal-Ligand Interfacial Bonds: Impacts on Intraparticle Charge Transfer. *Accounts Chem Res* **2016,** *49* (10), 2251-2260.

34. Chen, W.; Chen, S. W.; Ding, F. Z.; Wang, H. B.; Brown, L. E.; Konopelski, J. P., Nanoparticle-mediated intervalence transfer. *J Am Chem Soc* **2008,** *130* (36), 12156-12162.

35. Hu, P. G.; Chen, L. M.; Deming, C. P.; Kang, X. W.; Chen, S. W., Nanoparticle-Mediated Intervalence Charge Transfer: Core-Size Effects. *Angew Chem Int Edit* **2016,** *55* (4), 1455-1459.

36. Zhou, T. L.; Anderson, R. T.; Li, H. S.; Bell, J.; Yang, Y. A.; Gorman, B. P.; Pylypenko, S.; Lusk, M. T.; Sellinger, A., Bandgap Tuning of Silicon Quantum Dots by Surface Functionalization with Conjugated Organic Groups. *Nano Lett* **2015,** *15* (6), 3657-3663.

37. Kang, X. W.; Zuckerman, N. B.; Konopelski, J. P.; Chen, S. W., Alkyne-Functionalized Ruthenium Nanoparticles: Ruthenium-Vinylidene Bonds at the Metal-Ligand Interface. *Journal of the American Chemical Society* **2012,** *134* (3), 1412-1415.

38. Ding, F. Z.; Wang, H. B.; Wu, Q.; Van Voorhis, T.; Chen, S. W.; Konopelski, J. P., Computational Study of Bridge-Assisted Intervalence Electron Transfer. *Journal of Physical Chemistry A* **2010,** *114* (19), 6039-6046.

39. Peng, Y.; Lu, J. E.; Deming, C. P.; Chen, L. M.; Wang, N.; Hirata, E. Y.; Chen, S. W., Photo-Gated Intervalence Charge Transfer of Ethynylferrocene

Functionalized Titanium Dioxide Nanoparticles. *Electrochim Acta* **2016,** *211*, 704-710.

40. Liu, K.; Song, Y.; Chen, S. W., Defective TiO2-supported Cu nanoparticles as efficient and stable electrocatalysts for oxygen reduction in alkaline media. *Nanoscale* **2015,** *7* (3), 1224-1232.

41. Rivera, E.; Belletete, M.; Zhu, X. X.; Durocher, G.; Giasson, R., Novel polyacetylenes containing pendant 1-pyrenyl groups: synthesis, characterization, and thermal and optical properties. *Polymer* **2002,** *43* (19), 5059-5068.

42. Rivera, E.; Wang, R. P.; Zhu, X. X.; Zargarian, D.; Giasson, R., Preparation of cis-poly(1-ethynylpyrene) using (1-Me-indenyl)(PPh3)Ni-C C-Ph/methylaluminoxane as catalyst. *J Mol Catal a-Chem* **2003,** *204*, 325-332.

43. Hu, P. G.; Song, Y.; Chen, L. M.; Chen, S. W., Electrocatalytic activity of alkyne-functionalized AgAu alloy nanoparticles for oxygen reduction in alkaline media. *Nanoscale* **2015,** *7* (21), 9627-9636.

44. Terekhov, D. S.; Nolan, K. J. M.; McArthur, C. R.; Leznoff, C. C., Synthesis of 2,3,9,10,16,17,23,24-octaalkynylphthalocyanines and the effects of concentration and temperature on their H-1 NMR spectra. *J Org Chem* **1996,** *61* (9), 3034-3040.

45. Fulmer, G. R.; Miller, A. J. M.; Sherden, N. H.; Gottlieb, H. E.; Nudelman, A.; Stoltz, B. M.; Bercaw, J. E.; Goldberg, K. I., NMR Chemical Shifts of Trace Impurities: Common Laboratory Solvents, Organics, and Gases in Deuterated Solvents Relevant to the Organometallic Chemist. *Organometallics* **2010,** *29* (9), 2176-2179.

46. Allen, F. H.; Kennard, O.; Watson, D. G.; Brammer, L.; Orpen, A. G.; Taylor, R., Tables of Bond Lengths Determined by X-Ray and Neutron-Diffraction .1. Bond Lengths in Organic-Compounds. *J Chem Soc Perk T 2* **1987,** (12), S1-S19.

47. Serpone, N.; Lawless, D.; Khairutdinov, R., Size Effects on the Photophysical Properties of Colloidal Anatase Tio2 Particles - Size Quantization or Direct Transitions in This Indirect Semiconductor. *J Phys Chem-Us* **1995,** *99* (45), 16646-16654.

48. Hormann, U.; Kaiser, U.; Albrecht, M.; Geserick, J.; Husing, N., Structure and luminescence of sol-gel synthesized anatase nanoparticles. *Journal of Physics: Conference Series* **2010,** *209*, 012039.

49. Thulin, L.; Guerra, J., Calculations of strain-modified anatase TiO 2 band structures. *Phys Rev B* **2008,** *77* (19), 195112.

50. Patrick, C. E.; Giustino, F., GW quasiparticle bandgaps of anatase TiO2 starting from DFT+ U. *Journal of Physics: Condensed Matter* **2012,** *24* (20), 202201.

51. Wang, Y.; Zhang, H.; Liu, P.; Yao, X.; Zhao, H., Engineering the band gap of bare titanium dioxide materials for visible-light activity: a theoretical prediction. *Rsc Adv* **2013,** *3* (23), 8777-8782.

52. Martsinovich, N.; Jones, D. R.; Troisi, A., Electronic Structure of TiO2 Surfaces and Effect of Molecular Adsorbates Using Different DFT Implementations. *The Journal of Physical Chemistry C* **2010,** *114* (51), 22659-22670.

53. Yao, Z.; Zhang, M.; Wu, H.; Yang, L.; Li, R.; Wang, P., Donor/acceptor indenoperylene dye for highly efficient organic dye-sensitized solar cells. *J Am Chem Soc* **2015,** *137* (11), 3799-3802.

54. Wei, H.; Luo, J.-W.; Li, S.-S.; Wang, L.-W., Revealing the Origin of Fast Electron Transfer in TiO2-Based Dye-Sensitized Solar Cells. *J Am Chem Soc* **2016,** *138* (26), 8165-8174.

55. Long, R.; Casanova, D.; Fang, W.-H.; Prezhdo, O. V., Donor–Acceptor Interaction Determines the Mechanism of Photoinduced Electron Injection from Graphene Quantum Dots into TiO2: π-Stacking Supersedes Covalent Bonding. *J Am Chem Soc* **2017,** *139* (7), 2619-2629.

56. Goldey, M. B.; Brawand, N. P.; Voros, M.; Galli, G., Charge Transport in Nanostructured Materials: Implementation and Verification of Constrained Density Functional Theory. *Journal of Chemical Theory and Computation* **2017,** *13* (6), 2581-2590.

57. Amelia, M.; Lavie-Cambot, A.; McClenaghan, N. D.; Credi, A., A ratiometric luminescent oxygen sensor based on a chemically functionalized quantum dot. *Chem Commun* **2011,** *47* (1), 325-327.

58. Li, X. G.; Liu, Y. W.; Huang, M. R.; Peng, S.; Gong, L. Z.; Moloney, M. G., Simple Efficient Synthesis of Strongly Luminescent Polypyrene with Intrinsic Conductivity and High Carbon Yield by Chemical Oxidative Polymerization of Pyrene. *Chem-Eur J* **2010,** *16* (16), 4803-4813.

59. Briscoe, J.; Marinovic, A.; Sevilla, M.; Dunn, S.; Titirici, M., Biomass-derived carbon quantum dot sensitizers for solid-state nanostructured solar cells. *Angew Chem Int Ed Engl* **2015,** *54* (15), 4463-8.

60. Yun, H. J.; Paik, T.; Edley, M. E.; Baxter, J. B.; Murray, C. B., Enhanced Charge Transfer Kinetics of CdSe Quantum Dot-Sensitized Solar Cell by Inorganic Ligand Exchange Treatments. *Acs Appl Mater Inter* **2014,** *6* (5), 3721-3728.

61. Giannozzi, P.; Baroni, S.; Bonini, N.; Calandra, M.; Car, R.; Cavazzoni, C.; Ceresoli, D.; Chiarotti, G. L.; Cococcioni, M.; Dabo, I., QUANTUM ESPRESSO: a modular and open-source software project for quantum simulations of materials. *Journal of physics: Condensed matter* **2009,** *21* (39), 395502.

62. Garrity, K. F.; Bennett, J. W.; Rabe, K. M.; Vanderbilt, D., Pseudopotentials for high-throughput DFT calculations. *Computational Materials Science* **2014,** *81*, 446-452.

63. Hamann, D., Optimized norm-conserving Vanderbilt pseudopotentials. *Physical Review B* **2013,** *88* (8), 085117.

64. Heyd, J.; Scuseria, G. E.; Ernzerhof, M., Hybrid functionals based on a screened Coulomb potential. *J Chem Phys* **2003,** *118* (18), 8207-8215.

65. Marzari, N.; Vanderbilt, D.; De Vita, A.; Payne, M., Thermal contraction and disordering of the Al (110) surface. *Physical review letters* **1999,** *82* (16), 3296.

66. Sundararaman, R.; Letchworth-Weaver, K.; Schwarz, K. A.; Gunceler, D.; Ozhabes, Y.; Arias, T. A., JDFTx: Software for joint density-functional theory. *SoftwareX* **2017,** *6*, 278-284.

Chapter 7 Summary and perspective

Taken together, the central dogma of electrocatalytic performance is established, which contains 4 levels of design and understand of electrocatalysis: material synthesis, characterization and activity measurement; active sites identification; reaction mechanism understanding and exploration; electronic structure analyzing and manipulating. For rational synthesis of an electrocatalyst, the strategy loop is established with combination of theoretical and experimental works. The charter 2-6 introduces specific works on this loop.

Chapter 2 introduces a novel nitrogen and iron-based carbon nanowires with its excellent ORR activity suppress Pt/C in alkaline electrolyte. The active sites are identified as neighboring carbon of nitrogen atoms and the iron atoms of a FeN_4 structure embed in carbon matrix. In addition, the Stone Wales FeN_4 structure is the leading configuration with the best activity, it also can create nanowrinkles as proved in another work. The source of activity is also found. On one hand, the nitrogen atom with its great electronegativity can withdraw the electrons from neighboring carbon, causing a spin density on it. This process is in favor of the adsorption of oxygenic intermediate species. On the other hand, the d-orbitals of iron in the FeN_4 sites can provide great opportunity for binding of intermediate species.

Chapter 3 introduces a novel nitrogen and ruthenium-based carbon nanowires for HER in alkaline electrolyte. As one of best catalysts among all reported, its activity is much better than the commercial Pt/C, which is considered as best HER catalyst

previously. The most probable active site is RuC_2N_2, instead of RuN_4 or Ru nanoparticles. This site can provide ruthenium and carbon atoms to perform water dissociation efficiently, which process plays important part in HER in the alkaline electrolyte.

In chapter 4, starting from theoretical calculation, it is discovered the Pt single atom and few atom clusters (< 0.9 nm in diameter) on the nitrogen doped carbon have difficulty in ORR, due to their inert properties for oxygen adsorption. Moreover, it is demonstrated the Co dopants in the Pt few atom clusters can have significant activity enhancement. The source of this enhancement is also assigned to the enhanced density of states near fermi level. Experimentally, the series Pt or PtCo based carbon nanowires was synthesized and confirmed what theoretical calculation predicted. Among all of the samples, the one containing active species with PtCo 2-7 atom clusters shows the best mass activity and 48-fold enhancement compared to commercial Pt/C.

Chapter 5 introduces examples for interfacial charge transfer induced electrochemical activity change. The oxygen vacancy doped TiO_2 can donate electrons to Pd nanoparticles and enhance their activity toward ethanol oxidation reaction; In another work, the black phosphorus can donate electrons to Pt, Au and Ag nanoparticles, causing ORR activity decay for Pt and enhancement for Au and Ag.

Chapter 6 introduce a new way of manipulating the electronic structure of TiO_2 by alkyne functionalization. The unique -C≡C-O linkage can not only create a new state

inside of band gap, and also provide efficient one-way channel for electron transferring from ligand into TiO_2 surface.

These works contain every aspects of the strategy loop for electrocatalyst as introduced above. Based on the central dogma, the future research project can be developed from novel material synthesis, active sites identification, reaction mechanism exploration and electronic structure manipulation.

For the first aspect, new material system and novel fabrication techniques can be developed.

As an example of new material system, single atom electrocatalysts have a promising outlook toward a wide range of reactions with their very high atomic utilization, much cheaper price and high sensitivity to the coordinating structure. However, except Pt or Ru single atoms for HER and Fe or Co single atom for ORR, other single atom material and reaction are not reported extensively. This is because the activity cannot be anticipated or discovered straightforwardly due to the high complexity of the geometrical and electronic structure of single atoms. Thus, it's worth exploring and examining the electrochemical behavior of a certain single atom coordination system, in order to lay a solid foundation for summarizing the principles. For example, Ru or Ir single atoms loads on metal oxide can form Ru (Ir)-O-metal bond, which exhibit promising activity for OER. More materials with such coordination structures can be designed in order to attempt to achieve a high OER activity. In another example, Pt, Pd and Rh single atoms on metal or metal oxide may have high

activity for fuel oxidation reaction. Many novel catalysts can be prepared through this direction.

As an example of novel material fabrication techniques, in our current research project, the induction heating method has shown great outlook for synthesis materials. Compare to traditional hydrothermal method and tube furnace pyrolysis method, it has great advantage. Firstly, the induction heating method has very high efficiency, with its ultra-fast temperate increasing and decreasing rate (~10^3 K/s). Thus, the material can be prepared within several seconds. In comparison, the traditional heating method need 2-10 hours. This method provides unlimited opportunity for high-throughput screening of plentiful materials. Secondly, the induction heating can reach an ultrahigh temperature (up to ~2200 °C), way beyond the limit of hydrothermal method (up to ~ 200 °C) and tube furnace (up to 1200 °C). In this way, some new chemical structures maybe obtained in an ultrahigh temperature. Thirdly, the induction heating with fast quenching method can make it possible to achieve a certain phase that only exist in high temperature, such as the Au-Ni alloy nanoparticles, which is impossible to obtain in a traditional heating method due to strong phase segregation. Up to recent, it has been successfully prepared several electrodes with ultrahigh OER activity by induction heating method. I anticipate this method will be adopted widely for preparation nanomaterial in the foreseeable future.

For the level of active site understanding and reaction mechanism study, the works can be carried out from catalyst surface structure characterization, intermediate species identify and theoretical mechanism proposing. Specifically, the OER on metal

oxide surface has great complexity. So, the surface morphology and coordination change should be carefully examined by operando HRTEM and XAS. Moreover, the lattice oxygen change and other intermediate binding can be record by isotope labelling or other new developed methods. With these measurements, the reaction pathway can be better proposed and push forward the theoretical work for better simulation. Besides, the gap between the theoretical active sites activity and actual sample activities need further attention, such as local pH effect, reaction transition state barrier, solvent effect, diffusion problem, etc.

For the level of manipulation activity, more works can be done to observe charge transfer induced activity change and summarize the general principles. Moreover, new methods for interfacial charge transfer can be also developed, such as novel ligand functionalization or synthesis alloying nanoparticles. For example, in our latest study, it is revealed the alkyne ligands can withdraw the electron of an Ir surface hence increase the activity of HER and OER.